GEOMECHANICAL ASSESSMENT OF CONTINUUM-DISCONTINUUM CHARACTERIZATION OF CLAY SHALE CAPROCKS

by

Abeer Heikal

A thesis submitted in partial fulfillment of the requirements for the degree of

Doctor of Philosophy

in

GEOTECHNICAL ENGINEERING

Department of Civil and Environmental Engineering

University of Alberta

ABSTRACT

The Clearwater Formation is a stratigraphic unit of Early Cretaceous (Albian) age that is a laterally continuous unit consisting largely of shale with a minor component of interbedded siltstone or sandstone. Throughout its geological history, the depositional environment of this formation was exposed to complex weathering and loading/unloading processes that transformed and altered the typical sedimentary (argillaceous) formation to an over consolidated material with inherent epigenetic discontinuities such as fissures and fractures. From a stiffness or strength perspective, this clay shale formation can be considered a hard-soil or a soft-rock. For engineering assessment and design involving these clay shale deposits, careful geologic in situ characterization, detailed laboratory testing, and representative numerical modelling are needed.

In Alberta, Clearwater Formation clay shale (CCSh) serves as the caprock for almost all steam assisted gravity drainage (SAGD) projects. Prior to commencing a thermal recovery project, an assessment for caprock integrity is typically carried out to ensure the caprock will serve as an effective containment seal of reservoir fluids over the life of the elevated pressure and temperature SAGD operation. Shallow caprocks (e.g. less than 200 m depth) are generally more vulnerable to deformation due to their low confinement, hence there is a need for a more rigorous evaluation of its behaviour and integrity. This rigorous assessment includes accurate geological characterization including an estimation of normal and shear stiffnesses (K_n and K_s) of the potential discontinuities within a CCSh caprock. To date, limited research has been conducted on these properties with most approaches adopting assessment methods developed for fractured hard rocks.

This research initially examined the discontinuous nature of the CCSh through the processing of a unique light detection and ranging (LiDaR) dataset captured for an exposed mining bench of the Clearwater Formation. The LiDaR point cloud was used to extract the fracture

characteristics in the CCSh using MATLAB scripting and successfully constructed a 3D triangulated irregular network (TIN). A geologically constrained discrete fracture network (DFN) was subsequently built based on the LiDaR dataset.

Finite element analyses were conducted to explore the potential differences in fracture deformation mechanisms between a hard rock and hard soil/soft rock. The finite element models were validated against corresponding laboratory mechanical responses where subsequent analyses confirmed the expected response that fractured soft rock masses do not follow typical deformability and compliance conventional relationships developed for hard rock masses. A new boundary-identification scheme to identify the transition from soft rock to hard rock conditions was proposed based on a rock mass compliance ratio.

Three dimensional geomechanical simulations were conducted of a CCSh caprock (CCShC) overlying a SAGD reservoir. The simulations were conducted in order to determine the extent to which overburden confinement, caprock discontinuity configuration and the SAGD MOP affect caprock deformability. It was found that, mechanically modelling the fractured CCShC above SAGD as a continuum results in an inaccurate estimation of the surface uplift. The latter may lead to forming undesirable pathways within the caprock for the pressurized fluids underneath it, compromising the caprock basic hydraulic seal.

The three-dimensional distinct element code (3DEC) was used to study the equivalent mechanical parameters and representative elementary volume (REV) of a soft rock mass considering strength anisotropy and scale effect. Following various attempts, a mechanical REV could not be estimated for the soft CCSh. In addition, the equivalent mechanical parameters could not fit in a tensor form. Accordingly, the soft CCSh cannot be represented in an equivalent continuum model form. This provided additional evidence that soft rocks do not behavior in a

similar manner to hard rocks, and the mechanical models developed based on a hard rock matrix assumption must not be applied to soft rock masses such CCSh.

To constrain the values of normal (K_n) and shear stiffness (K_s) of fractures in a soft CCSh, results of consolidated drained (CD) direct shear laboratory tests on pre-existing discontinuities within CCSh specimens were analyzed. Based on numerical simulations of the tests, K_n and K_s of pre-existing discontinuities were estimated. A novel approach was introduced to generally estimate the K_n of discontinuities in soft rock masses at zero change of pore pressure using 3D coupled (hydromechanical) numerical simulations. While in general for hard rock systems, K_s will increase or remain constant for increasing discontinuity displacement, for the soft rock CCSh specimens analyzed, K_s was found to decrease with increasing discontinuity displacement.

ACKNOWLEDGMENT

I would like to start by expressing huge gratitude I own to all my family members for their understanding, support, patience, and love they generously provided me over the course of my study.

Thanks, and gratitude to my supervisor Dr. Rick Chalaturnyk who always helped, supported, advised and cooperated greatly with me over years. Many thanks to every member of my supervisory committee for their constructive feedback and valuable comments that enriched the final product of my research.

I wish to thank colleague Abel Sánchez Juncal for his help and advice in reviewing parts of the FISH language scripts and 3DEC codes soundness. I would like to thank colleagues; Marzieh Salami, Hossein Akbarzadeh, Dr. Stephen Talman, Keivan Khaleghi, Alireza Rangriz Shukri, Amir Haghi, Lang Liu, Alireza Khani and Alireza Ashrafi Moghadam for their feedback and input over the course of the thesis preparation. Also, the help from Nathan Deisman and Gonzalo Zambrano is much appreciated.

The members of the University of Alberta Center for writers and Academic Success Center (ASC) helped a lot in enhancing this thesis writing quality. Also, the financial support from the Energi Simulation Consortia industrial sponsors is much appreciated.

TABLE OF CONTENTS

LIST OF TABLES

LIST OF FIGURES

NOMENCLATURE

[C]	Compliance Tensor
[S]	Stiffness Tensor
2D	Two-Dimensional
3D	Three-Dimensional
3DEC	3D Distinct Element Code
AFN	Analogue Fracture Network
ASPRS	American Society for Photogrammetry and Remote Sensing
C	Compliance Tensor
CAE	Complete ABAQUS Environment
CCSh	Clearwater Clay Shale
CCShC	Clearwater Clay Shale Caprock
$\mathbf{C_d}$	Discontinuity Compliance
CHILE	Continuum-Homogeneous-Isotropic-Linear-Elastic
$\mathbf{C_m}$	Rock Matrix Compliance
CP	Confining Pressure
CS	Clay Shale
CV	Coefficient of Variation
DDA	Discontinuous Deformation Analysis
DEM	Discrete Element Method/Modelling
DgEM	Digital Elevation Model
DFN	Discrete Fracture Network
DFIT	Diagnostic Fracture Injection Test
DIANE	Discontinuous-Inhomogeneous-Anisotropic-Non-Elastic
DM	Deformation Modulus
DSE	Discontinuity Set Extractor
E	Young's Modulus or Modulus of Elasticity
$\mathbf{e^e}$	Elastic Strain
$\mathbf{E_i}$	Intact Modulus of Elasticity
$\mathbf{e^p}$	Plastic Strain
$\mathbf{E_{RM}}$	Rock Mass Modulus of Elasticity
FE	Finite Element
FEA	Finite Element Analysis
FEM/DEM	Finite Element Method/Discrete Element Method
FKM	Fuzzy K-Means
FME	Feature Manipulation Engine
FPZ	Fracture Process Zone
G	Shear modulus
GIS	Geographical Information System software
GMU	Geomechanical Unit
GUI	Graphical User Interface
InSAR	Interferometric Synthetic Aperture Radar
ISRM	International Society of Rock Mechanics
JCS	Joint wall Compressive Strength

JKN	Joint Normal Stiffness
JKS	Joint Shear Stiffness
JRC	Joint Roughness Coefficient
K	Bulk Modulus or Stiffness Tensor
K_n	Normal Stiffness
K_s	Shear Stiffness
LASER	Light Amplification by Stimulated Emission of Radiation
LCC theory	Linear Comparison Composite theory
LiDaR	Light Detection and Ranging
MC	Mohr-Coulomb constitutive model
MOP	Maximum Operating Pressure
NMD	Nodal Mixed Discretization
OB	Overburden
OC	Over Consolidated
OCR	Over Consolidation Ratio
OpenGL	Open Graphics Library
P21	Areal discontinuity intensity – Discontinuity length in unit area
P32	Volumetric discontinuity density – Discontinuity area in unit volume
PCL	Point Cloud Library
P-Sample	Samples are loaded in direction parallel to layering
REV	Representative Elementary Volume
RGB	Red-Green-and Blue
RMIB	Real Multi-dimensional Internal Bond
SHP	Shapefile shape format (GIS)
SRM	Synthetic Rock Mass
SS	Strain Softening constitutive model
S-Sample	Samples loaded in direction perpendicular to bedding
UC	Uniaxial Compression
UCS	Uniaxial Compressive Strength
UDEC	Universal Distinct Element Code
VMIB	Virtual Multi-dimensional Internal Bond
VRMLab	Virtual Rock Mass Laboratory
Y	Young's (elasticity) modulus
η	Packing density
ν	Poisson's ratio

CHAPTER 1 INTRODUCTION

1.1 INTRODUCTION

Rock masses contain non-uniform and irregular discontinuities of varying sizes, orientations, and locations, and these discontinuities have complex geometry with considerable uncertainties. In order to represent these rock masses in engineering applications, equivalent parameters are typically used in assessment and design. The equivalent strength of a discontinuous rock is an important factor in design and construction of civil, mining and petroleum engineering fields.

In western Canada and specifically Alberta, Clearwater clay shale (CCSh), often classified as a hard soil/soft rock, is a very crucial lithology since it serves as the primary caprock for most thermal in situ bitumen recovery projects. The CCSh's hydro-geomechanical characteristics are known for their anisotropic heterogeneous response due to the presence of various sorts of natural discontinuities - "*It's the Cracks that Matter*!" (La Pointe, 2012).

1.2 BACKGROUND

Canada is endowed with significant crude oil resources, estimated as nearly 2.2 trillion barrels of oil in place, although these oil deposits represent some of the most challenging in the world to develop. Canada is the top supplier of oil imports to the United States where Alberta alone is responsible for approximately 71.2 % of Canada's oil exports to the United States (AER, 2016). Almost 60 % of these exports (ASIA, 2010) are from the oil sands region seen in Figure 1-1. Typically, the bitumen in the oil sands is immobile at 8^{o} C. The production can be via surface mining or in situ enhanced recovery methods. The in situ production technologies of oil sands include:

1. Primary Oil Recovery
2. Cyclic Steam Stimulation (CSS)
3. Steam Assisted Gravity Drainage (SAGD)

Over the past two decades, the SAGD process has been field-tested and commercially expanded within the Lower Grand Rapids and Clearwater Formations in the Cold Lake area (Figure 1-1) in Alberta.

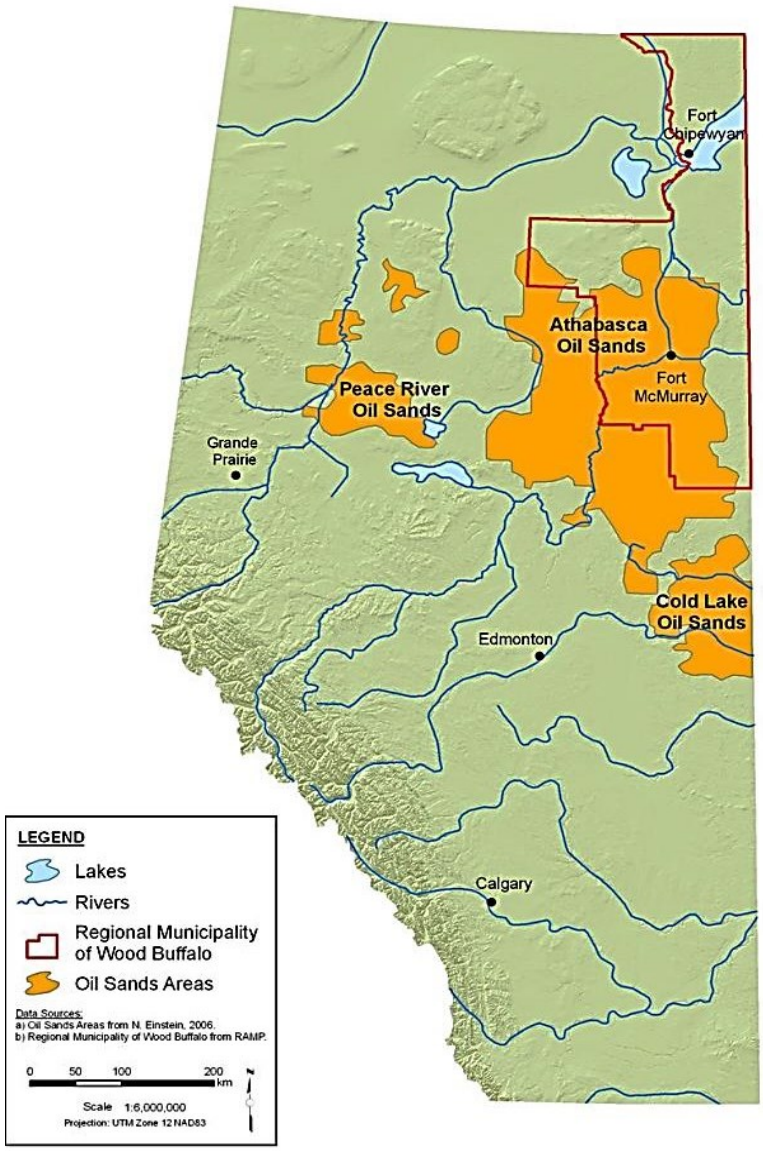

Figure 1-1 Oil sands regions of Alberta (Einstein, 2006)

In a typical SAGD process, the caprock is defined as the basic seal for and containment of steam and associated reservoir fluids (water and bitumen). The caprock is a "nonpermeable" stratum that efficiently traps oil, gas and/or water, preventing their migration to the surface. Accordingly, the caprock must also be able to effectively withstand stresses and strains induced from SAGD operations throughout the decades-long life of reservoir development (Uwiera et al., 2011). The main safety and design considerations in every caprock integrity assessment, as illustrated in Figure 1-2, are seal' integrity, capacity and continuity. In geotechnical engineering, these three basic considerations can be interpreted as deformability, strength and stress-dependent permeability.

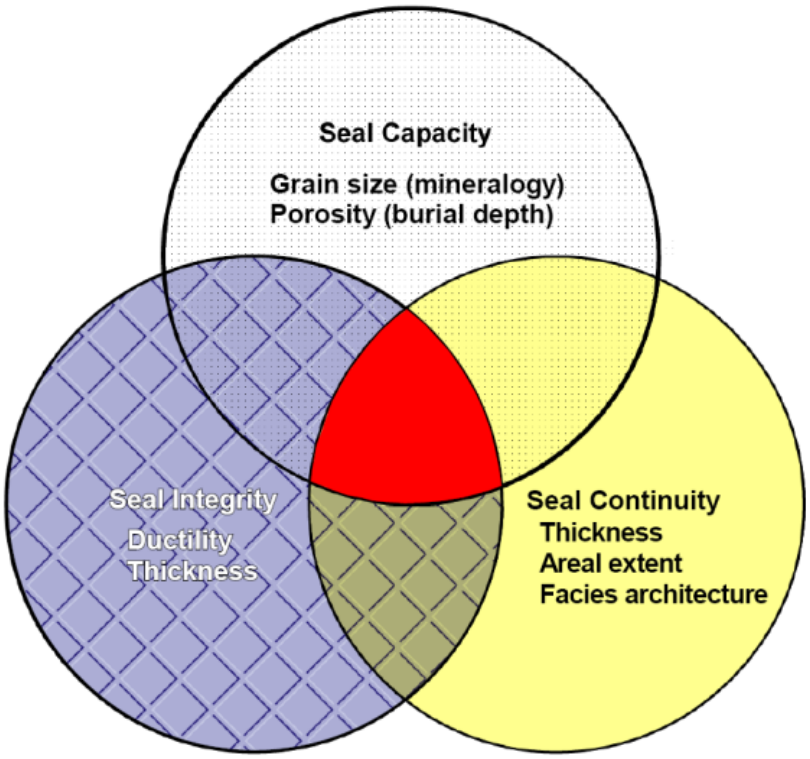

Figure 1-2 Seal integrity (Suter & D'Onfro, 2000)

An example of the consequences of a loss of caprock integrity occurred in 2006, when excessive steam injection pressure at the Joslyn Creek SAGD Project northwest of Fort McMurray, Alberta resulted in a breach of the reservoir caprock, creating a football field size crater on the ground surface (Figure 1-3) and blasting rocks hundreds of meters in the air. Of interest to this research was that the preliminary design report for the Joslyn project stated that the CCSh (the approved uppermost barrier/caprock for Joslyn Creek SAGD project) had a consistent thickness of 20 to 30 meters, had no pre-existing discontinuities, and was a good barrier to vertical flow (ERCB, 2010).

More recently, flow-to-surface events as a result of flow paths that developed in overlying caprocks was detected in 2014 at CNRL's Primrose Cyclic Steam Stimulation (CSS) oilsands project. It is suspected that bitumen leaks began in the summer of 2013 and continued leaking for months, eventually resulting in the release at surface of 7409 barrels of bitumen, and requiring the drainage of a water body and the removal and disposal of 82,508 tonnes of contaminated soil and vegetation (CNRL, 2015). In their report, CNRL acknowledged that the caprock could have been breached, through natural discontinuities.

Different scales of discontinuities form in rock masses as a result of geological processes such as diagenesis, loading, unloading, karsting, desiccation, and weathering resulting in a heterogeneous and anisotropic rock mass. Mechanical anisotropy influences the rock mass behaviour and seepage properties to a large extent (WeiZhong, Jianping, XianJun, & HongDan, 2011) nonetheless the discontinuity distribution patterns and properties produce not only a rock mass with anisotropic response, but also a significant scale effect on the value of its deformation modulus (Jianping, WeiZhong, Diansen, & Jingqiang, 2015).

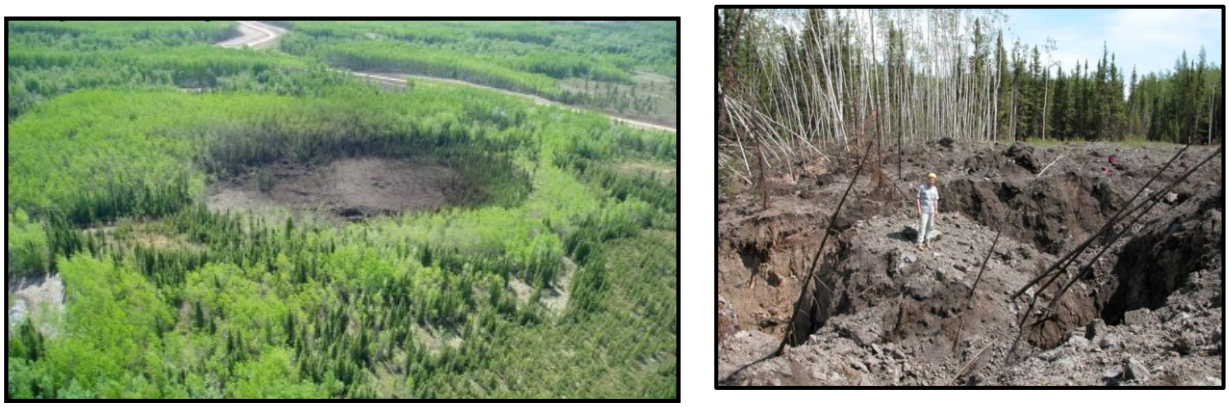

Figure 1-3 Joslyn Creek SAGD Project steam-release (ERCB, 2010)

In Western Canada, the Clearwater Formation, seen in Figure 1-4, typically consists of a grey, heavily faulted and jointed, over-consolidated silt/clay, and fully saturated clay shale, of an 'intermediate' to 'high' plasticity. The Clearwater Formation is a sequence of marine shales with occasional thin, argillaceous to silty sands that are not hydrocarbon-bearing (Laricina Energy Ltd. 2012). The CCSh is characterized by a preferably oriented micro-structure which resulted in a distinct anisotropy of its hydraulic and mechanical properties.

Clay shale generally has a very low permeability and is a very competent caprock; however, its overall integrity is difficult to assess. The main concerns about the Clearwater clay shale caprock (CCShC), include; their unforeseeable deformability, presence of complicated natural fracture networks, as seen in Figure 1-4, unpredictable evolution of new discontinuities and dramatic permeability changes.

A permeability increase of several orders of magnitude may generally be induced in a caprock due to coalescence of newly connected porosity as it deforms above a developing SAGD steam chamber. The favorable long-term isolation properties of an intact CCSh could be compromised by the disturbance and stresses induced from high-pressure-high-temperature long

term SAGD activities. Experimental research ((Warpinski & Teufel, 1992) and (J. Zhang, Standifird, Zhang, Roegiers, & Zhang, 2007)), empirical correlations (Lianyang Zhang, 2013) and field testing ((Pratt, Swolfs, Lingle, & Nielsen, 1977), (Lorenz et al., 1988), (Mayne, 2001), (J. Rutqvist, 2015), and (Frash et al., 2016)) confirmed that stress-deformation behaviour in discontinuities is a key factor governing their permeability tensor. Moreover, in a hydro mechanical coupling numerical simulation, based on laboratory and field data, it has been found that, the permeability of discontinuous rock masses tends to be most sensitive to stress changes at shallow depths (low stress) and in areas of low in situ permeability (Rutqvist & Stephansson, 2003).

Figure 1-4 Exposed CCSh in Alberta (personal communication)

Equivalent continua of hard rocks such as granite, basalt, limestone, chalk, sandstone, and marble have been studied extensively unlike the case of discontinuous mudrocks and/or weak clay shales. Hard rocks behave and deform differently than weak/soft mudstones (hard soil/soft rock formations) such as the CCSh. The circumstances, under which each was formed, deposited, compressed, and diagenetically altered are dissimilar.

The problem in understanding the clay shale mechanical behaviour is that, it is not solely deforming along the pre-defined grain contacts/intact rock boundaries, but the intact rock (rock

matrix) itself is deformable unlike hard rocks hence the soft rock matrix appreciably contributes to the rock mass deformability. The situation becomes even more complex considering that new discontinuities evolve as the CCSh deforms above an enlarging SAGD pay zone and steam chamber.

1.3 CHALLENGES FOR CAPROCK INTEGRITY ASSESSMENT

For subsurface injection/production processes, such as SAGD that typically last for tens of years, maintaining caprock integrity over decades to protect groundwater and surface infrastructure is important. Caprock integrity is a central issue in thermal stimulation projects involving steam-assisted-recovery processes as SAGD (Collins et al., 2013). SAGD operations may induce significant increase in pore pressure, temperature and volumetric deformation in the reservoir consequently stressing the overlying caprock, as depicted in Figure 1-5. These consequences can potentially lead to shear and/or tensile failures that may result in forming flow paths through the caprock (Pathak et al., 2014).

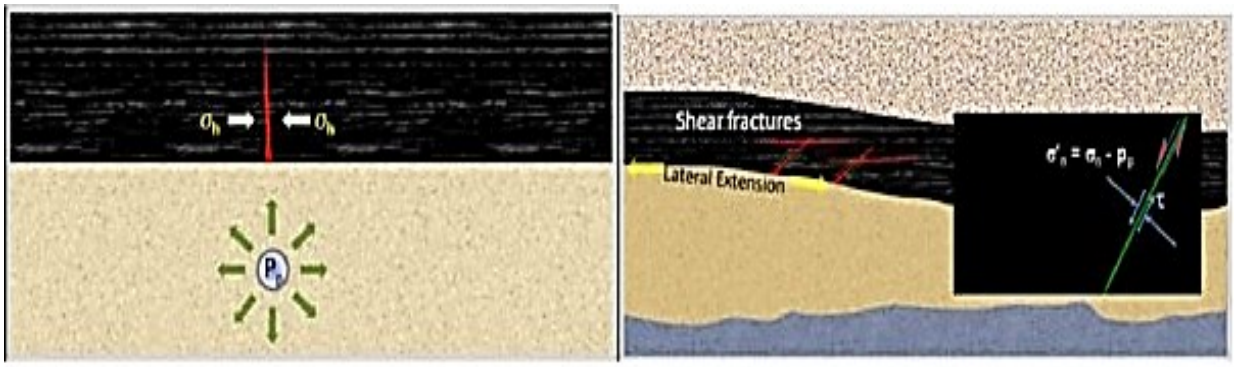

(a) (b)

Figure 1-5 SAGD induced stresses under caprock and possible caprock failure mechanisms (a) tesnile failure or hydraulic fracturing and (b) shear failure or fault reactivation (Khan et al., 2010)

Integrity assessment methods typically involve core sample acquisition for laboratory testing and numerical simulation studies. For the CCSh caprock interval, these methods may face challenges due to the highly overconsolidated state of the material. For instance, without careful attention to the drilling mud selected for coring operations, the CCSh core can imbibe excess water leading to specimen damage. In addition, exposure of the specimens to air can result in desiccation-related damage. Consequently, careful attention is required when selecting coring mud and core preservation techniques (Yuan, et al., 2013). Assuming core damage is minimized, laboratory

testing undertaken to develop constitutive parameters is almost always conducted on intact specimens. While this provides valuable information on the compressive strength, stiffness and permeability of intact CCSh, discontinuities present in the CCSh would suggest it is the rock mass properties rather than intact properties that is of the paramount importance in the caprock integrity assessment. It is a challenge, however, to reliably determine the attributes and properties of these discontinuities; roughness, persistence, normal stiffness, shear stiffness, etc., for this hard soil/soft rock material.

Ultimately, both the intact and discontinuity properties must be combined in defining the appropriate rock mass properties for numerical simulation studies conducted as part of caprock integrity assessments. Currently models used in these simulation studies, however, have conventionally assumed continuum, homogeneous, isotropic, linear elastic (CHILE) behavior for the CCSh caprock. As Figure 1-4 illustrated, CCSh formations are very much discontinuum materials and clearly are inhomogeneous. Despite the obvious discontinuous nature of the CCSh, there are many caprock integrity assessment submission to the Alberta Energy Regulator (AER) assigning constant mechanical parameters such as modulus of elasticity (E), Poisson's ratio (ν) and uniaxial compressive strength (UCS), to define the behaviour of the CCSh in simulation studies. Methodologies for establishing these parameters for discontinuous CCSh formations remains irresolute, in particular, methods for establishing appropriate representative element volumes (REVs) that are used to define an equivalent continuum rock mass model.

The equivalent continuum media approach, REV determination and equivalent mechanical parameters have been extensively studied in hard rocks such as granite, limestone, and marble. Hard soils/soft rocks, such as CCSh, exhibit a fundamentally different geomechanical behaviour than hard rocks since the intact component of the soft rock mass is extremely deformable more than in a hard rock mass (Figure 1-6).

In summary, the challenges discussed above lead to the following series of issues that served as motivations for this research:

- Lack of acknowledging by the practitioners that several classes of discontinuities (e.g. joints, fractures, faults, bedding planes) exist within the hard soil/soft rock CCSh formation;
- Unsuitable application of continuum modelling approaches (i.e. constant E and ν or K and G, i.e. CHILE) to studies of discontinuous CCSh caprock integrity;

- Impact of utilizing equivalent continuum modelling approaches originally developed for hard rock to hard soil/soft rock CCSh material on accurately designing the later;
- Dependence on 2D numerical simulations in caprock integrity assessments whereas discontinuities potentially result in significant three-dimensional response in caprocks overlying SAGD projects; and
- Significant lack of experimental testing results to constrain values of normal and shear stiffness of the CCSh discontinuities.

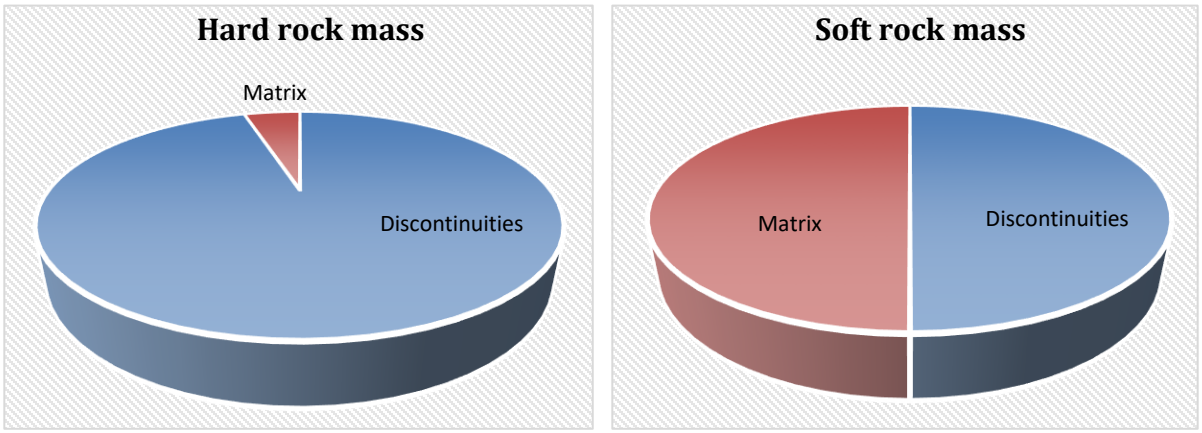

Figure 1-6 Schematic illustrating contribution of matrix versus discontinuities in deformability

1.4 SCIENTIFIC HYPOTHESIS

The scientific hypothesis for this research is that rock mass models originally developed for hard rock (e.g. granites) are not appropriate for describing the geomechanical behaviour of hard soil/soft rock masses (e.g. CCSh).

1.5 RESEARCH OBJECTIVES

Given the importance of CCShC integrity and seal capacity within SAGD operations, there is a necessity for a realistic evaluation and better understanding of the caprock's deformability, strength, stiffness, and potential failure mechanisms. Following from the research challenges identified earlier and the hypothesis established for this research that existing equivalent continuum approaches, originally developed based on hard matrix, are not applicable for deformable, soft fractured CCSh, the objectives for this research are:

1. highlight and illustrate the fundamental differences between hard and soft rocks at different scales;

2. develop a geological and geomechanical characterization procedure for the soft CCSh that allows fracture properties to be determined for this class of materials; and
3. assess how the inclusion of discontinuities in the CCSh impacts the geomechanical response of a CCSh caprock for a SAGD project.

1.6 RESEARCH SCOPE

For the current research, no experimental testing was conducted and all constitutive properties for CCSh were derived from existing laboratory records. For the purpose of caprock integrity assessment, this research has focused on the SAGD process. There are clearly other scenarios where caprock integrity is equally important, such as CO_2 sequestration and cyclic steam stimulation (CSS) but have not been considered within the scope of this research.

1.7 METHODOLOGY AND THESIS OUTLINE

The research objectives are pursued via an integrated use of; literature review, field data, mechanical laboratory testing results, FEA, DEM, 3D coupled numerical simulations and MATLAB scripting. This thesis consists of nine chapters followed by six appendices. Chapter 2 includes a literature review of the discrete fracture network (DFN) evolution, history, techniques, and models developed over time. Chapter 3 presents an important reflection on the geological history of the fractured clay shale in Alberta region. The chapter covers historical processes behind persistence of specific geological features regionally evident in this soft rock formation.

Chapter 4 provides a comparison between hard and soft rock masses at microscale, comparison of strain at failure, mode of failure, deformability, and compliance using existing public data, as well as 2D FEA and 3D DEM with a focus on an initial assessment of the difference between hard and soft matrix assumptions on rock mass geomechanical behavior. Chapter 4 mainly covers the first research objective. For the second research objective, Chapter 5 discusses analyses conducted on a unique LiDaR point cloud dataset acquired for an exposed CCSh mining bench in Alberta. Critically, this dataset allows the identification of geometrical statistics which are required in generating a realistic DFN. An illustration, of how that extracted DFN can be implemented in 3D DEM models for geomechanical modelling purposes, is presented. Chapter 5 is supplemented by Appendix A which provides a detailed description of the systematic procedure followed for the processing of the LiDaR dataset.

Chapter 6 includes an assessment of a discontinuous argillaceous caprock model above SAGD reservoir using 3D geomechanical numerical simulations aiming to fulfill the third research objective. Geomechanical parameters for the simulation were obtained from laboratory results. The DFN statistics were obtained from the field LiDaR dataset analyzed in Chapter 5. This chapter includes a sensitivity analyses on continuum versus discontinuum modelling approaches of fractured CCShC above a SAGD reservoir. Chapter 7 discusses an investigation conducted to examine issues surrounding establishing appropriate representative element volumes (REVs) for CCSh, which is a fundamental element in computing valid equivalent continuum model parameters. Chapter 7 aims to cover the first and second research objectives.

Chapter 8 reports on research conducted to estimate the normal and shear stiffness of natural discontinuities in CCSh based on results of four drained (CD) direct shear tests. This chapter presents a novel approach to estimate the mechanical stiffness in the soft CCSh. The chapter targets covering the second research objective. Chapter 9 is a summary of the conclusions reached in this dissertation, research contributions and recommendations for future research.

CHAPTER 2 HISTORY OF DISCRETE FRACTURE NETWORK

2.1 INTRODUCTION

The failure of rock is an issue in engineering practice and research, as it is directly related to the economy and safety of structures built in/on rocks. How rock fails, is a key element in geotechnical and petroleum engineering practices. The failure of rock generally refers to a rock or rock mass that suffers permanent damage which affects its ability to further sustain load (Zhao, 2010). A rock mass consists of intact rock and various forms of discontinuities. The discontinuities are typically known to play the main role in the deformability and mechanical behaviour of the rock masses (Wang et al., 2013).

A discrete fracture network (DFN) is a modelling approach in which discontinuities are represented as polygons or discs where the orientations, density and other geometrical properties are constrained by geological estimates. A discontinuity or a ‘‘fracture” in a DFN may represent a simple crack, nonetheless it may represent a more complex feature such as a fault zone (McClure & Horne, 2013). Complete geometrical description of a discontinuum rock mass in situ is always difficult due to its three-dimensional nature and the limited access to all needed geological information. Hence a DFN is often used to approximate a real discontinuum system. A DFN is an artificial fracture pattern which is generated stochastically but conditioned by statistics from borehole image interpretation or outcrop mapping observation (Lei et al., 2014).

Statistical analysis of a natural discontinuity system usually involves the identification of discontinuity sets and the estimation of different geometrical properties such as orientation, density and size. There are two fundamentally different concepts to transfer data to models: realistic and stochastic parametrization (Öhman, 2005).

This chapter provides a review of the evolution and development of DFN technique. The review includes the numerical tools developed for reproducing failure mechanisms of a discontinuum rock mass. Importance of studying the geological and structural characteristics of a heterogeneous rock mass is essential in assessing the change in the rock mass’ permeability and porosity.

2.2 CONTINUUM VERSUS DISCONTINUUM APPROACHES

Numerical simulation can be conducted on a geologically conditioned DFN model to estimate the mechanical and hydraulic properties of a discontinuum rock mass (Lei et al., 2014). A continuum approach assumes that, above a certain scale, a discontinuum medium behaves as a continuum. It operates with volume-averaged properties for discretized volumes of a discontinuum rock. The volumetric properties used must be equivalent to the properties of the fracture network within each volume. For its application, the influences of heterogeneous details must average out within the rock volume, such that the medium behaves as a homogeneous medium at some scale.

The deformation problem of discontinuum rock masses can make use of either an implicit (equivalent continuum) approach (Reyes & Osisanya, 2002) or an explicit (discrete) approach (Zhang et al., 2013) and (Ortega, 2010). The former DFN approach is distinct from effective continuum modelling, as it averages fracture properties into effective properties over volumetric grid blocks (Warren & Root, 1963; Kazemi et al., 1976; Lemonnier & Bourbiaux, 2010; and McClure & Horne, 2013). While, the latter considers the geological and mechanical properties of each fracture deterministically and is often adopted for large-scaled fractures (Chen et al., 2012).

The need to use implicit or explicit approaches depends on the size (scale) of the fractures with respect to the scale of the problem that needs to be solved, as illustrated in Figure 2-1. There are no clear quantitative guidelines to determine when one approach should be used instead of the other. The applicability of the implicit approach for the deformation problem of discontinuum rock masses is linked to the elastic compliance matrix and representative elementary volume (REV) (Chen et al., 2012). This will be explored in detail in Chapter 7.

The DFN simulations avoid the volume averaging required for traditional equivalent continuum models and can generally represent a wider range of transport phenomena. Displacements obtained for a discontinuum model is much more similar to those occurring in reality due to how that model is closely representing the media (Bagheri, Shafiezadeh, & Hajihassani, 2006). A discontinuum analysis generally predicts displacements higher than a continuum analysis.

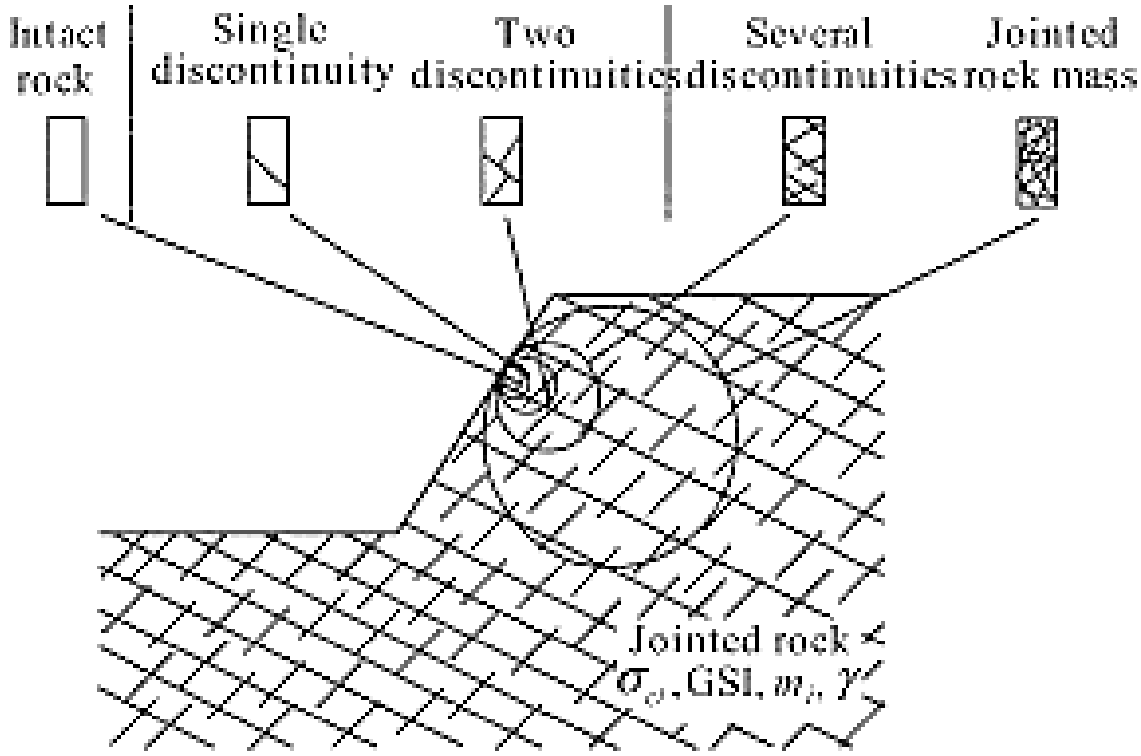

Figure 2-1 Rock mass scale effect clarifying continuum/discontinuum problems (Li, Lyamin, & Merifield, 2009)

2.3 DFN HISTORY

The DFN concept is considered the most realistic representation of fractures, as it accounts for individual fracture' pattern, geometry and connectivity of the network. Fracture network data are compiled from one dimensional or two-dimensional geologic observations (e.g., boreholes and trace maps). To parameterize its underlying true three dimensional fracture network, these data need to be extrapolated into the third dimension (Öhman, 2005). DFNs mimic natural discontinuum media by representing each discontinuity individually. DFN models have been used in a variety of studies in two dimensions (Long et al., 1982; Dershowitz, 1984; Endo et al., 1984; Robinson, 1984; and Smith & Schwartz, 1984) and in three dimensions (e.g., Amadei & Goodman, 1981; Shapiro & Andersson, 1985; Elsworth, 1986; Andersson & Dverstorp, 1987; Cacas et al., 1990; and Long et al., 1992). DFN simulation techniques could be in 2D (Blum et al., 2009 and Bidgoli, 2014) or 3D DFN (Zhang et al., 2013; Fox et al., 2007; Davy, Le Goc, & Darcel, 2013; and Wang et al., 2013) as illustrated in Figure 2-2. A three-dimensional numerical model in which fractures are represented as finite surfaces with specified mechanical and hydraulic properties (Fox et al., 2007).

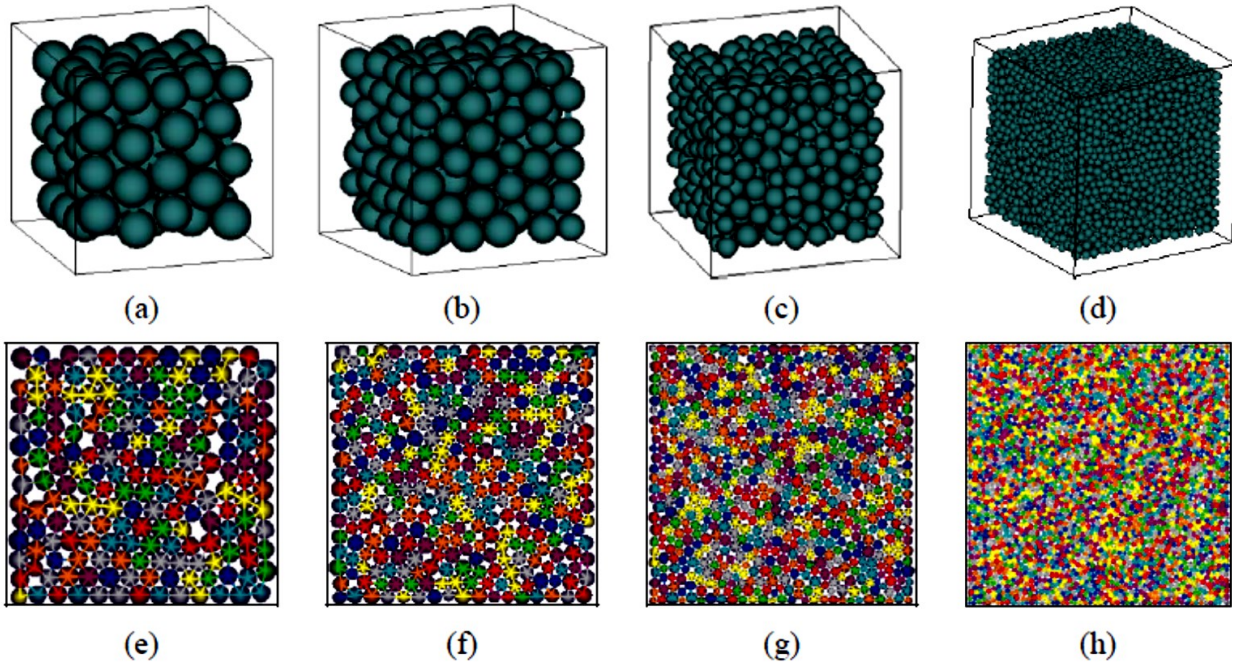

Figure 2-2 Different 3D (a-d) and 2D (e-h) model arrangements (Zhao, 2010)

2.4 DISTURBANCE FACTOR

The choice to use the DFN is affected by the rock mass disturbance factor. Figure 2-3 (a) shows a road cut in which the size of individual rock blocks is of the same order as the height of the cut. Rock mass classifications, based on the assumption of homogeneity, cannot be applied to this rock mass. However, Figure 2-3 (b) shows an excavated slope in the Chuquicamata open pit mine in Chile (Hoek & Diederichs, 2006). These slopes are 850 m high and individual rock mass units are treated as homogeneous.

2.5 ANALOGUE FRACTURE NETWORK (AFN)

(Lei et al., 2014) introduced an analogue fracture network (AFN) which can be obtained from geological mapping. It is often used to realistically characterize the geometrical attributes of a naturally discontinuum system. The AFN helps in describing the fracture pattern geometry in rock volumes of interest. Actual rock outcrops and the AFNs typically involve complicated intersections, terminations, bends and segmentations. Multiple AFN realizations could be created using the statistics of the analogue pattern. Statistical analysis need to be implemented by employing a suite of methods and characteristic parameters extracted from the AFN fracture state, including identification of fracture sets and geometrical characterization of fractures such as

orientation, length and density. The AFN and DFNs show certain similarity in their cluster frequency and proportion distributions. Multiple DFN realizations could be created using the statistics of an analogue pattern (Lei et al., 2014).

(a) (b)

Figure 2-3 Two different cases illustrating disturbance effect (Hoek & Diederichs, 2006)

2.6 DFN GENERATION TECHNIQUES

Several techniques can be adopted to generate a DFN such as Monte Carlo, fuzzy K-means, Fisher distribution, etc. Brief summaries of these techniques are provided below.

2.6.1 MONTE CARLO METHOD

The structural characteristics (midpoint, dip direction, dip angle, and trace length) of the fractures are correlated with each other. These correlations require several extra field measurements, which in engineering practice are difficult to obtain (Chen et al., 2012). Hence Monte Carlo method (Wu et al., 2012, Lu et al., 2013, and Zhang et al., 2013) is often used to generate DFNs in a sampling window to help in successfully building the DFN using statistical based algorithms.

2.6.2 FUZZY K-MEANS ALGORITHM

Fuzzy k-means clustering algorithm typically works on objects that can be represented in a certain dimension vector space and its distance measure is defined. Fuzzy (soft) clustering is a form of clustering in which each data point can belong to more than one cluster. The fuzzy k-means (FKM) procedure of Dunn and Bezdek (1981) allows each feature vector to have a degree

of membership in a cluster. The fuzzy k-means algorithm has been used to automatically cluster analogue fractures into sets based on their orientations. The orientation of a curved fracture is usually determined by the length-weighted average of all its segments (Lei et al., 2014).

2.6.3 FISHER DISTRIBUTION

Another commonly used statistical technique is the Fisher Distribution (Fisher 1953). Fisher distribution, also called continuous distribution, can fit fracture orientation in a given fracture set on the basis of statistical measurements, such as pole clusters. Fisher distribution parametrization has been used in DFN discussed in (Baghbanan & Jing, 2007). Its wide applicability and ease of use make the Fisher distribution the most commonly adopted technique for fracture orientation in a DFN generation.

2.6.4 POISSON MODELLING APPROACH

Poisson point statistical process (or Poisson statistical process) is one of the most widely used counting processes that randomly distributes points in a mathematical space. Baecher et al., (1983) developed a Poisson disk model in which the locations of the fractures are represented by their barycenters with seeding simulated using the Poisson process, while other properties are modelled by Monte Carlo sampling of corresponding probability distribution functions (Öhman, 2005). Poisson disk model has been continuously developed and has become popular and commonly used within DFN generation approaches; e.g. to investigate the geomechanical and hydraulic behaviour of discontinuum rock masses studied in (Lei et al., 2014).

2.6.5 COHESIVE-ZONE APPROACH

The progressive failure of a rock material can be modeled using a cohesive-zone approach; a technique that was first introduced in the context of the elasto-plastic fracturing of ductile metals. This approach aims at capturing the non-linear interdependence between stresses and strains that characterizes the zone ahead of a macro-crack tip known as the fracture process zone (FPZ). As depicted in Figure 2-4, the FPZ in brittle rocks manifests itself in a form of micro-cracking and interlocking related to the presence of micro-scale inhomogeneities (i.e. mineral grains and pre-existing defects or voids) (Lisjak et al., 2014). When using the cohesive-zone model, the failure of the material progresses based solely on the strength degradation of interface elements and therefore

emerges as a natural outcome of the deformation process without employing any additional macroscopic failure criterion. Since the material strain is expected to be localized in the cohesive zone, the bulk material (i.e., the continuum, or discontinuum, portion of the model) is treated as linear-elastic material using constant-strain triangular elements (Lisjak et al., 2014).

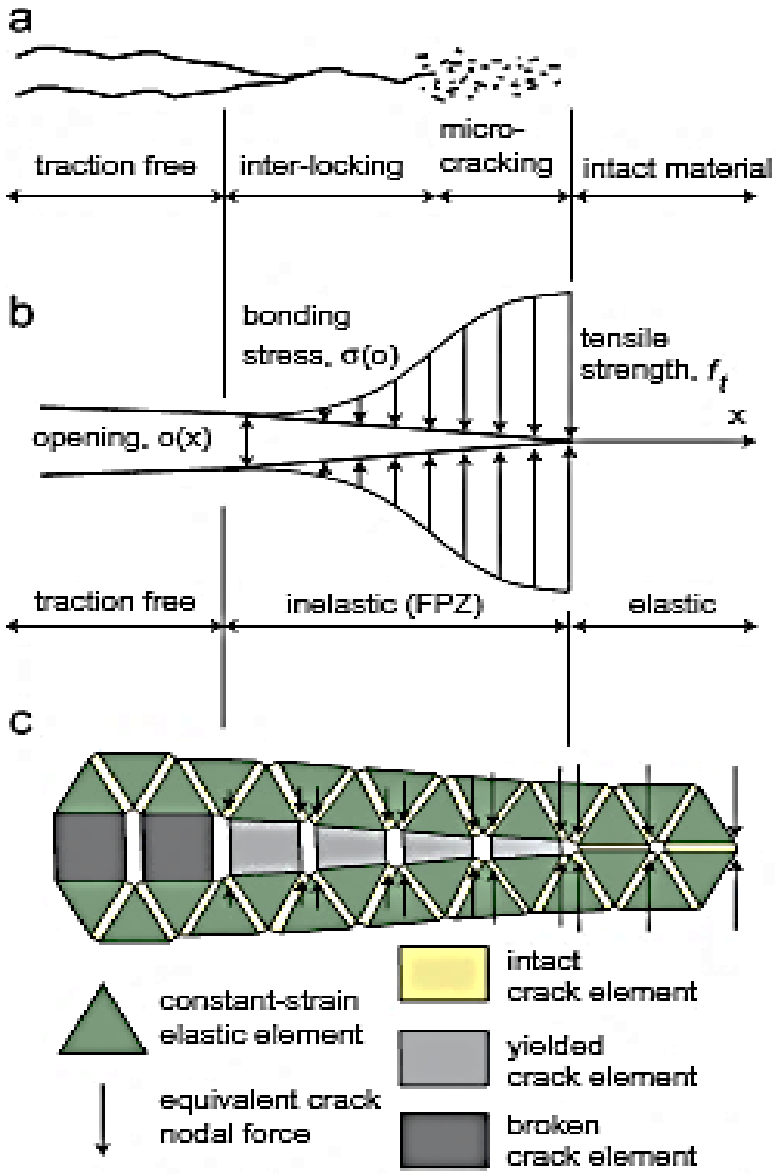

Figure 2-4 Cohesive-zone approach for material failure modelling in FEM/DEM (Lisjak, Grasselli, & Vietor, 2014)

2.7 FIELD GEOLOGICAL MEASUREMENTS

A real fracture network can be extracted from a geological map of a rock outcrop in situ. The field investigation can be carried out via:

- Geological Mapping (from borehole or trace maps) such as using ShapeMetriX 3D;
- Geophysical;
- Stereology; or
- X-Ray Micro Computed Tomography (CT) (Mahabadi et al., 2012).

The geological parameters typically measured in the field include fracture orientation, trace length, spacing, and areal intensity (P21) (Zhang et al., 2013).

2.8 DFN GEOMETRICAL COMPONENTS

Recently, some techniques started to powerfully emerge, e.g. LiDaR, as a field data capturing technique (Hardebol et al., 2015) that could be conveniently used to characterize realistic geometrical components needed for a DFN construction. The geometrical components of a DFN include aperture, length, orientation, spacing and density. Einstein et al. (1983) used a fracture system model which incorporated orientation (Wang et al., 2013), spacing, fracture length and rock bridge length to analyze the effect of fracture persistence on slope stability (Lei et al., 2014). The following subsections list these geometrical properties of fracture-related parameters in detail.

2.8.1 APERTURE

Fracture aperture is the perpendicular width of an open fracture; it is spatially variable and has complex configurations depending on fracture wall roughness, gouge, degree of mineral infill and lateral continuity. Detailed information concerning apertures is rarely available in practical cases due to how difficult it is to assess this in situ. DFN models often employ different types of "equivalent apertures" to automatically describe the aperture (Öhman, 2005). Aperture is critical in porosity and permeability estimations as stresses and deformations of the system vary.

2.8.2 LENGTH

A fracture length basically and traditionally implies its persistence. It is an important parameter as it negatively affects the rock mass integrity. Quantitative assessment of the connectivity state of fracture patterns can be evaluated using the distribution analysis of fracture cluster mass. That distribution analysis is defined as the total length of all member fractures in a cluster (Lei et al., 2014).

2.8.3 ORIENTATION

The orientation statistics are usually interpreted with a discrete probability distribution, through which DFNs are regulated to share same fracture orientation dataset with the original AFN to enhance their similarity (Lei et al., 2014). The principal of layering orientation was presented in (Lisjak et al., 2014). Fracture orientation is crucial in assessing a rock mass stability as well as potential failure mechanisms.

2.8.4 SPACING

Tollenaar (2008) found that the caveability in his model was most sensitive to changes in fractures spacing. Moreover, this geometrical element significantly affects the rock mass integrity.

2.8.5 DENSITY

Location of a fracture is represented by its barycenter, which is defined as the midpoint of a fracture trace (Blum et al., 2009 and Wang et al., 2013). The concept of 'fracture density cells' was introduced to analyze the spatial heterogeneity of fractures. In this concept, the whole domain is divided into a series of sub-regions with fracture density (Figure 2-5) (i.e. the number of fractures by unit area (P21)) calculated separately in an analogue barycenter pattern.

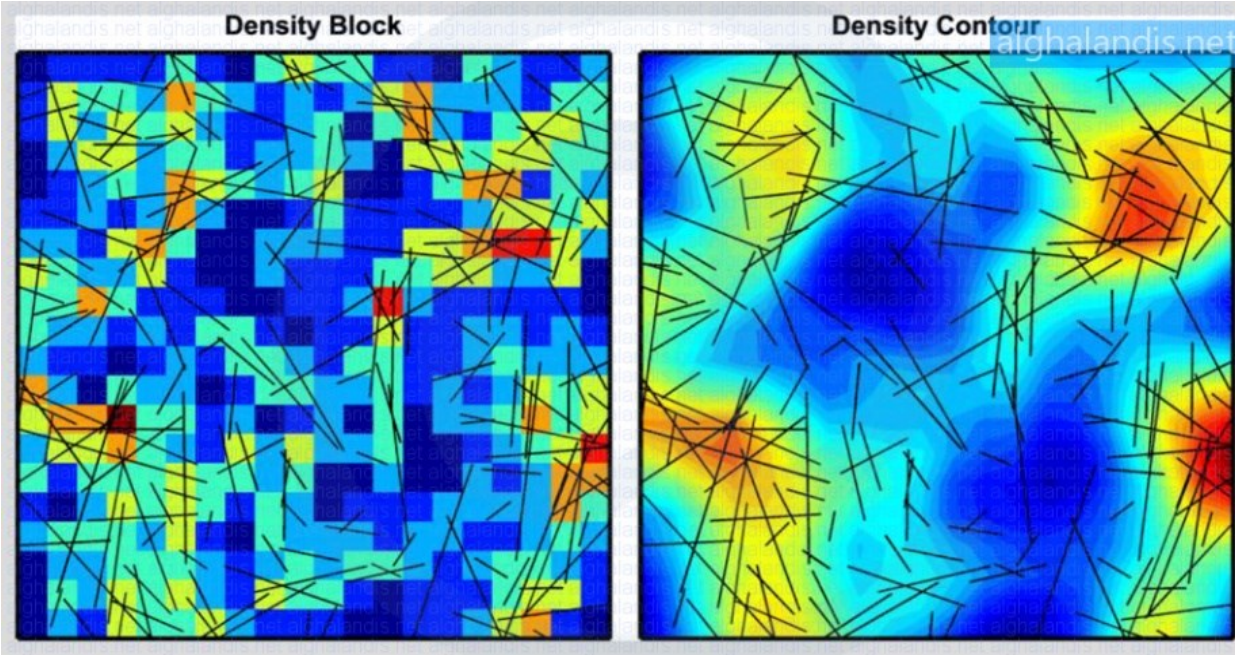

Figure 2-5 Density block and contour (Lei et al., 2014)

2.9 MATLAB

In 2011, Markovaara-Koivisto and Laine proposed a MATLAB script, for DFN generation, which was used in modelling of the hydraulic behaviour of a discontinuum media. The introduced MATLAB script was basically developed for visualizing results from scanline surveys as traces in 2D and disks in 3D. The script was able to cluster orientation data to present statistical summaries and reflect the change in degree of rock brokenness along a scanline (Markovaara-Koivisto & Laine, 2011). In 2016, Alghalandis introduced Alghalandis DFN Engineering (ADFNE) an open source software for DFN engineering in two and three dimensions. The software is a package of computer codes in MATLAB language syntax which consists of:

a) functions to generate fracture networks in two and three dimensions based on stochastic modelling principals,
b) functions for simplification of visualization of two- and three-dimensional fracture networks,
c) functions to characterize synthesized or imported two- and three-dimensional fracture networks including intersection analysis, density measures, connectivity indices, and clustering, and
d) functions to generically utilize the above stages moreover to extend their use for practical applications, to provide stable framework for further developments, and tools to save the resulting maps, tables and information in appropriate formats readable by many common standard software applications.

Recently, Healy et al. (2017) proposed a MATLAB toolbox called FracPaQ (in 2D); an open-source application that is based on MATLAB to model DFN, its connectivity and quantification of fracture patterns.

2.10 DFN MODEL BUILDING

The computational demand of a DFN model often restricts its usage to smaller scales which necessitates other methods at larger scales, e.g., models based on stochastic equivalent continuum concept. Nevertheless, DFN models are irreplaceable tools to model the influences that a fracture network has on processes at various scales (Öhman, 2005). Elements in DFN model building will be discussed in the following subsections.

2.10.1 DFN MECHANICAL PARAMETERS

The mechanical parameters of fractures in a DFN can be obtained directly or indirectly from laboratory testing (Mahabadi, 2012; Lei et al., 2014; and Singhal & Gupta, 1998). These parameters include:

- Normal stiffness, K_n
- Shear stiffness, K_s
- Cohesion
- Friction angle
- Dilation angle
- Critical shear displacement

2.10.2 GRID TOPOLOGY

Several DFN approaches have been developed to simulate the topology of complex fracture systems (Chen et al., 2012; Lei et al., 2014; and Lisjak et al., 2014). To fully capture bedding plane delamination, mesh topology must combines a random triangulation for the intra-layer material (i.e., matrix) together with fracture elements preferably aligned along the bedding plane as seen in Figure 2-6. For instance, in (Lei et al., 2014) discontinuum reservoir models have been discretized into triangular elements using an unstructured mesh technique. The overall response of the model was found to be linear due to the elastic deformation of the continuum triangular elements.

The topology of fracture walls in a hybrid finite/discrete element method (FEM/DEM) simulation, was represented by numerous triangular elements edges as seen in Figure 2-6 a. During the equilibrium process in these models, fracture walls might separate (Figure 2-6 b). Rather than using a median polyline, the determination of intersection between two fractures should be based on the connectivity analysis of fracture walls. Results indicated that the degree of strength anisotropy is dependent upon the introduction of preferably oriented planes in the mesh topology. The emerging elastic properties were found to be independent of the adopted element size and mesh topology, as the model deformability is governed by the continuum formulation of the triangular elements. To minimize the constraint imposed by the mesh topology on the model behaviour, randomly discretized meshes should be used in place of regularly discretized ones (Lisjak et al., 2014). The effect of the mesh topology on the model behaviour i.e. strength anisotropy is dependent upon the introduction of preferably oriented planes. Values of uniaxial

compressive strength (UCS) and associated anisotropy ratios appeared to trend to constant values as the number of layers increases.

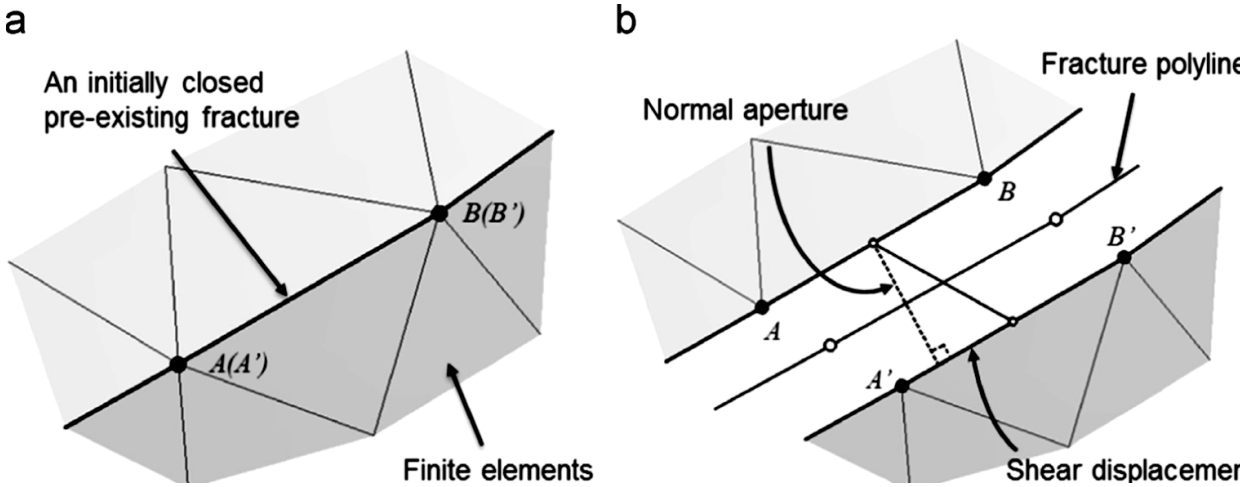

Figure 2-6 Representation of pre-existing fracture: a) initial closed case, b) deformed state after opening and sliding (Lei et al., 2014)

2.10.3 ELEMENT SIZE

A mesh sensitivity study indicated that element size and grid topology are not entirely free parameters of the model building. The element size in particular influences not only the model spatial resolution, but also the strength of the material and, for the case of a bedded material, where the minimum layer thickness can be incorporated into the model. It has been demonstrated that the simulated strength response tends to a constant value for decreasing values of the element size and layer thickness (Figure 2-7). However, in field-scale problems, computational demands require an increase of element size. Therefore, the cohesive strength parameters of a model should be checked and continuously recalibrated to match the evolution and extent of damage at the scale of interest (Lisjak et al., 2014).

2.10.4 BOUNDARY CONDITIONS

Model geometry should be chosen so that the boundary effects (Bidgoli, 2014 and Lisjak et al., 2014) on the solution are minimized. For example, to correctly simulate the prior-to-excavation stress state, a model basically requires two separate runs. In the first run, the vertical and horizontal in situ stress conditions are applied (Figure 2-8). Then the loading conditions of interest can be typically applied after the first step reaches a steady state.

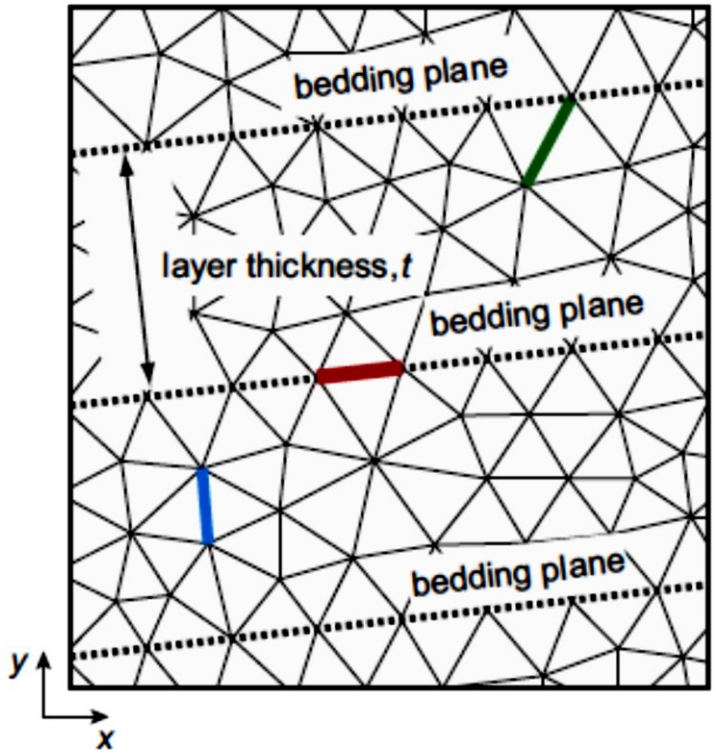

Figure 2-7 Mesh combining Delaunay triangulation for intra-layer material with edges preferentially aligned along bedding planes directions (Lisjak et al., 2014) – inclinations of 0º, 60º, 90º are indicated in red, green, and blue respectively

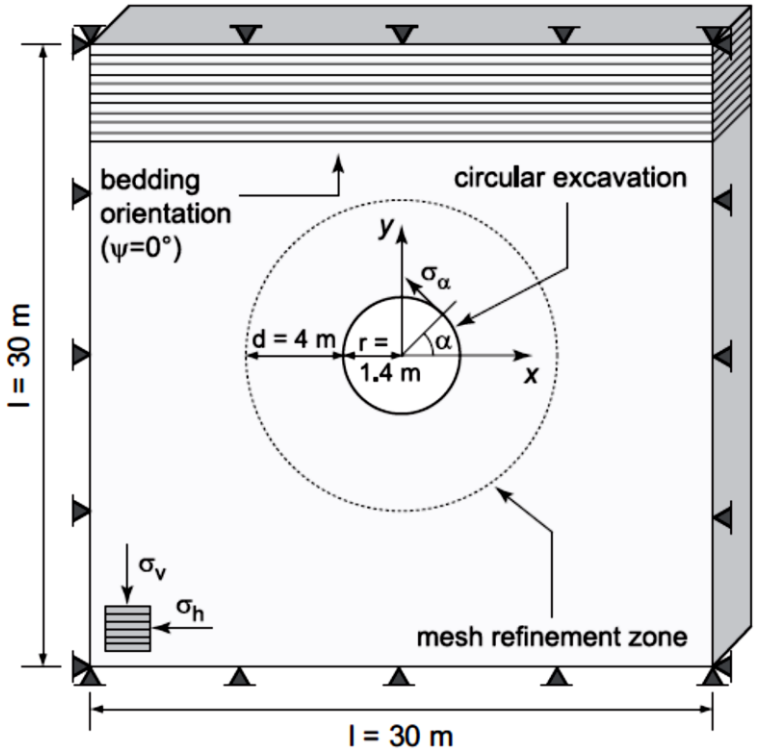

Figure 2-8 Geometry and boundary conditions of excavation tunnel model (Lisjak et al., 2014)

2.11 GEOMECHANICAL MODELLING APPROACHES

DFNs play an important role in conceptual model evaluation (Figure 2-9), but site specific applications are generally limited to near-field scales (50 – 100 m). Many applications, particularly those involving geological disposal of high-level nuclear waste, involve spatial scales of a few hundred meters to a few kilometers in three dimensions (Painter & Cvetkovic, 2005). However, because DFN simulations are computationally intensive they are usually limited to small scales.

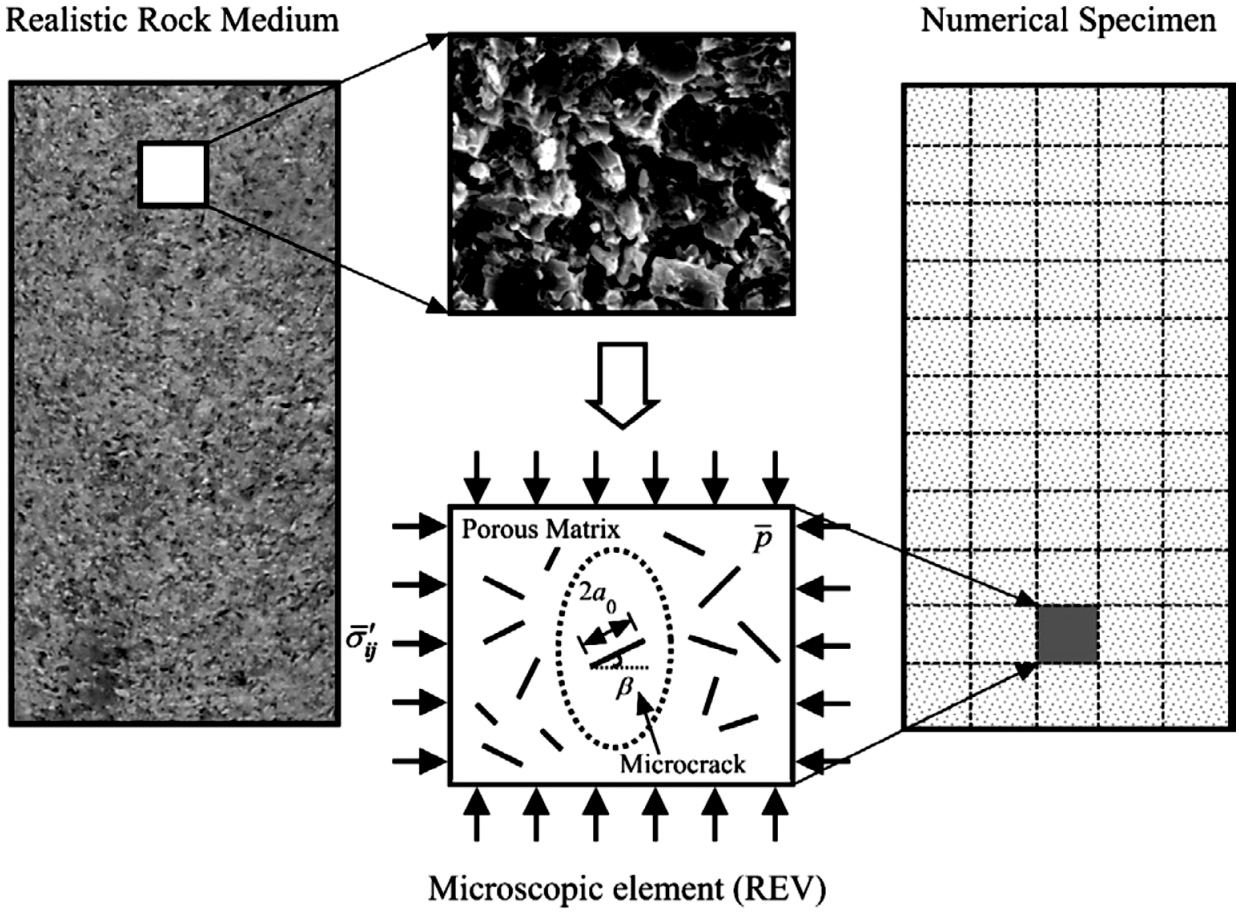

Figure 2-9 Two-scale conceptual model representing realistic rock medium (Lu, Elsworth, & Wang, 2013)

Accurate characterization of fracture behaviour requires systematic geomechanical modelling of discontinuum rocks which can simulate well-interconnected fracture systems, capture the deformability in an interaction of matrix blocks and incorporate fracture propagation when appropriate, to eventually obtain a realistic stress distribution (Lei et al., 2014). There are several well-known approaches that were introduced in literature to geomechanically model a

DFN. For example, Amadei and Goodman (1981) developed a 3D constitutive relationship for discontinuum rock masses using numerical simulation results.

Approaches such as distinct element method (DEM) (Bobet et al., 2009 and Bidgoli, 2014), hybrid discrete fracture network-distinct element method (DFN-DEM) (Öhman, 2005 and Mahabadi et al., 2012), Voronoi finite-discrete element method, boundary element method (BEM), finite-discrete element method (FDEM) (Lisjak et al., 2014), discontinuous deformation analysis (DDA) (Bobet et al., 2009 and Lisjak et al., 2014), transversely isotropic elastic model (Lisjak et al., 2014), distinct lattice spring model, DLSM (Zhao, 2010), bonded particle method (Bobet et al., 2009), orthotropic elasto-plasticity (critical state failure model), and finite difference method (FDM) were all been introduced in literature as geomechanical modelling approaches incorporating DFNs.

2.11.1 DISTINCT ELEMENT METHOD (DEM)

With the distinct element method (DEM), fractures are explicitly represented in the numerical model (Lu et al., 2013 and Bidgoli, 2014). The DEM medium is typically modeled as an assembly of rigid or deformable zones (representing blocks) with interaction laws governing the behaviour of the material. Due to the large computational demand that tends to limit the DEM applicability to small-scale problems, the DEM approach offers unique advantages. These advantages become clear when an extended loss of continuity inside the material occurs, for example due to progressive breakdown, which makes continuum constitutive models inappropriate (Lisjak et al., 2014). Using the DEM approach, the simulated failure plane was found to be generally steeper than the bedding plane orientation and delamination of bedding planes as seen in Figure 2-10. This cannot be precisely captured using a continuum approach. The main advantages of DEM technique include the ability to readily account for the presence of rock mass discontinuities, to capture large displacements, and rigid block rotations that typically characterize the failure of discontinuum rock masses.

2.11.2 COMPOSITE ELEMENT METHOD (CEM)

The application of the composite element method (CEM) enables a large quantity of stochastic tests for a series of discontinuum rock samples with different sizes and orientations to be extracted from a DFN. The information of a composite element (CE) mesh is obtained by

topology calculation using fracture network and a regular grid. In this way the pre-process in the computation is facilitated greatly. Conventional finite element (FE) mesh combined with rock fracture system produces the mesh for CE computation (Chen, He, & Shahrour, 2012) as illustrated in Figure 2-12. Compared to the conventional finite element method (FEM), the main advantage of CEM is the simplicity in the pre-processing; since the fractures are explicitly embedded within the elements hence the mesh construction would not be limited by the irregularly distributed fractures (Chen et al., 2012).

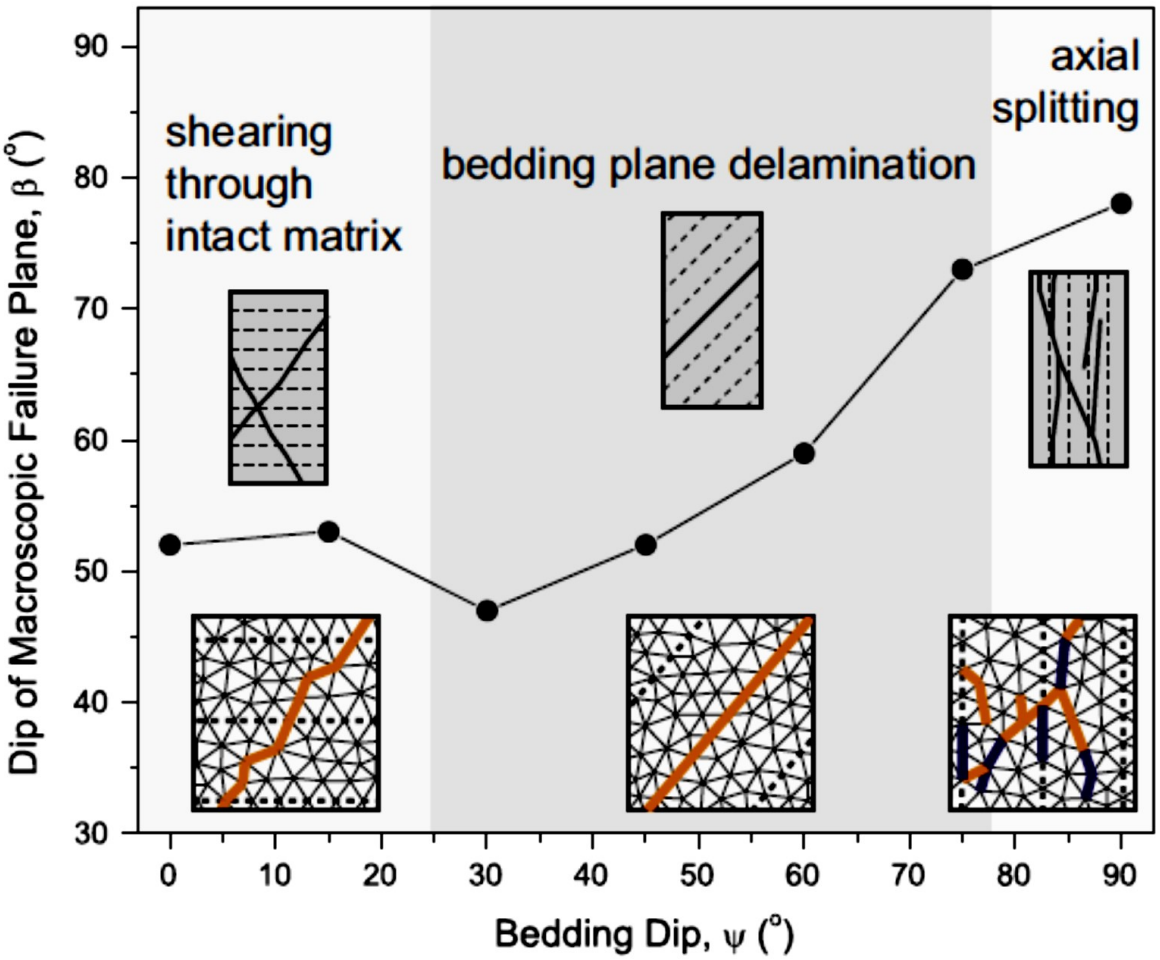

Figure 2-10 Inclination of failure plane versus dip of specimen bedding. Relationship between mesh topology, orientation of bedding planes and discontinuities (Lisjak et al., 2014)

2.11.3 LINEAR COMPARISON COMPOSITE (LCC)

The linear comparison composite (LCC) homogenization method represents a general framework for the rational upscaling of strength properties in complex material systems such as cohesive porous solids with microstructures described by the composite spheres assemblage.

These systems include cohesive double-porosity materials subject to internal pressures and anisotropic visco-plastic porous solids with ellipsoidal morphologies. The second-order LCC approach confirms the applicability of the effective stress concept. The concept was previously proposed in literature as homogenization of cohesion and friction in porous solids for double-porosity materials subject to similar pressures in the pore space (Ortega et al., 2011).

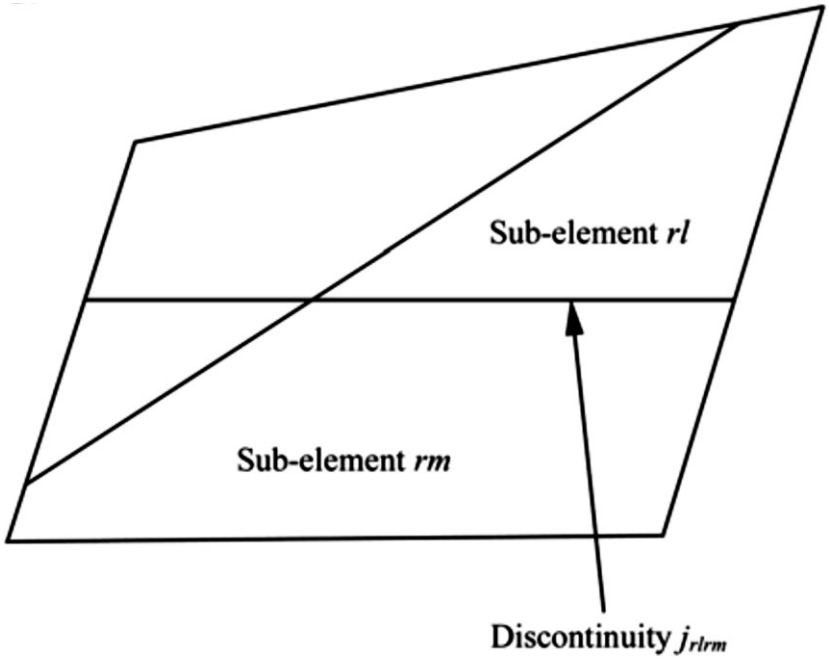

Figure 2-11 Composite element mesh (Chen, He, & Shahrour, 2012)

2.11.4 COMBINED FINITE-DISCRETE ELEMENT METHOD (FEM/DEM)

Combined finite-discrete element method (FEM/DEM) (Lei et al., 2014) or FDEM (Zhang et al., 2007 and Mahabadi et al., 2012) also called hybrid continuum/discontinuum approach (Lisjak & Grasselli 2014; Lisjak et al., 2014; and Lisjak, 2014) combines DEM techniques to represent zones affected by strong non-linear behaviour due to material failure with a continuum approach for the remaining small-strain elastic regions. The method represents a hybrid approach whereby the elastic deformation of the material is described using continuum mechanics theory while DEM algorithms and non-linear fracture mechanics principals are employed to capture fracture mechanisms that are typical of brittle and quasi-brittle materials such as rocks.

In FEM/DEM, each solid is discretized as a mesh consisting of nodes and (triangular) elements. An explicit second-order finite-difference integration scheme is applied to solve the equations of motion for the discretized system and to update the nodal coordinates at each

simulation time step. FEM/DEM was pioneered by Munjiza in 2004 as a numerical method capable of modeling a discontinuum system consisting of numerous deformable discrete bodies, which are discretized into a number of finite elements. Further development was accomplished by Xiang et al., 2009 for 3D solid modelling (Lei et al., 2014).

With the FEM/DEM smeared approach, the strength anisotropy (Lisjak, 2013) can be captured from the variation of specimen rupture mechanisms induced by the directionality introduced in the cohesive response of fracture elements preferably aligned along bedding plane direction (Figure 2-6). The simulated fracture patterns together with the orientation distribution of broken fracture elements highlight a distinct variation of bedding influence on the macroscopic failure response of the sample as a function of the anisotropy direction (Lisjak et al., 2014). Major fractures develop sub-parallel to the loading direction consisting of a combination of tensile split along layers and steeply inclined shear fractures (Figure 2-10). It was shown that, the FEM/DEM approach can capture both the deformation and strength anisotropy (Lisjak, 2013) that are typical of layered materials.

Geomechanical modelling based on the FEM/DEM approach can characterize the deformation and interaction of rock matrix bonded by pre-existing fractures. Several important geological phenomena can be simulated in the modelling experiments, such as fracture dependent stress heterogeneity, re-activation of shear on pre-existing fracture walls, new fracture propagation as well as variability of aperture distribution (Lei et al., 2014).

The FEM/DEM was used to investigate the damage process and failure mechanisms around underground openings. Unlike continuum-based methods, FEM/DEM explicitly simulates the growth of fractures in rocks, thus allowing to reproduce typical brittle failure processes involving loss of material continuity, large displacements and rigid block rotations (Lisjak et al., 2014). Lisjak et al., 2014 found that, the anisotropic strength characteristic of shales was captured with a simple directional dependence on the cohesive strength parameters of the fracture elements. When modelling large-scale problems, this approach was shown to overcome some of the limitations of a previously developed discrete approach based on an explicit incorporation of the pre-existing fractures oriented along the direction of bedding (Lisjak et al., 2012).

A constitutive law was implemented in the Y-Geo FEM/DEM code, and a procedure to populate the model with a distribution of preferably oriented fractures was developed. It was shown that the proposed approach can capture both the deformation and strength anisotropy that

are typical of layered materials. The layering-induced directionality of deformation properties is commonly captured using the theory of elasticity for transversely isotropic materials (Lisjak et al., 2014).

2.11.5 CONTINUUM MODELING METHOD

Lu et al. (2013) proposed a numerical model that predicts the tensile strength of a borehole with sufficient accuracy from the microscopic standpoint using a microcrack propagation criterion instead of a macroscopic fracturing criterion related to the tensile strength. The proposed numerical model can capture the evolution of fracturing and flow in a physically realistic manner.

2.11.6 SMEARED APPROACH

In the smeared approach illustrated in Figure 2-12, it is assumed that the macroscopically observed strength anisotropy is induced by a similar anisotropy at the crack element level. Hence, directionality is directly introduced in the discontinuum model by imposing the cohesive strength of each crack element as a function of the relative orientation, between the crack element itself and the bedding planes as illustrated in Figure 2-13. An embedded smeared crack model permits capturing the emergence of new fractures, which potentially leads to critical changes in the connectivity of the fractures system (Lei et al., 2014).

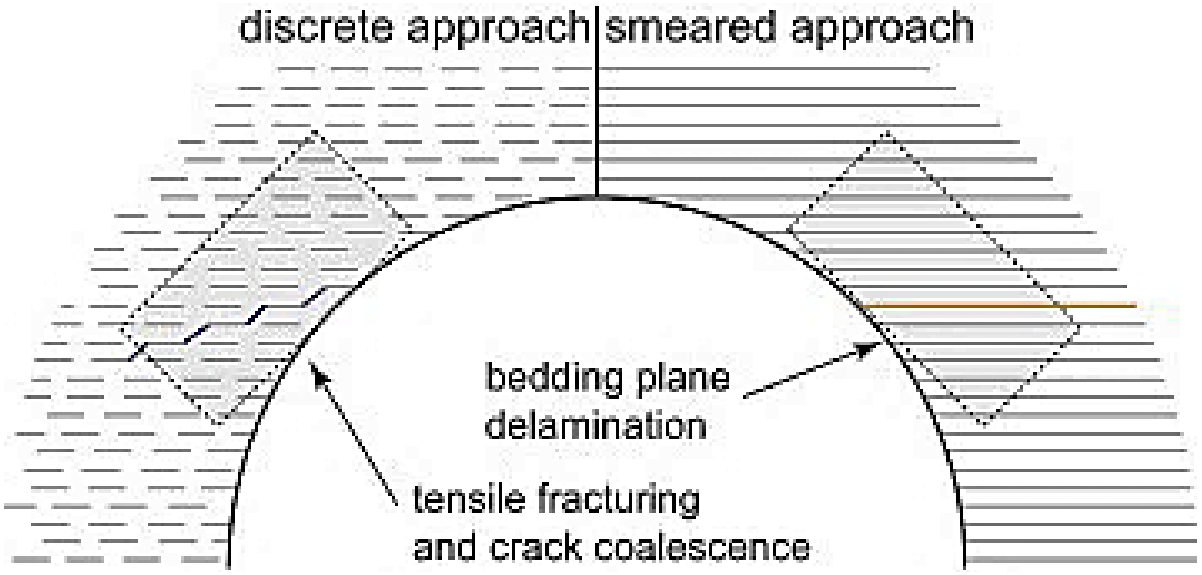

Figure 2-12 Conceptual model illustrating different crack propagation mechanisms associated to discrete and smeared approaches for capturing strength anisotropy (Lisjak et al., 2014)

2.12 DFN-BASED GEOMECHANICAL BEHAVIOUR

Generally, in rock mechanics, as the confinement is increased, the strength anisotropy (Bidgoli, 2014 and Wang et al., 2013) is governed by the reduced shear strength. The strength can be mobilized in the direction parallel to layering along cohesion-less DFN fractures. However, macroscopic shear failure along the layering direction, is responsible for the reduced strength. As illustrated in Figure 2-14 such a failure was captured as a step-path surface resulting from the coalescence of the pre-existing fractures, which undergo tensile propagation from their tips. The strength of the sample is ultimately controlled by the tensile strength of the intact material and the fracture set topology (i.e., spacing, length, bridge length) (Lisjak et al., 2014). The effect of rock formation generic characteristics on its macroscopic strength can be reflected in the mechanical behaviour characteristics as will be discussed in the following subsections.

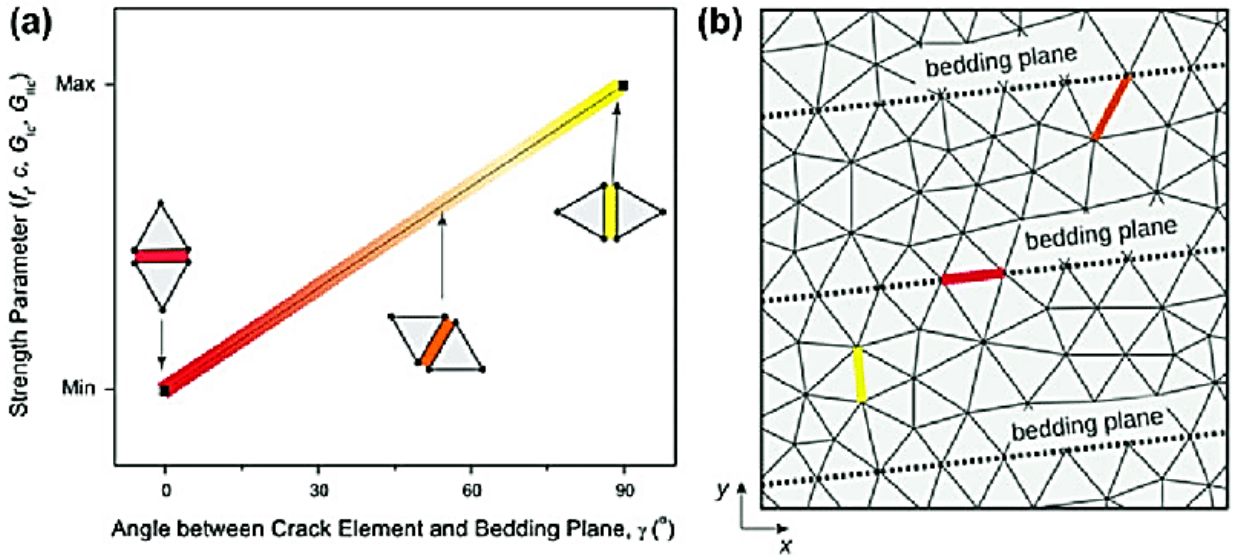

Figure 2-13 Smeared approach (Lisjak et al., 2014)

2.12.1 SHEAR DISPLACEMENT

Stresses caused by fracture opening are very heterogeneous spatially, and effects on neighboring fractures are dependent on their relative orientations and locations (McClure & Horne, 2013). High shear displacement often happens along pre-existing fractures with favorable orientation. It accompanies forming of newly propagated fractures, which usually develop obliquely to pre-existing fractures. Shear displacement develops with large magnitudes along relatively persistent fractures or around isolated matrix blocks. Lei et al. (2014) reported that DFN

fractures seemed to be slightly more active in sliding, which might be attributed to the straight-line simplification in the DFN method.

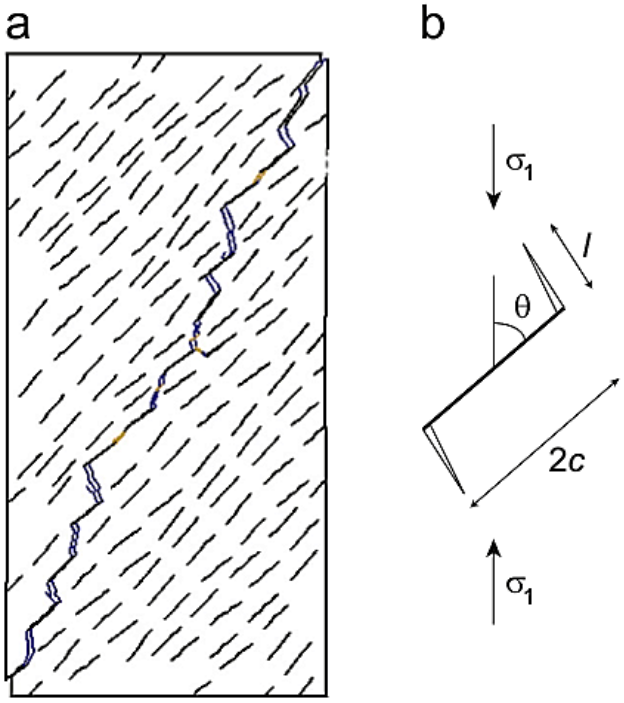

Figure 2-14 (a) Simulated fracture pattern of UCS sample (θ=45°), (b) Sliding crack model showing wing cracks nucleating from pre-existing linear defect (Lisjak et al., 2014)

2.12.2 NORMAL APERTURE

Due to compressive effective in situ stresses, most fractures do not explicitly exhibit significant opening. Higher in situ stress ratio (e.g. ≥ 3) are expected to trigger more significant aperture dilation and consequently flow localization, as well as increased overall connectivity caused by fracture propagation (Lei et al., 2014). Higher normal aperture often occurs in four cases as shown in Figure 2-15:

1. Secondary fractures in which shear dilation induces evident separations (Figure 2-15a),
2. Boundaries of isolated matrix blocks which deform with translation and rotation (Figure 2-15b),
3. Fracture intersection nodes in which dislocation engenders voids at matrix block corners (Figure 2-15c), and
4. Wing fractures in which the local tensile stress splits opposite fracture walls (Figure 2-15d).

2.12.3 FRACTURE PROPAGATION

Fracture propagation is simulated as an explicit separation between edges of adjacent unstructured elements. Sliding of pre-existing fracture walls can engender stress concentration near the fracture tips and induce the formation of wing cracks or secondary cracks as depicted in Figure 2-15. The initiation of new fractures is, therefore, greatly correlated to the shearing activeness of pre-existing fractures, which was repeatedly observed in numerical simulations. It is noticeable that, the orientation of wing cracks varies with the change of applied far-field stress orientation as they attempt to follow the distribution patterns of maximum principal stress (Lei et al., 2014). Fracture propagation caused by stress concentration at the tips of pre-existing fractures may connect fractures in different clusters and result in larger occupations.

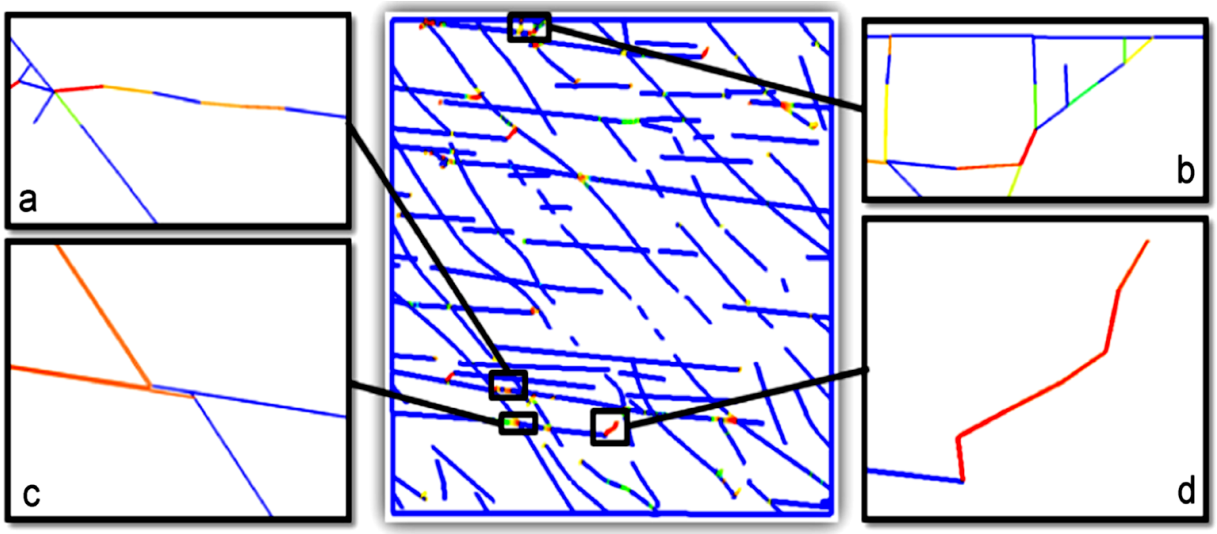

Figure 2-15 Locations of fracture opening (Lei et al., 2014) (a) secondary, (b) boundary of isolated matrix block, (c) intersection, and (d) wing crack

2.12.4 CONNECTIVITY

The connectivity nature of a fracture pattern can be characterized by the properties of clusters, in which member fractures intersect to form connected sub-networks. Identification of clusters is accomplished by a fracture connectivity algorithm. The algorithm first establishes a connection matrix for a fracture network to record the intersection relationship between different fractures. It further groups connected fractures into clusters via manipulating a connection matrix (Lei et al., 2014). Importance of studying the connectivity characteristics of a rock mass is essential in assessing the change in its permeability and porosity.

2.12.5 SCALE EFFECT

Fracture network properties are scale-dependent (Figure 2-16) and exhibit fractal scaling, i.e., self-dissimilarity at various scales (Chen et al., 2011; Wu et al., 2012; and Khaki et al., 2013). Variety of techniques have been developed for generating numerical fracture networks. Statistical analyses of geologic and hydraulic data provide means to select the most appropriate technique for a particular site (Öhman, 2005).

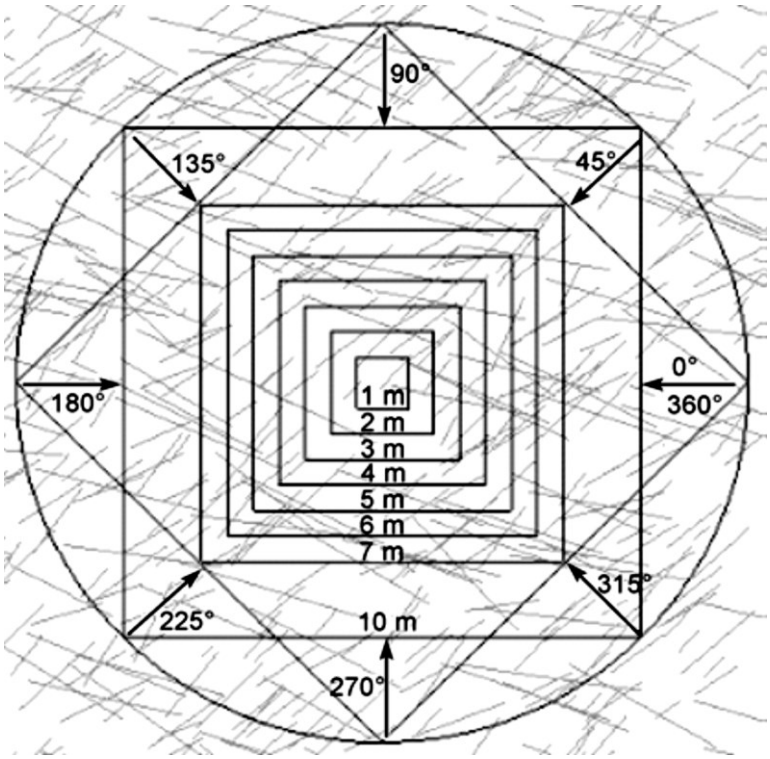

Figure 2-16 Studying scale effect (WeiZhong et al., 2011)

Before embarking on choosing the size of a network domain for analysis, it is instructive to consider scale effects and explore whether the concept of REV holds true (Chen et al., 2011; Chen et al., 2012; Wu et al., 2012; Wang et al., 2013; Zhang et al., 2013; Bidgoli, 2014; and Lei et al., 2014). The anisotropic, inhomogeneous, and discontinuous features of rock masses are strongly affected by the stochastically distributed fractures; thus, it is of great importance to analyze the REV size considering the fractures in the rock mass. To confirm the REV size, fracture system attributes such as density, strike, dip angle, and length maybe used. Based on a 3D fracture network, Zhang et al. (2013) chose the fracture frequency to calculate and validate the REV size. To build a relationship between the fracture frequency value and the REV size, scan lines with different lengths were set. An example illustrating REV determination based on fracture frequency

is given in Figure 2-17. Because the fractures were distributed stochastically, it made sense to set numerous scan lines to acquire a mean fracture frequency value (Zhang et al., 2013).

Scale dependencies of hydraulic and mechanical properties were investigated by using multiple realizations of the fracture system geometry with increasing model sizes until properly defined hydraulic and mechanical REVs were reached. The DFN factors influenced that investigation included diameter, length, and shape (Zhang et al., 2013).

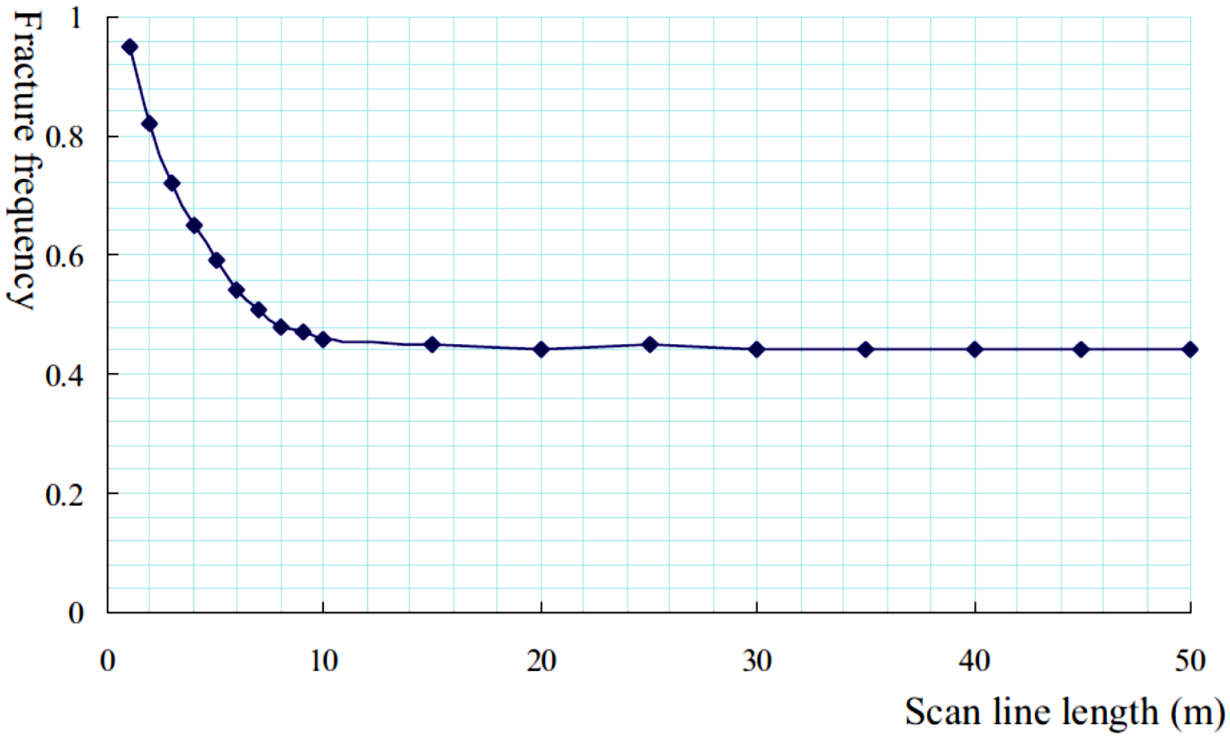

Figure 2-17 Fracture frequency with scan line lengths in X- direction (Zhang et al., 2013)

2.13 DFN IN ROCK MODELLING

Studying the geological and structural characteristics of a heterogeneous rock mass is essential in modelling the change in the rock mass permeability and porosity. As seen in Figure 2-18DFNs were used in a discontinuum modelling of Granite (as in Fox et al., 2007; Khajeh, 2013; Bidgoli, 2014; Lisjak, 2014; and Lisjak & Grasselli 2014) and Gneiss (as in Geier et al., 2012).

2.13.1 ANISOTROPY

At the rock mass level, anisotropy can be related to the presence of physical discontinuities such as joints, fractures and tectonic structures (Lisjak et al., 2014). A discontinuum rock displays anisotropic behaviour in strength and deformability, depending on fracture system geometry

(Bidgoli, 2014). Zhang et al. (2013) considered the DFN discontinuities in basalt as discs where each fracture was represented by a set of parameters; coordinates (x, y, z), disc diameter, strike, and dip angle. These 3D fractures were visualized using an OpenGL platform.

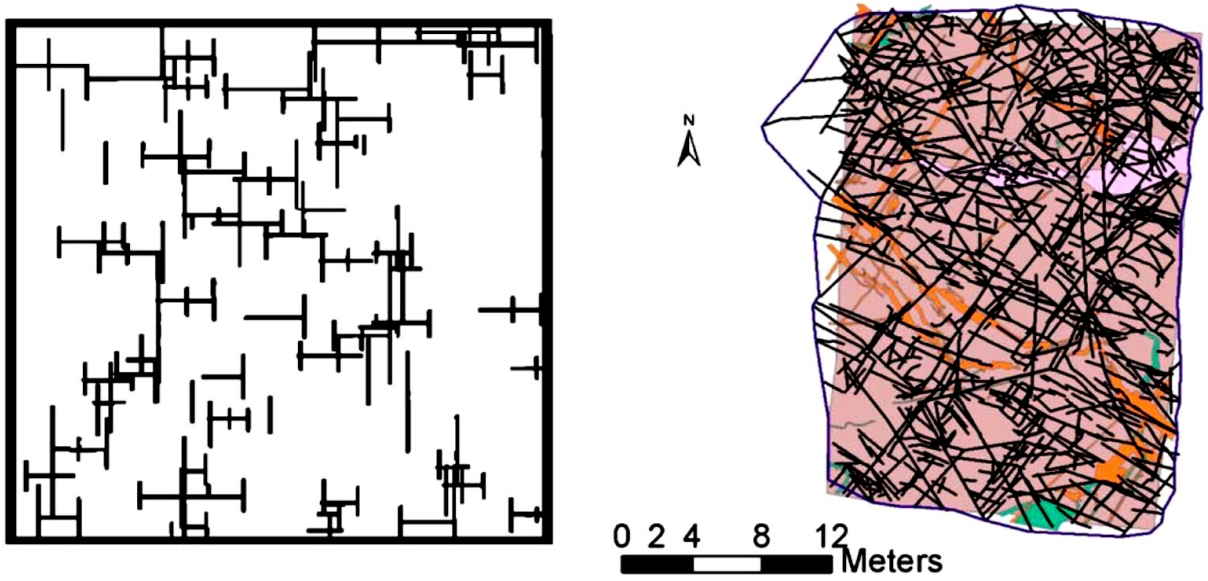

(a) (b)

Figure 2-18 Fracture networks obtained from (a) numerical simulations (Renshaw, 1996) and (b) mapped from granitic outcrop, Forsmark, Sweden (SKB, 2004) (Davy et al., 2013)

2.13.2 HETEROGENEITY

Due to the presence of discontinuities at various scales, rock masses are generally heterogeneous in both mechanical and hydraulic properties. Brittle rock generally contains numerous pre-existing defects (initial damage). Such initial damage leads to virgin mechanical and hydraulic properties varying randomly from point to point and with direction in the material, i.e. heterogeneity. This heterogeneity plays a vital role in determining fracture patterns and flow paths (Mahabadi et al., 2012; Lu et al., 2013; Lei et al., 2014; and Lisjak et al., 2014). Accordingly, stress concentration can be quite different in local areas because of the discontinuity-dependent heterogeneity effect. It results in distinct discontinuity propagation and coalescence patterns in the DFNs, which can cause significant uncertainty in connectivity properties of the DFN. Figure 2-19 shows an example of fracture-dependent heterogeneity of maximum principal stress in deformed areas in an AFN and a DFN (Lei et al., 2014).

High compressive stress bands are likely to distribute along the orientation of the applied maximum far-field stress. But as seen in Figure 2-19 they are considerably influenced by the spatial

organization of the fractures. The spacing distribution in the DFN models may contribute to a distinct difference in stress pattern. The DFN geometries lack self-organized spatial relations of geologically formed natural fractures and may lead to a certain bias when being used to estimate the stress heterogeneity in rock masses (Lei et al., 2014).

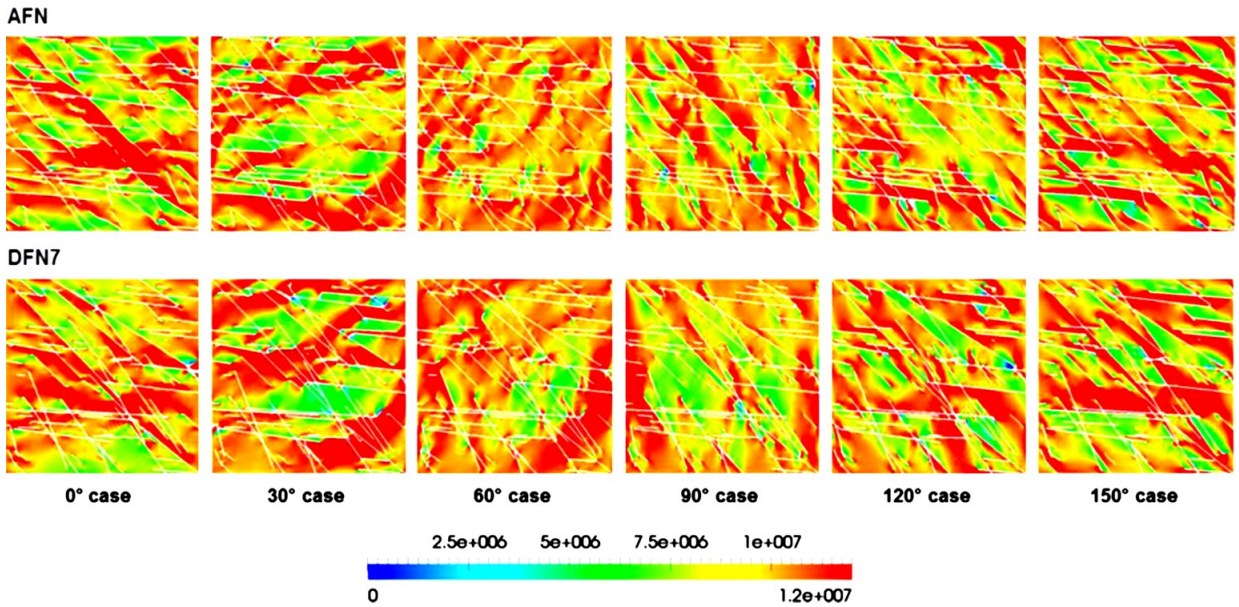

Figure 2-19 Contours of maximum principal stress of AFN and DFN (Lei et al., 2014)

2.14 DFN CONSTRUCTION AND MANIPULATION

Currently, there is a large number of commercial platforms specific for generating DFNs such as PETREL, FracMan, and MoFrac in addition to a significant number of research based codes that is beyond the scope of this review to summarize.

2.14.1 PETREL

PETREL software (Schlumberger 2007) can be used for visualizing fractures as equal sized disks along a measuring line. It can be used in analyzing the fracture sets for subsequent DFN modelling via implementing certain algorithms as introduced in (Chesnaux, Allen, & Jenni, 2009).

2.14.2 FRACMAN

In 1987, Golder's Associates introduced FracMan as a 3D DFN software that allows simulating and analyzing of heterogeneous and fractured rock masses. FracMan can be used to characterize complex fracture systems, test conceptual understanding, determine the best strategies, and quantify risks and uncertainties in rock masses. It considers fracture size distribution

as reported in (Zhang & Einstein, 2000) which enabled it to provide a geologically realistic, 3D quantitative description of spatially varying natural fractures and its hydro-mechanical properties. FracMan has multiple simulation editions for geotechnical, reservoir, nuclear and hydro applications.

2.14.3 MOFRAC

MoFrac is a DFN modelling software provided by Mirarco Mining Innovation. MoFrac can generate 3D fracture network models for rock masses extensible for geotechnical engineers and researchers. Properties such as fracture intensity, orientation, truncation rules, size, shape and undulation can be defined for each fracture group. A single fracture may connect multiple traces. This joining behaviour can arise from geometric inference or from explicit constraints.

Several analyses of DFNs can be carried out using MoFrac platform such as identifying continuous unfractured sub-volumes and building metrics plug-ins that can assess the DFN models for constraints and/or agreeance with mapped data. Custom fracture group properties can be governed by the platform plug-ins, allowing for control over distributions and strategies for intensity, orientation, and undulation. MoFrac DFNs can be used in a broad range of geomechanical and hydraulic flow modelling applications, such as:

- Mine design,
- Rock characterization,
- Kinematic analysis of wedge failure,
- Blast optimization,
- Block size distributions for block caving operations,
- Fracture mechanics,
- Reservoir modelling,
- Contaminant transport, and
- Hydraulic fracturing.

2.15 DFN APPLICATIONS

The DFN approach was first designed toward homogenizing fractured media (Long et al., 1982). It was further applied in understanding the flow mechanisms in complex fracture networks (Dreuzy et al., 2001b, 2001c, 2002, 2004a; Davy et al., 2006a; and Leung & Zimmerman, 2010),

permeability and dispersivity upscaling (Snow, 1969; Charlaix et al., 1987; Park et al., 2001; Dreuzy et al., 2001a, 2010; Mettier et al., 2006; Baghbanan & Jing, 2007; and Frampton & Cvetkovic, 2007, 2009). It is a modelling prerequisite to determine which fracture properties are essential for hydraulic and transport properties (Figure 2-20), as introduced in (De Dreuzy et al., 2012).

The DFN approach is typically used to "precondition" equivalent continuum heterogeneous approaches, to which it becomes complementary rather than competitive (Hsieh, 1998 and Neuman, 2005). For example, Wang et al. (2012) transformed a DFN into a grid-based equivalent continuum model.

2.15.1 DFN IMPLICATIONS ON ROCK MASS' FLOW CHARACTERISTICS

Fracture networks are the major components in subsurface flow systems (Renshaw, 1996). Min et al. (2004) analyzed the hydro-mechanical behaviour of discontinuum rock masses by conducting a series of numerical experiments on multiple DFN realizations. Several phenomena were observed in the discontinuum region, such as flow concentration caused by shear dilation, sensitivity of permeability under different in situ stress ratios and anisotropy induced by differential stresses. In some cases, fluid flow was calculated by upscaling the DFN to an effective continuum model (Lanyon et al., 1993; Willis-Richards et al., 1996; Jing et al., 2000; Rahman et al., 2002; Tezuka et al., 2005; Kohl & Mégel, 2007; Cladouhos et al., 2011; Du et al., 2011; Fakcharoenphol et al., 2012; Wang & Ghassemi, 2012; and McClure & Horne, 2013).

2.15.2 DFN IMPLICATIONS ON ROCK MASS' EQUIVALENT CONTINUUM PROPERTIES

A reliable fracture system characterization should be provided if the DFN approach is to be applied for site-specific investigations in 3D studies. It has been proved that sufficient generation of DFN models in number provided an adequate data basis for clear tendency of convergence of results for different values of fracture density (Khani et al., 2013). Fracture density of DEM models plays a key role in estimating the equivalent elastic mechanical parameters and behaviour of discontinuum rocks at field scale. The deformation modulus and Poisson's ratio were found to significantly decrease when fracture density increases. An increase in the fracture density

in the discontinuum models results in a decrease in the isotropic behaviour, mainly due to the increase in the number of fractures in the rock mass.

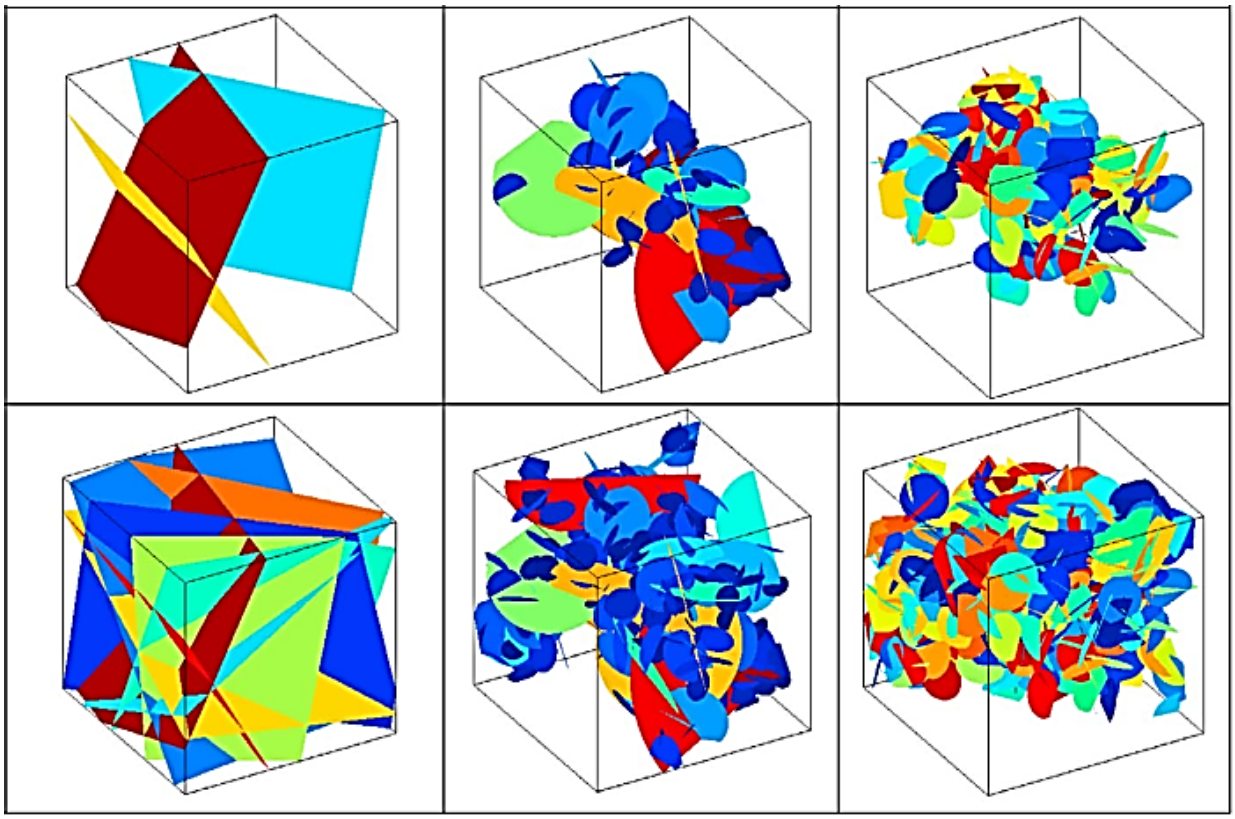

Figure 2-20 Examples of DFNs (Dreuzy, Méheust, & Pichot, 2012)

2.15.3 DFN IMPLICATIONS ON ROCK MASS MODEL' STABILITY

Tollenaar (2008) examined a range of DFN models by varying fracture spacing, persistence, block shape and size. All were found to affect the model' stability but unequally. The stability of generated blocks was evaluated based on the factors of safety obtained from FracMan stability analysis. It was found that fracture persistence had the largest influence on the stability calculations.

2.16 DISCUSSION AND SUMMARY

The consideration of sophisticated correlations that are compatible with fracture genesis (location, spacing, length, orientation, etc.) supported with an incorporation of geological history information (formation and superposition sequence of fracture sets) into a DFN method is a valuable asset in rock mechanics. It is important to study the geological, geometrical, and structural

characteristics of rock masses as this is essential in assessing the change in the rock mass' permeability and porosity. A DFN can realistically characterize a natural fracture system quite well however it is worth noting that, DFN simulations are computationally intensive.

In this chapter, the history of DFN evolution, attributes, methods and models presented in literature have been discussed. This chapter basically covers the first segment within the research methodology illustrating the DFN reliability, capabilities and power implying privilege to employ it in rock masses characterization problems.

Over decades the DFN approaches as discussed in this literature review chapter were repeatedly applied to hard rocks because DFN is generally powerful in the structural characterization of rock masses. The DFN notion is capable of being applied to soft rocks in a similar fashion. However it is not easy to find such procedure investigated, used and studied for soft rock masses in literature since it is important to equip any generated DFN with realistic geometrical distribution. This literature survey constitutes for chapters 5, 6, and 7 investigations where a realistic DFN will be derived based on insitu geological survey acquired using LiDaR technique. The uniquely realistic DFN will be used in building a 3D numerical model of a discontinuum argillaceous rock formation scanned in a mine site in Alberta. Analogues and realistic DFNs will be generated and used in geomechanical analyses of soft as well as hard rock masses for a comparison of the fundamental differences between the two rock type extremes.

CHAPTER 3 PERSISTENCE OF GEOLOGICAL FEATURES IN CRETACEOUS SUCCESSIONS IN ALBERTA

3.1 INTRODUCTION

Shale is a sedimentary rock (Hitherto; geological classification of rocks) that is believed to be the most commonly encountered material in civil construction works (Hsu & Nelson, 1993). The special term "clay shale" is associated with problems in the shale characteristic classification. Argillaceous bedrock materials could be referred to as pre-consolidated clay shales, over consolidated (OC) clays (Hencher, 2013), OC plastic clays, and clay shales (Mollard, 1977). The OC clay shales exhibit behaviour that lies somewhere on the boundary between rock and soil, posing unique and complex challenges when estimating and predicting their geomechanical behaviour (Powell, 2010). Geologists refer to clay shales as poorly indurated argillaceous bedrock. They are famous of their stratigraphy, lithology, and geotechnical properties within the Upper Cretaceous argillaceous bedrock in the Interior Plains.

A variable thickness of glacial drift mantles Upper Cretaceous argillaceous bedrock, especially bentonitic marine clay shale, silty shale, and mudstone with, sand, and tuff intervals (Mollard, 1977). Cretaceous (time period) clay shale formed post glacial time was subsequently covered by alluvial deposits. Strong diagenetic bonding (Corkum & Martin, 2007) have developed between the clay shale particles because of the high overburden (OB) pressure imposed upon the material. With time and the heavy loads imposed on clay particles at localized contact points, various physical and chemical alterations (e.g. recrystallization, molecular adhesion, and cementation) have occurred at these contacts.

Clay shales are hard clays with a very complicated fabric and microstructure originated over their geological history. That geological history was associated with sedimentation, diagenesis, ageing and/or precipitation of carbonates, tectonism, softening, swelling and weathering. The clay shale typically has numerous weak pre-sheared layers which can cause engineering instabilities. Hence, clay shale may govern the geotechnical performance if encountered. Clay shales are widespread globally as there are reports on its behaviour from all six continents. This very fragile material is widespread in the world and responsible for many hydrological and geotechnical concerns and issues. According to (Morgenstern, 1979), clay shales

can be treated on a regional basis. Within the North American Plains, geotechnical complexity is a common characteristic of glacial sediments which often vary laterally and vertically. Morgenstern and Cruden (1977) postulated that geotechnical complexities are due to three main geological processes:

1. Genetic or natural material formation process during early/preliminary deposition stages;
2. Epigenetic or subsequent modification due to deformation, diagenesis (i.e. cementation), and tectonic rebound producing discontinuities in the natural material that dominate the material geotechnical behaviour. Epigenetic geological features were imposed later than the surrounding or underlying rock genesis formation; and
3. Weathering processes (such as surface or immediate subsurface phenomenon) produced complexity within the formation.

Detailed site investigation and reasonable material characterization require a good knowledge of each of the above three processes. When a site demonstrates geological complexity, concept of facies comes into action with a valuable role. In geology, the use of facies concept is most common when dealing with sedimentary rocks (Morgenstern & Cruden, 1977). Facies concept implies and indicates a degree of constancy and continuity within a rock mass being compared to or distinguished from others.

Directions of regional jointing (Figure 3-1) in an underlying Cretaceous bedrock control the behaviour of the soft clay shale. Regional mapping of fracture traces and joint patterns (Mollard, 1957, 1958; Babcock, 1973, 1974; and Westgate, 1976) reveals that distinct orthogonal jointing systems dominantly characterize the regional jointing over much deposits of the plains area of Alberta, Saskatchewan, and Manitoba (Mollard, 1977).

The Clearwater Formation in North America is divided into several units and subunits displaying variety of material properties dependent on their clay mineralogy, lithology, and degree of weathering (Morgenstern et al., 1988). The Clearwater Formation (Figure 3-2) is a layered, shallow marine deposit, composed of varying amounts of clay, silt, and sand. The presence of cohesionless seams can be detected via conventional site investigation techniques, and the interpretation of their significance on any specific site is hampered by the lack of an adequate genetic process model (Morgenstern, 2000). The process model may not be correct in every detail however it should be capable to explain general assemblage of properties of the site being

investigated. That model may assist the geologist and/or geotechnical engineer to anticipate features that may not be accessible for mapping.

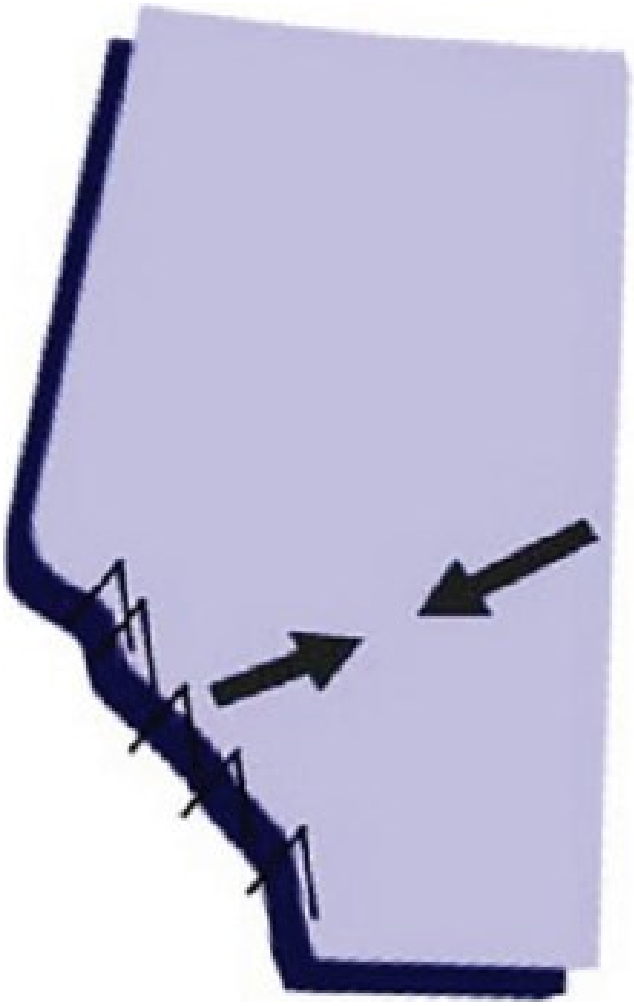

Figure 3-1 In situ stresses in Alberta (Guindon, 2015)

Discontinuity arrangement that dominates the engineering properties in a rock mass is referred to as the fabric of that rock mass (Morgenstern & Cruden, 1977). Time dependent rebound and loosening conditions post excavation produced various patterns of discontinuities which are referred to as fabric facies. These fabric facies include:

1. Pre-existing shears on a glaciotectonic shear zone within Alberta plains.
2. Common structural characteristics around fault (Figure 3-1) movement areas and shear zones.
3. Fractures and minor shears that extend through the external layers of aggregations forming local planes of weakness, which cause the mudstone to break into lumps under finger pressure (Tsui, Cruden, & Thomson, 1989).

3.2 SUBSURFACE STRATIGRAPHY AND GEOMORPHOLOGY

Geotechnical engineering embraces soil mechanics, rock mechanics, and engineering geology. The work of a geologist to determine appropriate geological classification is an absolute essential. For instance, common characteristics around fault movement areas and shear zones (Figure 3-2) are always of a concern and should be addressed, assessed, and characterized precisely (Morgenstern & Cruden, 1977). To properly characterize material need to be geologically investigated in situ.

Figure 3-2 Fault in Clearwater clay shale (CCSh) and McMurray Formation

3.3 GEOLOGICAL HISTORY

Before starting civil engineering projects, evaluation of the site geotechnical complexity is mandatorily required. Geotechnical complexity arises from heterogeneity in the geotechnical properties due to genetic, epigenetic, and weathering processes where the concept of facies comes into action and applied. Hansen (1971) noted that, facies concept in geology is defined as the present rock expressing and reflecting its condition of formation history. He suggested that formations with same facies have indeed developed in a similar fashion. Facies analysis forms a rational basis for predicting, synthesizing, and analyzing the geotechnical behaviour of clay shales (Morgenstern & Cruden, 1977).

Martin (2007) referred to the strong impact of the geological history on rock mass conditions that exist today. Natural material maybe complex geologically but not geotechnically (Morgenstern & Cruden, 1977). Geological complexity arises from mineralogical, chemical or structural considerations, but the engineering implications of these may be insignificant. Martin (2007) stated that geological complexity in sedimentary rocks can be reasonably understood by a comprehensive and proper site investigation.

During late Cretaceous age, shale rebounded following the glacial melting, rapid downward and lateral river erosion. Movements in the region could have taken place in periglacial, interglacial, glacial, or early postglacial time (Mollard, 1977). Pre-glacial stream erosion was followed by Pleistocene glacial erosion, resulting in "over-deepened" and "over-steepened" valleys and in the "daylighting" of steeply dipping, layered rock units. Postglacial marine submergence and uplift formed sensitive fine-grained marine deposits. Old tectonic movements coupled with postglacial isostatic rebound (which induced slip along bedding, foliation, joint, and fault surfaces as seen in Figure 3-2) have decreased the cohesion and frictional components of shear strength on potential rupture surfaces (Mollard, 1977) of mudstones that are jointed, weathered, brecciated, and sheared, (Tsui et al., 1989). The geological history (Figure 3-3) and the resulted micro-structure of these argillaceous weak rocks (mud rocks) may control much of their characteristic behaviour (Corkum & Martin, 2007). The major geological events can be summarized as:

Event 1; Developing of badlands topography on the periglacial surface. Deep weathering, erosion, and slumping, lasting more than 70 million years. Estimated depth of the periglacial subaerial erosion is 450 to 750 m, with an average depth of removal of about 600 m.

Event 2; Multiple glaciation, ice erosion, and deposition. Pre-existing bedrock valleys partly filled with sand and gravel. Formation and burial of interglacial valleys, glacial erosion and ice-thrusting of the upper shale zone; detachment and transport of small and large blocks of bedrock. Local brecciation, shearing, and drag, folding of the upper 15 m or so of bedrock strata. In Saskatchewan, an estimated 1000 m of ice load may have resulted in the development in the shale and sand interbeds within the shale.

Event 3; Stagnation and melting of glacier. Postglacial lakes formation and drainage. Beginning of fluvial erosion within the drift.

Event 4; Unloading caused by rapid postglacial stream erosion and producing raised valley rims and upward flexure of valley sides (Mollard, 1977).

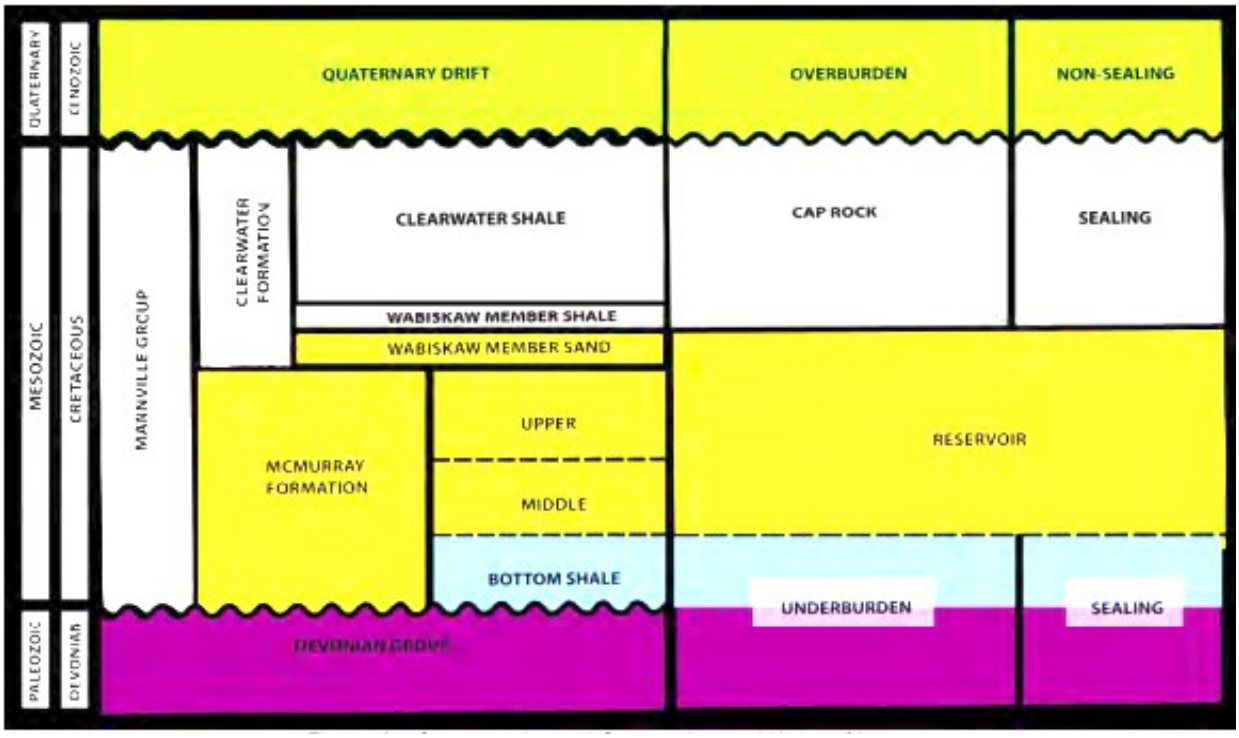

Figure 3-3 Stratigraphy and geological units showing Clearwater shale (Uwiera-Gartner et al., 2011)

3.4 DEPOSITIONAL CONDITIONS

Present characteristics of a sedimentary rock such as particle size, sorting and bedding are indicative of a certain depositional environment. Sedimentary rocks display same geological characteristics were deposited under similar environmental conditions. Cretaceous clay shales were under huge amount of OB and now this disappeared due to erosion. The current stress state is much less than what it was once experienced before (Morgenstern, 1979). Today's shales are older material or glacier deposits with over consolidation (OC) due to the weight of the ice used to be on it.

The Clearwater Formation is an OC clay shale marine sequence deposited during the Cretaceous period. It is subdivided into several stratigraphic units based on the characteristics of their lithology, stratigraphy, and depositional environment. Old glacial sediments are likely reworked Clearwater (Guindon, 2015). Figure 3-2 and Figure 3-3 showed a cross section and a geological stratigraphy of Cretaceous Clearwater Formation in Northern Alberta. This Cretaceous

clay shale interval ranges from about ten meters to several hundred meters below the surface, dependent on different locations (Zadeh, 2016). The Cretaceous clay shales are usually interbedded with siltstone, sandstone, limestone, and bentonite (Scott & Brooker, 1968). This laminated and interbedded nature causes shales to behave anisotropically, and localized shear failures may develop along weaker and/or bentonitic layers because of shearing along bedding planes during stress changes related to deposition, faulting, glaciation, and erosion (Mollard, 1977) and (Zadeh, 2016). Cretaceous shales typically suffer from minor shears and remoulded laminations in addition to various types of discontinuities, such as fissures which are common in the stiff heavily OC mudstone. These fabric features may have different surface characteristics, particle gradations, and/or mineralogizes, hence their strength may differ from any other rock/soil masses (McGown, 1982).

3.5 FISSURING

Fissures are shear planes resulting in slickenside and they can be compared to tectonic minor shears; in the displacement, Riedel, and thrust shears (Cruden, Thomson, & Tsui, 1989). Typically shear failure produces fissures which may result in catastrophic permeability changes. Presence of fissures and pre-sheared failure surfaces is not uncommon within the Cretaceous clay shales. Fissuring is characteristic of clay shales (Morgenstern, 1979). When fissuring exists, the macrostructure dominates the mechanical behaviour since full shear strength cannot be generated. Origin of fissures in heavily OC clays may be due to:

1. Unloading (shear fissuring); this is a typical because marine deposits were subject to huge OB loading, then unloading post glacial in the erosion state. The problem arises because the unloading path follows different pass and imposing plastic (permanent changes) as illustrated in Figure 3-4.
2. Local shearing.
3. Tectonic folding and faulting as seen Figure 3-2.
4. Desiccation or drying (Figure 3-7); these cracks open and close seasonally and they are vertical tensile failure formed due to material contraction. Typically, they are irregular surface features.
5. Systematic jointing (Figure 3-5); because of stiffness variation as in case of sandstones and shales sequence. They form vertical joints (Figure 3-7) due to tensile failure.

6. Syneresis (colloidal phenomena); which is shrinkage of a newly deposited material.
7. Local stress concentrations.
8. Weathering (Martin & Hencher, 1986); loading, unloading and ice thrusting producing various deformed fabrics in the ice-thrust mudstones (Tsui et al., 1989).

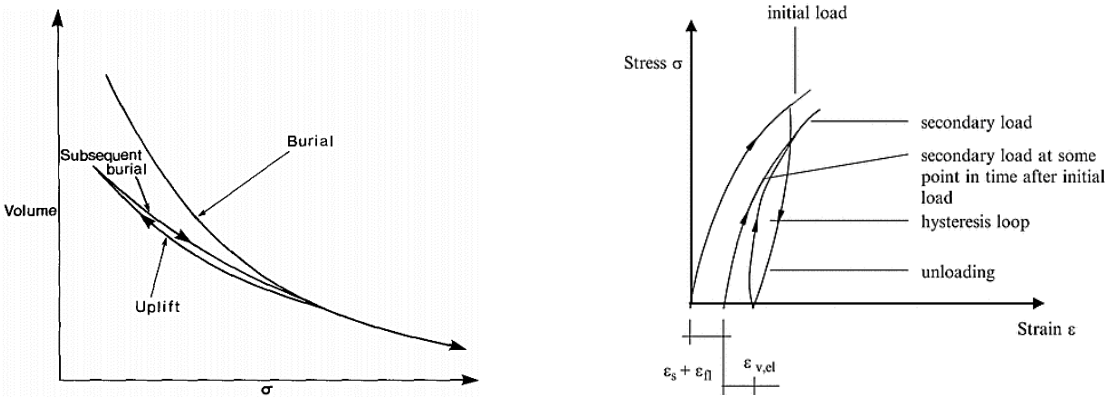

(a) (b)

Figure 3-4 (a) Burial path (Jones & Addis, 1986) and (b) loading-unloading cycles

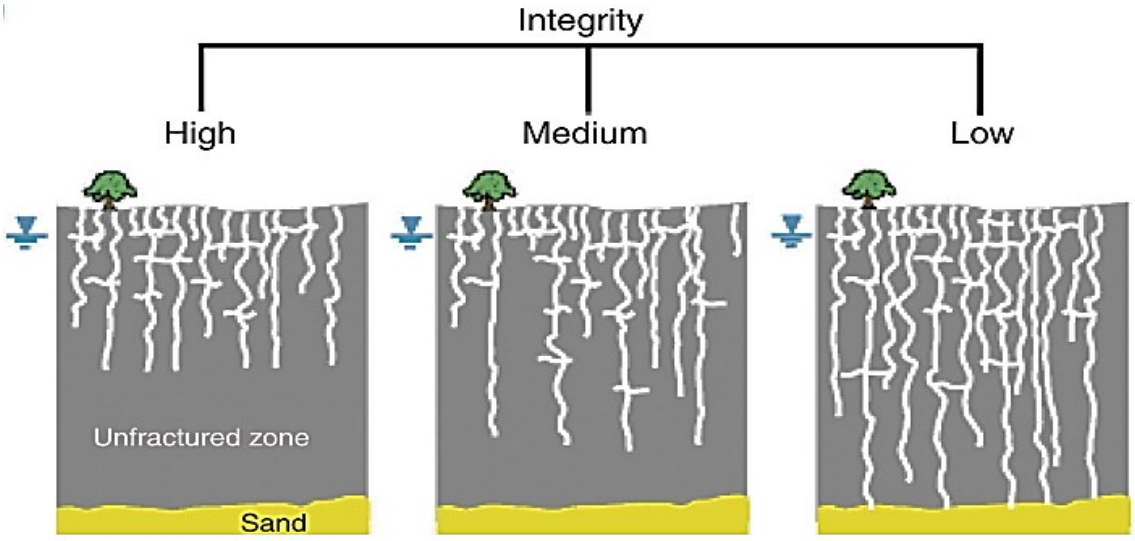

Figure 3-5 Shale integrity as function of discontinuities connectivity (Guindon, 2015)

3.6 CLAY SHALES

A soil will disintegrate when exposed to water in an unconfined manner, whereas a rock will not. Clay shales are of a marine origin and according to many classification schemes are transition materials between soil and rock as illustrated in Figure 3-6. Like most sedimentary argillaceous rocks, its laboratory properties are transversely isotropic in nature, i.e. properties change when tested parallel versus normal to bedding planes (Corkum & Martin, 2007).

Clay shales are often deposited over areas of large lateral extent (hundreds of kilometers). The primary vertical deformations they experienced subsequent to deposition were essentially one dimensional, in the absence of horizontal tectonic loading. Clay shales are predominantly made up of clay particles which are primarily oriented parallel to the horizontal plane resulting in the formation of pronounced laminations or continuous beddings (Wong, Schmitt, Collis, & Gautam, 2008). The pronounced micro-fabric of the clayey matrix was formed during sedimentation and a complex history of burial, physical compaction, development of strong diagenetic bonding, tectonic faulting (Figure 3-2), uplift, folding, and erosion (Marschall et al., 2005). Clay shales are either weakly cemented or uncemented (Morgenstern, 1979) where that cementation is usually due to diagenesis.

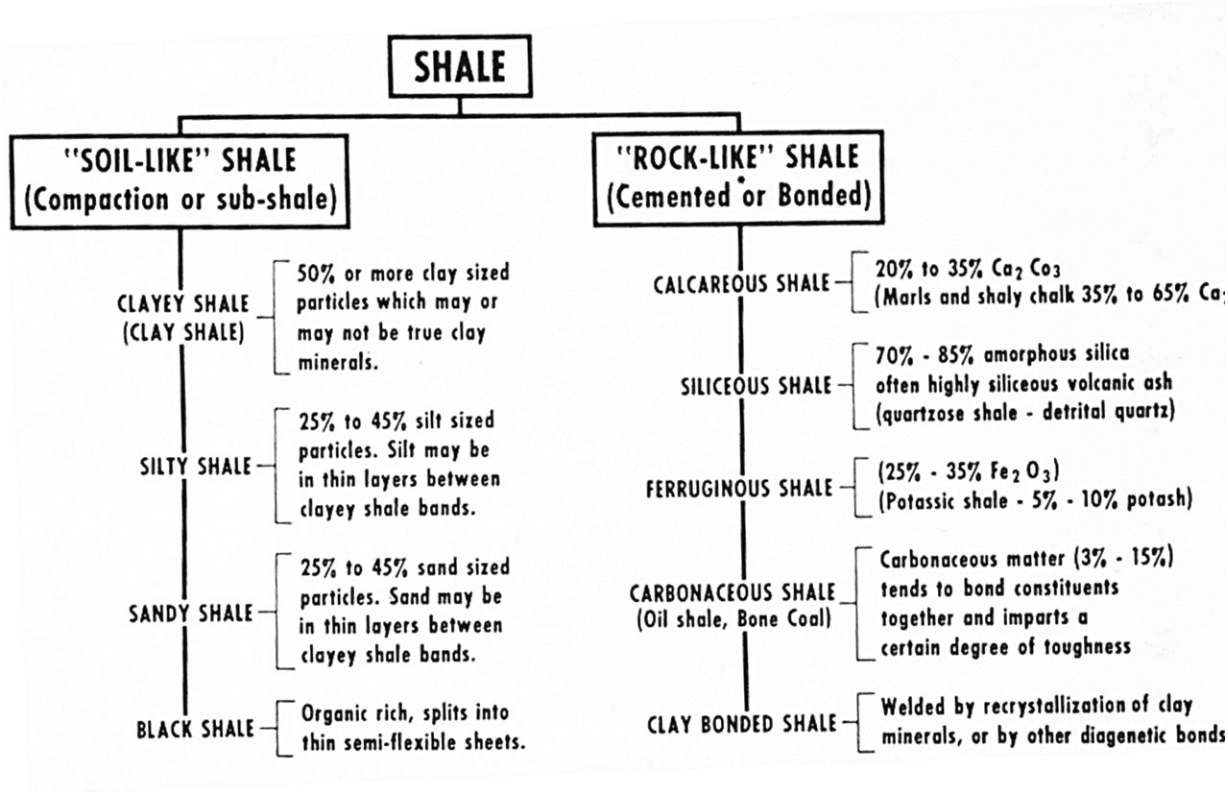

Figure 3-6 Classification of shale (Morgenstern, 1979)

3.7 GEOLOGICAL FEATURES IN CLAY SHALES

Detailed geological data of past histories of loading and identification of existing failure and weak planes in clay shales are essential. Fine grained clay shales mineral particles were initially deposited at high void ratio and water content. With continued OB deposition and as the

total stress increases under zero lateral strain conditions, in situ failure of low strength shale may have occurred. With time, diagenesis and cementation were introduced. Along their formation, clay shale masses significantly suffered from distinct features as a result of remarkable geological history incidents such as valley rebound. Clay shales are weak, anisotropic and susceptible to slacking upon exposure as seen in Figure 3-7. Whenever encountered, these low strength clay shales may control the design.

Figure 3-7 Exposed Clearwater clay shale in Alberta

3.8 VALLEY REBOUND

Three main geomorphological settings, susceptible to glaciotectonic deformation, are recognized in central Alberta, namely; escarpment, valley, and plains (Tsui et al., 1989). During the valley down cutting, weak bedding planes may have sheared in situ resulting in very low shear strength clay shales (Matheson & Thomson, 1973). The post glacial valley rebound processes affected the Plains environment containing these weak clay shales. Valley rebound process included flexure and slippage between bedding planes resulting in pre-sheared surfaces and significantly reduced the bedrock frictional values.

3.9 STRATIGRAPHY SEQUENCE

In the floodplain area in Alberta, the stratigraphy comprises a fine grained alluvial deposit overlaying alluvial sand and gravel, which is underlain by bedrock (Ruban, Patrick, & Skirrow, 2004). The bedrock comprises interbedded clay shale, siltstone and sandstone. In the floodplain area, the upper bedrock has been softened and weathered due to water flowing over it early of its geologic history. The well jointed bedrock (Figure 3-7) is generally uncemented and weathered near surface.

The Clearwater West property, in the northeastern region of Alberta Basin, is part of the Western Canadian sedimentary basin (WCSB). The WCSB is divided into two major components; a passive margin and a foreland basin, where the two are separated by the sub-Cretaceous erosional unconformity. The passive margin developed after the late Proterozoic rifting of the North American craton, depositing shield-derived clastic, carbonates and intervening shales, between the Middle Cambrian and Middle Jurassic Periods.

The foreland basin developed from the collision of the allochthonous terrains with the western margin of the craton between the Middle Jurassic and Tertiary Periods (Uwiera-Gartner et al., 2011). The foreland basin succession generally consists of Late Jurassic to Early Cretaceous clastic, shale-dominated and sand dominated materials (Porter et al., 1982 and Bachu et al., 1993). This succession is overlain by Pleistocene and recent deposits. The regional stratigraphy and geomechanical units (GMUs) of interest in this study were shown in Figure 3-3 (Uwiera-Gartner et al., 2011).

The Lower to Middle Devonian aged strata is comprised of the Lower Elk Point Group, red bed evaporite successions, which unconformably overlie the Precambrian basement. The Middle Devonian Upper Elk Point Group is comprised of clastic, carbonates, and evaporates. The Prairie Evaporite Formation has undergone salt dissolution near the eastern edge of the Alberta Basin during the Devonian Period which influenced the characteristics of the Devonian and Cretaceous strata (Bachu et al., 1993).

The GMU generally consists of calcareous shales and carbonates overlain by the sub-Cretaceous unconformity. Karsting events of the Devonian Period have been known to impact the geological structure of the Devonian and Cretaceous strata in northeast Alberta. The Mannville Group forms the Lower Cretaceous (Figure 3-8) strata of the foreland basin, which overlies the

sub-Cretaceous unconformity. The Mannville Group is comprised of the Lower Mannville, McMurray Formation, which is usually a target oil sands reservoir in Alberta. The Upper Mannville, Grand Rapids Formation and Colorado Group are eroded strata (Uwiera-Gartner et al., 2011). Cretaceous clay shales are usually interbedded (Figure 3-7) with siltstone, sandstone, limestone, and bentonite (Scott & Brooker, 1968).

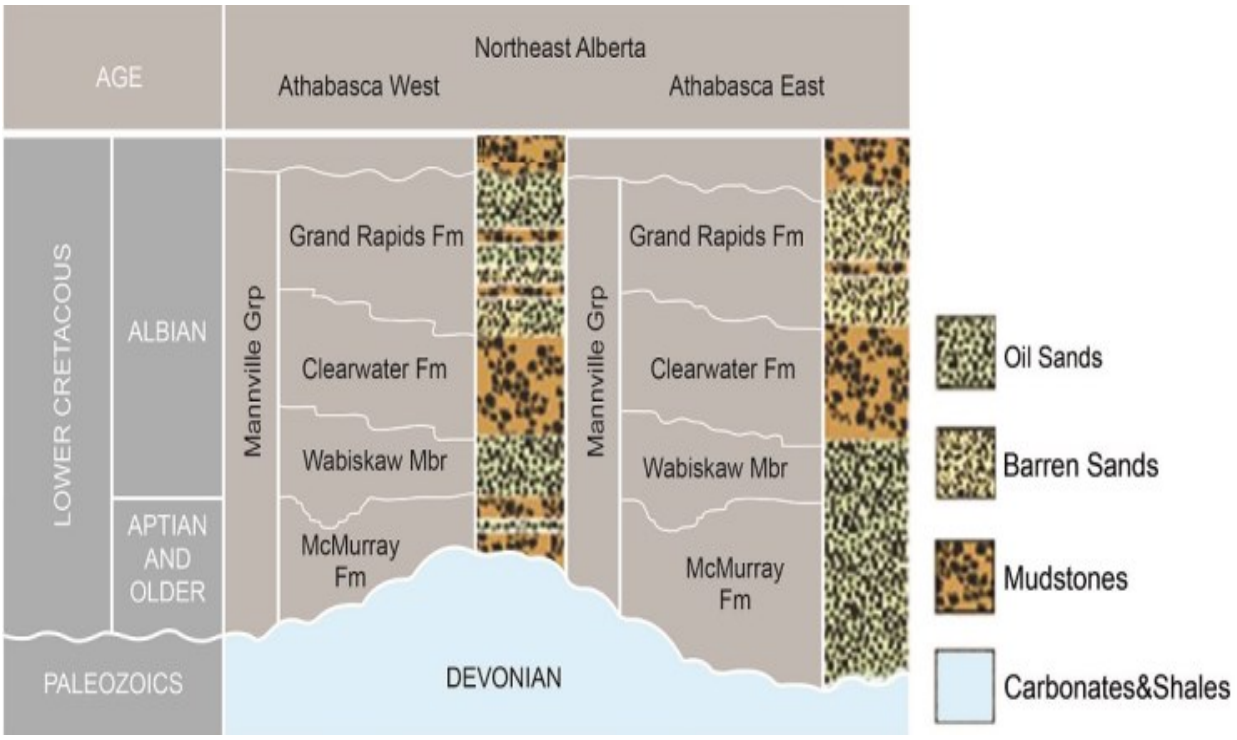

Figure 3-8 Lower Cretaceous stratigraphy (Zadeh, 2016)

Quaternary aged sediments uncomfortably overlie the Clearwater Formation. The pre-Quaternary unconformity separates the Quaternary and Clearwater Formation strata (Andriashek, 2003). In Alberta, overlying the McMurray Formation are gray marine shales of the Wabiskaw Member and Clearwater Formation (Figure 3-2). The Clearwater Formation is shale-dominated, consisting primarily of mudstones and clay shales, with sand and silt laminations or interbeds (Figure 3-7).

3.9.1 INHERENT DEFECTS

Clay shales are weak, brittle and sensitive to local strain concentrations. Inherent defects such as fissures and slickensides are common in clay shales (Hsu & Nelson, 1993). Defects often control the overall behaviour of a clay shale mass. Such distinct defects in the Cretaceous succession in Alberta region were developed:

- During deposition and digenesis processes, where defect zones may have developed around stiffer material. Differential stiffness produced depositional facies and/or differential cementation.
- Due to shear stresses and strains experienced during glacial loading and unloading.
- During erosion; where several phenomena can occur such as induced shear stresses, differential rebound, and differential swelling. These consequences may cause differential movements and slips along bedding planes especially the weak ones and along pre-existing (past) shear planes.

3.9.2 SECONDARY STRUCTURE

Large shear strains, softening effects and filling or mineralization along secondary planes in a shale mass decreases its shear strength (Hsu & Nelson, 1993). Various discontinuities including faults (Figure 3-2) are not uncommon in clay shales owing to low shearing resistance along the secondary planes.

3.10 WEATHERING

Clay shales are very sensitive to weathering hence proper attention must be given to the depth of the topographic control in weathering profiles. Shales in weathered zones may behave like soils. Weathering can be physical or chemical (Hsu & Nelson, 1993) where:

- Physical weathering is defined as a disintegration from the original structure due to slacking, cycles of wetting (swelling) and drying (shrinking), freeze and thaw, and stress changes due to erosion (Figure 3-7).
- Chemical weathering is defined as decomposition, alteration and degradation of clay shale such as oxidation and/or formation of gypsum. Chemical weathering causes volume changes, changes in water content, and lowers both strength and stiffness.

3.11 DISCUSSION AND SUMMARY

Geotechnical engineering handles problems by practically employing a wide variety of techniques ranging from site mapping and geological characterization to advanced theoretical analysis and performance monitoring. During engineering activities, problems may arise with expositing zones of failure reactivated. Differential movements along faults, for instance, are often

experienced whenever disturbed due to excavation or tunneling activities since failure can be induced as a result of stress relief and/or stress redistribution.

Considerable complexity is clear in the distribution of the geotechnical properties of mudstones. It all starts by describing the genesis of the material present. Geotechnical complexity can be analyzed by applying the concept of facies to the genetic, epigenetic and weathering processes that affect the properties of any encountered rock mass. Various sedimentary facies can be identified using process models which are paradigms to organize and analyze the characterization of geotechnically complex materials including the fabric studies of brecciated mudstones matrices.

Highly over consolidated (OC) ice-thrust stiff mudstone is brecciated, sheared, and contains continuous and flat-lying principal displacement shears. The ice-thrust mudstone is composed of platy clay minerals in aggregations having unique and remarkable diagenetic bonds. In Alberta, glacially deformed soft clay shales are a branch of these heavily OC mudstones. This chapter illustrated that, the heavily OC mudstones in Alberta are not only known of their medium density but also of a regular joint pattern that contributes to a material with relatively well-defined geological properties. The Cretaceous Clearwater clay shale (CCSh) in Alberta poses universal epigenetic features inclusive for that class of material genesis formation. There are non-changing and key geologic features governing and are intrinsic to clay shales in North America.

CHAPTER 4 FUNDAMENTAL DISTINCTION BETWEEN ROCK TYPE EXTREMES

4.1 INTRODUCTION

Engineering materials such as rocks may be categorized according to their hardness. Based on classification schemes such as the ISRM (1978), rocks maybe categorized as hard (i.e. stiff), medium hard, or soft (i.e. very weak). Igneous and metamorphic (crystalline) rocks such as granite and gneiss are harder than sedimentary rocks, such as shale. Researchers have been using geotechnical spectrums for classifying materials according to their stiffness (Schmidt hammer rebound test) and uniaxial compressive strength (UCS), such as the ISRM scheme given in Figure 4-1. Koncagül & Santi (1999) stated that the compressive strength is the most widely used parameter to characterize rocks in engineering practice.

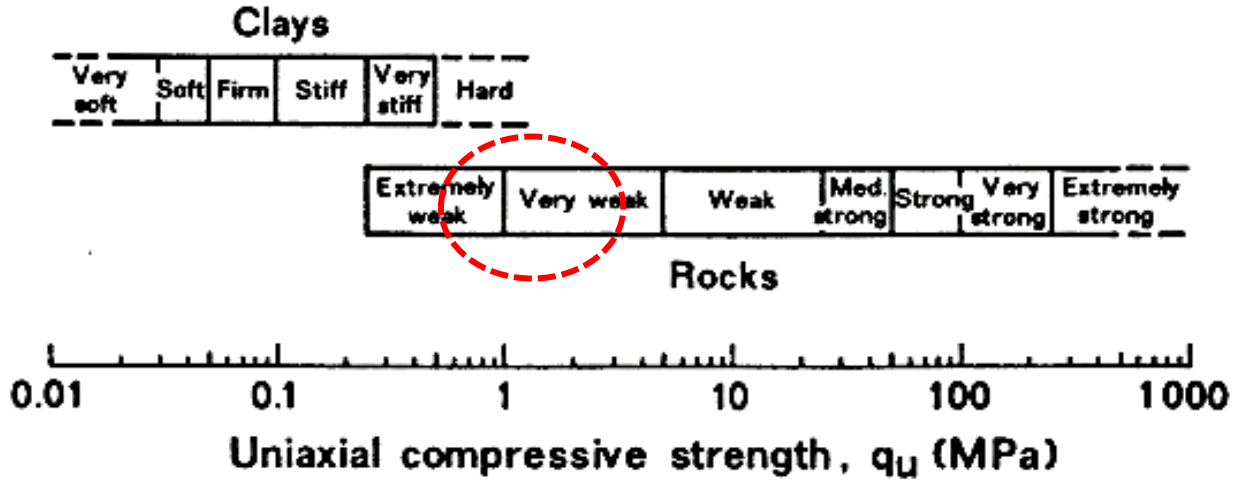

Figure 4-1 ISRM classification scheme (Brown, 1981)

As stated in Chapter 1, the scientific hypothesis of this research was based on that, hard and soft rocks are unlike, accordingly the first research objective was to highlight the fundamental differences between these two rock type extremes. In this chapter, marble and Clearwater clay shale (CCSh) are investigated, as examples of the rock type extremes, in a comparison utilizing literature published data, laboratory observations, FEA, and DEM. Required input mechanical parameters used in this chapter are of a marble deposit from the Apuan Alps in Italy and a CCSh deposit in northeastern Alberta in Canada. Generically, marble is a highly metamorphic rock composed mainly of calcite. The fusion and re-crystallization of calcium carbonate produces its

typical aspect of white-ivory look with small faded grey veins (Grasselli & Egger, 2003). On the other hand, the CCSh is a heavily over-consolidated soft rock that consists of a sequence of marine shales with occasional thin argillaceous and silty sand facies.

Rock masses in general consist of intact rock blocks separated by discontinuities (Bidgoli, Zhao, & Jing, 2013). Conventionally, overall deformation of a rock mass consists of two components:

1. deformation of intact rock, which is claimed to exhibit a linear elastic behaviour
2. deformation of the discontinuities, which may behave in an anisotropic, nonlinear and plastic manner (Agharazi, 2013)

Rock failure generally involves combined failure mechanism where a complex interaction occurs between pre-existing discontinuities and intact rock bridges. The respective strengths of the two elements are not necessarily mobilized simultaneously. It is therefore critical to consider not only sliding and/or opening along pre-existing discontinuities but also the possibility of rock bridge failure especially if the rock mass is very weak (soft).

Discontinuities have a major effect on the deformability and strength in hard rock masses. It was stated in (Chen & Zhou, 2011) that due to a stiffer/stronger rock matrix, most deformations are taken up by the discontinuities, in the form of normal and/or shear displacements. On contrary, in soft rock masses, the intact rock bridges deform significantly. Feng et al. (2012) carried out a rock comparative modelling where they have shown that in a soft rock zone, the range of plastic deformation was obviously larger than in the hard rock zone. Figure 4-2 schematically illustrates the fundamental difference in the relative contributions of deformability between hard and soft rock masses components, basically constituting the basis of the research scientific hypothesis.

The objective of this chapter is to highlight and manifest the fundamental distinction between hard and soft rock masses such as on the geomechanical behaviour. The underlying target from the scientific hypothesis of this dissertation is to emphasize on that mechanical models, derived based on a rock mass with a hard-rock matrix, are not capable to representatively capture the behaviour of a rock mass with a soft-rock matrix. It is important to provide some guidance on this misconception in the state of the art since it is unfortunately common in engineering practice to apply continuous homogeneous isotropic linear elastic (CHILE) approaches to discontinuum inhomogeneous anisotropic non-elastic (DIANE) soft rock masses. For the argillaceous, over

consolidated CCShs studied in this research, it is distinctively a bedded material as illustrated and explained in the previous chapter. These soft CCShs pose anisotropic and heterogeneous distinct mechanical behaviour, as illustrated in Figure 4-3 (Lu et al., 2013).

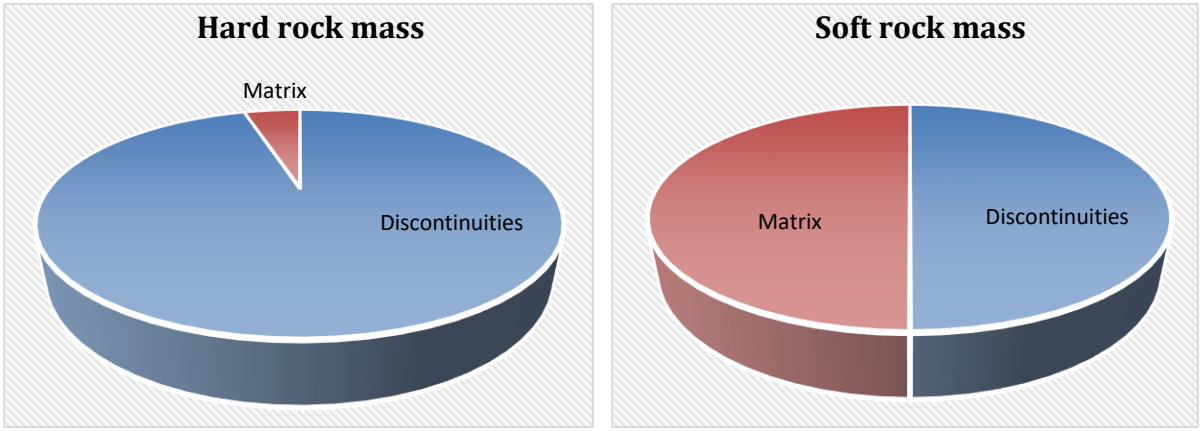

Figure 4-2 Schematic illustrating contribution of matrix versus discontinuities in deformability

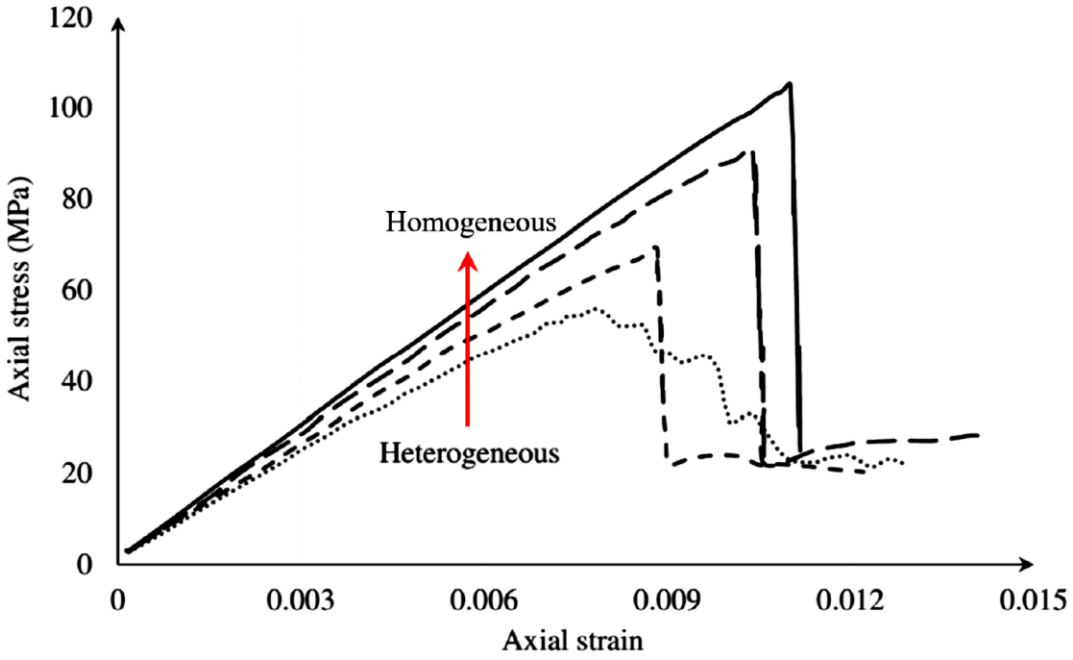

Figure 4-3 Intact (homogeneous) versus fractured (heterogeneous) stress-strain relationships (Lu et al., 2013)

4.2 METHODOLOGY

To achieve the objective of this chapter, a multi-level comparative investigation to demonstrate the fundamental differences between two rock type extremes is carried out. The methodology adopted can be divided, based on the level of investigation, into; micro, laboratory,

and macro-scale as illustrated in Figure 4-4. Scanning electron microscope (SEM) and laboratory geomechanical testing results of marble and CCSh are published and publicly available in multiple references such as in (Kemthong, 2006) and (Zadeh & Chalaturnyk, 2015) respectively. SEM images of marble and CCSh are depicted in Figure 4-5 to compare the fundamental distinction between the two rocks at the microscale. Clearly, it can be noticed that there are distinctive differences between the two rock types at the microscale in shape, nature, size, packing, ponding, layering, arrangements of grains, etc.

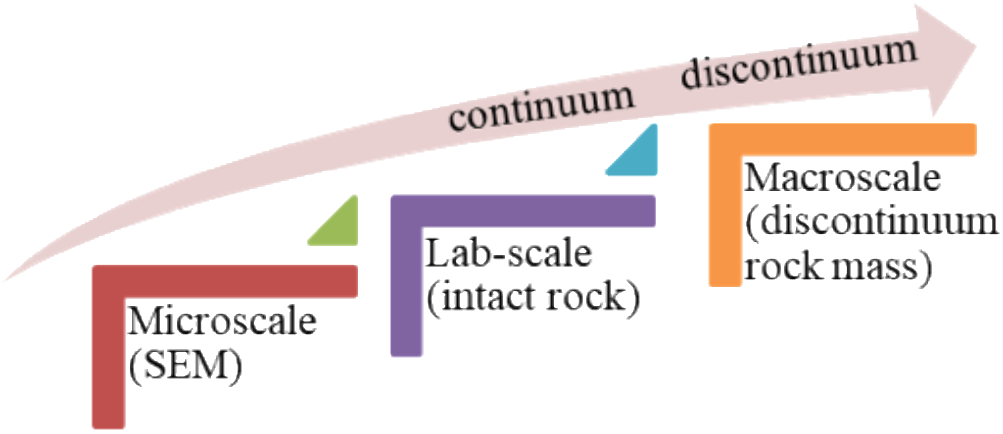

Figure 4-4 Multi level analyses of rock extremes

At the laboratory scale, plots of stress-strain relationships of intact specimens of marble and CCSh are plotted in Figure 4-6 to show the rocks' geomechanical behaviours as confinement pressure (CP) increases. The pre-peak portions of the stress-strain curves are almost linear regardless the CP in case of marble unlike in case of the CCSh. Moreover, the strain each specimen suffered to failure is diverse. Physical comparison between two failed cylindrical specimens of the two rocks can be seen in Figure 4-7.

In macroscale investigations, numerical simulations are generally utilized due to the:

- high expenses of field-scale testing,
- inability to always secure representative undisturbed samples enough for laboratory testing, and
- lack of a laboratory testing apparatus with an appropriate stiffness and scale to accurately test soft rock specimen.

The methodology for the macroscale comparison included literature survey, finite element analysis (FEA) and distinct element method (DEM) numerical simulations of 2D and 3D models of the two rock type extremes as follows:

1. The rock mass compliance ratio of a wide range of rock types collected from literature,
2. FEA using SIMULA™ Complete ABAQUS Environment (CAE) by Dassault Systèmes®, comparing single-discontinuity 2D models (Bisdom, Bertotti, & Nick, 2015), and
3. DEM using 3D Distinct Element Code (3DEC) from Itasca.

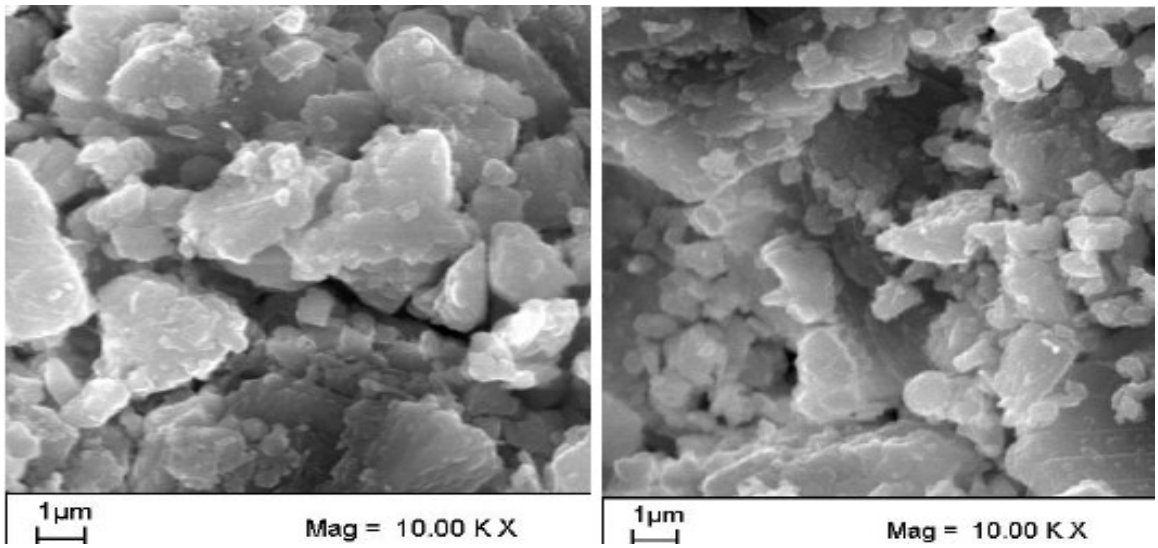

(a)

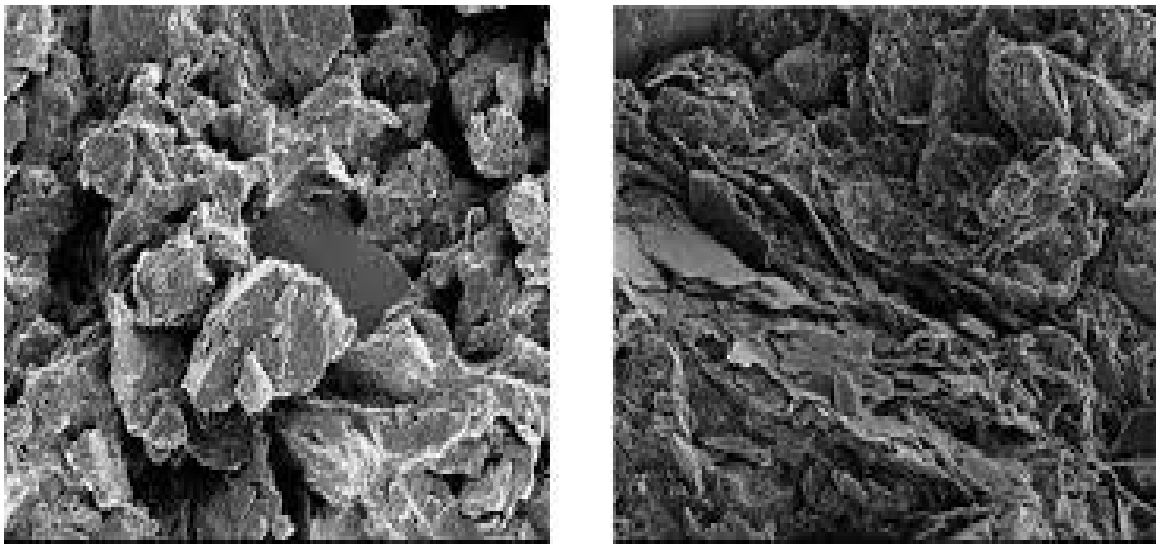

(b)

Figure 4-5 SEM images of (a) marble (Ince, 2013) and (b) Clearwater clay shale (CCSh) (Zambrano-Narvaez & Chalaturnyk, 2014)

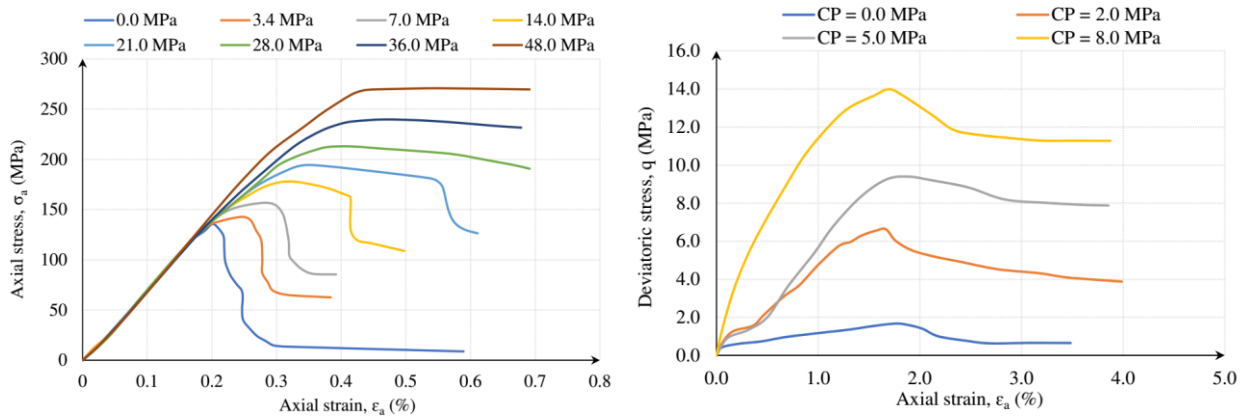

(a) (b)

Figure 4-6 Stress-strain laboratory results of (a) marble (Yang et al., 2013) and (b) clay shale – reproduced after (Xu et al., 2013)

(a) (b)

Figure 4-7 Cylinders failed under compression of (a) marble (Liu & Shao, 2017) and (b) CCSh (Zambrano-Narvaez & Chalaturnyk, 2014)

4.3 COMPLIANCE RATIO

The stiffness [K] is defined as the ratio between the stress and the strain. The stiffness is the inverse of the compliance [C] as illustrated in Table 4-1. Both can be expressed in a fourth-rank tensor.

Table 4-1 Compliance and stiffness tensors

Symbol	Name	Units
C_{ijkl}	Compliance	$Stress^{-1}$
K_{ijkl}	Stiffness	Stress

The normal stiffness (K_n) of a discontinuity is defined as the normal stress increment required for a small closure of a (usually very tight) discontinuity, at a given level of effective stress (Barton, 2007). The K_n (MPa/m) is calculated per (Goodman et al., 1968):

$$K_n = \frac{\sigma_n}{\delta_n} \tag{4-1}$$

where σ_n is the normal stress (MPa), and δ_n is the normal displacement (m) of the discontinuity aperture. The K_n will increase with increasing the σ_n. The compressibility of a discontinuity or the discontinuity normal compliance (Zimmerman, 2008) is the inverse of the discontinuity stiffness. Generally, it is the element compliance of a given rock mass that matters, i.e., the discontinuities' compliance (C_d) compared to the matrix compliance (C_m).

In order to compare values of C_m versus the C_d in different rock types, a literature survey was carried out. As expected, it is a challenge to measure discontinuity K_n of a weak deformable rock in conventional laboratory setting. Normally, in hard rocks, K_n is determined in a direct shear box apparatus. Though, due to the mentioned difficulty in the case of weak deformable rocks, the data available for K_n of discontinuities in this rocks category, such as clay shales, was very minimal to rare.

The literature survey was meant to gather the C_d to C_m ratios for a wide range of rocks, from hard granite to soft mud rocks, as reported and summarized in Figure 4-8 (a). To better illustrate and quantify the differences in the ratios, a 3D graph was generated as seen in Figure 4-8 (b). The left end of the graph represents compliance ratios in soft/weak rock masses, where the rock matrix is weak and soft; its compliance is comparable to its discontinuities. Hence, the left end of the graph displays ($\frac{C_d}{C_m}$) values of almost unity or greater. On the other hand, the right end of the graph represents the hard rocks, where the matrix is hard/stiff, and consequently, it has a strong compliance compared to its discontinuities. Hence, the ratio at the right end is much smaller ($0.01>\frac{C_d}{C_m}$).

It is usually hard to clearly delineate definite boundaries between rock types for categorization and group characterization. Especially the hard-soil-soft-rock materials which represent a challenge in their classification within the geo-materials conventional schemes. Hence, it is conveniently significant to propose a pioneer classification criterion for discontinuous rock masses spectrum. To interpret the data provided in Figure 4-8, the relationships below can be used as guide boundaries defining categories of discontinuum rock types based on their elements (discontinuities and matrix) compliance ratios.

$$\frac{C_d}{C_m} \leq 0.001 - 0.01 \text{ for hard rocks} \quad (4\text{-}2)$$

$$\frac{C_d}{C_m} = 0.01 - 0.1 \text{ for medium} - \text{hard rocks} \quad (4\text{-}3)$$

$$\frac{C_d}{C_m} \geq 0.1 - 1 \text{ for soft rocks} \quad (4\text{-}4)$$

4.4 TWO-DIMENSIONAL (2D) FINITE ELEMENT ANALYSES (FEA)

The thesis scientific hypothesis stated in Chapter 1 is based on that, soft rocks are unlike hard rocks not only in stiffness and strength but also compliance and deformability as schematically illustrated in Figure 4-2. In case of loading a hard rock model, discontinuities deform much more compared to the hard matrix. Contrarily, in a soft rock model, due to the close compliance between the soft matrix and discontinuities, the two rock mass elements comparably contribute in the overall deformability.

Bisdom et al. (2015) studied subsurface flow and geometry-based permeability in dsicontinuum rock masses using 2D FEA of a single-discontinuity 100 × 100 m square-shaped models (Figure 4-9a). The FE models were assigned wide range of rock mechanical parameters under different normal stress magnitudes. The researchers started by studying the change in a discontinuity mechanical aperture under varying normal loading, and the results are illustrated in Figure 4-9b. The normal aperture of a fracture is usually a function of initial fracture roughness, strength and normal stress acting on the fracture. They concluded that there is a negative exponential relation between the mechanical aperture and the applied normal stress.

Rock Type		$\frac{C_d}{C_m}$
Marl		5.000
Conglomerate		5.000
Siltstone/Mudstone	*joint*	3.738
Clay Shales	*joint*	3.123
Siltstone/Mudstone	*bedding*	2.941
Clay Shales	*bedding*	2.458
Sandy Mudstone	*joint*	2.110
Sandy Mudstone	*bedding*	1.660
Gas Shale		1.571
R3 Granite		0.968
Shale	*Class II*	0.750
Sandstone		0.706
Limestone	*Fault F2*	0.530
Welded Tuff	*Ks (GPa/m)*	0.311
Hard Rock		0.194
Limestone	*Bedding-Planes*	0.170
Granite	*Lab*	0.147
R5 Granite	*81-m depth*	0.027
Granodiorite		0.006
hard Granite	*417-m depth*	0.004
Gneiss		0.003

(a)

(b)

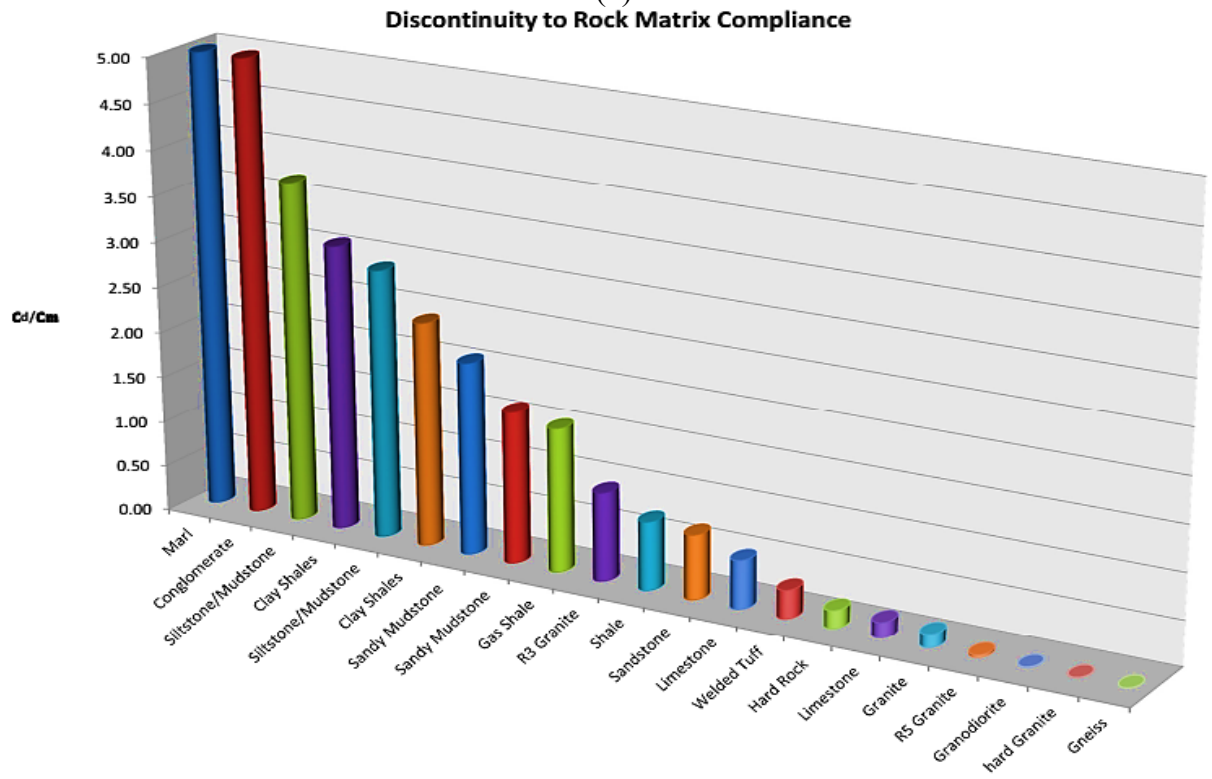

Figure 4-8 (a) Ratios of discontinuity- to matrix-compliance (C_d to C_m) and (b) 3D plot of compliance ratios

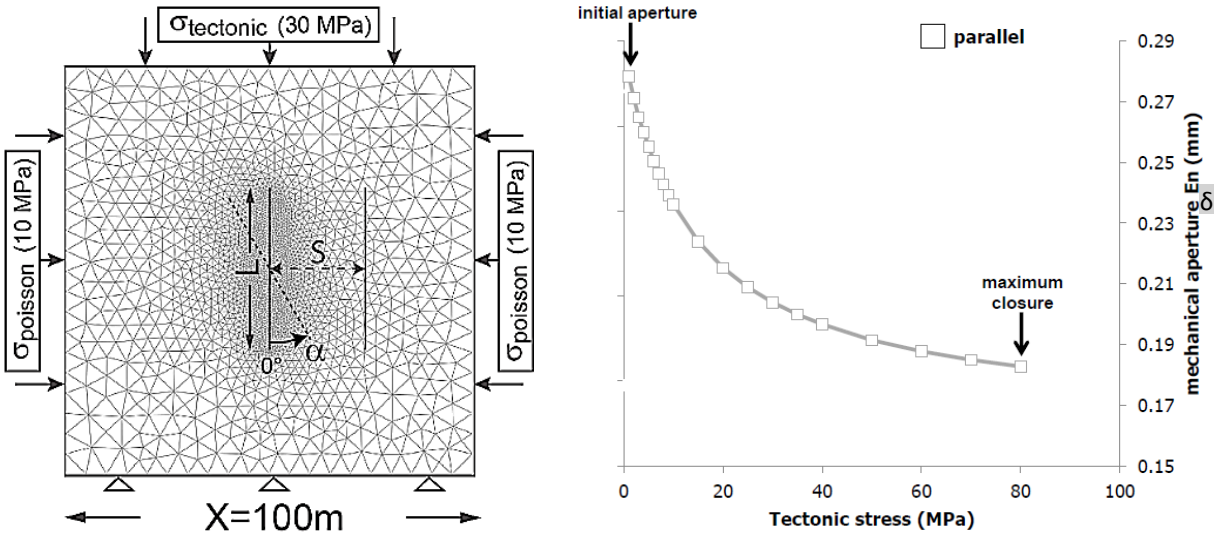

(a) (b)

Figure 4-9 (a) Single-discontinuity 2D FEA model and (b) mechanical aperture behaviour with normal stress (Bisdom et al., 2015)

The intent of this chapter was not to replicate the work of (Bisdom, Bertotti, & Nick, 2015) article, rather partially adopting the FE simulation procedure, used software, discontinuum model geometry and loading conditions in order to simply and fundamentally compare the deformability of hard versus soft rocks. The FEA software ABAQUS 6.13-4 was similarly used in this chapter in the comparison between two rock types: marble (hard rock) and CCSh (soft rock). Two 2D FE models were built, as seen in Figure 4-10. The hard rock model was assumed to have an E_i of 5×10^{10} Pa and an ν_i of 0.3 (Schmitt, Smither, Ahrens, & Jensen, 1986), while the soft rock model was assigned an E_i of 5×10^{8} Pa and ν_i of 0.35 (Islam & Skalle, 2013).

As can be interpreted from Figure 4-10, the rock model settled suffering a downward deformation of 1.5 orders of magnitude in case of the soft rock model. The soft matrix considerably carried up from the whole model deformability as the model is subject to loading, unlike in the hard rock model. The change in the aperture was monitored and plotted in Figure 4-11. In case of the hard rock, the discontinuity is the main contributor in the system deformability (Figure 4-2), and accordingly, the change in the aperture is quantitively bigger.

4.5 DEM USING 3D DISTINCT ELEMENT CODE (3DEC)

In the recent decades, DEM has provided valuable insights into the characterization of failure mechanisms in cohesive frictional materials such as rocks. With the advantage of their

discontinuous nature, distinct models representatively deal with the initiation and propagation of micro cracks inside heterogeneous media. Therefore, DEM the constitutes as a powerful tool for studying how a microstructure affects the macroscopic behaviour in geomaterials (Scholtès & Donzé, 2013). Advantages of the DEM include the explicit representation of discontinuities' system geometries and their constitutive behaviours besides that of the intact rock matrix.

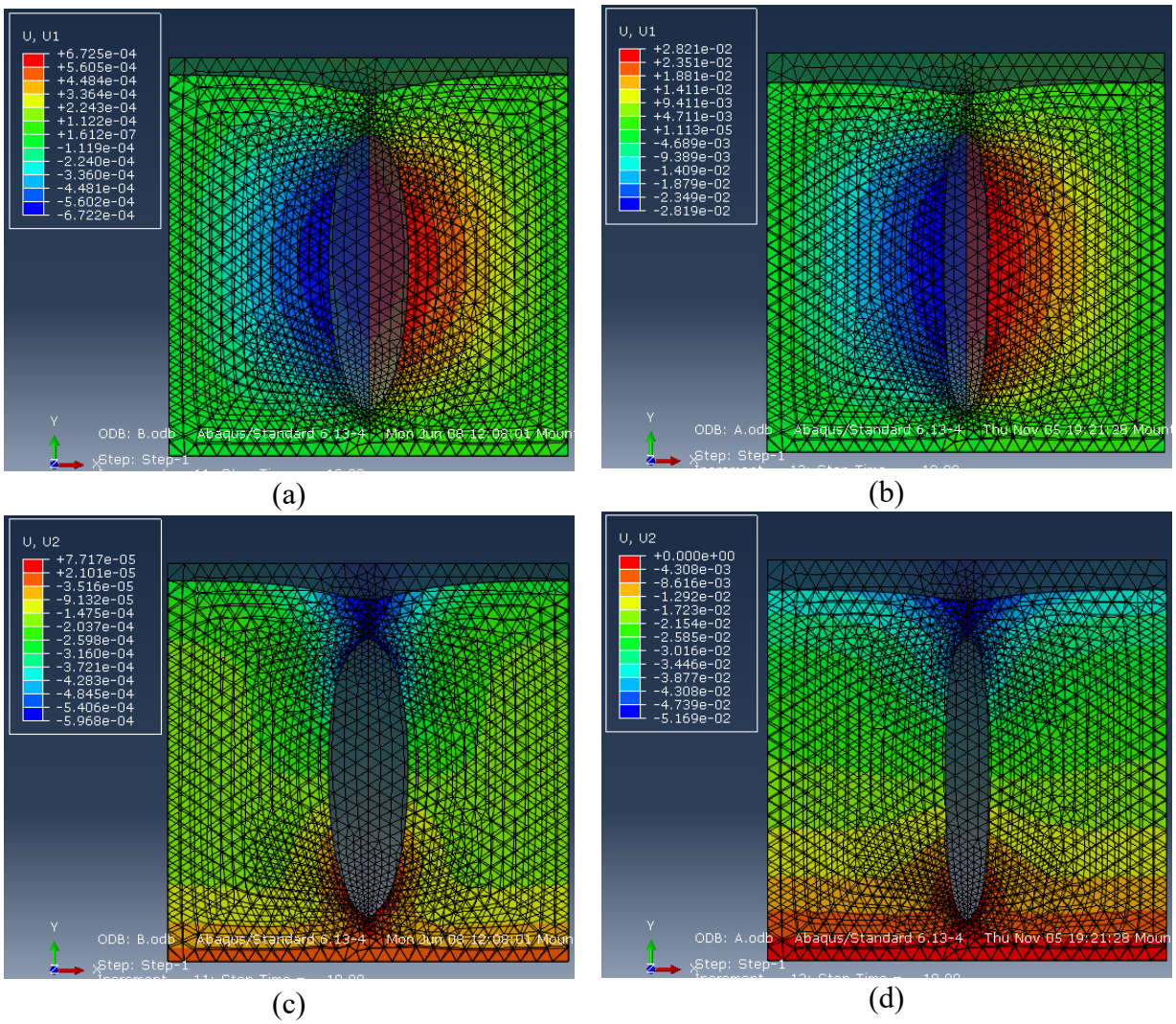

Figure 4-10 Comparison of X-Displacement (U1) between (a) hard versus (b) soft model and comparison of Y-Displacement (U2) between (c) hard versus (d) soft model

In this chapter, block models of marble and CCSh have been modeled using Itasca DEM code 3DEC^{HD} which is mainly offered to deal with modelling discontinuum and blocky materials in 3D. The index geomechanical parameters listed in Table 4-2 of the marble as the hard rock extreme were adopted from (WeiZhong et al., 2011), whereas the parameters of the CCSh as the

soft rock extreme were adopted from the constitutive properties provided in (Zadeh & Chalaturnyk, 2015).

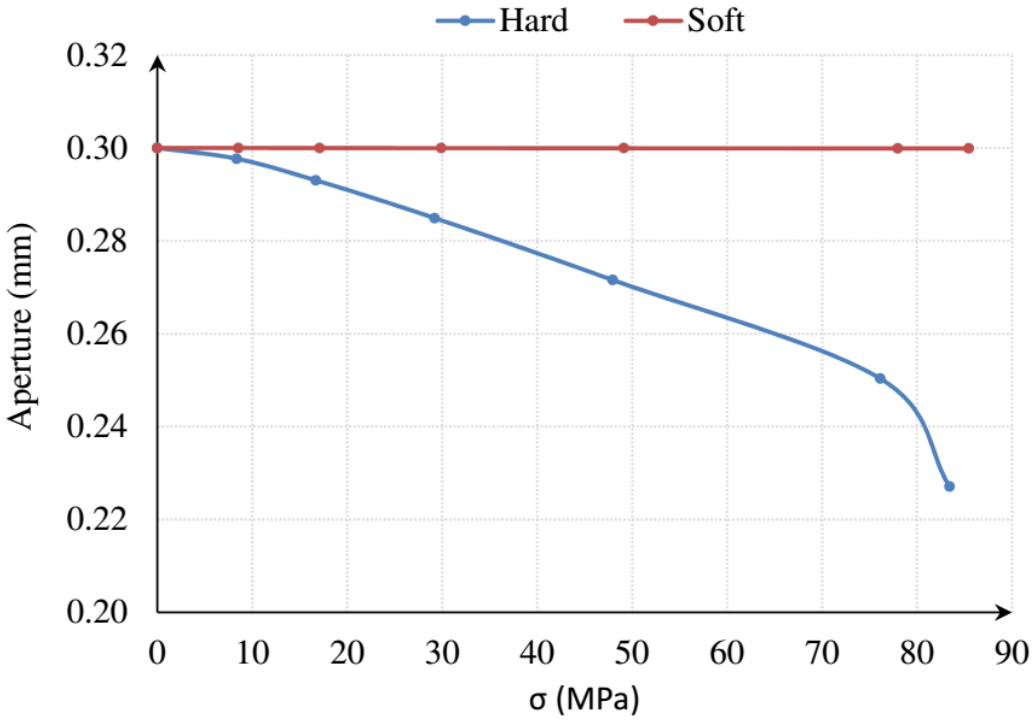

Figure 4-11 Change in discontinuity aperture in hard and soft rock masses

Table 4-2 Input geomechanical parameters for intact models for two rock extremes

Rock type	Density (kg/m^3)	K (GPa)	G (GPa)	Cohesion (MPa)	Friction angle (°)	Dilation angle (°)	Tensile str. (MPa)
Marble	2580	33	20	19.44	43.8	25	2.84
CCSh	2129	0.83	0.18	0.15	30	20	0

4.5.1 MESH CONSTRUCTION

A six-sided "brick-shaped" mesh region seen in Figure 4-12 was created in 3DEC using *brick* keyword in the FISH script composed to build the DEM models. The model zones were constructed using tetrahedral meshes. During the numerical simulation runs, the nodal mixed discretization (NMD) feature was turned on allowing for plasticity calculations as it provides a more accurate solution especially when associated with the tetrahedral meshes (Itasca Consulting Group, Inc. 2016).

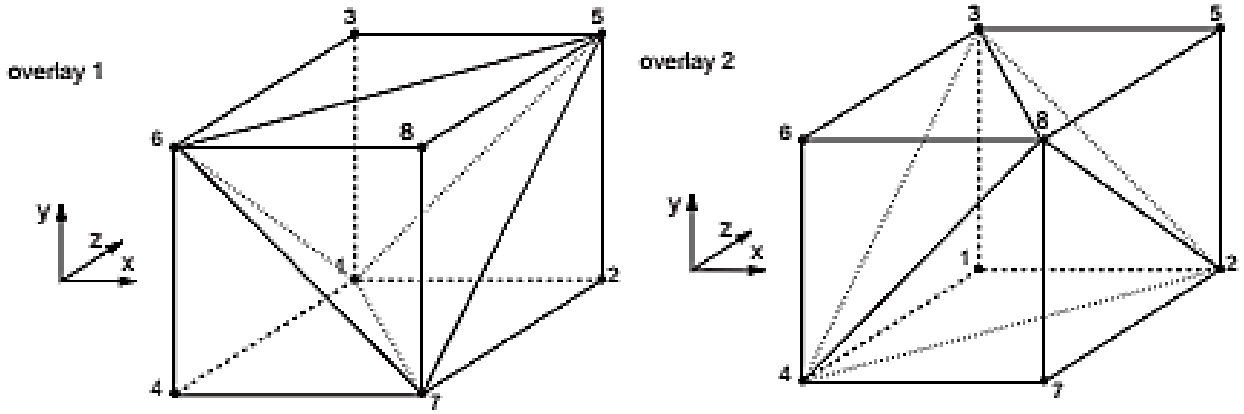

Figure 4-12 Eight-node zone with two overlays of five tetrahedra in each overlay (Itasca Consulting Group, Inc. 2016)

4.5.2 UNIAXIAL COMPRESSION TESTING

Reviewing literature, the most common method selected to characterize the mechanical properties of rocks, is by performing UC numerical tests (a general schematic is illustrated in Figure 4-13). In this section, numerical UC tests were carried out using 3DEC on intact 1 × 1 × 1 m block models of marble and CCSh. The models built were fed with input mechanical parameters values adopted from laboratory mechanical testing results of intact marble and CCSh specimens reported in literature. The models were first checked to produce mechanical parameters (E and UCS) values reasonably matching the input values and a constitutive behavior (axial stress-strain) similar to the laboratory observed and reported behaviour. After a close match is achieved, the calibrated models were approved for analyses.

4.5.3 STRESS-STRAIN RELATIONSHIP NON-LINEARITY

Comparing the plots in Figure 4-14 of the 3D DEM results, of intact marble and CCSh blocks, highlighted and supported the fact that there are fundamental differences in stiffness, linearity, deformability, and strength between the two rock type extremes under consideration at same scale and under same boundary conditions. The difference in the stiffness was found to be two orders of magnitude. The non-linearity of the stress-strain curves' pre-peak stress in the case of intact CCSh rock is clear unlike marble. The strain values at failure in the case of CCSh are higher than those in the case of marble by at least one order of magnitude. Large plastic strain at failure indicates softening of the CCSh rock compared to marble, which suffers less at failure.

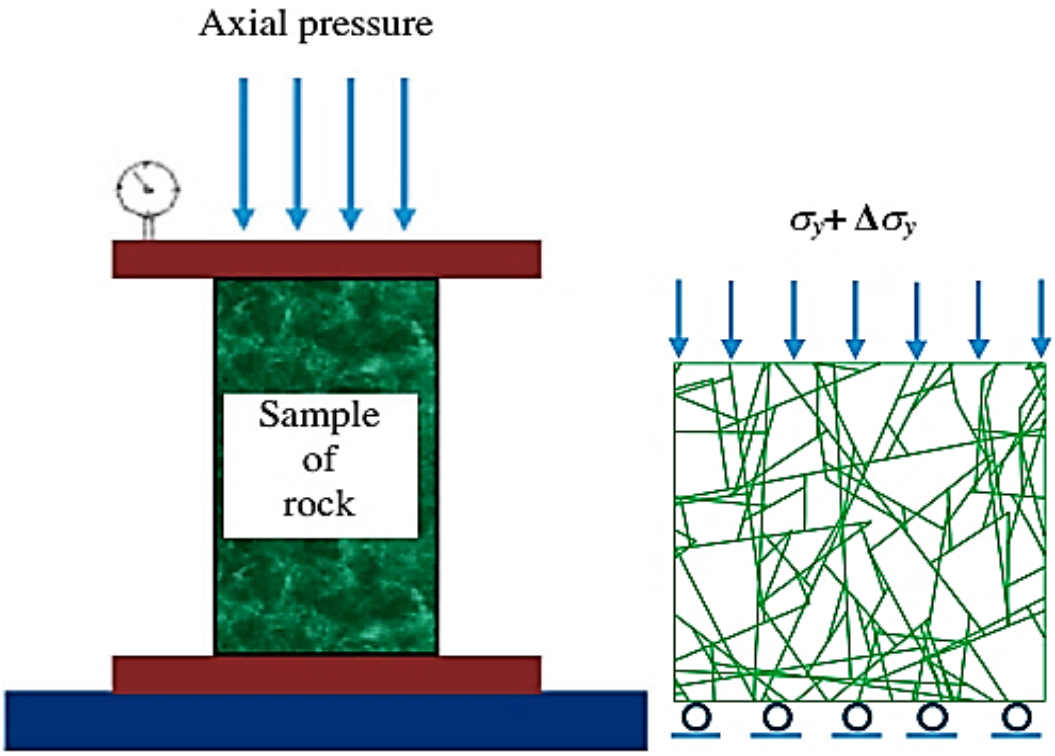

Figure 4-13 Uniaxial compression (UC) (Bidgoli et al., 2013)

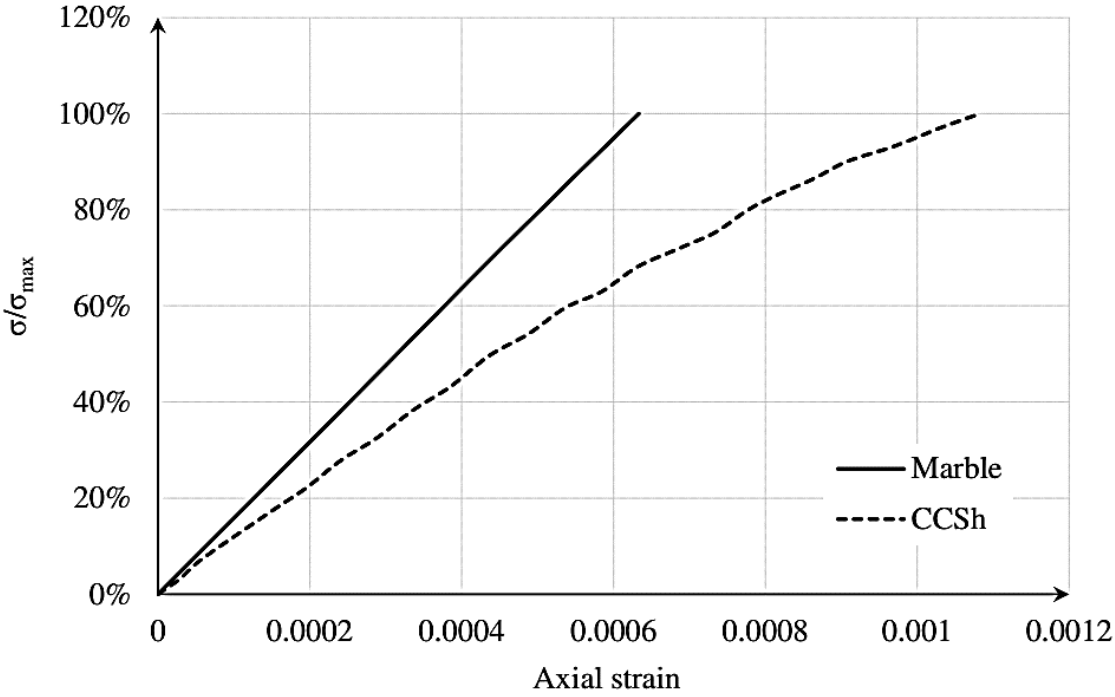

Figure 4-14 Normalized axial stress versus axial strain relationships comparing linearity and strain level at peak of marble and CCSh

4.6 SUMMARY AND CONCLUSIONS

Rock masses consist of intact rock intersected with discontinuities; hence, the rock mass' properties are described by combining the intact rock properties and the discontinuities properties. Hard rock masses are unlike soft rock masses. As stated in Chapter 1, this research first objective is to illustrate and manifest the fundamental distinction between hard and soft rock masses. When a hard rock mass is loaded, the discontinuities are the main contributor in the overall deformability since the rock matrix is much stronger and stiffer than the discontinuities. Hence, in hard rock masses, the discontinuities dominate the failure mode. On the other hand, the intact matrix of soft rocks is weak and deformable and comparably contributes to the rock mass deformability alongside with the discontinuities.

A literature survey of compliance values based on stiffness values reported in laboratory were selected from academically trusted sources such as peer-reviewed articles. Cases like filling material (gouge) in the discontinuities or rough unfilled discontinuity were not included in this compliance survey. Matrix- to discontinuities-compliance (C_m to C_d) ratios further emphasized on the difference between rock type extremes.

New boundaries based on this compliance ratio were set delineating rock categorization borders. According to the collected C_d to C_m ratios, the following relations were observed:

1. Hard rocks pose a value of a $\frac{C_d}{C_m} \leq 0.001 - 0.01$ because the C_m value is high. This is applied to hard rocks such as granite, basalt, and marble,
2. Medium-hard rocks pose a value of $\frac{C_d}{C_m} \sim 0.01 - 0.1$, and
3. For soft and weak rocks such as mud rocks and clay shales, this value is from 0.1 to more than unity.

In the FEA, the mesh was found to be of an importance, especially in the discontinuum analyses, because the discontinuity propagation is mesh dependent in ABAQUS. The sensitivity of the mesh was not examined nor investigated in detail in this chapter though. The early portion of the stress-strain relationship corresponding to a low axial stress resulted from the 2D FEA, showed a closely matching distinct behavior to the reported conventional laboratory UC testing typical results.

3D DEM geomechanical modelling was used to further illustrate the differences in the behaviour between the two rock type extremes under investigation. It was noticed that during the

numerical uniaxial testing, the early portion of the stress-strain relationship in case of the CCSh suffered significant nonlinearity compared to marble, at the same scale and under same boundary conditions. The strain at which the CCSh failed was more significant than that in case of marble by at least two orders of magnitude. It was found that the DEM is more capable of realistically representing the UCS laboratory testing and producing closer results than the FEA. Moreover, 3D analysis is more representative to the real behaviour than 2D analysis.

To conclude, multi-level comparisons employing 2D FEA and 3D DEM modeling of two rock type extremes revealed that, even at the same scale and with same boundary conditions, the two rock types behaved, deformed, had diverse compliance, and failed at strain levels. These comparisons in addition to the compliance ratios literature-based study support the research scientific hypothesis basis of the need to consciously acknowledge the fundamental differences between hard and soft rocks. The problem is that there is still widespread shortcoming in industrial and academic practices applying CHILE-based approaches to soft discontinuum Clearwater clay shale (CCSh) formations, perhaps because it is simpler, easier, and faster in numerical modelling. Based on the results of this chapter, awareness and caution should be exercised when exploring or examining the applicability of hard-rock geomechanical equivalent models and constitutive relations to soft-rock masses.

CHAPTER 5 FROM GEOLOGICAL MAPPING TO GEOMECHANICAL MODELLING

5.1 INTRODUCTION

In naturally fractured rocks, the spatial distribution, size and orientation of the discontinuities are rarely regular or follow a probabilistic distribution. As a result, the size and shape of each block in the rock mass maybe different. Rock mass analysis requires geometric description and knowledge of the discontinuity patterns and their structural statistics. Characterizing the discontinuities in heterogeneous rocks helps in not only anticipating but also evaluating the rock porosity and permeability changes. Presently, many slope stability codes can readily include input individual discontinuity information in a spreadsheet format, where, for each discontinuity, this information includes position, orientation, intensity, size, length, spacing, etc. Also, the spatial positions of the discontinuities can in turn be fed in into geomechanical numerical simulation codes.

Characterization of a rock mass' geological properties enhances the estimation of the thermal, hydraulic and mechanical rock behaviour, which is necessary for engineering developments. This characterization helps to better understand how an argillaceous rock mass would geomechanically respond to loads induced due to thermal stimulation operations in situ. The issue is that, mine benches and caprock locations are both dangerous and difficult to access, limiting the ability to geologically map their detailed structural features and perform volumetric measurements necessary for integrity assessment.

Over the past decades, light detection and ranging (LiDaR) remote sensing technique has become increasingly useful in geology and engineering fields. The advantages of using LiDaR in geological investigations include the convenience and speed at which scans are performed. A LiDaR scan can be used to generate 3D discontinuities projections on stereonet. The use of LiDaR technique for structural characterization of a rock face is widely documented, though limited research has been undertaken to improve the understanding of the importance of the derived data in constructing 3D geomechanical models. Previous researchers used a hypothetical statistics, carry out assumed virtual, or stochastic discrete fracture network (DFN) to build their geomechanical modelling for discontinuous rock masses. A widely-recognized disadvantage of

stochastic DFN simulations is its poor representation of the real fracture systems (Lei et al., 2014) compared to realistic DFN simulations.

Structural feature identification and extraction are the most commonly researched and studied use of high-resolution LiDaR data in geotechnical engineering. Similarly, the aim of this chapter is to geologically characterize a Clearwater clay shale (CCSh) formation in Alberta using a LiDaR point cloud. A systematic workflow to build a realistic DFN for geomechanical simulation purposes from a point cloud is presented in Figure 5-1.

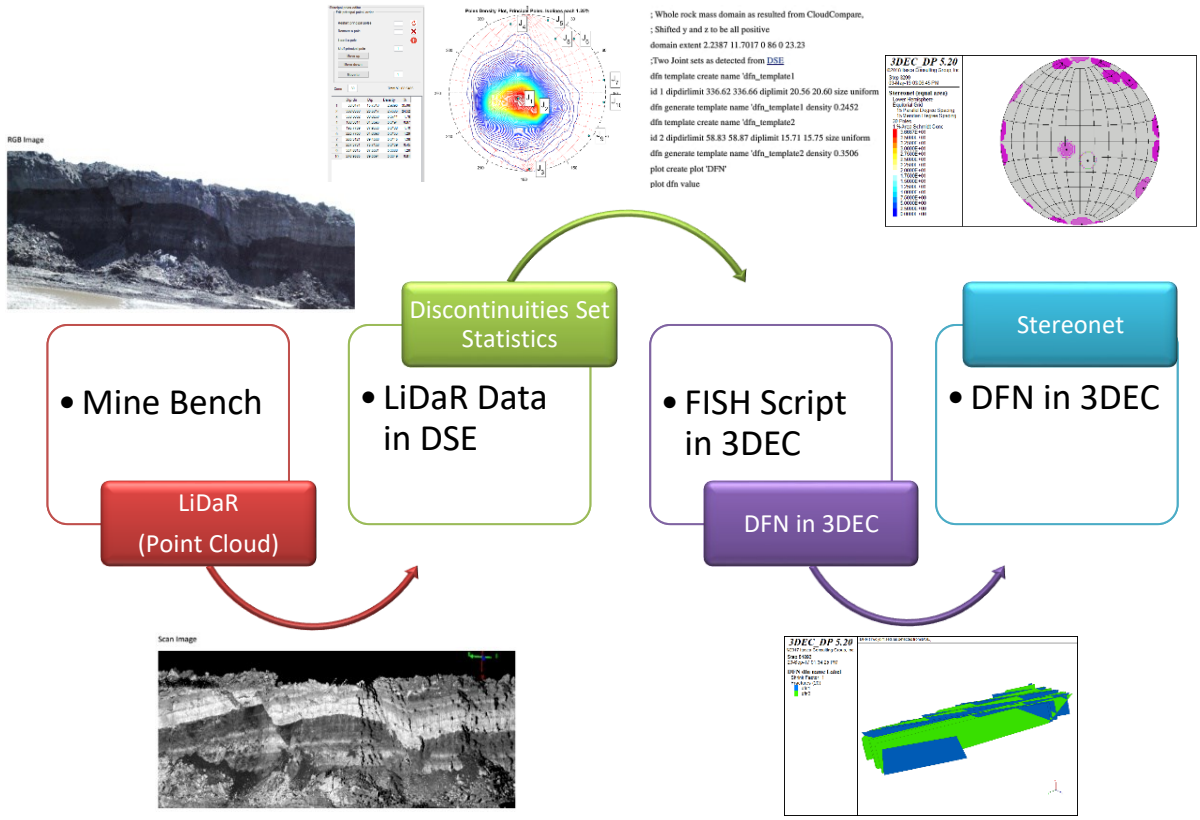

Figure 5-1 Analysis and investigation procedure workflow

The work in this chapter partially constitutes for the second research objective, as stated in Chapter 1, by basically performing realistic geological characterization of a CCSh formation. The deliverables of this chapter are needed later to conduct robust and representative geomechanical modelling via employing realistic 3D DFNs.

As illustrated in detail in Appendix A, a rare terrestrial-based LiDaR scan, of a CCSh mine bench in Alberta, became available for processing to constrain the CCSh formation structural geology. Discontinuity planes normals as well as dip angles and dip directions have been

identified. Using these discontinuity statistics, 3D triangulated irregular networks (TINs) were generated. In this chapter, realistic 3D DFNs will be built from the TINs. The DFNs will be implemented using MATLAB and FISH scripts in Itasca 3D distinct element code (3DEC). Eventually a 3D geomechanical model of the naturally fractured rock mass will be constructed, mechanically loaded, investigated and analyzed.

5.2 GEOLOGICAL BACKGROUND OF THE MINE SITE

It is critical to understand a regional geologic setting in order to relatively locate positions of discontinuities and perhaps anticipate their structural configuration. The location of the mine bench under investigation in this chapter is near Fort McMurray - Northern Alberta in Canada as marked with a red star on the map in Figure 5-2. The mine bench falls within the Cretaceous Albian Lower CCSh unit overlaying the Wabiskaw-McMurray bitumen (oil sands) deposit. The CCSh is an over consolidated clay-shale marine sequence deposited during the Cretaceous geologic period. It is subdivided into several stratigraphic units based on the depositional environment. As can be seen from Figure 5-4 interlayers of siltstone and fine sand facies are typically encountered within the clay shale formation.

5.3 POINT CLOUD

The rock characterization and structural information extraction from point clouds have lately become easier. Recent advances in digital technology provide tools for generating realistic terrain models at a centimeter-scale. Ground-based laser scanners allow capturing 3D survey datasets (millions of points) of a surface, within few minutes. The relatively new high-resolution 3D scanning techniques integrated with image processing and appropriate numerical simulations have been extensively used to identify geological parameters in shales (Saraji & Piri, 2015). The high-resolution LiDaR scan used and processed in this thesis was captured of an exposed CCSh mine bench in Alberta (Figure 5-4). The raw point cloud of 11,836,391 points Figure 5-4 (a) was saved in .LAS file format. This dense point cloud covered extents of: X=25.06 m, Y=119.63 m, and Z= 101.89 m with an original file size of 393,006 KB.

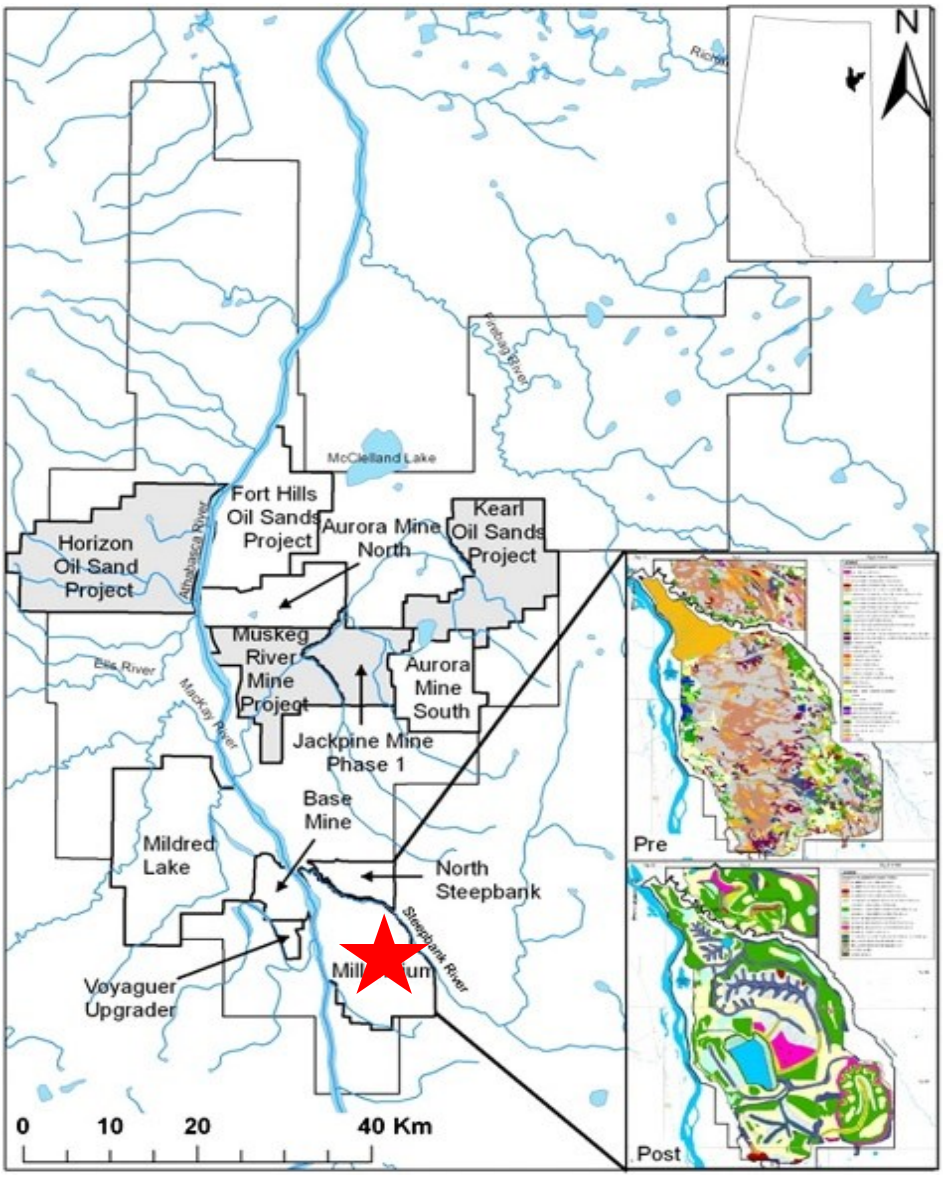

Figure 5-2 Location of Clearwater clay shale (CCSh) mine bench in Alberta

5.4 STRUCTURAL ATTRIBUTES OF DISCONTINUITIES

Discontinuities within a rock mass, when exposed in an outcrop or cut, manifest themselves in one of two ways:

1. On flat planar rock cuts, where the intersection of the plane of the discontinuity and the planar rock cut results in a visible line (discontinuity trace) that lies on both planes as seen in Figure 5-5 (a), or

2. On rock cuts that are irregular, where the actual face of the discontinuity maybe exposed as depicted in Figure 5-5 (b).

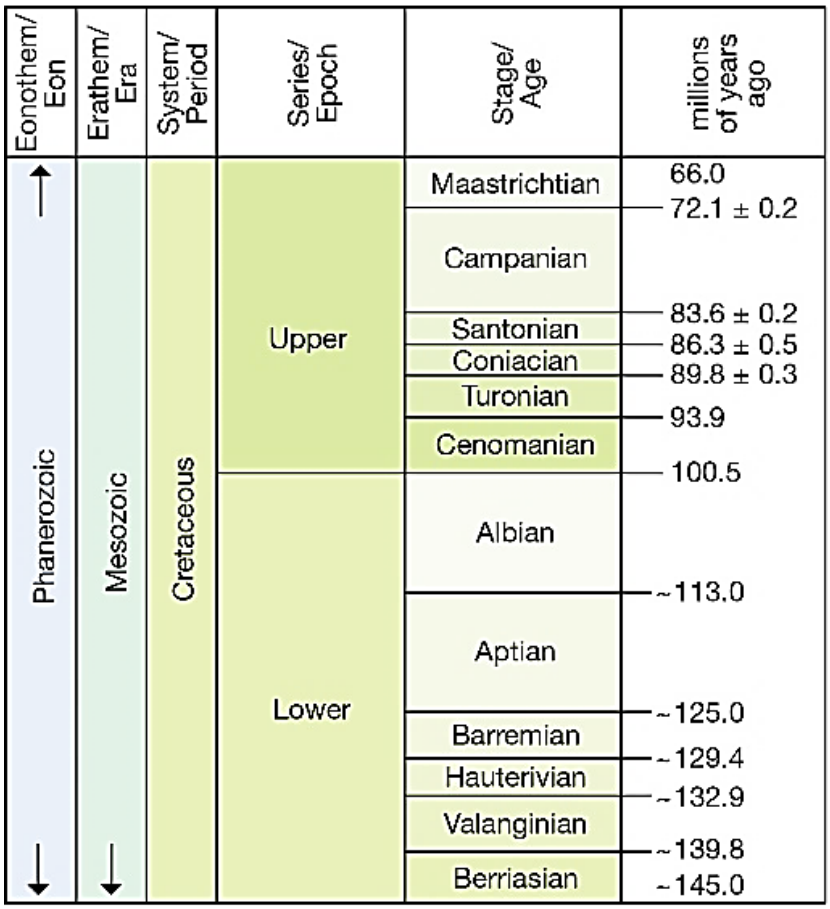

Figure 5-3 Cretaceous period – stratigraphy of Albian stage (ICS 2012)

In 1974, Hoek and Bray honored the stereonet projection method where each data point represents a normal vector to an individual discontinuity plane and joins a discontinuity set by a certain clustering logic. The stereograph, of the detected joint sets, was generated in the DSE software (Figure 5-15a).

Prediction of discontinuities persistence in the third dimension is difficult but for modelling purposes it might be assumed that discontinuities exist as finite ellipses within the rock mass or terminate against other discontinuities. A discontinuity third dimension can be statistically estimated on the basis of the discontinuity daylight trace length and an approximated diameter (Umili, Ferrero, & Einstein, 2013).

In this chapter, a thrust fault (Figure 5-6 (c)) can be clearly identified on both the red, green and blue (RGB) and scan images in Figure 5-4. The unique raw LiDaR scan given in Figure 5-4 (a) was processed, and the structural attributes statistics were extracted using CloudCompare and Discontinuity Set Extractor (DSE) programs as presented and illustrated in detail in Appendix A.

(a)

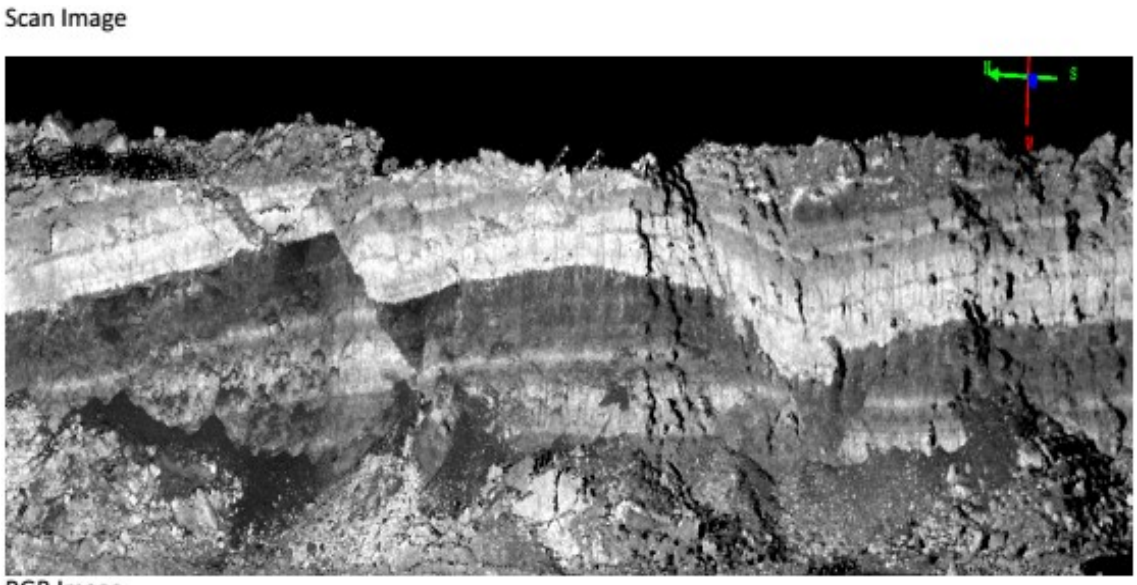

(b)

Figure 5-4 (a) Scan and (b) RGB images of CCSh mine bench in Alberta

5.5 MATLAB

The structural attributes statistics of the facets (discontinuities) generated from processing the raw point cloud using CloudCompare software are listed in Table B-1 in Appendix B. Using these statistics, MATLAB scripts were composed to build, generate, display, visualize, plot and manipulate each discontinuity as a 2D polygon in 3D space as seen in Figure 5-7. Examples of the MATLAB scripts are included in Appendix C. It is worth noting that MATLAB helped in deriving other pieces of information required in next FISH scripting in the geomechanical modelling in the next chapters.

(a) (b)

Figure 5-5 Rock cut showing (a) systematic (yellow and red) discontinuities (Otoo, 2012) and (b) discontinuity traces (red line) and facets (cyan polygon) (Duan, Li, Maerz, & Otoo, 2011)

(a) (b) (c)

Figure 5-6 Fault types; (a) normal, (b) strike-slip, and (c) thrust (Heidbach et al., 2018)

5.6 DISCRETE FRACTURE NETWORK (DFN)

To characterize a rock mass in a 3D mechanical simulation, it is conventional to consider the discontinuity system as a DFN. The use of DFNs, particularly constructed based on digitally derived in situ structural data, has a significant potential in geomechanical characterizations. Realistic DFNs help assessing not only potential failure mechanisms, but also spotlighting potential key blocks. Several computer codes generate DFN models for rock mechanics applications, including the Itasca 3DEC (Itasca, 2016).

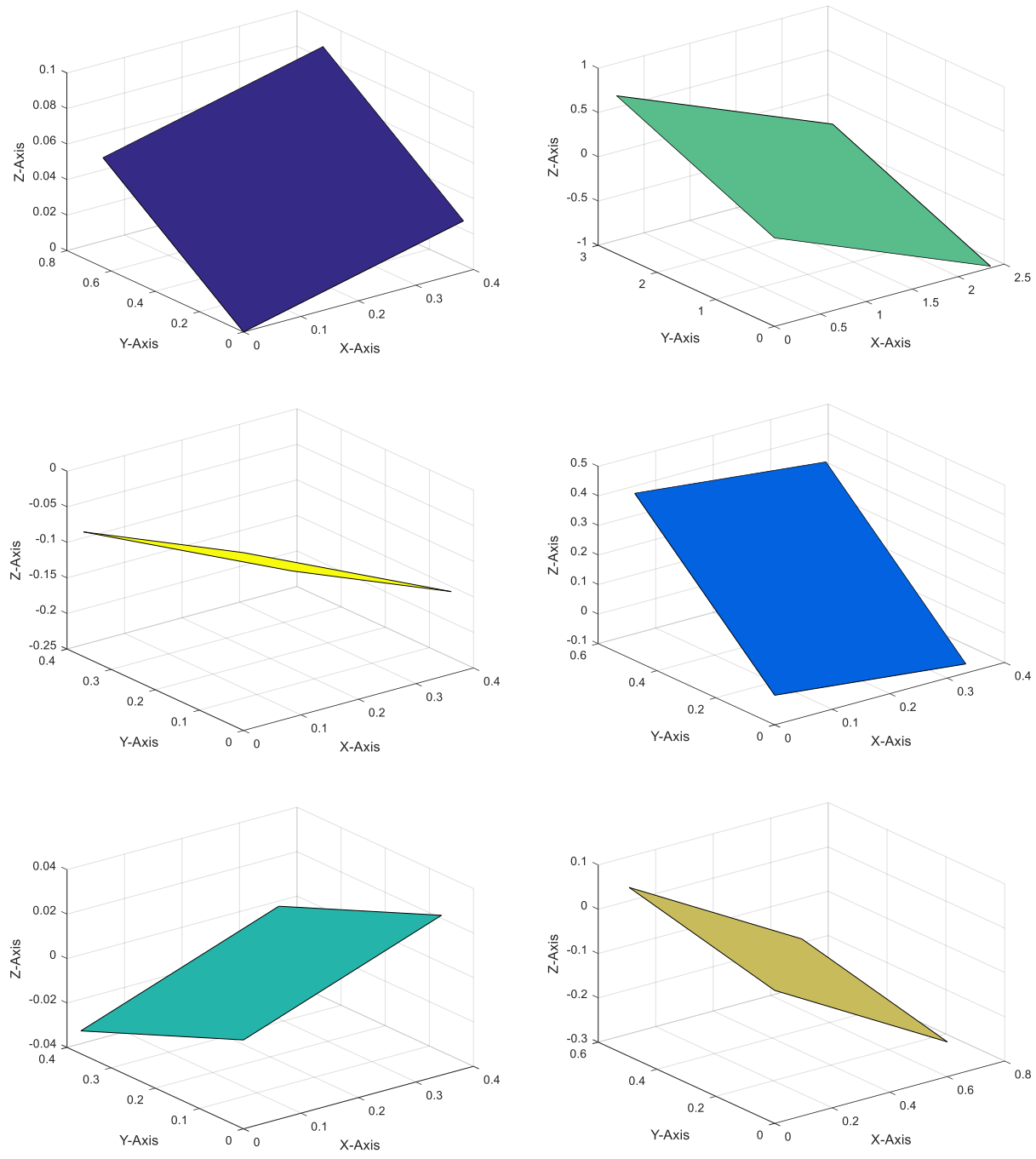

Figure 5-7 Examples of facets plotted in space using MATLAB – all axes dimensions are in meters

As illustrated in Appendix A, two built-in segmentation algorithms from CloudCompare were investigated to identify the discontinuities statistics from the point cloud. The geological attributes statistics were extracted in a .csv format and complied in a spread sheet (Appendix B),

afterwards, two DFNs were scripted using FISH language in 3DEC and generated as depicted below in Figure 5-8.

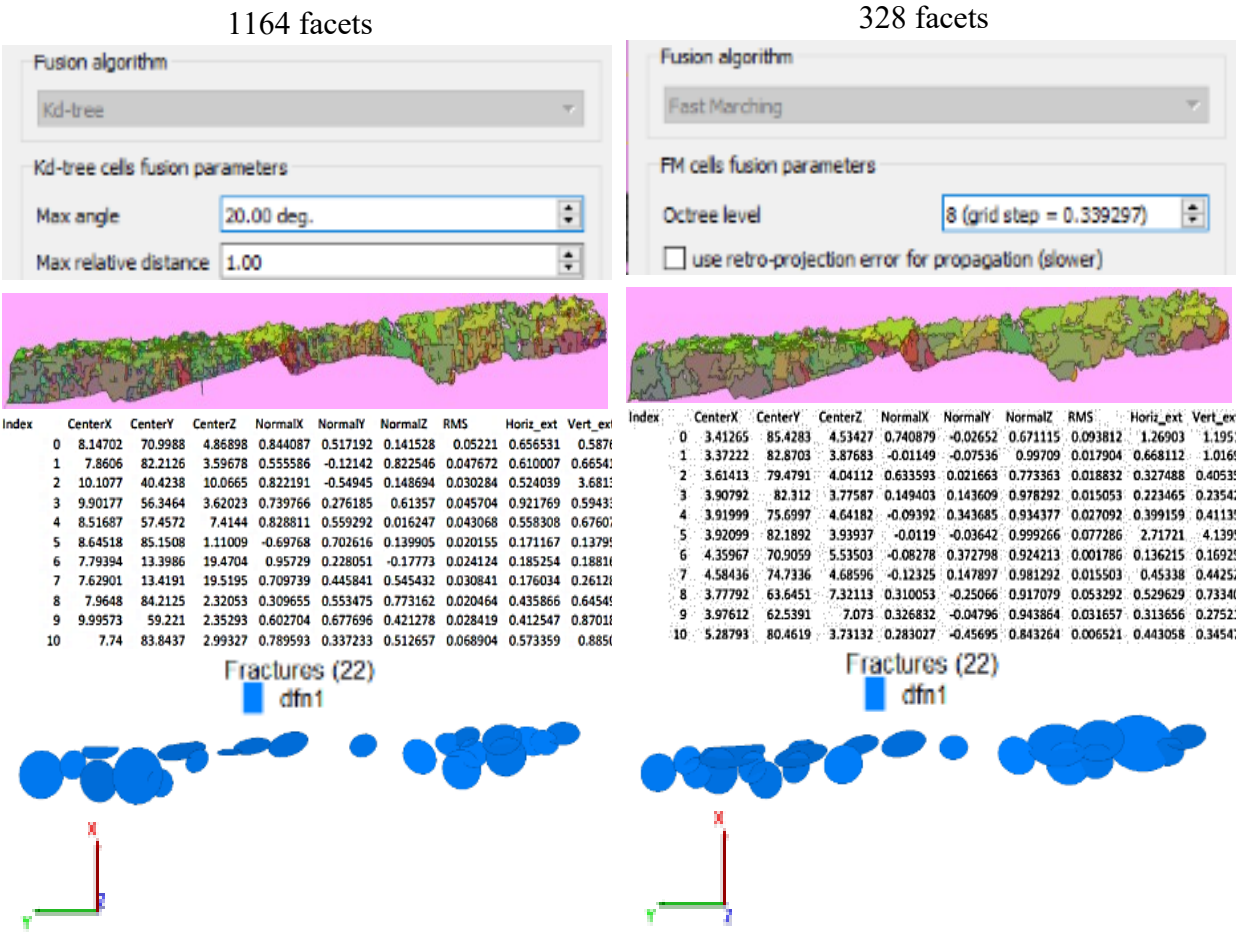

(a) (b)

Figure 5-8 Comparison between CloudCompare algorithms; (a) Kd-algorithm and (b) FM-algorithm in point cloud manipulation, facets configuration, discontinuities statistics, and generated DFNs in 3DEC

5.7 DISTINCT ELEMENT MODELLING (DEM)

Using distinct element modelling (DEM) to assess engineering issues such as rock fall, sliding or slope instability, one has to invest significant effort in identifying intact rock blocks from the discontinuities (Boon, Houlsby, & Utili, 2015). Itasca DEM code 3DEC will be used in the next chapters to carry out a geomechanical modelling of the CCSh rock mass being investigated. The top two (density wise) discontinuity sets (discrete fracture network # 1 i.e. dfn1 and discrete fracture network # 2 i.e. dfn2), extracted using DSE, are displayed in the 3DEC GUI as seen in Figure 5-9. Two views of the discontinuous model of the CCSh mine bench are given

in Figure 5-10 and Figure 5-11. The CCSh mine bench face and side views, with the discontinuities traces, can be seen in Figure 5-12 and Figure 5-13, respectively. Part of the FISH script, composed to generate the joint sets extracted from processing the raw field geologic data, is included in Appendix D.

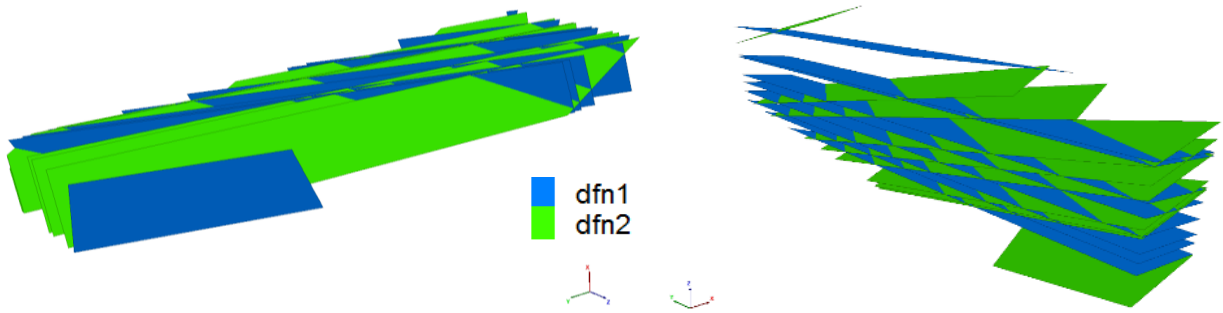

Figure 5-9 Two views of top highest-intensity discontinuity sets dfn1 and dfn2 extracted from DSE as coded in 3DEC using FISH language scripting

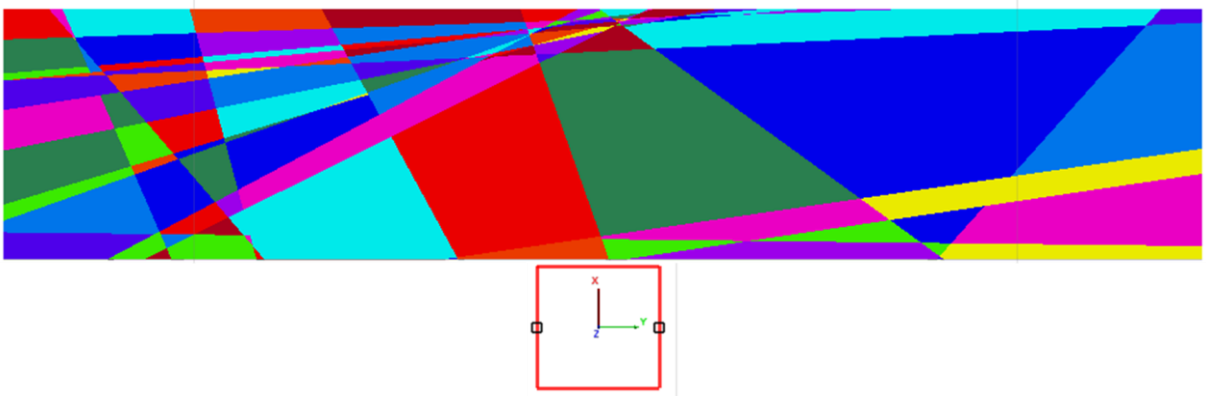

Figure 5-10 Side view of discontinuous CCSh model

5.8 DISCUSSION

Rock masses are made up of numerous polyhedral blocks, cut out by discontinuities (Boon et al., 2015). Importance of studying the geological and structural characteristics of a heterogeneous rock mass helps in assessing potential changes in the permeability and porosity. In this chapter, a workflow has been crafted and proposed to reproduce a 3D DFN from an exclusive LiDaR field (raw) survey as illustrated in Figure 5-14. Application of the procedure proposed is of significant benefits in academia and industrial engineering practices.

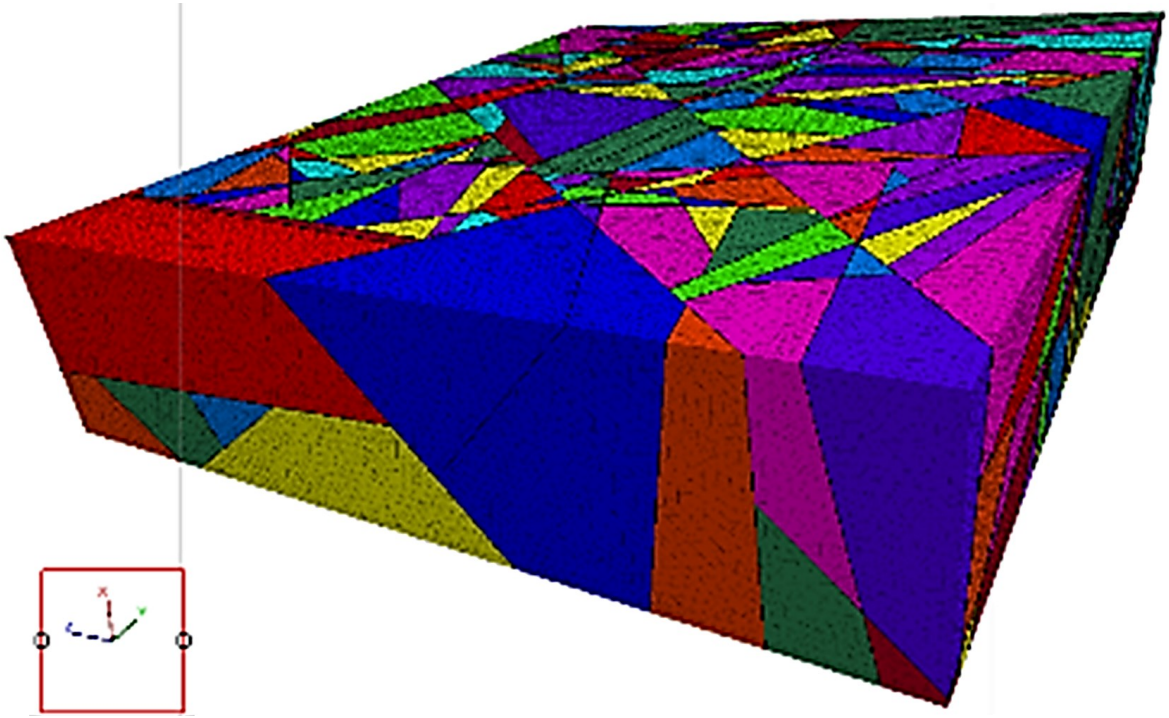

Figure 5-11 3D model of CCSh mine bench

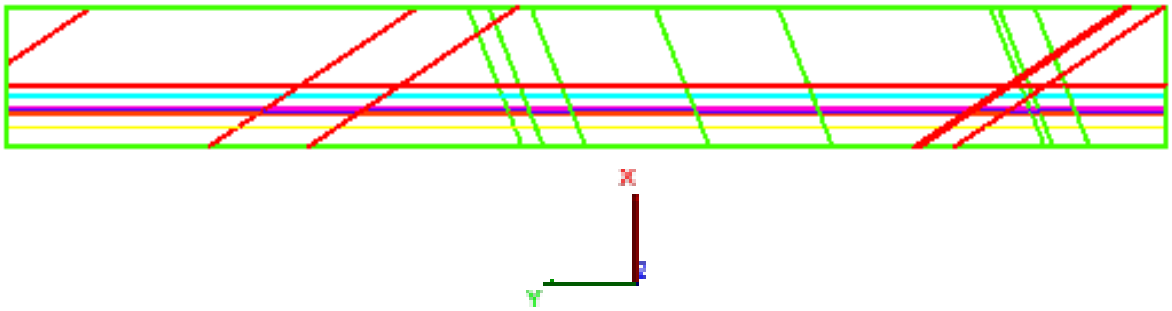

Figure 5-12 Face view of trace map of CCSh mine bench

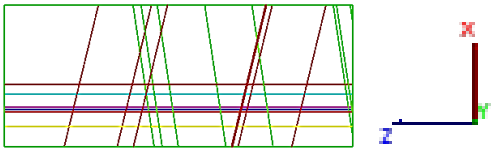

Figure 5-13 Side view of trace map of CCSh mine bench

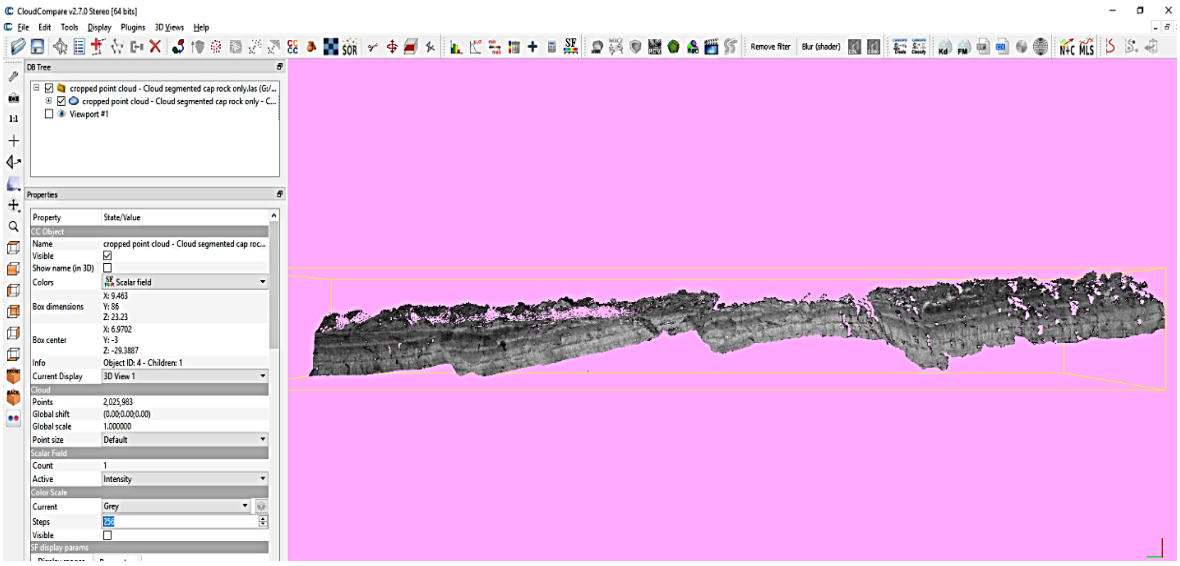

(a)

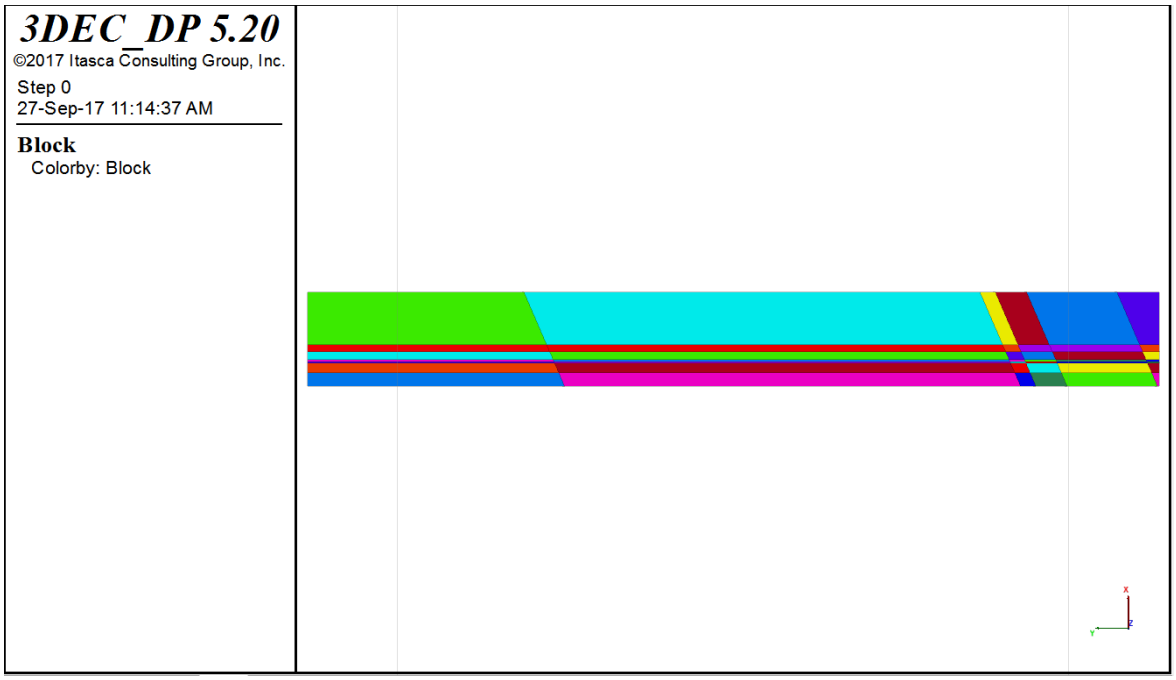

(b)

Figure 5-14 From (a) in situ LiDaR point cloud displayed in CloudCompare to (b) 3D DEM model in 3DEC

The novelty of this study is inherited in the integration of exploring and examining several platforms with variable capabilities in manipulating LiDaR .LAS raw data files. The study presented in this chapter in addition to Appendix A included registering raw point cloud, displaying, manipulating, processing of the field geologic data, identifying, generating the discontinuities, plotting stereonet, visualizing the discontinuities in 3D space individually using

MATLAB scripts, generating FISH scripts in 3DEC to reconstruct the fractured mine bench and building a 3D DEM model (Figure 5-14).

Quantitative and qualitative validation of the stereonet generated in DSE from the raw point cloud acquired in situ against the stereonet generated in 3DEC using FISH scripting was conducted as seen in Figure 5-15. The total number (ten) of the identified joint sets, joint sets distribution, each joint set intensity and location were verified. This is a necessary step to validate the FISH script developed for building the DFN and to approve it to be subsequently implemented in the 3DEC modeling investigations to be addressed in the subsequent chapters.

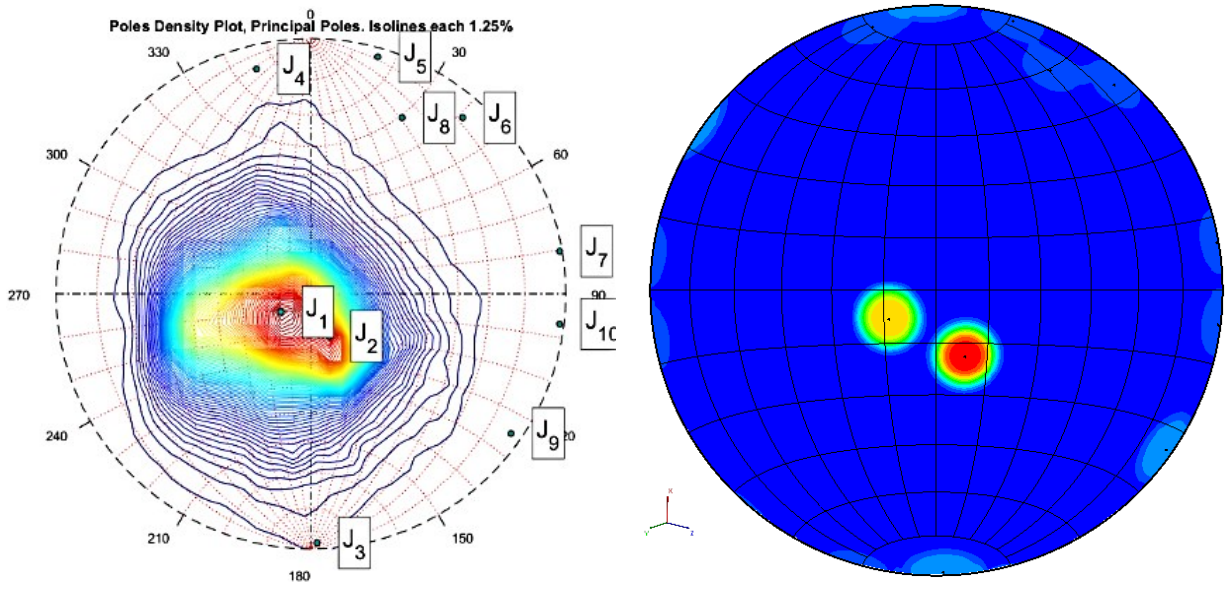

(a) (b)

Figure 5-15 Stereonets of joint sets generated from; (a) raw LiDaR data in DSE and (b) FISH scripting in 3DEC

5.9 SUMMARY AND CONCLUSIONS

Over last decades, geomatic techniques have been increasingly used in the geological and structural characterization of rock masses. For example, terrestrial laser scanning and digital photogrammetry were employed in characterizing discontinuum rock surfaces. Currently, light detection and ranging (LiDaR)-based applications for geological characterization purposes proven to be highly reliable and accurate in discontinuity remote-detection and quantification. Terrestrial LiDaR survey methods can provide high-resolution data needed for volumetric and structural analyses in rock masses, potentially making these analyses straightforward. Benefits of remote LiDaR data collection include speed, safety, accessibility, coverage, convenience and efficiency.

The targets of this chapter included geologically characterizing a Clearwater clay shale (CCSh) mine bench located in Alberta using a rare high-resolution LiDaR scan. Another objective was to generate a 3D realistic DFN of the exposed mine bench. That DFN is necessary for numerical simulations because it is the first input needed in these simulations. The final goal was to present a workflow that begins with acquiring point cloud in situ as LiDaR-data to importing, registering, manipulating and processing this data set, through generating a TIN then extracting the realistic geostatistics, plotting stereonet and ending with constructing a realistic 3D DFN. Extracting geostatistics includes identifying length of each discontinuity, dip/strike, and radius.

Geologic assessment of the CCSh mine bench under consideration was carried out in this chapter essentially to fulfill the thesis second objective as stated in Chapter 1. Structural measurements of the studied mine bench were derived from the dense point cloud acquired in situ. The total scanned volume of the CCSh mine bench was of extents with an X = 25.06 m, Y = 119.63 m, and Z = 101.89 m. This chapter beside Appendix A included proposing an integrated workflow for analyzing a LiDaR dataset of argillaceous (over consolidated) soft rock to quantify it geologically all the way until fully describing a DFN needed for 3D DEM purposes. The extracted discontinuity sets were confirmed with the in situ LiDaR scan as the goal of this chapter was to construct a realistic DFN, a task that first requires an accurate quantification of the spatial positions and geometries of the discontinuities. The DFN generated in this study represents a realistic realization of site-specific conditions and will be employed in Chapters 6 and 7.

Point clouds can be conveniently used to create 3D structural models which can be imported into other software. This chapter presented observations showing how field LiDaR datasets can be filtered, registered, and georeferenced to tailor their applicability in rock structural geology characterization. That geological characterization process can be applied to similar range of scale fractured rock masses that are controlled by visible and distinct discontinuities.

CHAPTER 6 GEOMECHANICAL INTEGRITY OF ARGILLACEOUS CAPROCK ABOVE SAGD RESERVOIR

6.1 INTRODUCTION

Assessing the geomechanical behaviour of hard soils/soft rocks is challenging and the Clearwater clay shale (CCSh) caprock investigated in this thesis falls into this material classification category. In northeastern Alberta, the CCSh formation serves as a caprock for most SAGD projects. The CCSh is an over consolidated sedimentary formation with an average "intact" Young's modulus of ≈ 0.5 GPa, and an average uniaxial compressive strength of 1 MPa placing it, according to the ISRM classification system, within the hard clay (S6) to extremely weak/soft rock (R0) range.

Evaluating the stiffness, strength and deformability of these hard soil/soft rock materials is a complex task especially if pre-existing discontinuities are present because they lead to formation anisotropy and heterogeneity issues. In addition to the presence of natural discontinuities, when these materials form the caprock above high-pressure-high-temperature steam assisted gravity drainage (SAGD) processes there is consequently an added complexity in predicting the CCShC geomechanical behaviour. As a SAGD steam chamber evolves within an oil sands reservoir, changes in the effective stress in addition to thermal expansion together induce deformations beneath and within the overlying CCShC, potentially resulting in the development of shear and tensile stresses. Moreover, the discontinuities in the CCShC deform consequently the caprock basic seal (hydraulic) characteristic may be compromised. Assessing the ability of the naturally fractured CCShC to maintain its integrity with these evolving conditions requires solid understanding of the geomechanical behaviour of the CCSh, both intact and discontinuities. In industry, conventional practice for caprock integrity assessments overlooks the presence of discontinuities within the CCShC and equivalent properties are being assigned based on continuum modelling approach known for hard rocks.

This chapter provides results of a study conducted to assess the role discontinuities play in the geomechanical behaviour of the CCShC, composed of a soft rock. This basically constitutes towards the third research objective as stated in Chapter 1. In this chapter, sensitivity studies were conducted using 3D distinct element method (DEM) to simulate continuum (intact) and

discontinuum models of CCShC. The values of the caprock heave were analyzed and compared with the change in the degree of discontinuity configuration, presence of overburden (OB) i.e. confinement, and magnitude of maximum operating pressure (MOP) within the underlying reservoir.

For the fracture network within the CCShC, a discrete fracture network (DFN) was constructed based on light detection and ranging (LiDAR) data acquired from a mine bench excavated through the CCSh in northeastern Alberta formation that serves as the primary caprock for most SAGD projects. The unique LiDAR data is illustrated in Figure 6-1a in form of a point cloud. The point cloud processing was discussed in detail in Chapter 5 and Appendix A.

The average OB characteristic for shallow SAGD projects in Alberta, e.g. McKay river, Firebag, and Joslyn creek, is approximately 150 m. For the sensitivity analyses purposes in this chapter, two confinement conditions were considered; 1) unconstrained caprock surface (i.e. OB = 0) as an upper bound case and 2) 150 m of OB overlying the caprock.

The distinct element code (3DEC) was used in the modeling in this chapter. The modeling involved first the application of in situ stresses on the model and subsequently running the model until initial equilibrium is reached. Once equilibrium is established, all displacements in the model were reset, afterwards an equivalent upward distributed load representative to SAGD steam chamber development, due to reservoir MOP, is applied at the base of the caprock model as illustrated in Figure 6-3. Maximum horizontal in situ stress was assumed to be acting NE-SW as detected from the thrust faulting seen in Figure 6-1a. At the CCShC macroscale model (Figure 6-3), the vertical stress (σ_v) was assumed to act on the caprock model along X-axis, maximum horizontal stress (σ_H) was assumed to be acting along Y-axis, while the minimum horizontal stress (σ_h) was chosen to be acting along Z-axis.

6.2 DISCRETE FRACTURE NETWORK (DFN)

The DFN used in the current study was extracted from a geologic laser survey opportunely captured in situ using LiDAR technique. Discontinuity set extractor (DSE) software was used in processing the raw field data. Ten joint sets were detected from the point cloud where their statistical attributes are provided in Table 6-1 and a stereonet for the interpreted joint sets was provided in Figure 5-15 (a). The geostatistics were used to build a realistic DFN in Itasca's 3DEC using the built-in scripting language; FISH. Upon FISH composing completion, the syntax of the

script portion for DFN defining was checked by generating a stereonet in 3DEC (Figure 5-15b) for a qualitative and quantitative comparison against the DFN extracted from the LiDAR raw field data (Figure 5-15a) in the DSE software. Typically, to create a discontinuum model in 3DEC, a DFN is built first then it is used to cut an intact block forming a discontinuum model to represent a rock mass. The DFN intersection structural trace on the face of the generated CCSh caprock (CCShC) model is depicted in Figure 6-2.

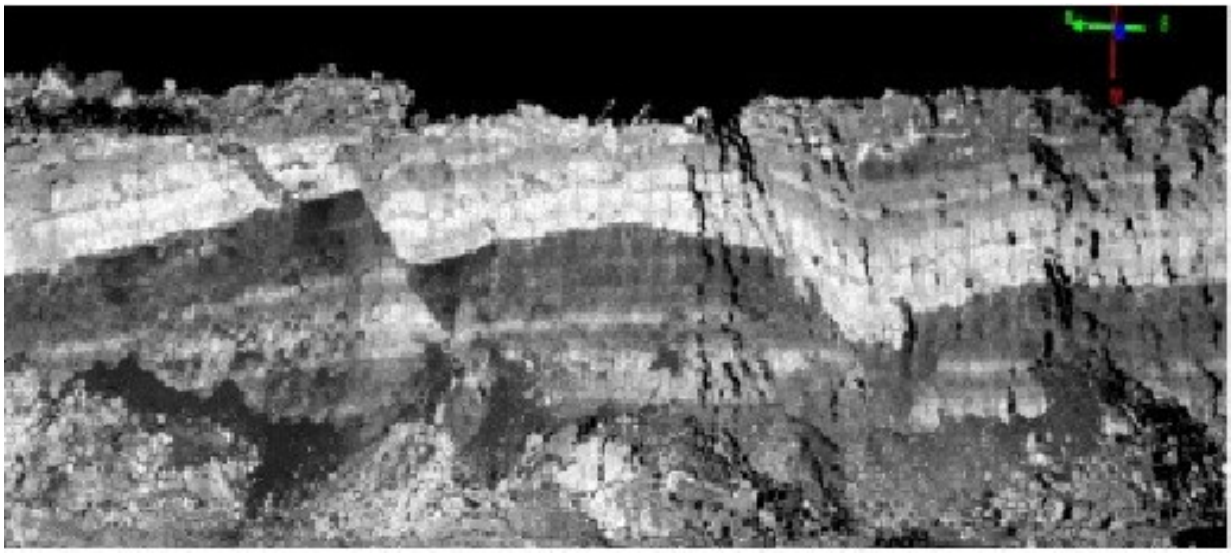

(a)

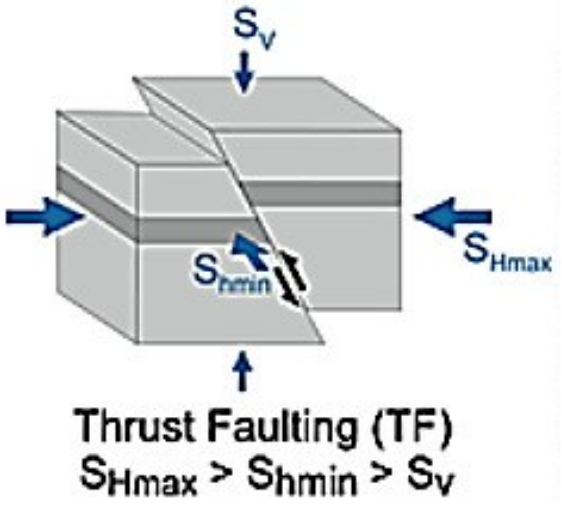

(b)

Figure 6-1 (a) LiDaR field data (Appendix A) (b) stress field for thrust faulting conditions

In addition to the joint sets (Table 6-1) depicted and extracted from the field LiDaR survey, bedding planes and a major geologic fault were detected insitu as seen in Figure 6-1a and they will be included in the CCShC models investigations. The sensitivity of the geomechanical behaviour

of the CCShC model to the degree of discontinuity inclusion (discontinuity configuration) is studied by investigating 13 different degrees of model fracturing as given in Table 6-3.

Table 6-1 Joint sets (J.S.) information (Appendix A) as extracted using DSE

J. S.#	Dip direction (°)	Dip angle (°)
1	58.9	15.7
2	336.6	20.6
3	358.6	88.6
4	166.4	84.4
5	195.8	87.9
6	220.8	84.7
7	260.3	89.4
8	207.4	75.7
9	304.9	87.5
10	277.0	89.0

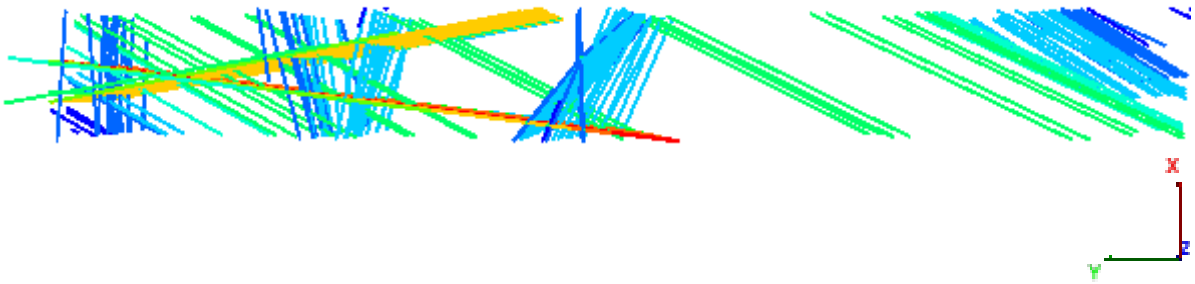

Figure 6-2 Trace of joint sets intersections on the caprock model face

6.3 MAXIMUM OPERATING PRESSURE

According to Alberta Energy Regulatory (AER), the maximum operating pressure (MOP) in a SAGD operation is typically estimated based on the shallowest depth of the caprock base. Using a margin of safety (MOS) of 0.8, the MOP is calculated as follows:

$$\text{MOP (kPa)} = \text{MOS} \times \text{caprock minimum stress gradient (kPa/m)} \times \text{depth at shallowest base of caprock (m)} \quad (6\text{-}1)$$

where, the minimum stress gradient is generally interpreted as the fracture closure pressure obtained from diagnostic fracture injection tests (DFITs).

The MOP for a SAGD project can exert significant influence on the overlying fractured caprock deformability and consequently induces surface heave (Khani, Rangriz-Shokri, & Chalaturnyk, 2018). Prior to the 2006 steam release incident, substituting in AER formula in Equation 6-1, the highest MOP value would be 1800 kPa in a location like Joslyn creek, in Alberta. After the steam release incident, AER modified their formula, specifically the MOS, and the upper bound of the MOP currently would be 1400 kPa in the same location as reported by TOTAL in (TOTAL E&P Canada Ltd., 2007). A lower bound MOP of 739 kPa would result from Equation 6-1 (Khani et al., 2018). In another industry report the SAGD reservoir operating pressure was designed to be 900 – 1200 kPa. In the present chapter, three magnitudes of reservoir MOPs; 739, 1200, and 1800 kPa, were investigated through a sensitivity analysis. The equivalent stress underneath the caprock base, consequent to the steam chamber dilation corresponding to the reservoir MOP, was applied incrementally (on time step wise) as an upward distributed X-load at the middle (third) extent of the caprock model as illustrated below in Figure 6-3.

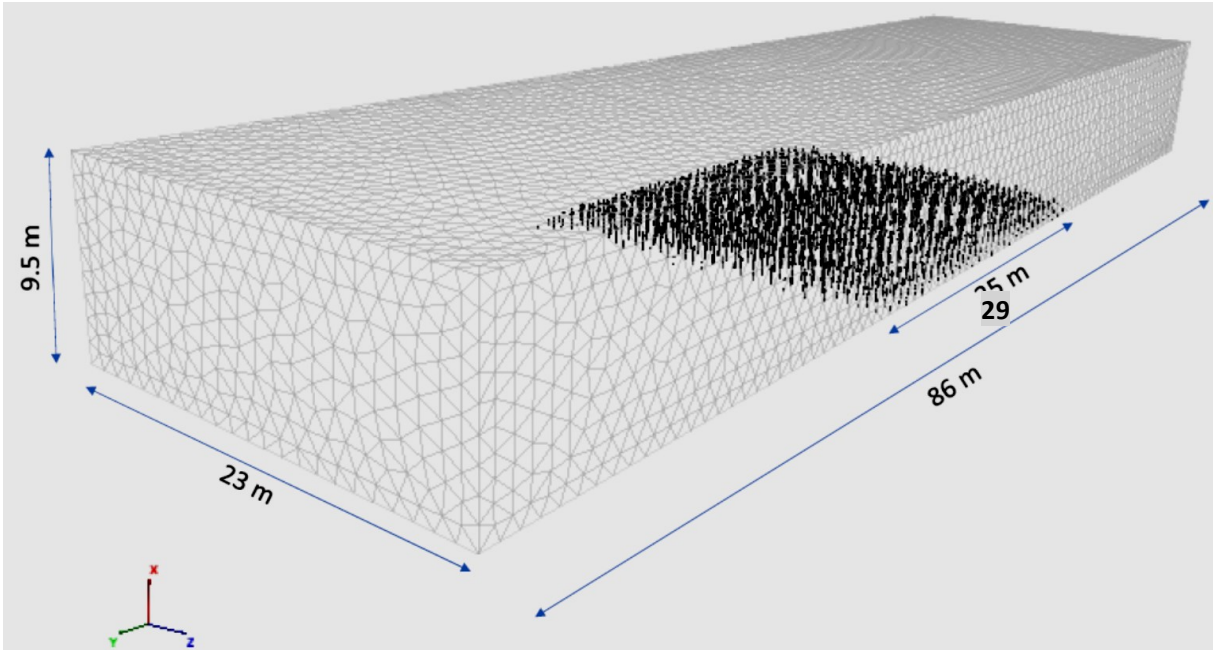

Figure 6-3 Upward distributed loading representing steam chamber dialtion underneath the caprock corresponding to reservoir MOP consequences

6.4 DISCONTINUUM MODELLING

Modelling was conducted using Itasca 3DEC version 5.2 HD. The extents of the caprock model were 9.5 × 86 × 23 m^3, as determined from the processed field data using CloudCompare

software (Appendix A). Strain softening constitutive model, representing nonlinear and irreversible failure behaviour (Itasca, 2016), was used for the intact CCShC zones. The intact CCShC mechanical properties were assumed to be as follows: E_i = 0.5 GPa (Chin, Tomberlin, Ramos, & Chalaturnyk, 2012), ν_i = 0.4 (Rahmati, 2016; Saeedi & Settari, 2016) and UCS_i = 1 MPa (Yuan et al., 2013; Canadian Natural Resources Limited, 2014; Khani et al., 2018).

Estimating normal stiffness (K_n) and shear stiffness (K_s) of the discontinuities in any rock type is challenging but with the soft rock characteristics of the CCShC, it becomes more complex task. For the purpose of this sensitivity study, the friction (jfric), cohesion (jcoh), normal stiffness (jkn) and shear stiffness (jks) values as listed in Table 6-2 were assumed for the CCShC discontinuities (Khani et al., 2018). Appendix D includes an example FISH script used in the 3DEC modeling in these sensitivity analyses. The plan and side views, of the caprock (major fault with bedding planes model) with two locations (green and blue diamonds) for heave displacement monitoring, are depicted in Figure 6-8a and b, respectively. The models X, Y, and Z boundary conditions assumed in this study are as seen in Figure 6-5.

Table 6-2 Input mechanical parameter values for discontinuities (Khani et al., 2018)

Property	Value	Unit
jfric	20	(^{o})
jcoh	1×10^5	(Pa)
jkn	4.5×10^8	(Pa/m)
jks	4.5×10^7	(Pa/m)

In order to investigate the caprock geomechanical behaviour accounting for geological heterogeneity, as schematically illustrated in Figure 6-4, various discontinuity configurations were examined to cover a wide spectrum range from continuum to discontinuum rock mass models. Table 6-3 includes the description of each model built of a total of 13 different geologic configurations simulated in this chapter. These configurations include intact, one fault (no glue/unjointed) (F), intact with (six) bedding planes (joined) (BP), one fault with bedding planes (F+BP), two joint sets with fault (F+2JS), two joint sets with bedding planes (BP+2JS), two joint sets with bedding planes and fault (F+BP+2JS), five joint sets with fault (F+5JS), five joint sets

with bedding planes (BP+5JS), five joint sets with bedding plans and fault (F+BP+5JS), ten joint sets with fault (F+10JS), ten joint sets with bedding planes (BP+10JS) and ten joint sets with bedding planes with fault (F+BP+10JS). Table 6-4 provides the features information for each DEM model and Figure 6-6 includes structure of selected caprock models. To isolate the discontinuities, the meshed bedding planes case and bedding planes with a major fault case are depicted in Figure 6-7.

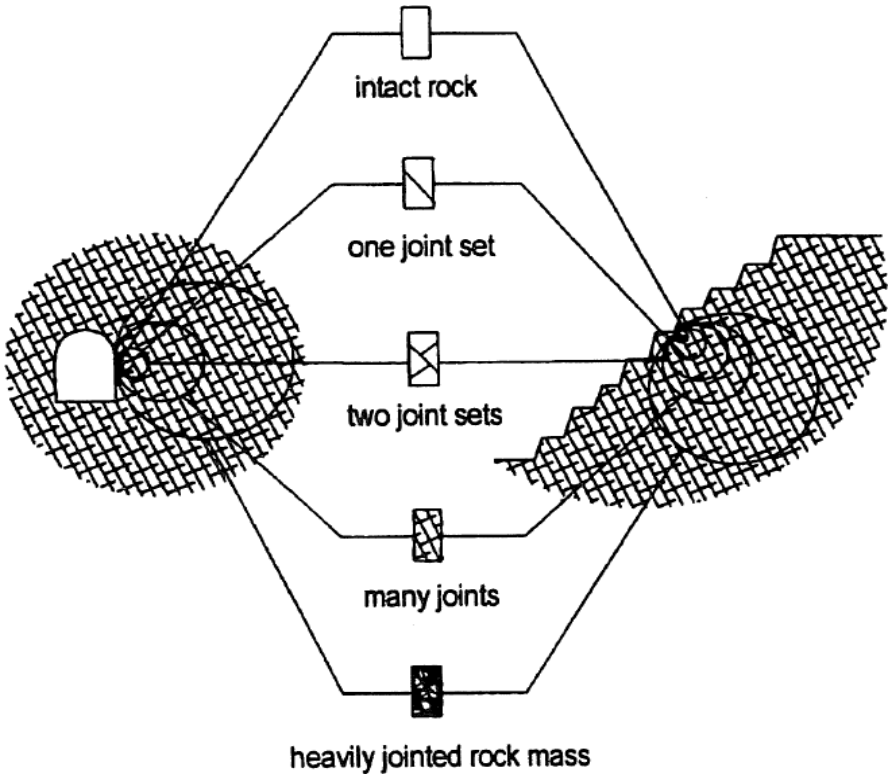

Figure 6-4 Geological heterogeneity and scale effect (Hoek & Brown, 1997)

6.5 RESULTS

The discussion of the sensitivity study results will be presented at two levels; the geomechanical behaviour at macroscale i.e. the caprock model and the geomechanical behaviour at the microscale or at the discontinuity level. At the macroscale; heave magnitude, effect of the degree of fracturing, effect of the MOP, effect of confinement, profiles of the upward displacement, tensile and shear stresses development within the caprock models will be discussed. At the microscale, discontinuities normal and shear displacements and slippage will be studied. For vertical upward displacements (heave), 18 locations were chosen on the model surface to monitor the upward displacement.

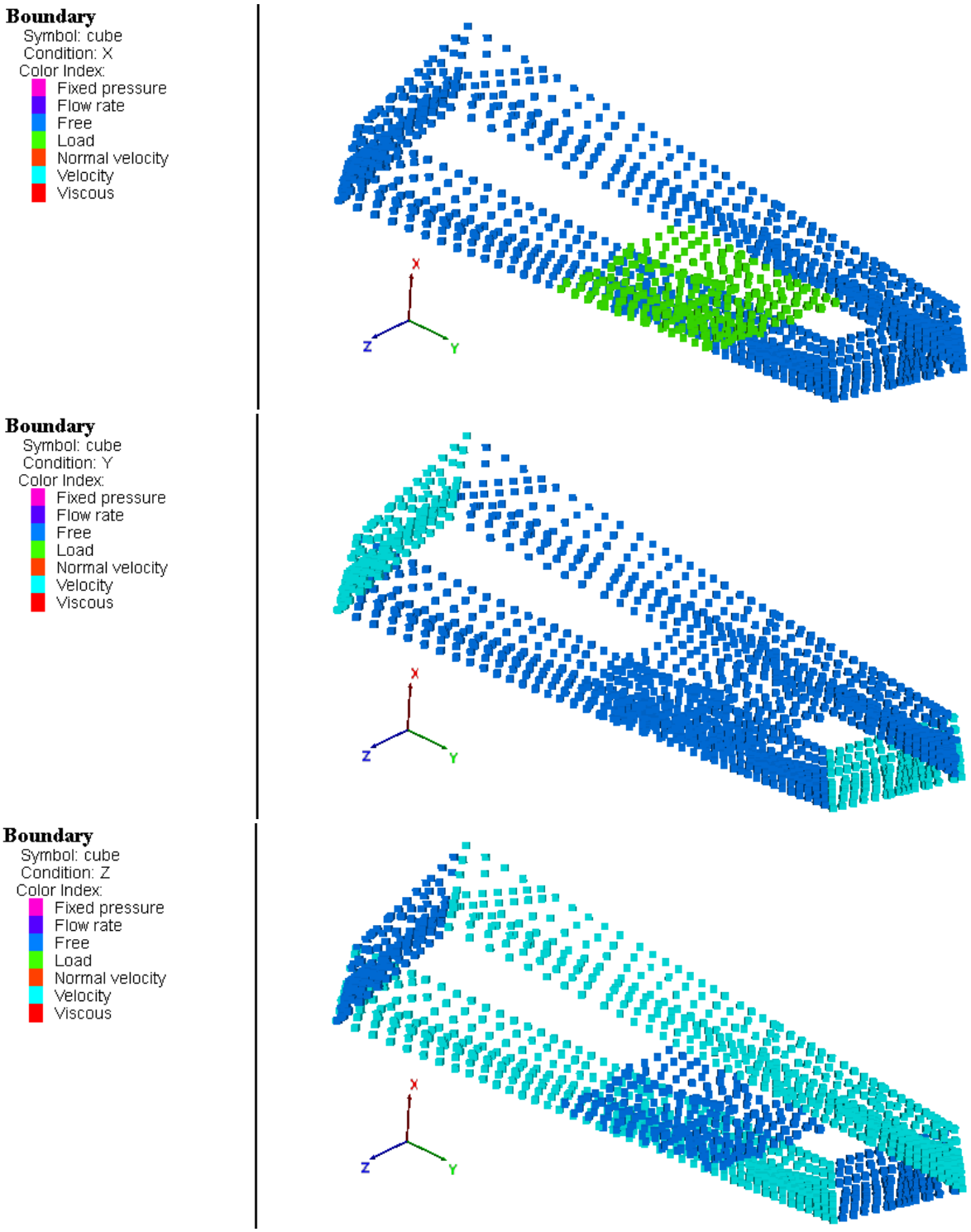

Figure 6-5 X, Y, and Z boundary conditions

The heave pattern and distribution were found to qualitatively match reported behaviour in literature and documented observations in field (Ito & Ipek, 2005) for example as depicted in Figure 6-9 and Figure 6-10. The result heave magnitudes were found to be quantitively comparable

to 0.12 – 130 cm, 36.0 cm, 17.7 – 42.0 cm reported in (TOTAL E&P Canada Ltd., 2007), (Juncal 2018), and (Khani et al., 2018), respectively. In general, the values of the upward displacement (heave) was found to be increasing as the MOP increases.

To demonstrate the structural geology, discontinuities inclusion and how these may impact the geomechanical response and integrity of the caprock, the analyses will be divided into fault based configuration and bedding planes configuration based, forming a total of 13 cases as listed in Table 6-3. Basically as you go down the table rows, more discontinuities are being added in the caprock models, where:

Table 6-3 Investigated caprock 13 models based on structural geology

Model ID	Structural geology element	
	Fault	Bedding planes
Intact	Intact	
F BP	One fault	Intact with bedding planes
F+BP	One fault with bedding planes	
F+2JS BP+2JS	One fault with 2 joint sets	Bedding planes and 2 joint sets
F+BP+2JS	One fault with bedding planes and 2 joint sets	
F+5JS BP+5JS	One fault with 5 joint sets	Bedding planes and 5 joint sets
F+BP+5JS	One fault with bedding planes and 5 joint sets	
F+10JS BP+10JS	One fault with 10 joint sets	Bedding planes and 10 joint sets
F+BP+10JS	One fault with bedding planes and 10 joint sets	

* F = fault, BP = bedding planes, and JS = joint sets

Fault-based configuration, models start with an intact model all the way till one fault with bedding planes and 10 joint sets being the most discontinuum model in this category.

Bedding planes-based configuration, models start with an intact model all the way to one fault with bedding planes and 10 joint sets being the most discontinuum model in this simulation category. Each model in Table 6-3 will be studied twice, confined i.e. with an OB of 150 m and

without confinement as an upper bound extreme case to illustrate the constraint effect on the caprock geomechanical response overlying a SAGD dilating steam chamber.

Table 6-4 Attributes information of all 3D DEM caprock models investigated

Model ID	Number of				
	Discontinuities	Deformable blocks	Faces	Zones	Intersections
Intact	0	1	1	14329	0
F	1	2	610	14464	0
BP	0	7	4209	27217	0
F+BP	1	14	9652	27248	0
F+2JS	1 + 20	84	73955	21195	44
BP+2JS	20	398	535440	38801	44
F+BP+2JS	1 + 20	505	701750	40561	44
F+5JS	1 + 24	191	181586	21683	104
BP+5JS	24	850	1144778	40440	104
F+BP+5JS	1 + 24	975	1326222	41717	104
F+10JS	1 + 30	583	640385	24289	211
BP+10JS	30	1544	2060402	45534	211
F+BP+10JS	1 + 30	1730	2342204	47565	211

6.5.1 ESTABLISHING INITIAL EQUILIBRIUM

Before applying any loading, each model was first subject to in situ stresses and was set to run until initial equilibrium (steady state) is achieved. The vertical insitu stress (σ_v) was assumed to = 0.021 MPa/m, minimum horizonal stress (σ_h) = 0.024 MPa/m, and the maximum horizontal stress (σ_H) = 0.029 MPa/m (TOTAL E&P Canada Ltd., 2007), (Abel 2018) and (Khani et al., 2018). Table 6-5 includes the number of time steps needed for the stresses and displacements to redistribute and adjust among the model various elements under the effect of the insitu stresses till a steady state is reached. The time steps to reach the initial equilibrium are indicators of the model geometrical and mechanical complexities. Reviewing the time step values in Table 6-5 may indirectly justify why some practitioners choose not to model the caprock as it exists insitu (for instance as the (F+BP+2JS) discontinuum model). The time steps were found to be dependent on

the model discontinuity configuration. As listed in Table 6-5, discontinuum models took longer to reach initial equilibrium than continuum models.

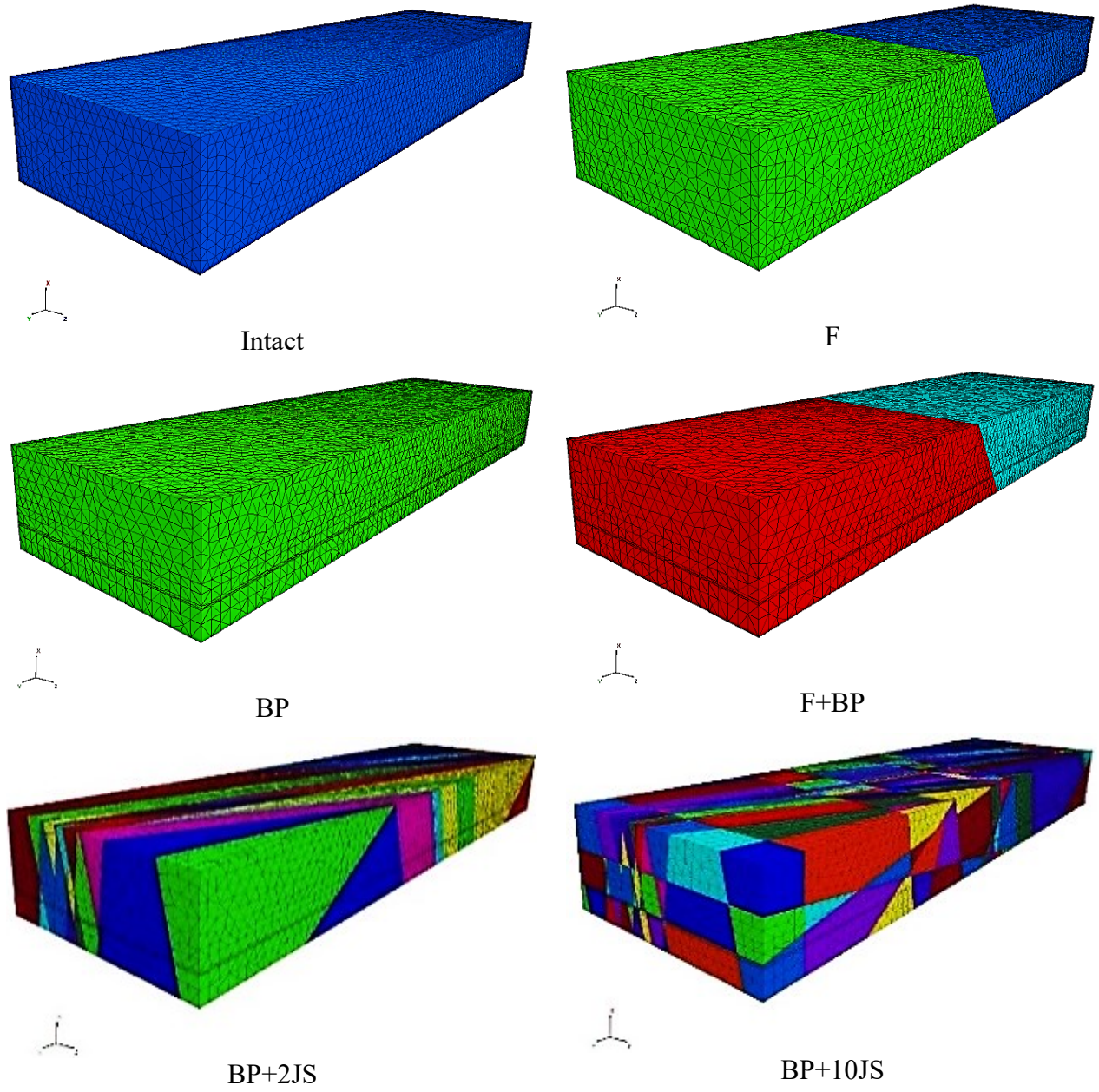

Figure 6-6 Selected meshed models of caprock illustrating the geological configuration advancement as investigated in this chapter

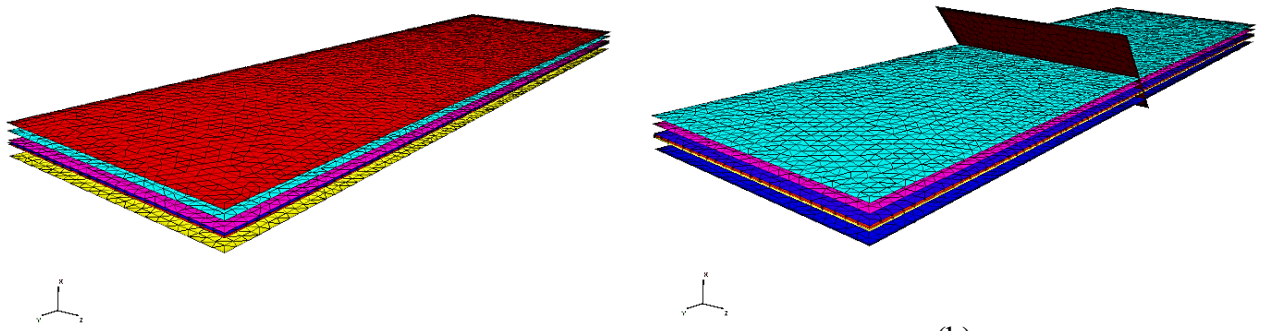

(a) (b)

Figure 6-7 Two cases of geologic configuration; (a) bedding planes and (b) bedding planes with one fault

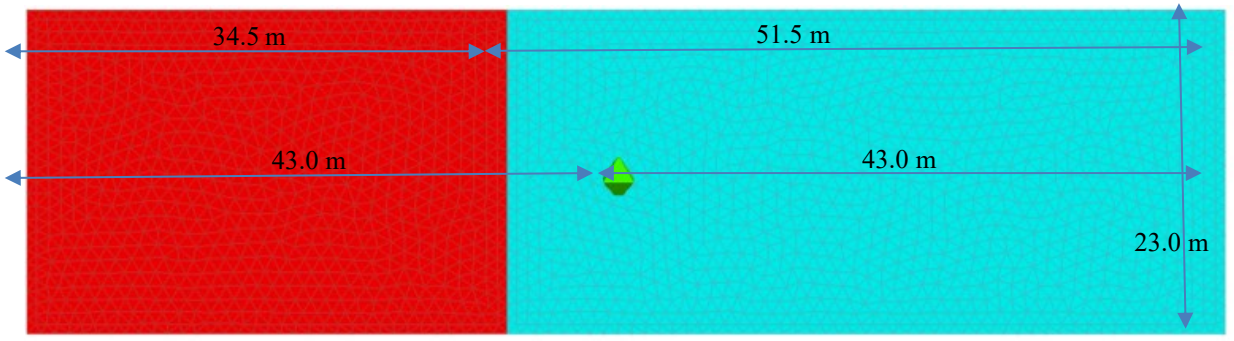

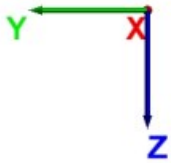

(a)

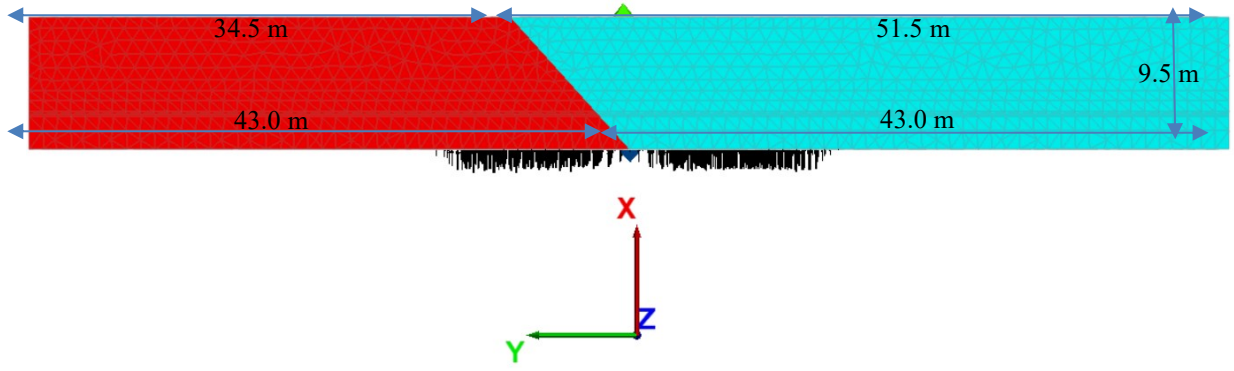

(b)

Figure 6-8 (a) Plan and (b) side views, of the major fault with bedding planes model, including the two locations of upward displacement (heave) monitoring as green and blue diamonds, respectively

Table 6-5 Number of time steps for caprock models to reach initial equilibrium due to in situ stresses

ID		Model		Time steps	
Intact		Intact		2	
F	BP	One fault	Intact with bedding planes	2	2
F+BP		One fault with bedding planes		194	
F+2JS	BP+2JS	One fault with 2 joint sets	Bedding planes and 2 joint sets	20	2
F+BP+2JS		One fault with bedding planes and 2 joint sets		568	
F+5JS	BP+5JS	One fault with 5 joint sets	Bedding planes and 5 joint sets	17	62
F+BP+5JS		One fault with bedding planes and 5 joint sets		487	
F+10JS	BP+10JS	One fault with 10 joint sets	Bedding planes and 10 joint sets	97	292
F+BP+10JS		One fault with bedding planes and 10 joint sets		478	

After reaching the initial equilibrium, all displacements were reset at the macro and micro inter-contacts scales. Next, each caprock model was subject to a gradually increasing upward distributed load equivalently representing the pressure exerted at the caprock base due to the steam chamber dilation consequent to the reservoir MOP. The upward stress exerted at the caprock base as the steam chamber dilates is qualitatively simulated as in Figure 6-3.

6.5.2 MACROSCALE GEOMECHANICAL BEHAVIOUR

As thermal steam injection continues, under the designed MOP, over tens of years into the oil sands reservoir during the SAGD process, a steam chamber forms and grows due to the increase in pressure and temperature within the pay zone. The pay zone deforms, dilates, and starts to enlarge underneath the caprock and with time the caprock may be differentially pushed up where increasing levels of shear and tensile stresses develop within it, as schematically illustrated in Figure 6-9. Figure 6-10 shows contours of recorded ground surface heave after five years of running SAGD operations (Ito & Ipek, 2005). This section includes a discussion of the macroscale geomechanical behaviour of caprock models as result from the 3D DEM geomechanical coupled modelling.

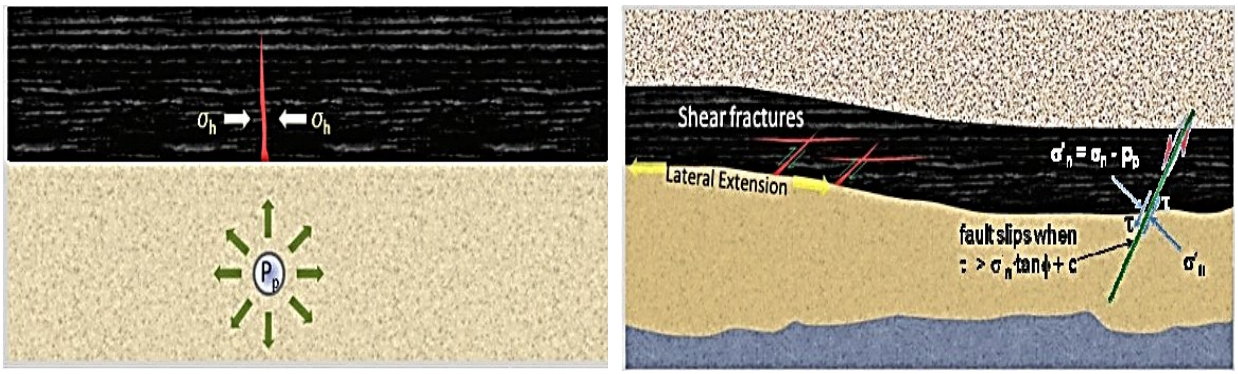

(a) (b)

Figure 6-9 Caprock possible (a) tensile or (b) shear failure mechanisms due to underlying SAGD dilating steam chamber (Khan et al., 2010)

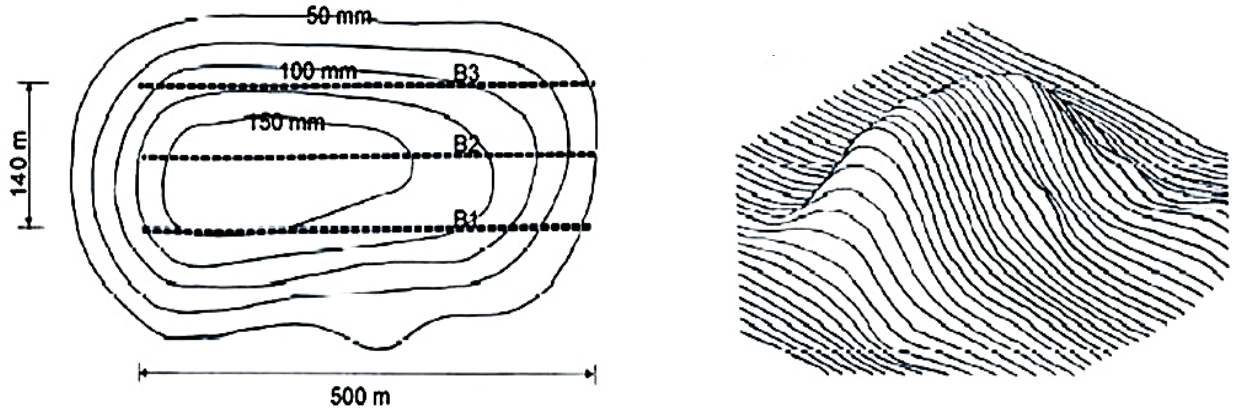

(a) (b)

Figure 6-10 Heave contours result from reservoir thermal dilation after 5 years of running SAGD (a) plan view – 2D and (b) 3D view (Ito & Ipek, 2005)

6.5.2.1 SAGD-INDUCED HEAVE

All published and publicly available in situ performance reports submitted to the AER declare and disclose ground surface uplifts in SAGD projects. Similarly, heave deformations have been resulted in all modelling cases investigated in this chapter. Contours of heave deformation within selected caprock models are as depicted in Figure 6-11. The heave values listed in Table 6-6 and Table 6-7 for fault and bedding planes configurations, respectively were resulted. The upward displacement ranged from 7 cm to a shear failure or slip (i.e. > 1 m). The upward displacements in cases without OB (= unconstrained/unconfined) are generally bigger, and ranged from 11 cm to shear failure or slip along a vulnerable geologic feature, compared to the confined models where the heave deformation ranged from 7 cm to 93 cm. In the following subsections the

effect of different structural geology elements, MOP, and confinement on both heave magnitude and distribution will be presented and discussed in detail.

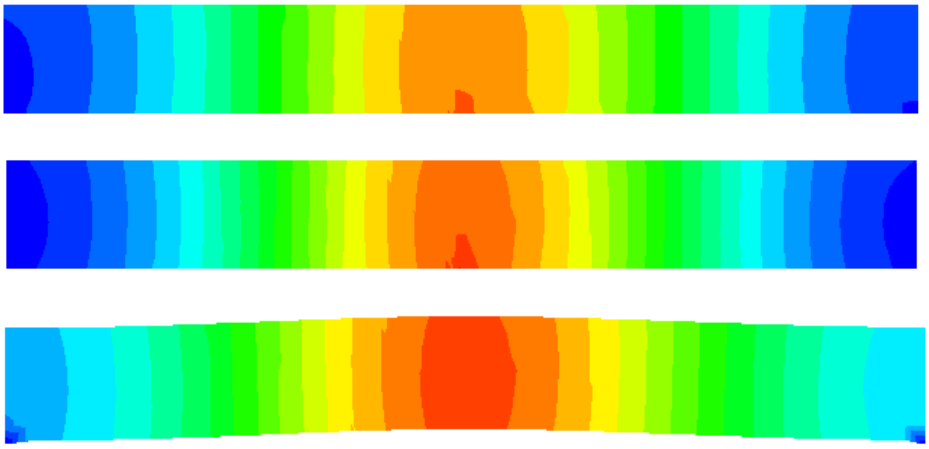

Figure 6-11 Contours of heave deforamtion evolution within caprock models

Table 6-6 Caprock heave in fault-based configuration models

Displacement (cm)	MOP (kPa)					
	739		1200		1800	
Case ID #	confined	unconfined	confined	unconfined	confined	unconfined
Intact	7.6	37.7	29.1	61.2	51.1	93.1
F	8.7	38.5	32.5	62.5	55.9	Failure
F+BP	8.8	15.8	13.8	29.9	20.8	45.98
F+2JS	27.5	53.1	45.7	94.8	69.4	Failure
F+BP+2JS	15.2	23.4	24.4	38.8	36.6	Failure
F+5JS	29.0	Failure	47.8	Failure	72.4	Failure
F+BP+5JS	17.4	29.3	28.0	78.8	41.9	Failure
F+10JS	36.6	Failure	60.6	Failure	92.8	Failure
F+BP+10JS	Failure	Failure	Failure	Failure	Failure	Failure

Table 6-7 Caprock heave in bedding planes-based configuration models

Displacement (cm)	MOP (kPa)					
	739		1200		1800	
Case ID #	confined	unconfined	confined	unconfined	confined	unconfined
Intact	7.6	37.7	29.1	61.2	51.1	93.1
BP	7.0	11.9	11.2	19.3	16.9	28.9
F+BP	8.8	15.8	13.8	29.9	20.8	46.0
BP+2JS	16.2	23.3	26.2	48.1	39.3	Failure
F+BP+2JS	15.2	23.4	24.4	38.8	36.6	Failure
BP+5JS	16.2	22.6	26.0	43.6	38.9	Failure
F+BP+5JS	17.4	29.3	28.0	78.8	41.9	Failure
BP+10JS	Failure	Failure	Failure	Failure	Failure	Failure
F+BP+10JS	Failure	Failure	Failure	Failure	Failure	Failure

6.5.2.1.1 EFFECT OF DIFFERENT STRUCTURAL GEOLOGY ELEMENTS

Modeling results reflected that as the degree of fracturing changes, the upward displacements magnitude and distribution change under same MOP and confinement conditions. The simulations further demonstrated the issue of the relative compliance embedded in caprock systems with discontinuities where local deformations within the fracture system contribute to the model overall displacement. It is apparent that the scale of the geological heterogeneity, as sketched in Figure 6-4, significantly affects the upward displacement magnitude and distribution. As interpreted from Table 6-6 the fault-based (F) configuration models produced different results trend compared to the bedding planes-based (BP) configuration models (Table 6-7). The trend in the BP configuration is generally showing a decrease in the model's maximum upward displacement as the degree of discontinuity inclusion increases unlike in case of fault configured models. This again can be practically interpreted as to emphasize on the need to carefully consider and include structure geology elements that would exist in reality when assessing and designing SAGD CCShC integrity because it proves to have a significant influence on the expected heave. Uniform heave distribution in case of the intact models can be seen in Figure 6-12. This distribution trend is unlike what resulted from the discontinuum models where the contours tend

to follow the discontinuities locations, e.g. along the narrowly spaced bedding planes as depicted in Figure 6-13.

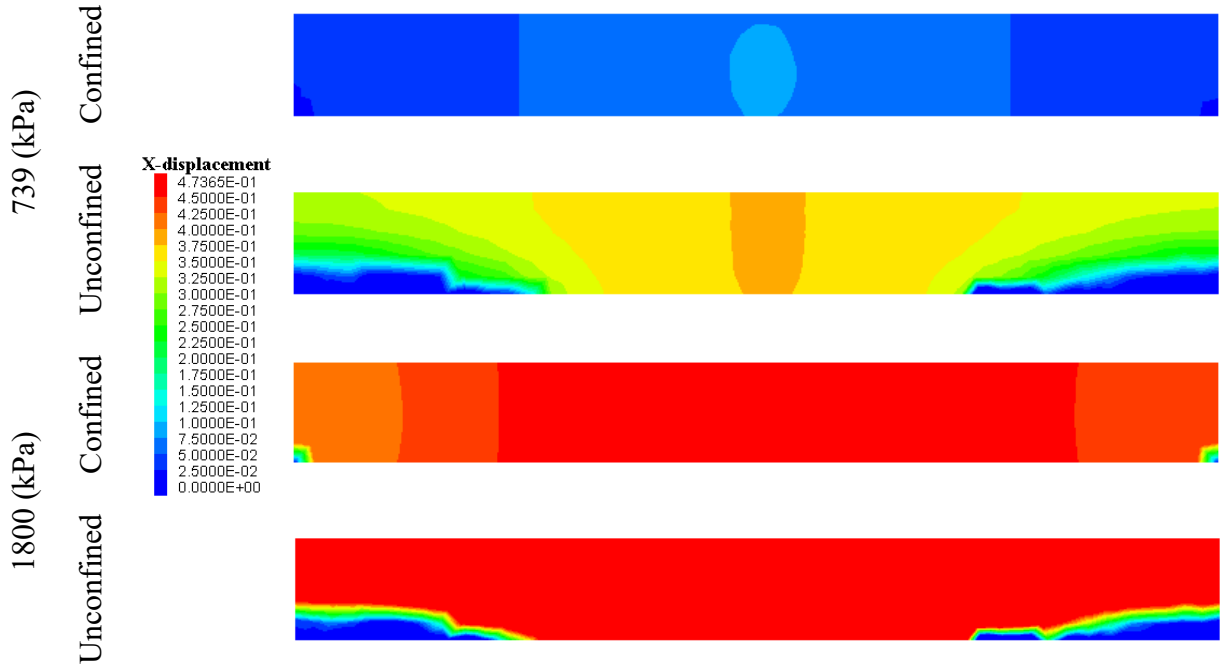

Figure 6-12 Heave (X) displacement in meters for continuum (intact) models

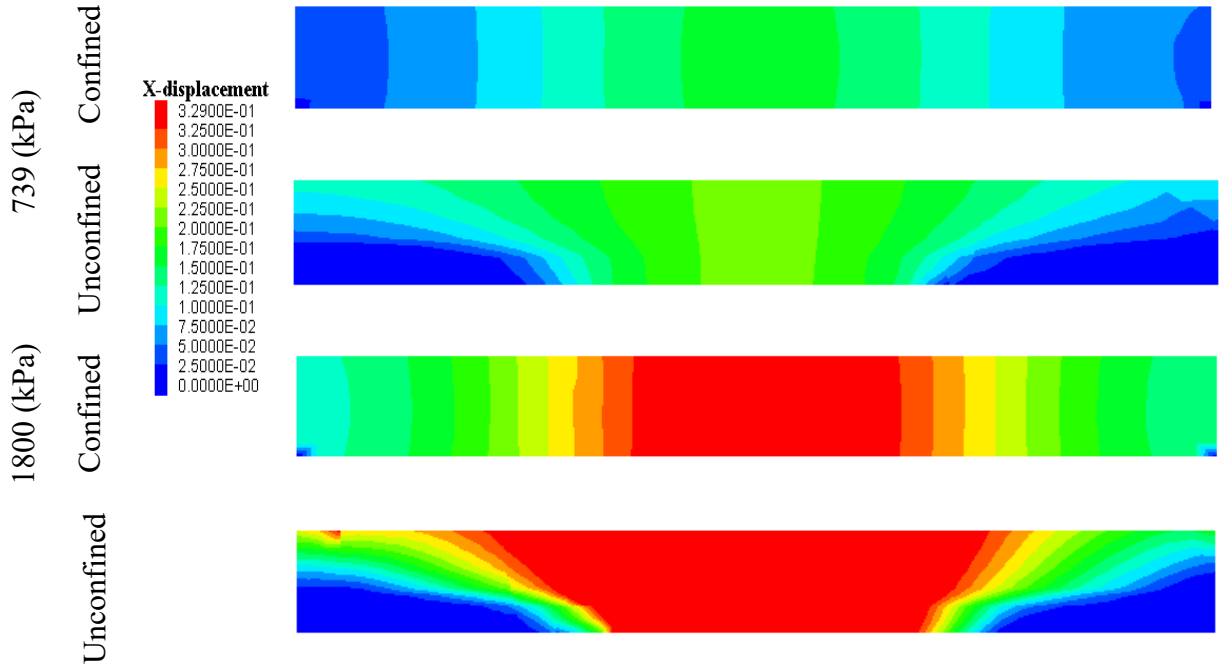

Figure 6-13 Heave (X) displacement in meters for discontinuum (BP+5JS) models

Discontinuities in the models appreciably carry up and deform at the microscale as the rock mass deforms. The findings stress the importance of a detailed geological assessment of the CCShC prior SAGD operation planning. These results clearly show the significant role of the discontinuities in the geomechanical behaviour of the caprock. Discussion of the change in the SAGD-induced heave will be categorized based on the models geological configuration as follows:

- Effect of a major fault
- Effect of bedding planes
- Effect of number of joint sets

i. EFFECT OF A MAJOR GEOLOGIC FAULT

As the degree of fracturing intensity increases, in the fault-based configuration models, the magnitude of the uplift increases regardless the MOP and the confinement as listed in Table 6-6 and summarized in Table 6-8. This indicates that, the fault itself locally takes up from the system deformation causing an increase in the model (overall) upward displacement. The fault effect, on the model' heave value, out weighted both the MOP and confinement effects. Results in Figure 6-14 indicate that the fault carries a reasonable portion (Figure 1-6) from the deformation and itself locally suffers displacement. This differential displacement may result in forming potential pathways for the pressurized thermal fluids within the reservoir underneath the caprock. This is not a safe condition for the main safeguard stratum above a high pressure high temperature dilating SAGD reservoir. It is strongly recommended to avoid areas known for geologic faults (e.g. triple graben) whenever possible, otherwise strict monitoring program must be implemented is not thick enough.

Table 6-8 Heave (cm) in caprock models considering fault configuration

Heave (cm)	MOP (kPa)	Intact	F	F+10 JS
Confined	739	7.6	8.7	36.6
	1800	51.1	55.9	91.8
Unconfined	739	37.7	38.5	Failure
	1800	93.1	Failure	Failure

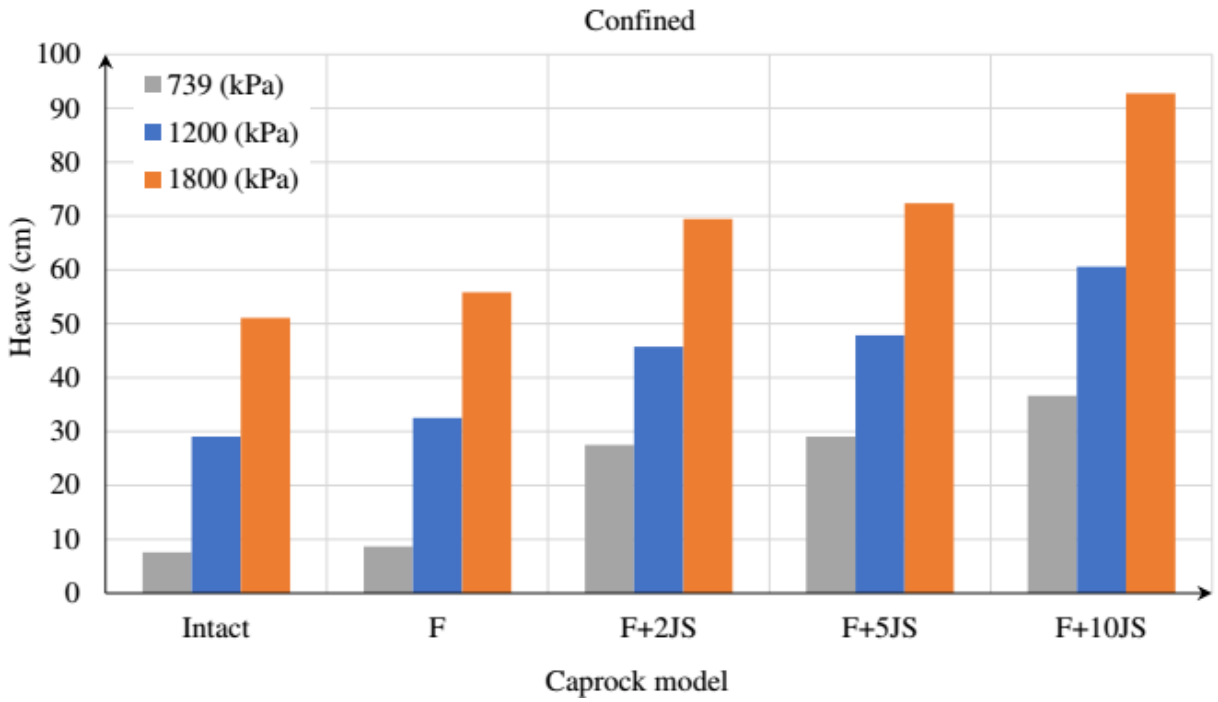

(a)

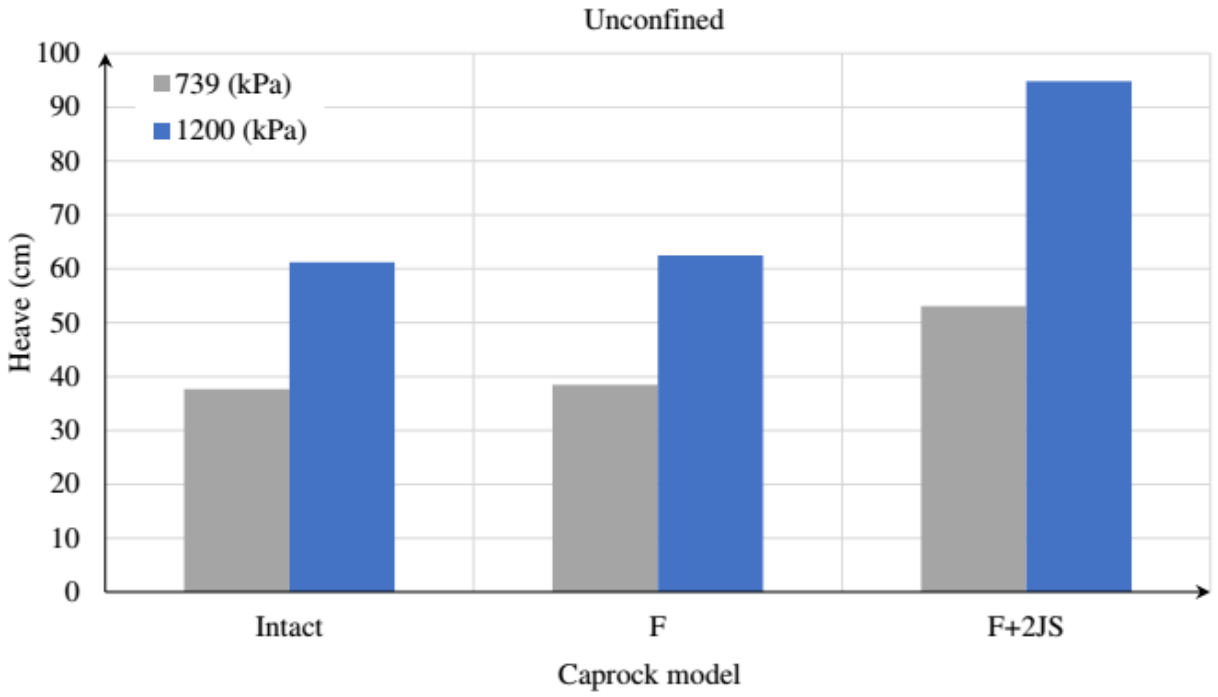

(b)

Figure 6-14 Effect of adding joint sets to fault configuration on (a) confined and (b) unconfined models heave

ii. EFFECT OF BEDDING PLANES

The values listed in Table 6-7 and summarized in Table 6-9 indicate that as the degree of fracturing intensity increases, in the bedding planes configuration caprock models, the magnitude of the macroscale model uplift decreases, except for the confined models subject to an MOP of 739 kPa as plotted in Figure 6-15a. The discontinuities themselves locally take up from the system deformation causing decrease in the model (overall) upward displacement.

Table 6-9 Heave (cm) of caprock models with regard to bedding planes configuration

Heave (cm)	MOP (kPa)	Intact	BP
Confined	739	7.6	7.0
	1800	51.1	16.9
Unconfined	739	37.7	11.9
	1800	93.1	28.9

iii. EFFECT OF NUMBER OF JOINT SETS

As the number of joint sets increases, the magnitude of the macroscale model uplift changes depending on the other geologic element included; fault (Figure 6-14) or bedding planes (Figure 6-15). Nonetheless, Figure 6-16 includes the heave values as the number of joint sets increases in models include both fault and bedding planes, where a similar increasing trend clearly governed by the fault as presented in Figure 6-14. This generally indicates that the discontinuities themselves locally take up from the system deformation causing a change in the model (overall) upward displacement. This finding confirms the chapter main motivation of the need to conduct and collect in situ geologic mapping information of the region of interest prior commencing planning for operations.

Local shear failure (slip) occurs along a favorably oriented discontinuity of a joint set in the most discontinuum models subject to any MOP regardless the confinement (Table 6-6 and Table 6-7). Shear failure was also noticed once joint sets introduced in the caprock models, in case of the MOP of 1800 kPa in all unconfined models. Shallow caprock are more vulnerable to failure due to the low confinement. Practically past the Joslyn creek steam release incident in 2006, an MOP of 1800 kPa is currently considered extremely high in Alberta and is not recommended especially in shallow reservoir SAGD projects.

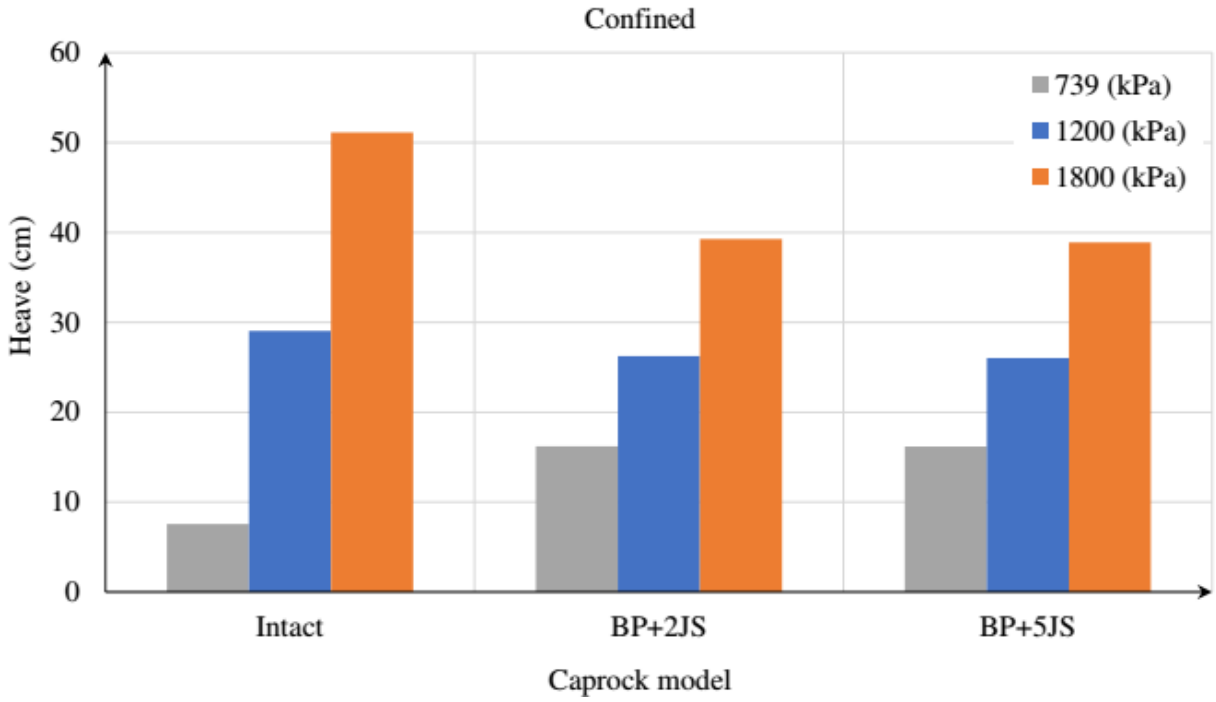

(a)

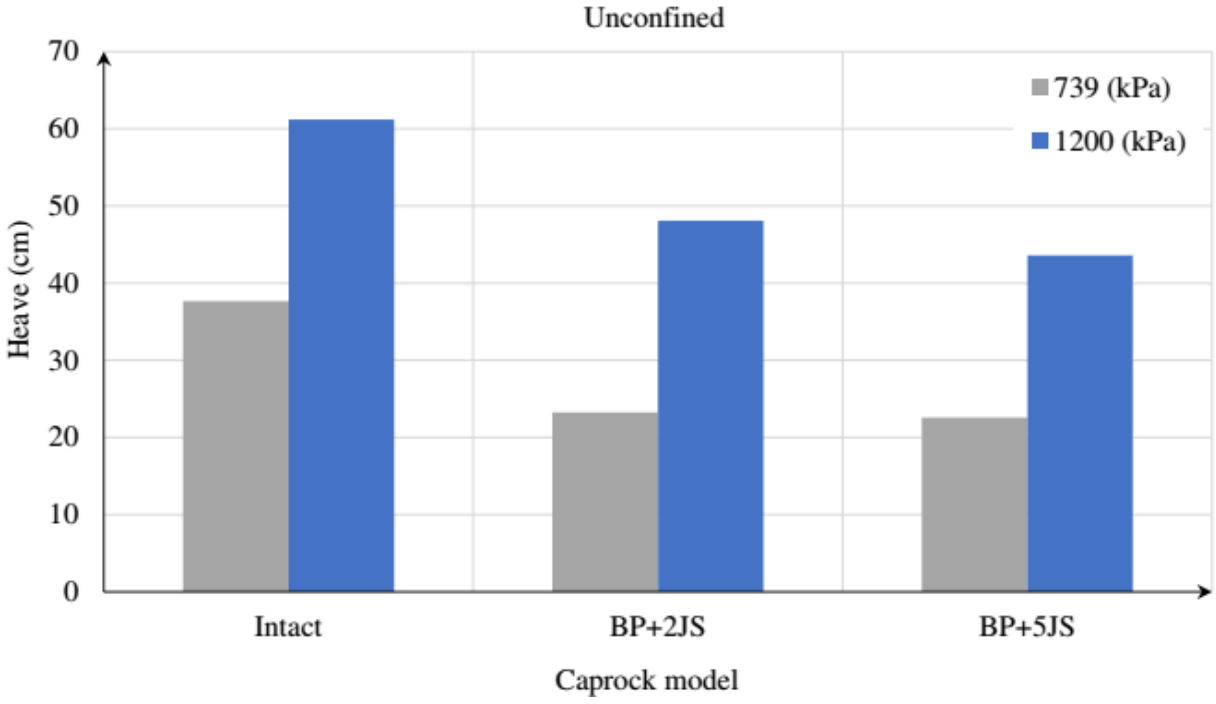

(b)

Figure 6-15 Effect of adding joint sets to bedding planes configuration on (a) confined and (b) unconfined models heave

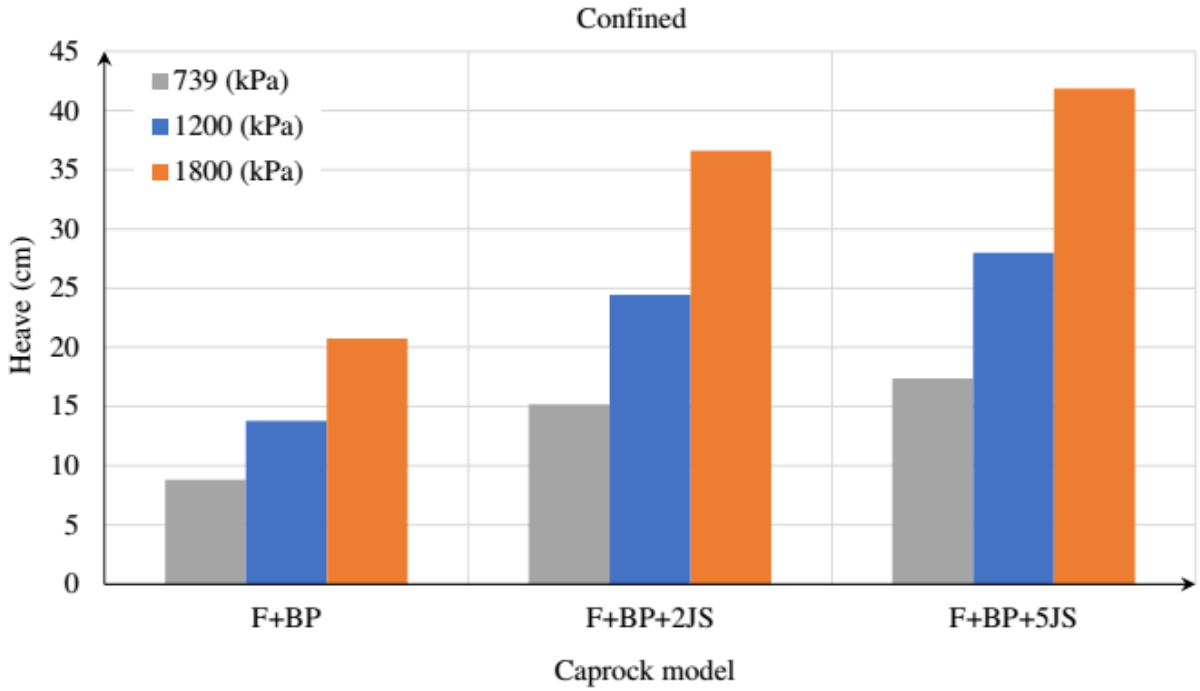

Figure 6-16 Effect of increasing the joint sets on heave values

6.5.2.1.2 EFFECT OF MOP

The application of an equivalent upward loading at the base of the model in a stepped fashion provides an opportunity to study how caprock displacements evolve with time. The effect of three MOPs on the model upward heave is illustrated in Figure 6-17 fault and BP configurations. For the same degree of fracturing, regardless the confinement, increasing the MOP increased the value of the model heave displacement.

The increase in case of the intact or continuum models (slope) is higher than the increase in case of the discontinuum models. This is expected as the intact model has no other way the deformation will be taken up with. However, in case of the discontinuum model, the rate in heave displacement increase is lower, which again supports and confirms the research scientific hypothesis basis that the discontinuities carry up appreciably in rock masses deformability. However, this proven relative microscale deformation occurring at the discontinuities level alerts of a potential compromise to the caprock main essential merit as a hydraulic seal. In a similar fashion, the confinement helped increasing the discontinuities contribution, the slope decreased in case of confined models compared to unconfined model, posing less interactive response the MOP increase.

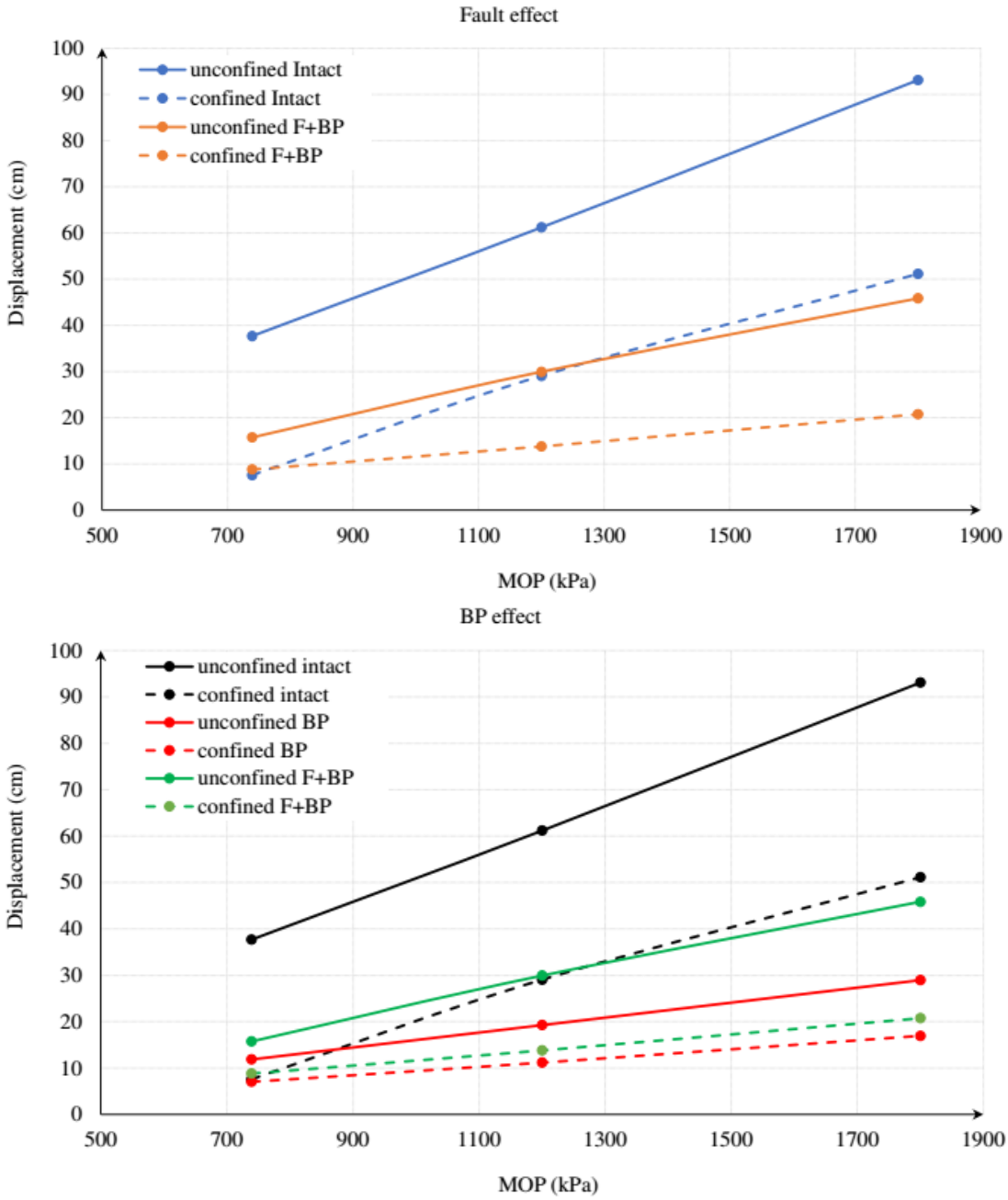

Figure 6-17 Heave displacement as MOP changes for fault and BP configurations

Detailed and stringent field geological assessment of the CCShC prior SAGD project planning in addition to comprehensive monitoring of the MOP fluctuations and field heave surveying (e.g. InSAR) during operation are mandatorily needed. It is strongly recommended to plan and follow a strict monitoring protocol as the MOP values oscillate during SAGD operation especially with shallow reservoir as a guarantee to safely maintain the caprock integrity.

6.5.2.1.3 EFFECT OF OVERBURDEN (OB)

As included in previous sections and illustrated with plots, graphs, and tables for all the simulations conducted in this chapter, the impact of having a 150 m OB layer above the caprock, which mimics increasing depth of the caprock was assessed. Adding OB (confinement) was found to reduce the surface heave in all cases under same MOPs. In confined discontinuum models, the discontinuities are more stressed and relatively deforming much at the microscale. This on the other hand highlights the importance of paying attention when assessing the OB and special attention towards shallow SAGD reservoirs because their caprocks are more vulnerable to deformation and failure due to the low confinement.

6.5.2.1.4 UPWARD DISPLACEMENT PROFILE

In all the caprock simulation cases examined, the upward displacement was monitored at 18 locations (5 meters apart) at the model's surface as illustrated in Figure 6-18. Figure 6-19 and Figure 6-20 include surface heave profiles of models due to two extreme MOPs for unconfined and confined caprock models, respectively. In these plots, continuum basically is the intact model and the discontinued is the F+BP+5JS model (Table 6-6).

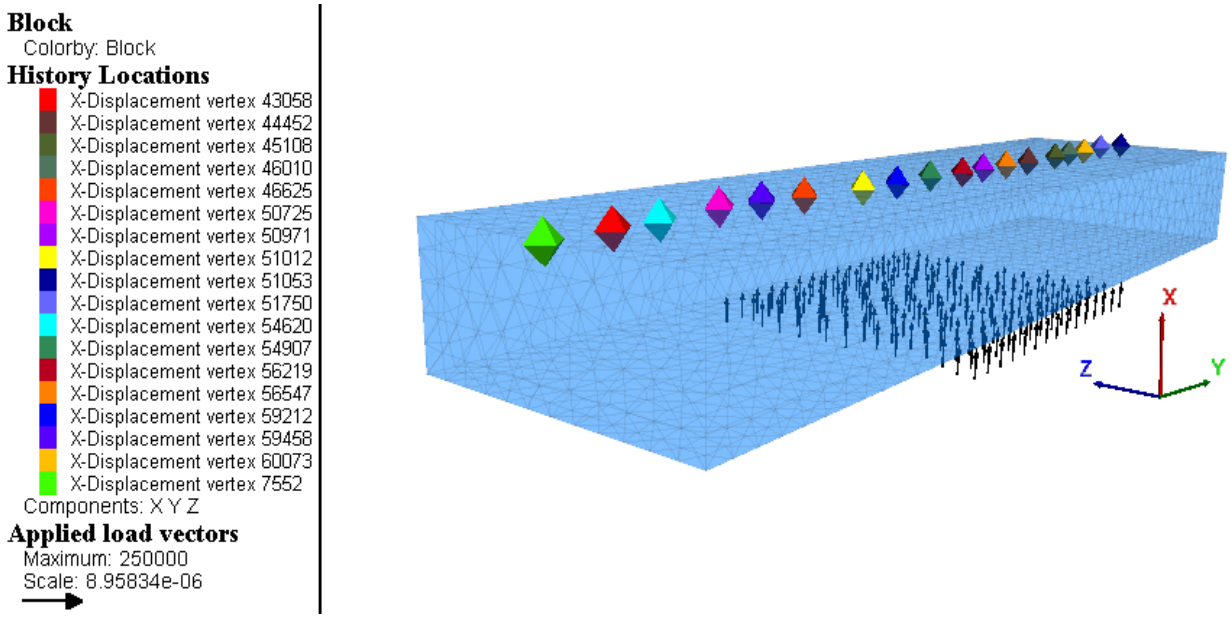

Figure 6-18 Surface heave monitored at 18 locations

The confinement again resulted in a decrease in the surface heave in all cases. While in all simulation cases, increasing the MOP led to an increase of the surface heave. This emphasis on the importance to properly design and monitor the MOP in order to maintain a safe caprock.

It was noticed that, more uniform closely spaced heave profiles resulted in case of unconfined models regardless the discontinuities configuration per the plots in Figure 6-19. However, under the high MOP, the discontinuum model showed wide spaced profiles reflecting the fact that various model elements differently responding by heaving prior and leading to a shear failure (Table 6-6). In Figure 6-20 an abrupt change, in the profiles of the confined continuum model subject to 739 kPa MOP, can be seen where the rate of heave increase was subtle for a while before starting to increase again. This highlights the importance of accurately characterizing the caprock in situ because continuum and discontinuum models proved to behave differently.

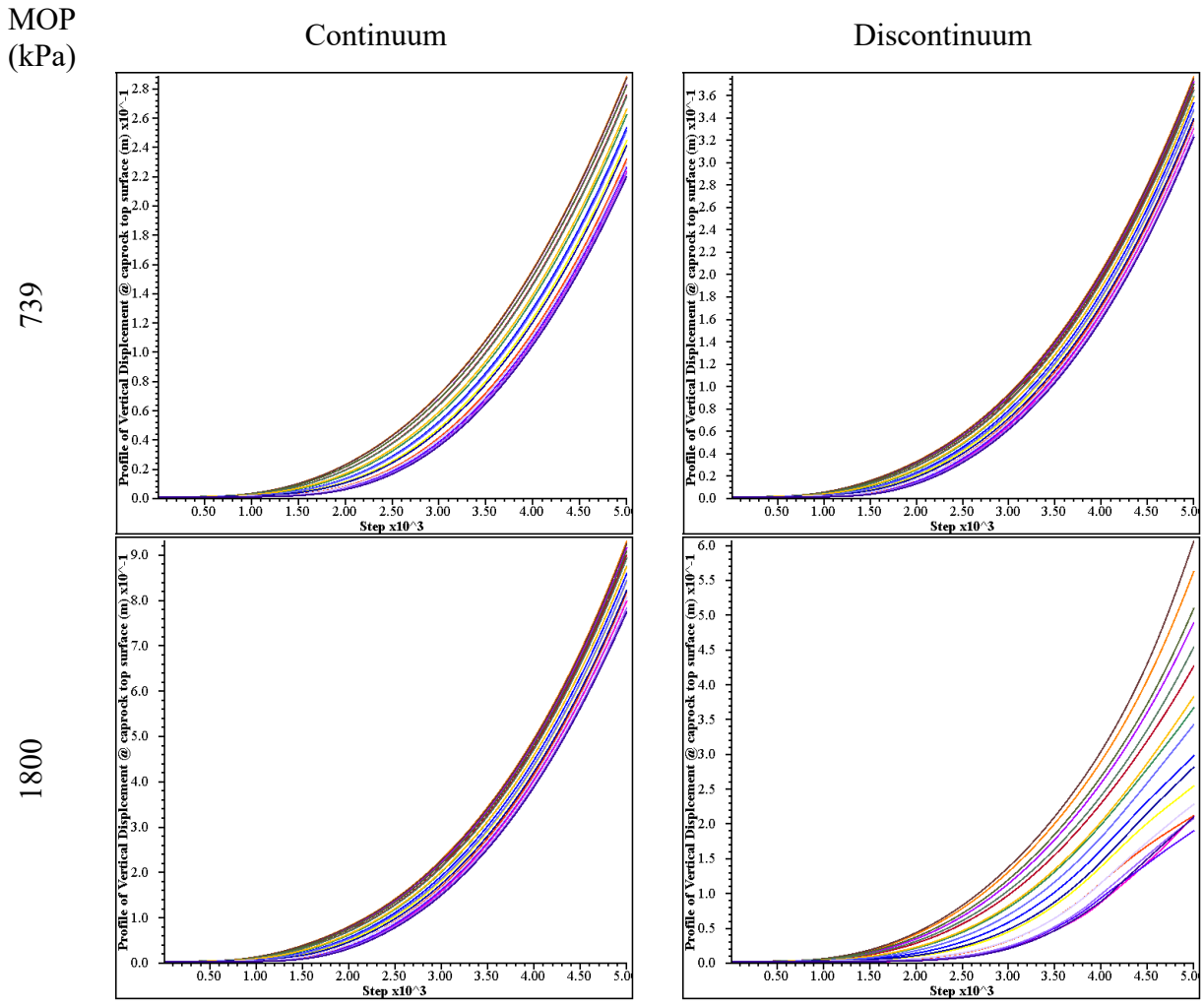

Figure 6-19 Surface heave profile at 18 monitoring locations – unconfined caprock models

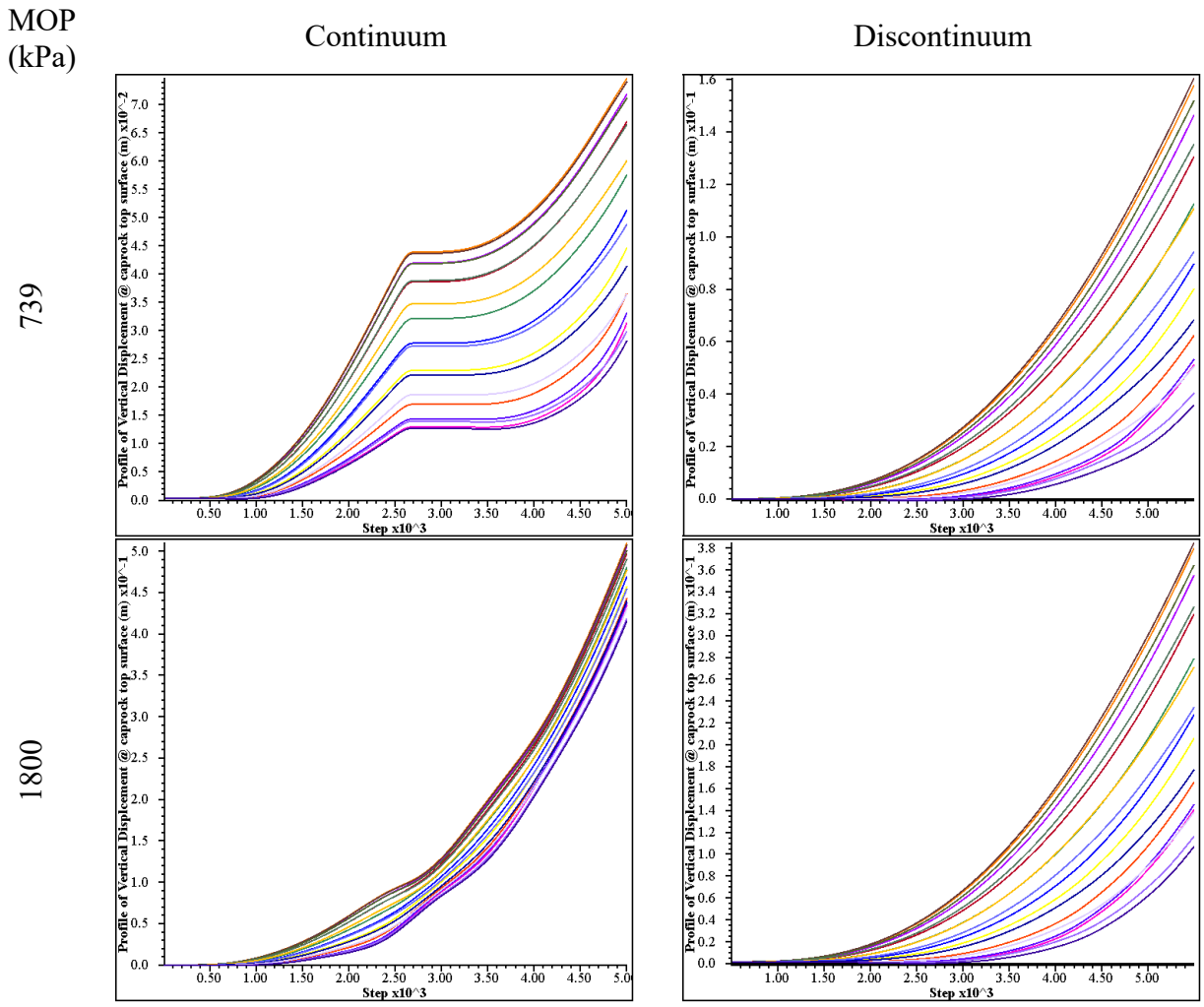

Figure 6-20 Surface heave profile at 18 monitoring locations – confined caprock models

6.5.2.2 TENSILE STRESS

As repeatedly reported and published in literature and earlier emphasized in this thesis and illustrated in Figure 6-9, increasing imposition of deformations on the caprock, with the thermal growing of the steam chamber, underneath it generates tensile and shear stresses within the naturally fractured caprock. The tensile (-ve) stress distributions in the CCShC models are illustrated in Figure 6-21 and Figure 6-22 for unconfined and confined cases, respectively. Nonuniformity in the stress distribution in the discontinuum models are noticed as the stresses tend to follow favorable paths. More tensile stresses generated due to increasing the MOP regardless the model's degree of fracturing.

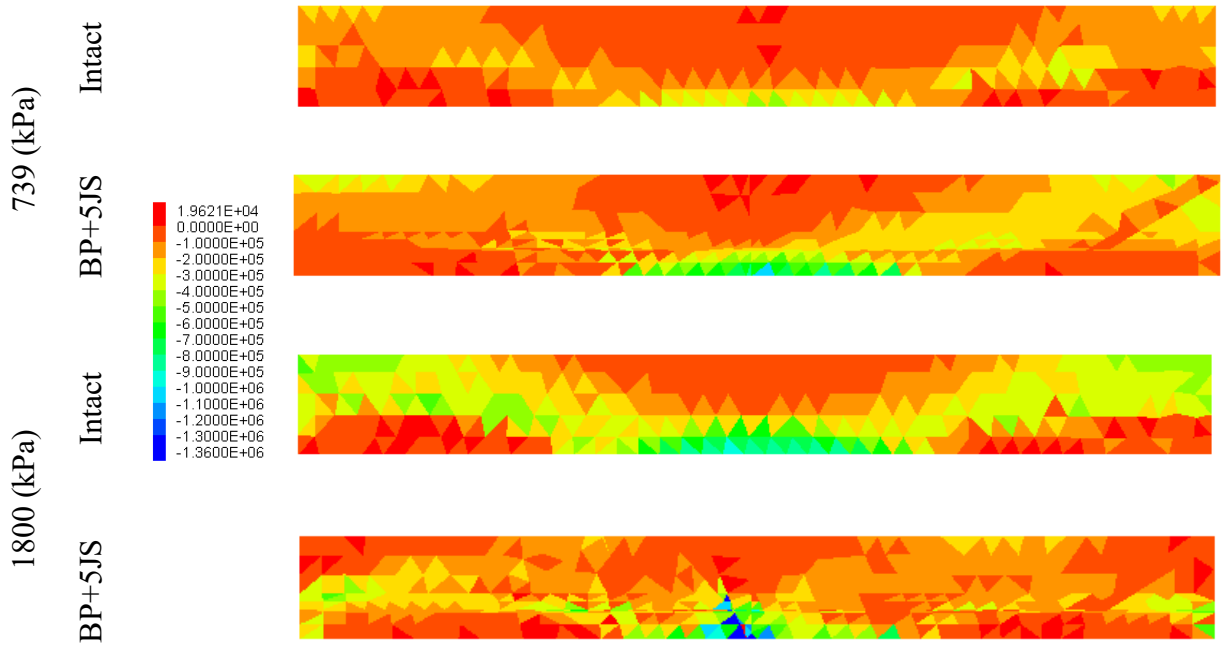

Figure 6-21 Tensile (-ve) stresses (Pa) developed in unconfined caprock models

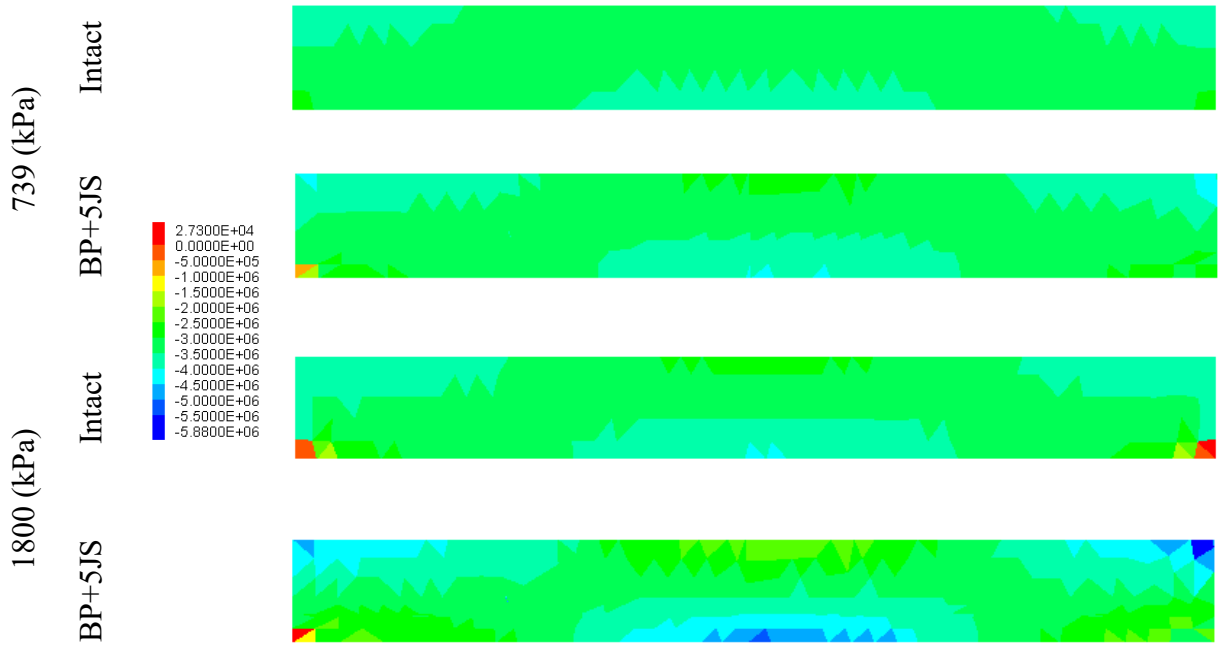

Figure 6-22 Tensile (-ve) stresses (Pa) developed in confined caprock models

Similarly, tensile stresses are higher in discontinuum models compared to continuum models regardless the MOP as listed in Table 6-10. But more importantly, adding an OB (confinement) increased the tensile stresses generated in the models due to the suppressing of the

upward heave movement. All these patterns and critical locations of tensile stress generation are in a good agreement with literature reported records, e.g. (Rahmati, Nouri, & Fattahpour, 2015) and (Khani et al., 2018).

Table 6-10 Maximum tensile stress

Maximum tensile stress (kPa)	MOP (kPa)	739	1800
Unconfined (no OB)	continuum	16.9	930
	discontinuum	2520	6492
Confined (OB of 150m)	continuum	3760	4020
	discontinuum	5840	7965

6.5.2.3 SHEAR STRESS

The shear stress distributions are illustrated in Figure 6-23 and Figure 6-24 for unconfined and confined models, respectively. Increasing the MOP generally increased the shear stress in all caprock models. Comparing the shear stress values, the intact models suffered less than the fractured system subject to same MOP. Shear tends to follow and occur along easiest path/s, which in the discontinuum model case is along the pre-existing discontinuities. That justifies the increase in the maximum shear stress in case of the discontinuum model compared to the continuum model. This is an alerting indicator of the importance to include and study a discontinuum CCShC if that is the case in reality and not overlook that critical design consideration.

The maximum shear stresses recorded in the investigated caprock models are listed in Table 6-11 to illustrate the confinement influence. Adding an OB on top of the caprock models significantly increased the generated shear stresses in all cases. As stated above, adding an OB suppresses the upward displacement of the caprock which is reflected in the reduction in the measured heave magnitudes, suppressing and trapping energy, consequently a generation of higher shear stresses within the caprock. A local slippage (shear failure) occurred:-

- In the most discontinuum model regardless the MOP nor the confinement
- In the unconfined discontinuum models subjected to an MOP of 1800 kPa

This illustrates the importance of precisely considering and evaluating not only the CCShC structural geology, but also MOP inevitable fluctuations for securely maintaining the caprock integrity, especially in shallow SAGD projects.

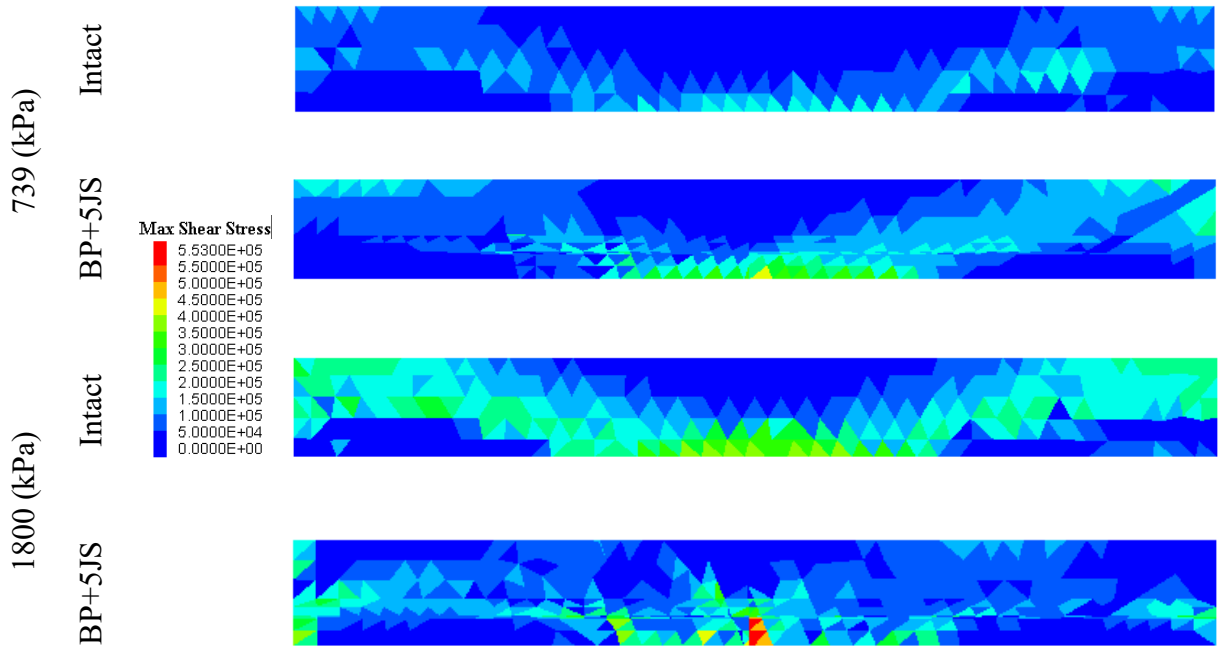

Figure 6-23 Shear stresses (Pa) developed in unconfined caprock models

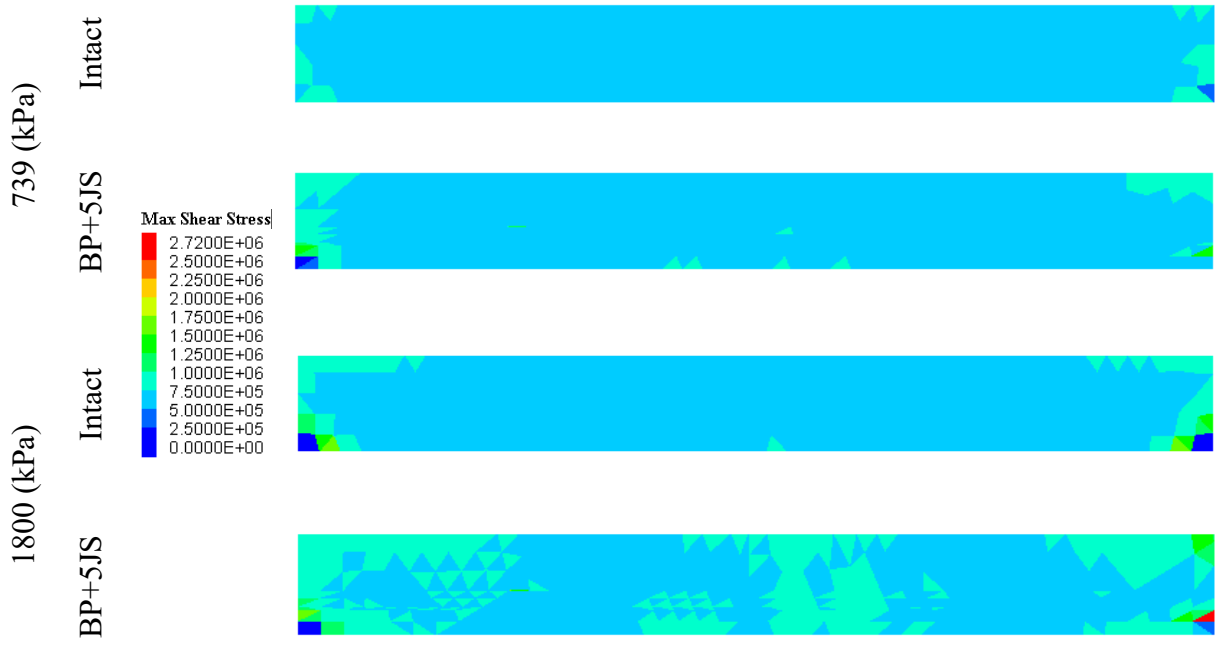

Figure 6-24 Shear stresses (Pa) developed in confined caprock models

Table 6-11 Maximum shear stress

Maximum shear stress (kPa)	MOP (kPa)	739	1800
Unconfined (no OB)	continuum	209	386
	discontinuum	1090	2700
Confined (OB of 150m)	continuum	1166	1940
	discontinuum	2160	2900

6.5.3 MICROSCALE GEOMECHANICAL BEHAVIOUR

This section provides a discussion of the geomechanical behaviour at the microscale, such as discontinuity normal (opening) and shear displacements, as the MOP changes under the two confinement conditions. For the unconfined fault model case, Figure 6-25 illustrates the deformation or slip along the fault. Due to the upward bending of the caprock, responding to the reservoir dilation underneath it as the MOP increases with time, tensile failure (light blue markers) occurs on the upper section of the fault while shear slippage (green markers) is occurring along the middle and lower sections of the fault.

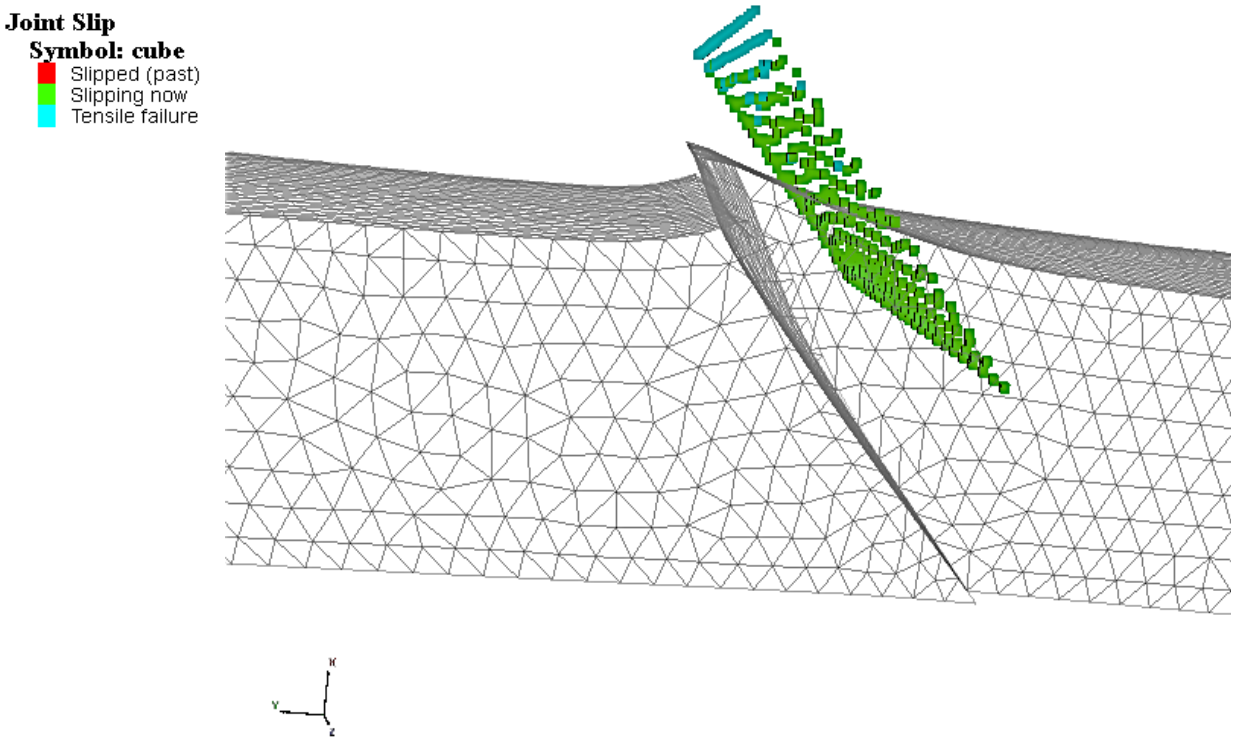

Figure 6-25 Deformed caprock model with a major geologic fault (unconfined condition)

Presence of a favorably oriented discontinuity can qualitatively and quantitively influence the deformation within the caprock interval hence severely compromising its hydraulic integrity. The discontinuum model cases will be analyzed in this section. Firstly, as a qualitative examination, the normal (opening) and shear displacements distributions, along discontinuities for F models (Table 6-3), are illustrated in Figure 6-26 and Figure 6-27, respectively.

The confinement significantly changed the shear displacement distribution regardless the MOP. Secondly as a quantitative evaluation, Table 6-12 and Table 6-13 include values of the joint displacements due to the MOPs of 739 and 1800 kPa, respectively. Examining the displacement magnitudes in these two tables, it can be noticed that the shear displacement values are always higher than the normal displacement values, indicating that the model's main failure mode is shear. Increasing MOP increased both joint displacements. And again, the confinement mainly suppresses the joint displacements consequently increasing the stresses within the models as discussed earlier.

Increasing discontinuities in the model generally increased both normal (opening) and shear joint displacements. This indicates at the microscale the discontinuities locally deform (open and/or shear) significantly carrying up in the caprock deformability (Figure 1-6). This is an undesirable consequence for a caprock overlying a thermal stimulation decades-long operation. Interpreting the values in Table 6-12 and Table 6-13, the following can be observed:

- Increasing the MOP from 739 – 1800 kPa:
    i. The normal (opening) displacement substantially increased in the unconfined caprock model cases. However, for the confined models, the normal displacement negligibly (48%) increased although the huge (≈144%) MOP increase as in Figure 6-28.
    ii. The shear displacement increased in the confined caprock model cases as seen from the plot in Figure 6-29.
- As the degree of fracturing increased:
    i. The normal displacement generally increases regardless the confinement with both MOP loading cases.
    ii. The shear displacement increased in all cases. Shear slip occurred as the degree of model fracturing increases, regardless the confinement nor the MOP.

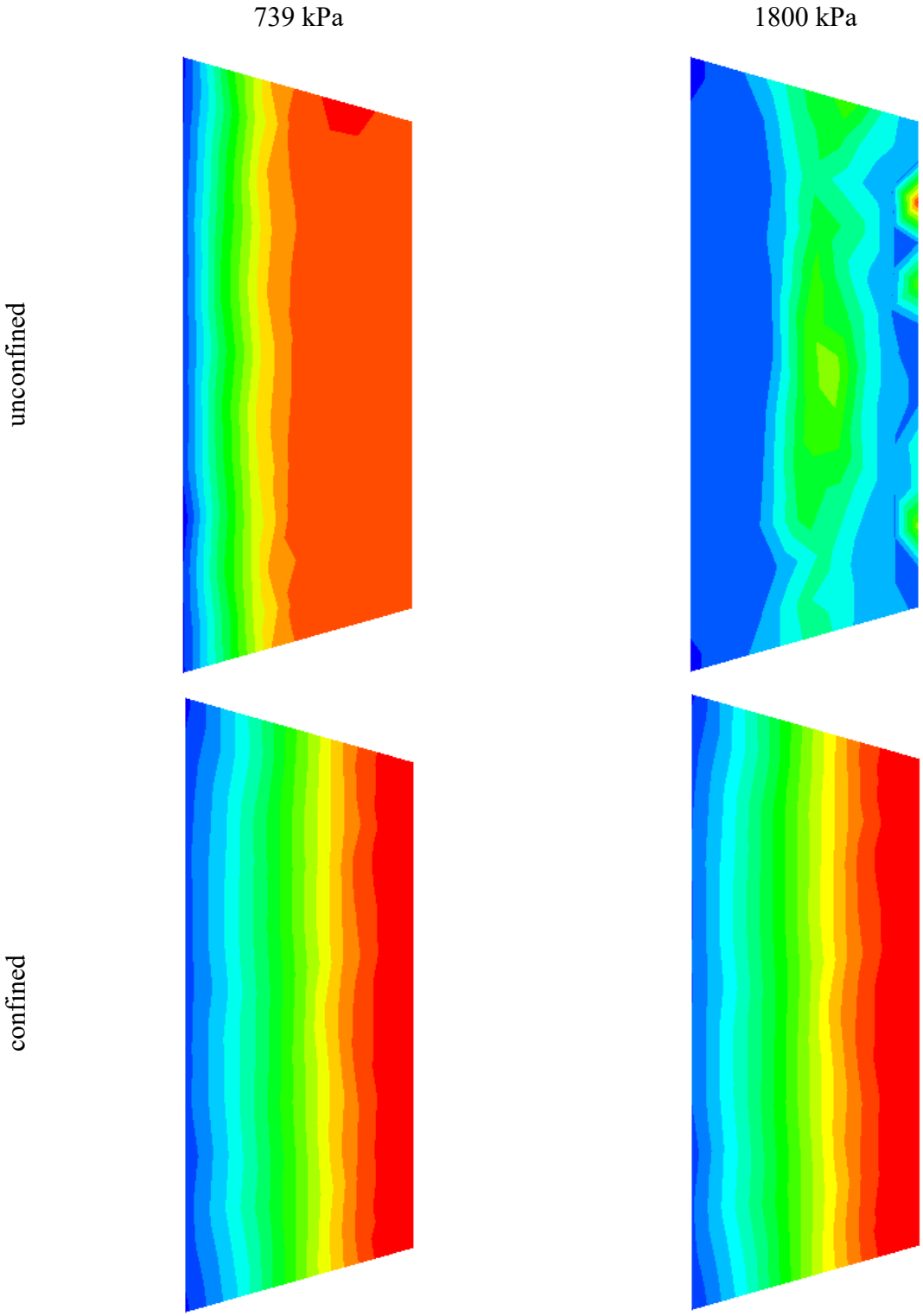

Figure 6-26 Joint normal (opening) displacement distribution Model F - unconfined model failed due to an MOP of 1800 kPa

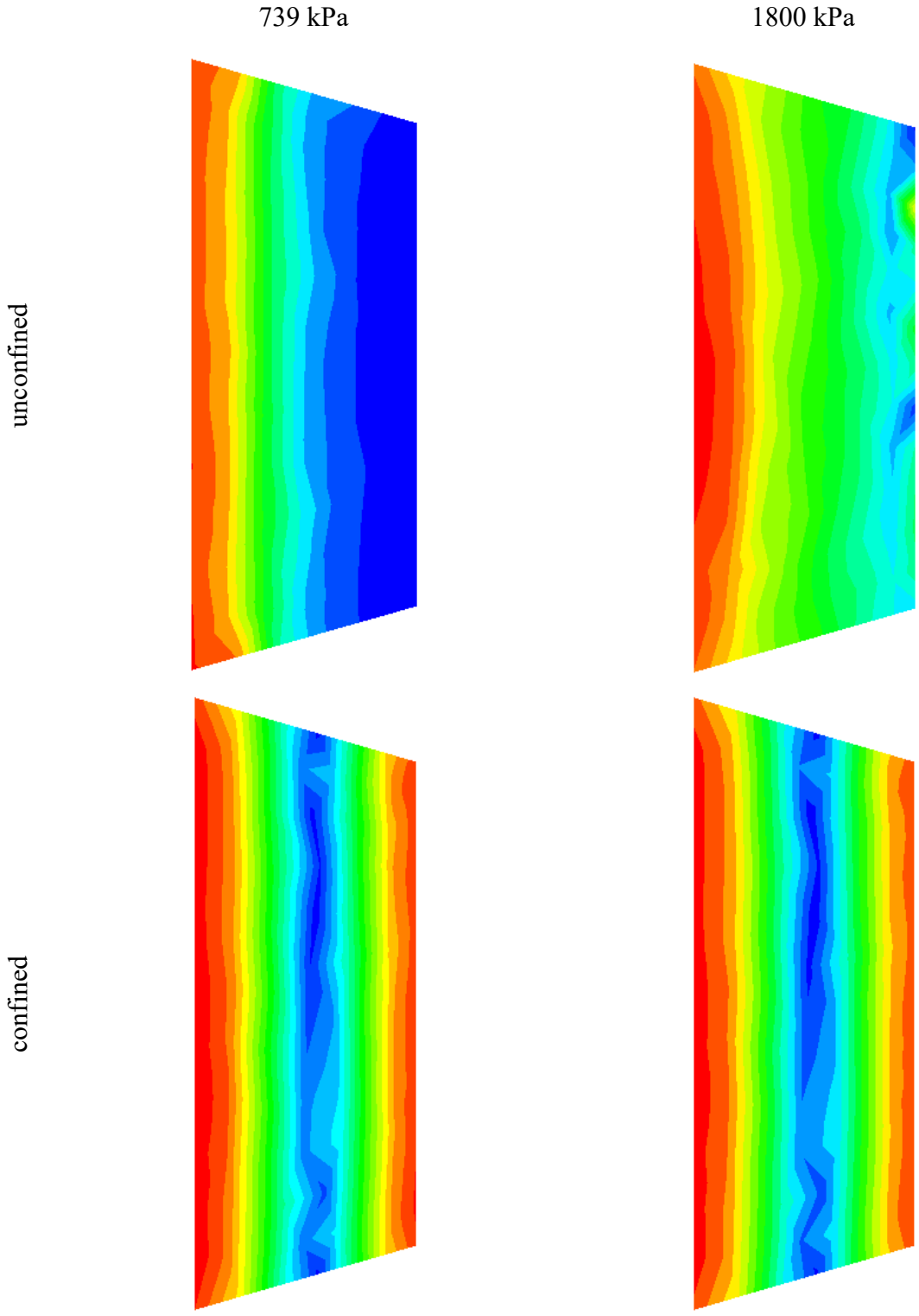

Figure 6-27 Joint shear displacement distribution Model F - unconfined model failed due to an MOP of 1800 kPa

Table 6-12 Joint displacements due to an MOP of 739 kPa

	Model	Joint normal displacement (mm)	Joint shear displacement (mm)
unconfined	F	0.04	3.3
	F+BP	2.6	14.6
	F+2JS	43.2	Shear failure
	F+BP+2JS	10.1	Shear failure
	F+5JS	Failure	Shear failure
	F+BP+5JS	26.9	Shear failure
confined	F	0.29	1.7
	F+BP	0.36	2.1
	F+2JS	7.1	24.1
	F+BP+2JS	70.6	Shear failure
	F+5JS	7.1	23.6
	F+BP+5JS	78.2	Shear failure

* joint normal displacement is opening – failure means dispalcment > 1 m

Table 6-13 Joint displacements due to an MOP of 1800 kPa

	Model	Joint normal displacement (mm)	Joint shear displacement (mm)
unconfined	F	9.3	Shear failure
	F+BP	11.4	Shear failure
	F+2JS	91.9	Shear failure
	F+BP+2JS	28.3	Shear failure
	F+5JS	Failure	Shear failure
	F+BP+5JS	Failure	Shear failure
confined	F	0.6	3.4
	F+BP	0.63	3.5
	F+2JS	7.7	28.4
	F+BP+2JS	Failure	Shear failure
	F+5JS	6.72	26.5
	F+BP+5JS	78.2	Shear failure

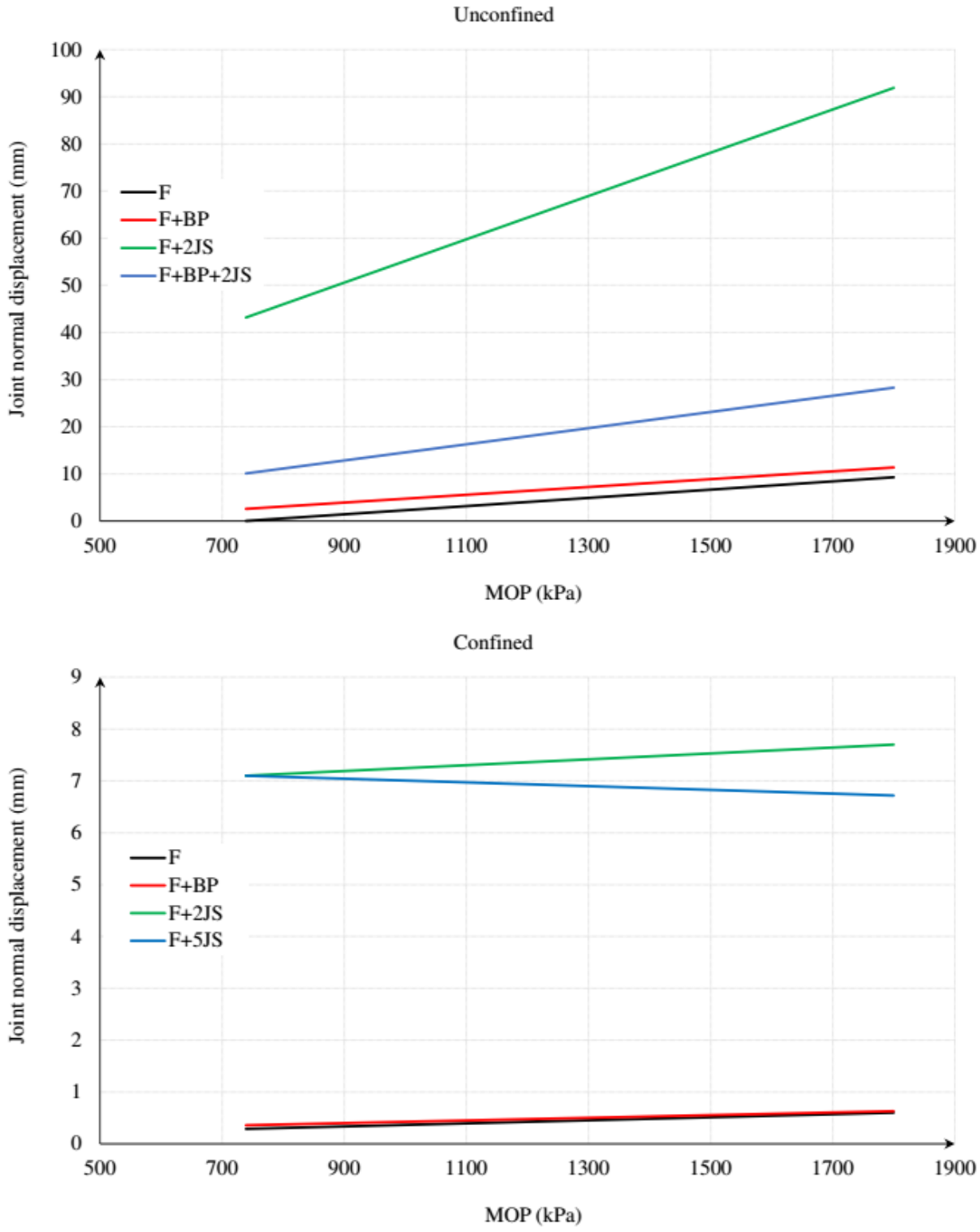

Figure 6-28 Joint normal displacement in unconfined and confined models

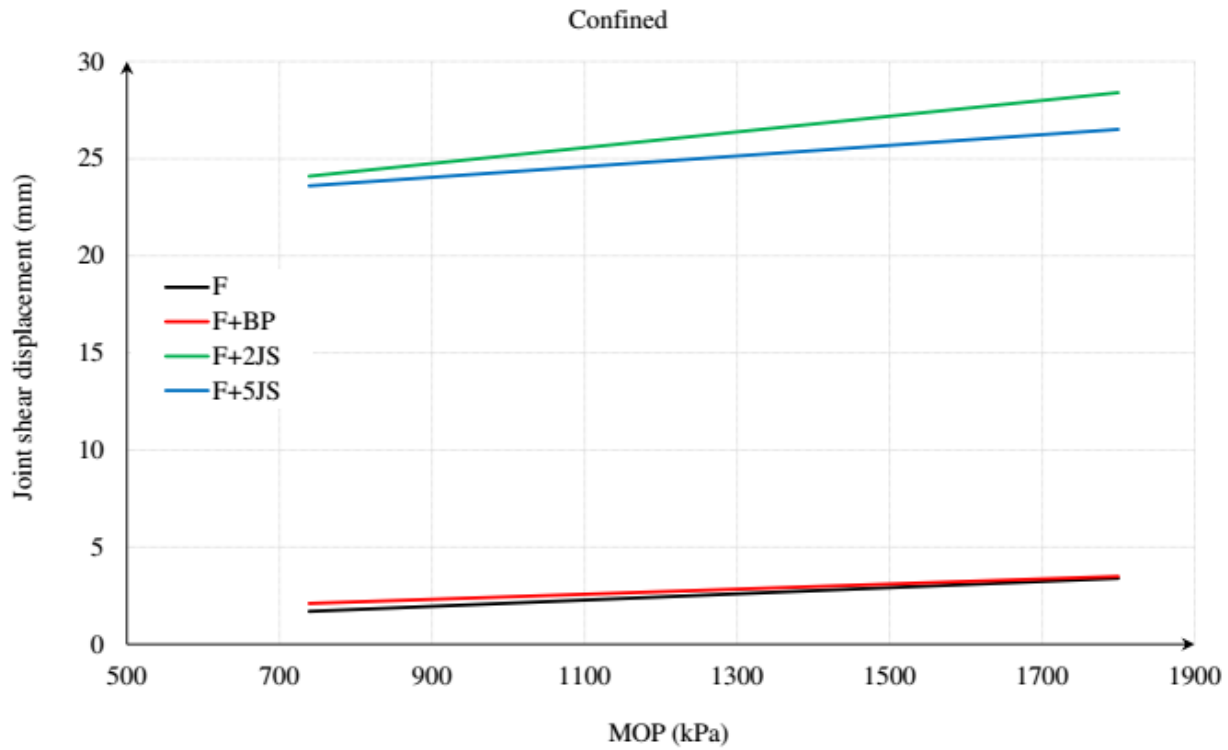

Figure 6-29 Joint shear displacement

The joint shear slip in the discontinuum models subject to different magnitudes of MOPs are shown in Figure 6-30. Increasing the MOP increased the shear failure locations significantly in the unconfined models (Table 6-6 and Table 6-7). Unlike the tensile failure zones which were influenced slightly due to the increase in the MOP.

6.6 SUMMARY AND CONCLUSIONS

One of the unconventional energy resource stimulation techniques used in Alberta is SAGD. It is crucial to assess and design the integrity of the SAGD caprock. Currently the conventional (CHILE) equivalent continuum modelling for designing the SAGD caprock integrity is being used in industry. Given the plenty of evidence that the over-consolidated Clearwater clay shale caprock (CCShC) contains significant discontinuities, such as bedding planes, faults, joints, fractures and fissures, treating this interval using continuum mechanics approaches can lead to inaccurate predictions of deformability and strength. Discontinuity systems may compromise the caprock seal and hydraulic integrity especially when the system is deformed or uplifted.

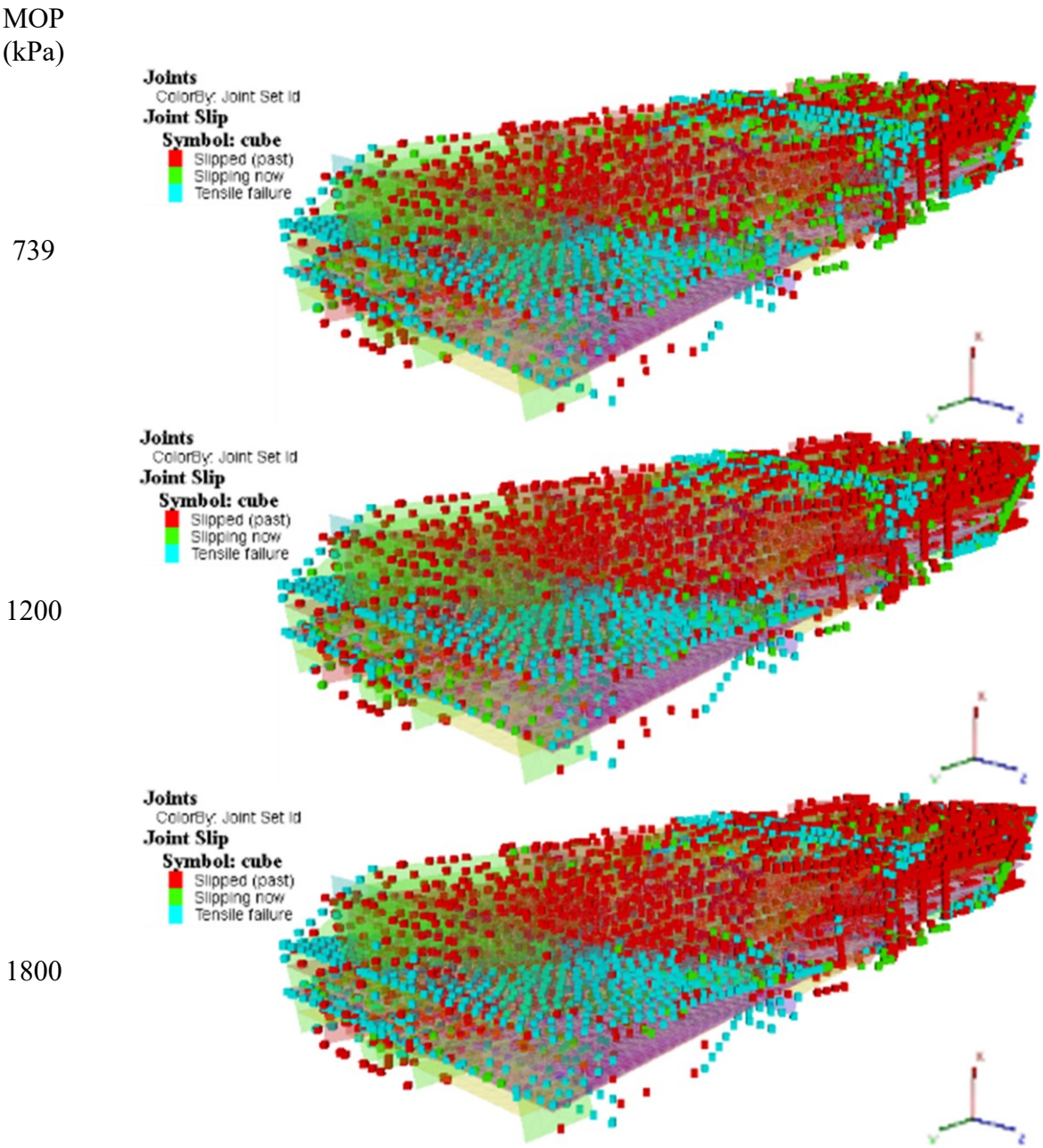

Figure 6-30 Joint slip in unconfined disocntinuum models

An investigation to evaluate the role of discontinuities in CCShC over SAGD reservoir was carried out as to fulfill the thesis third research objective. The study was extended to include evaluations of the effect of MOP magnitude and the confinement on the caprock geomechanical macro and microscale behaviours. The novelty of the current study stems from implementing a realistic DFN based on geologic field data captured in an Albertan mine site. The analyses in this chapter were performed using 3D DEM. The geomechanical input parameters for the intact CCSh

were used as reported in literature of geomechanical laboratory testing on preserved undisturbed specimens. Discontinuities mechanical parameters were similarly adopted from literature.

As the number of discontinuities increase, the maximum upward macroscale displacement of the caprock model changes under same MOP alerting to a fact that, the discontinuities themselves locally respond and deform. That was clearly supported when the slip and displacement magnitudes were investigated at the microscale, where the discontinuities underwent significant joint normal (opening) and shear displacements. Slippage along the discontinuities was primarily governed by the geometry of the DFN and increased significantly with the increase in the MOP. The presence of a favorably oriented discontinuity has the potential to qualitatively and quantitively change the deformation pattern within the caprock interval. Although not investigated in this study, it is likely that these deformations may potentially influence the overall permeability of the caprock.

The OB interval was found to have a substantial impact on the macro and microscale geomechanical behaviour of the caprock models. Simulation results indicated that confinement suppresses the caprock from moving upward as a normal response to reservoir dilation pushing it up. Consequently, an increase in the model stresses and local shear failures along the discontinuities was resulted. Based on the simulation predictions over a range of caprock conditions, it is clear a shallow reservoir (i.e., less OB) is likely more vulnerable to joint relative (shear) displacements as MOP is increased in SAGD projects with the potential of compromising the seal capacity of the interval. For the assumptions in this chapter, shear failure was the dominant mode of failure in the CCShC above SAGD oil sand reservoir. It is worth noting that, the recommendations of the study presented in this chapter are limited to caprocks with the index mechanical values assumed and every other case needs to be assessed individually.

In the shadow of the research scientific hypothesis basis, results of the evaluation demonstrated that, the degree of model fracturing was a strong factor in the caprock geomechanical response. These findings fulfill the research third objective as identified in Chapter 1. The geomechanical simulations conducted in this chapter provided a better understanding of the importance of modelling the CCShC as a discontinuum using a representative constitutive model. This chapter reflects the mandatory need to model the CCShC as it actually is in reality in order to better assess the anticipated deformations.

While the simulation results were not intended to match specific field case data, the geological range of cases (13 configurations as listed in Table 6-3) studied does indicate that it is essential to ensure a realistic structural geological characterization of the CCShC is completed during the caprock integrity assessment. Especial attention needs to be paid when a shallow reservoir SAGD project is anticipated, where changes in the MOP significantly affects the geomechanical response of a discontinuous caprock. This may potentially lead to jeopardizing the caprock essential seal integrity above a high pressure high temperature SAGD enlarging steam chamber.

CHAPTER 7 APPLICABILITY OF EQUIVALENT CONTINUUM MODELLING TO CLAY SHALES

7.1 INTRODUCTION

Rock is distinguished from other engineering materials by the presence of inherent discontinuities, such as fractures, joints, bedding planes and faults, that control its geomechanical behaviour (Sitharam, Sridevi, & Shimizu, 2001). Characterization of the strength and deformation of discontinuous rocks is needed for safe design of civil and mining engineering structures. Estimating strength and deformation of rock masses presents a challenge due to their complex structural geometry (Figure 7-1) and mechanical behaviour.

Figure 7-1 Clearwater clay shale (CCSh) – Alberta

Treating the rock mass with equivalent material properties for obtaining the overall response has been advocated in recent years (Sitharam et al., 2001). The equivalent continuum approach assumes that the macroscopic behaviour of a large scale rock mass can be described by

principles of continuum mechanics (Min & Jing, 2003; Gutierrez & Youn, 2015; and Chen, Wu, & Yang, 2018). Equivalent continuum modelling of hard rocks, such as sandstone, limestone (Khani, Baghbanan, & Hashemolhosseini, 2013), granite, basalt, and marble (WeiZhong et al., 2011) have been extensively studied and assessed. Two conditions must be satisfied for the equivalent continuum approach to be applicable for a fractured rock mass (Min & Jing, 2003) as follows:

* **Firstly**, a representative elementary volume (REV) must be quantified and estimated for a certain problem in order that a basis of statistical equivalence between the sampled rock mass and numerical models can be established. Averaging techniques can then be applied over that REV to derive the equivalent properties of homogeneity such as the equivalent strength and stiffness (modulus). The equivalent modulus for rock and discontinuities in a rock mass can be estimated as:

$$\frac{1}{E_{eq}} = \frac{1}{E_{matrix}} + \frac{1}{s.k_n} \tag{7-1}$$

where E_{eq} is the equivalent Young's modulus, E_{matrix} is the intact rock modulus, K_n is the normal stiffness and s is the discontinuity spacing per meter. Investigating the existence of an REV for fractured rock masses needs site specific characterization, especially regarding effects of discontinuity distribution, size, density and persistence (Min, 2002).

* **Secondly**, the derived equivalent properties must be able to fit in a tensor form to be used in the constitutive equations for continuum analysis (Min & Jing, 2003).

For harder or stiffer rocks, the linear elastic (CHILE) conventional assumption of pre-failure behaviour of the intact is quite satisfactory. It is worth recalling that, this dissertation scientific hypothesis was based on the need to acknowledge the fundamental differences between hard and soft rock masses. Soft rocks present great challenge in their classification under the conventional mechanical modelling systems. These systems were originally developed for continuous-homogeneous-isotropic-linear-elastic (CHILE) assumption and the fractured media based on a hard rock matrix. There are still practices applying CHILE based models to soft argillaceous rock masses, e.g. Abdi & Evgin (2013) mentioned that *"…constitutive models applicable to hard rock could be adapted to argillaceous rocks*!". When modelling the CCSh in engineering projects, it is reasonable and more representative to model it as a discontinuous-inhomogeneous-anisotropic-non-elastic (DIANE) not as CHILE material. The motivations behind

this chapter include another manifestation of the fundamental differences between rock type extremes sufficing the research first objective through examining conventional (hard rock) equivalent continuum procedures applicability to a soft rock mass, and in an align with the dissertation second objective.

Argillaceous Clearwater clay shale (CCSh) receives a great deal of design consideration as it is encountered in majority of civil and petroleum engineering projects in Alberta. While majority of design approaches usually adopt a continuum methodology, the focus of this chapter is to evaluate the applicability of this approach for CCSh material. To date, no attempts have been reported in literature to date for estimating the CCSh equivalent mechanical parameters, its representative elementary volume nor its equivalent compliance tensor.

This chapter procedure includes a systematic investigation of the scale effect (assessing the existence of an REV) and estimating the equivalent deformation modulus (DM), Poisson's ratio (v), and shear modulus (G) of a macroscale fractured CCSh. The work here also includes, studying the strength anisotropy of a fractured argillaceous "soft" rock and examining the possibility of the equivalent mechanical parameters to fit into a tensor form. Collectively these two lead to evaluating the equivalent continuum modeling applicability in CCShs. A schematic of the methodology to tackle these objectives is illustrated in Figure 7-2.

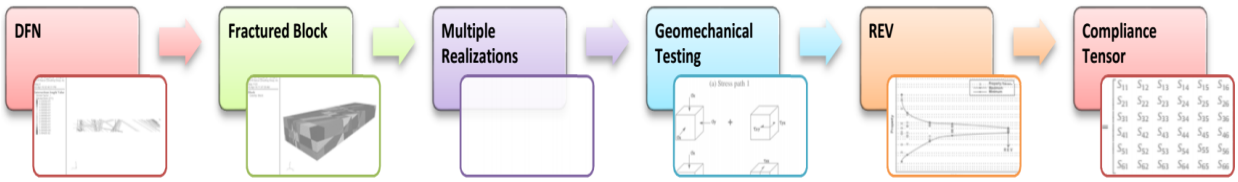

Figure 7-2 Workflow for REV and compliance tensor estimation

Numerical mechanical testing was carried out using distinct element modelling (DEM) where (strength and stiffness) anisotropy and scale effect (Figure 7-3) of a soft rock mass were investigated and compared versus the behaviour of marble, which served as a hard rock analogue whose geomechanical parameters were extracted from WeiZhong et al. (2011). The geomechanical parameters for the CCSh, which served as the soft rock analogue were derived from (Zadeh & Chalaturnyk, 2015). First, a procedure adopted from (WeiZhong et al., 2011) was utilized to examine the mechanical REV approach validity for a fractured soft CCSh. Second, a 3D numerical investigation comparing two rock type extremes was carried out in order to estimate equivalent continuum model mechanical parameters accordingly compliance tensor components.

7.2 DISTINCT ELEMENT MODELLING

With the rapid growth of computing capacity, numerical methods are becoming suitable to determine mechanical properties such as equivalent strength or deformability of fractured rock masses (Min & Jing, 2003). For example, distinct element modelling (DEM) has brought interesting insights to the characterization of failure mechanisms in geomaterials, and now it is usually used in the numerical modelling of discontinuous and heterogeneous rocks.

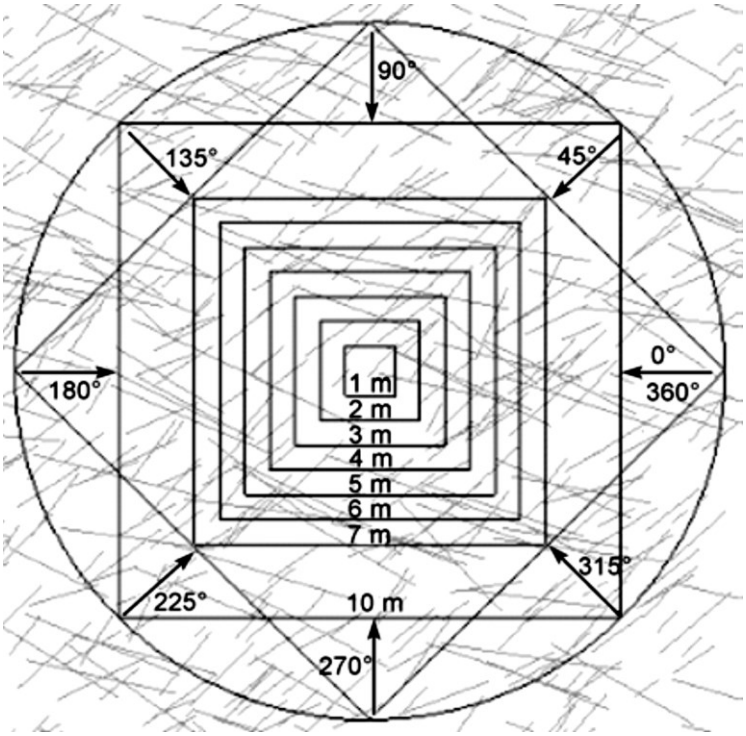

Figure 7-3 Schematic of study cases for assessing anisotropy and scale effect (WeiZhong et al., 2011)

In this chapter, validation of an equivalent continuum modelling approach for marble (as a hard rock extreme), was carried out using block models built in 3DEC and numerically tested following a workflow outlined by WeiZhong et al. (2011). The validation included confirming an acceptable match between the output and the input mechanical parameters values; i.e. the UCS, stiffness, Poisson's ratio (Table 7-9), the constitutive behaviour, the convergence in the equivalent mechanical parameters marble results, and the mechanical REV size. These will be discussed later in detail in each corresponding section in this chapter. After achieving satisfactory validation with respect to the methodology and the procedure portions, the scale effect and anisotropy investigations, for the hard rock extreme were approved and adopted for CCSh (as a soft rock extreme).

7.3 DISCRETE FRACTURE NETWORK

With the advantage of their discontinuous nature, discrete models can powerfully deal with the initiation and propagation of micro discontinuities inside heterogeneous media. Discrete models constitute effective means to study how the microstructure affects the macroscopic mechanical behaviour in geomaterials (Scholtès & Donzé, 2013). Hence, discrete fracture network (DFN) was used in this chapter to assess the validation of the REV concept in CCShs. Both stochastic and realistic DFNs (Table 7-1) were constructed and used in the numerical mechanical testing comparing fractured blocks of marble versus CCSh. Basically, from each generated fracture network, increasingly larger models were cut out from the domain center as illustrated in Figure 7-3.

Table 7-1 DFN cases investigated

Case study #	I	II
Type	Stochastic	Realistic
Source / based on	(WeiZhong et al., 2011)	Field data
Number of models	8	13
Number of joint sets	2	10
Number of DFN realizations	1	5

In DFN Case I, eight models ranged in size from 1 m × 1 m × 1 m to 10 m × 10 m × 10 m were tested. In DFN Case II, thirteen models ranged from 0.1 m × 0.1 m × 0.1 m to 9.4 m × 9.4 m × 9.4 m scale were tested. Five realistic DFN realizations were investigated in Case II (based on Chapter 5 findings). It is worth mentioning that, in comparing the two rock type extremes, the same scale, geometry, boundary conditions, and DFN were employed in each comparison. Table 7-2 includes the probability distribution of the two joint sets in Case I stochastic DFN as adopted from WeiZhong et al., 2011. The dip angle (in degrees) is measured in the negative *z*-direction from the global *xy*-plane, while the dip direction (in degrees) is measured in the global *xy*-plane clockwise from the positive *y*-axis.

In the comparison of the FISH language scripts in 3DEC, the keyword "*template"* was used for creating statistical parameters to generate the DFNs. These parameters, in DFN Case I, include the fracture size distribution, position distribution and orientation distribution (Table 7-2). The keyword "*orientation"* was used to define the generation rule for fracture orientations in the

stochastic DFN. The stochastic DFN built in 3DEC and the corresponding fractured block are illustrated in Figure 7-4.

Table 7-2 Probability distribution of two joint sets for stochastic DFN – Case I (WeiZhong et al., 2011)

Fracture set	Dip direction (°)		Dip (°)		Size (m)			Density
	mean	Standard deviation	min	Max	distribution	mean	Standard deviation	
1	160	10	10	25	Uniform	1.5	0.2	0.3
2	40	10	10	35	Uniform	0.6	0.2	0.6

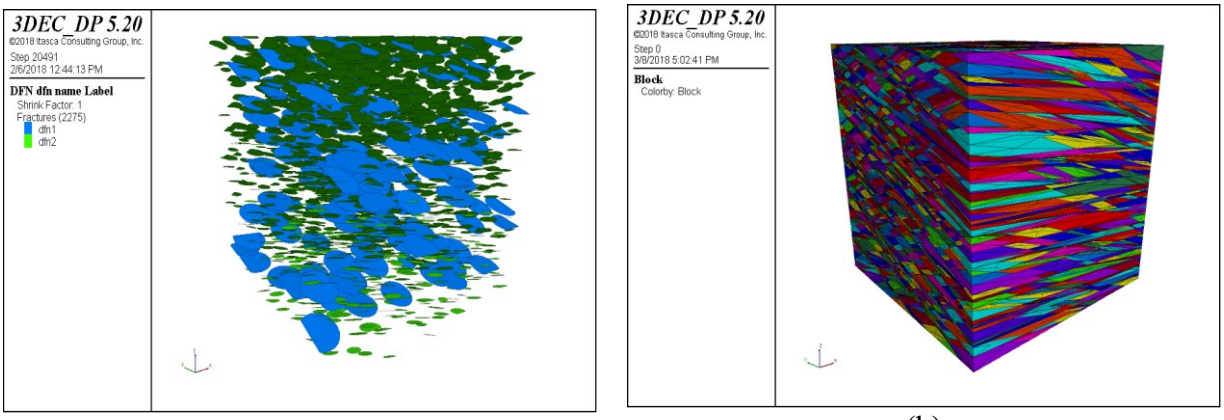

(a) (b)

Figure 7-4 (a) Stochastic DFN Case I having two joint sets and (b) fractured block

In order to illustrate the scale effect on the degree of fracturing of the rock models, the number of discontinuities corresponding to each block scale is plotted as seen in Figure 7-5. Please note the 1-m block size contains three discontinuities in the case of the stochastic DFN or Case I in Table 7-2. The realistic Case II DFN (Table 7-1) was extracted from geological mapping of an exposed CCSh mine bench in Alberta using LiDaR technique (Figure 7-6). The fractured model of the scanned mine bench was built in 3DEC as depicted in Figure 7-7 (Chapter 5 and Appendix A). Figure 7-8 includes five fractured block models realizations generated using the Case II DFN.

7.4 INDEX PARAMETERS

Two rock type extremes were investigated in this chapter; marble and CCSh. Marble is stable with a compact structure and pure mass (WeiZhong et al., 2011). The Baishan group marble

of middle Triassic series forms the main mountain range of Jinping mountain system in China. On the other hand, CCSh is a heavily over-consolidated, fully saturated "soft" rock that typically consists of a sequence of marine shales with occasional thin, argillaceous to silty sands. Undisturbed CCSh samples, from Fort McMurray, Alberta, were tested in the University of Alberta geomechanics laboratory. Due to difficulty to find references of index mechanical parameters of the discontinuities in CCSh needed for the DEM numerical simulations, three sets of values were assumed as listed in Table 7-3, Table 7-4 and Table 7-5 along with all.

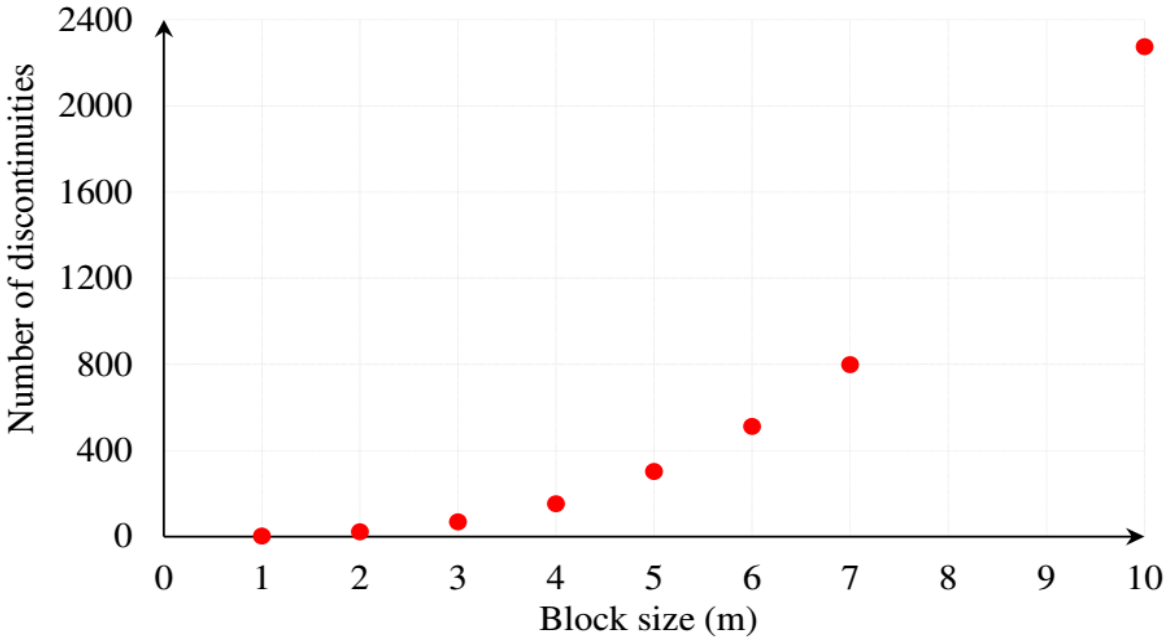

Figure 7-5 Number of discontinuities per block model size – (Case I)

7.5 CONSTITUTIVE MODELS

One of the challenges in describing a rock mass behaviour is assigning its elements appropriate constitutive models. With the progress in discrete element programs, this limitation may be minimized as the user is not required to prescribe a constitutive model for the whole rock mass. Alternatively, the micro-scale properties of the intact rock (model zones) and discontinuities are defined beforehand then the macro-scale response results based on those input properties and the geometry of the problem (Park, Martin, & Christiansson, 2004).

7.5.1 MODEL ZONES (INTACT)

Two cases of constitutive model assignments were investigated. To start simple and for verification purposes, Mohr-Coulomb (MC) constitutive model was tried, also the strain softening

(SS) constitutive model was studied as illustrated in Table 7-6. In their FEM analyses, (WeiZhong et al., 2011) used SS constitutive model to study marble. Similarly, (Pijaudier-Cabot & Bažant, 1987) and (Rahmati, 2016) stated that, CCSh as a SS material would continue to deform and soften once the strength has reached.

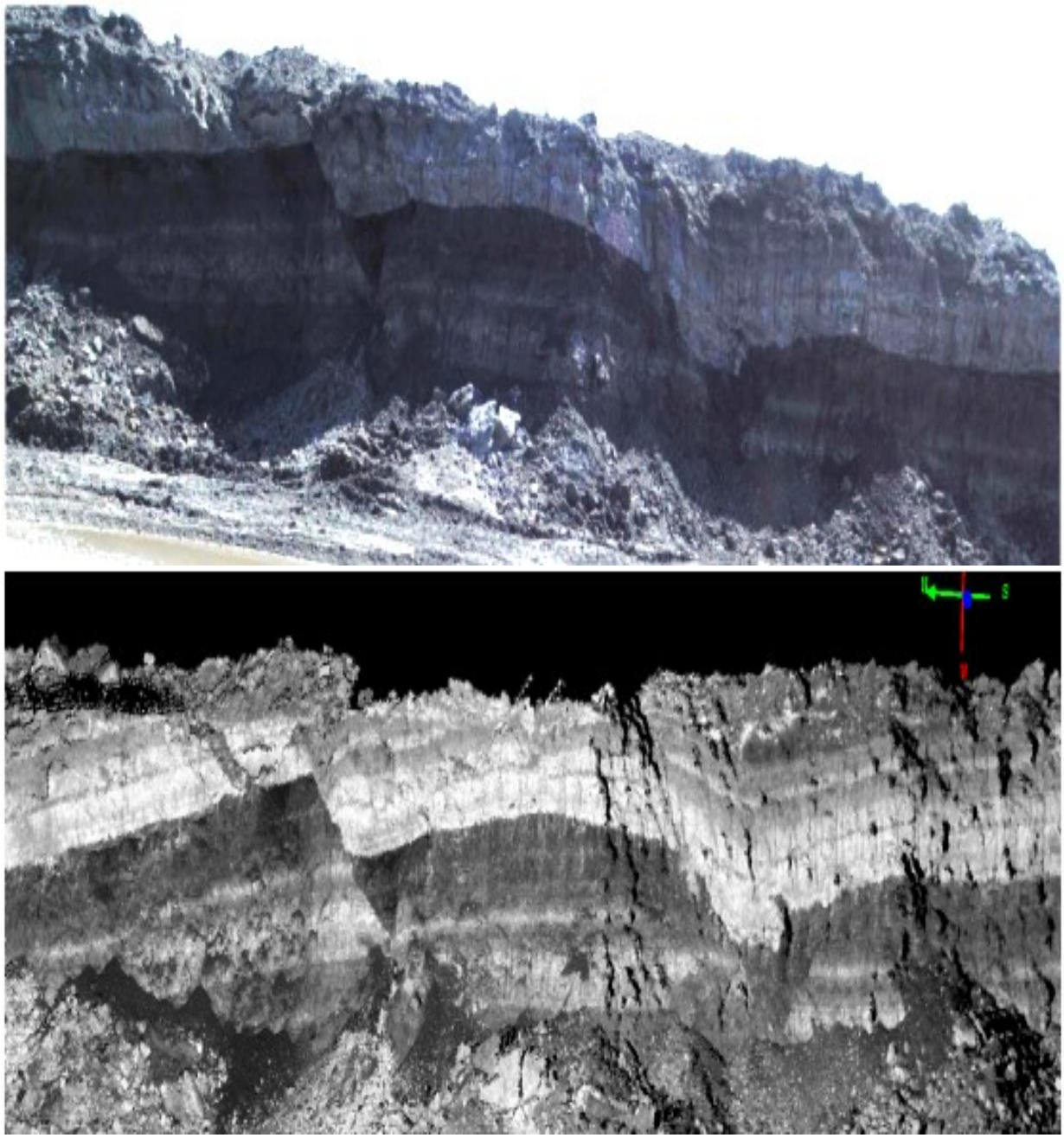

Figure 7-6 RGB image (top) and scan image of Clearwater clay shale (CCSh) in Alberta

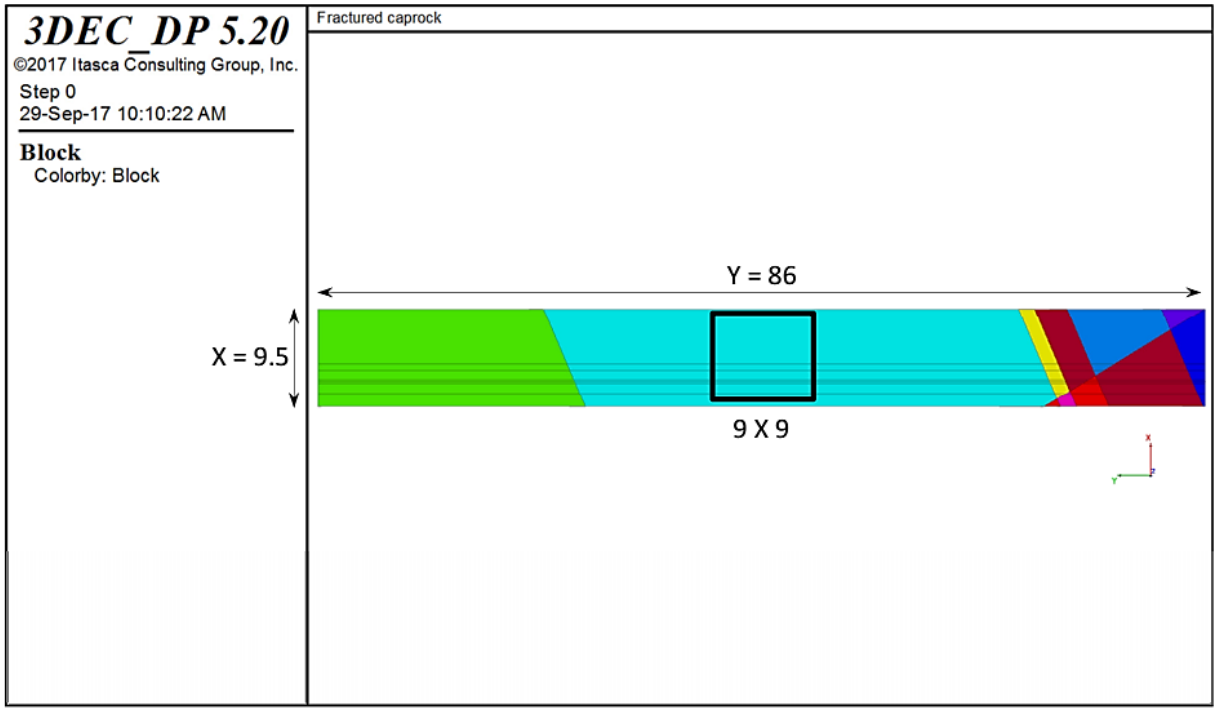

Figure 7-7 Fractured model of the mine bench scanned in situ

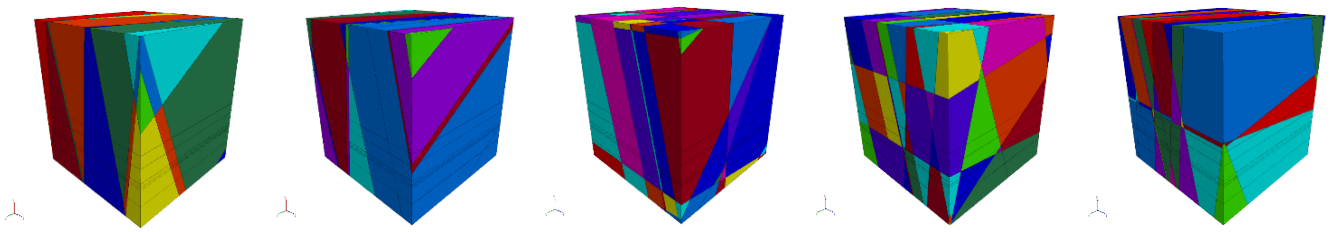

DFN # 1 DFN # 2 DFN # 3 DFN # 4 DFN # 5

Figure 7-8 Five realizations of DFN Case II

Plots in Figure 7-9 include results from geomechanical laboratory testing showing the behaviour of CCSh specimens as a SS material. As seen from these plots, the CCSh strength softens after the onset of plastic yield where residual geomechanical values are reached and maintained. The strain-softening constitutive model allows representing non-linear material softening behaviour, post peak, based on prescribed variations of the input geomechanical values as functions of the plastic strain (e^p). Consider a stress-strain relationship as the one depicted in Figure 7-10a, which softens upon yield and attains some residual strength. After yield, the total strain is composed of elastic and plastic parts per:

$$e = e^e + e^p \tag{7-2}$$

Table 7-3 Index parameters (based on laboratory testing results) of intact marble and intact Clearwater clay shale (CCSh) – discontinuities index mechanical parameters Case I

Property	Marble	Clearwater Clay Shale (CCSh)
Bulk density (kg/m^3)	2,580 (Małkowski, 2015)	2,129 (Zadeh & Chalaturnyk, 2015)
Shear modulus (MPa)	20,000	178 (J. Wu, Zambrano-Narvaez, & Chalaturnyk, 2015)
Bulk modulus (MPa)	33,000	833 (Wu et al., 2015)
Dilation angle (^{o})	40	20 (Wu et al., 2015)
Friction angle (^{o})	43.8 (WeiZhong et al., 2011)	30 (Zadeh & Chalaturnyk, 2015)
Residual friction angle (^{o})	30 (Kemthong, 2006)	9.8 (Bitcan 2001)
Cohesion (Pa)	19.44×10^6 (WeiZhong et al., 2011)	150×10^3 (Zadeh & Chalaturnyk, 2015)
Residual cohesion (Pa)	19×10^4 (Kemthong, 2006)	0 (Chalaturnyk, personal communication)
UCS (MPa)	105 (Chen W Z, et al., 2011)	0.15 – 0.53 (BigGuns, 2013)
K_n (Pa/m)	17×10^9 (WeiZhong et al., 2011)	17×10^5 (assumption)
K_s (Pa/m)	9×10^9 (WeiZhong et al., 2011)	9×10^5 (assumption)
Discontinuity cohesion (kPa)	0.07×10^6 (WeiZhong et al., 2011)	0.07×103 (assumption)
Discontinuity friction (^{o})	30 (WeiZhong et al., 2011)	20 (assumption)

Initial friction, cohesion, tensile strength and dilation (Table 7-4) input values before peak were defined in 3DEC. Similarly, four residual mechanical parameters (based on laboratory testing results) for marble and CCSh were defined as functions of e^p where each function consists of two linear segments as seen in Figure 7-10b. Examples of friction and cohesion are sketched for illustration in Figure 7-11 as specified for marble and clay shale. In the FISH language script defining the SS constitutive model, the friction angle function is determined in table 1, the cohesion in table 2, the dilation in table 3 and the tensile strength is described in table 4 (Appendix E).

Table 7-4 Geomechanical parameters of CCSh – Case II

Intact			Discontinuities		
Density	2129	(kg/m3)	Friction angle	3	(º)
Bulk modulus	0.833	(GPa)	Cohesion	0.015	(MPa)
Shear modulus	0.178	(GPs)	Jkn	83.3	(MPa/m)
Friction angle	30	(º)	Jks	17.8	(MPa/m)
Cohesion	0.15	(MPa)			
Tensile strength	4.34	(Pa)			
Dilation angle	20	(º)			
Residual parameters			Fictitious		
Friction angle	9.8	(º)	Friction angle	30	(º)
Cohesion	0	(MPa)	Cohesion	0.15	(MPa)
Dilation angle	0	(º)	Jkn	833	(MPa/m)
Tensile strength	0	(MPa)	Jks	178	(MPa/m)

Table 7-5 Mechanical parameters of discontinuities for CCSh – Case III

Discontinuities Parameter	K_n (GPa/m)	K_s (GPa/m)	Cohesion (MPa)	Friction angle (º)
CS	0.45	0.05	0.001	20

Table 7-6 Cases of constitutive models investigated

Case study #	I	II
Constitutive model	Mohr-Coulomb	Strain Softening
Abbreviation	(MC)	(SS)

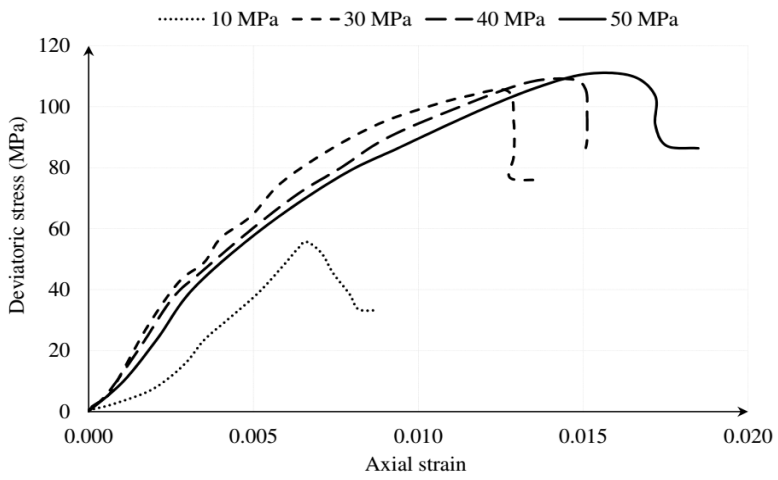

(a)

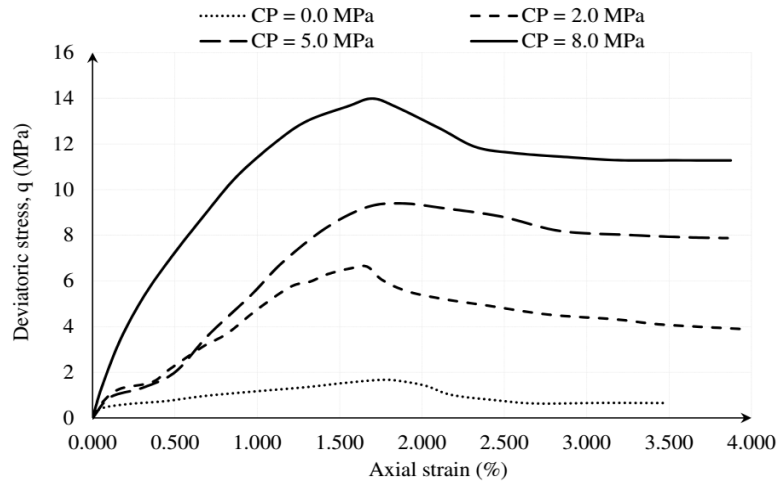

(b)

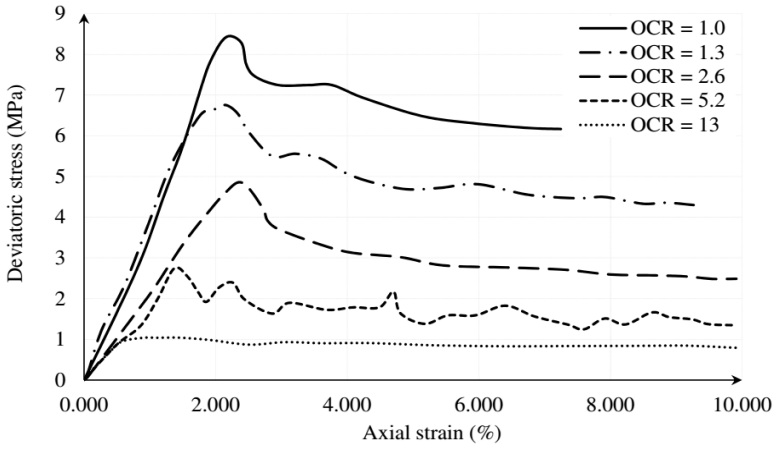

(c)

Figure 7-9 Stress-strain of (a) Tournemire shale (Niandou, Shao, Henry, & Fourmaintraux, 1997), (b) Christina Lake CCSh (Xu et al., 2013), and (c) Clearwater CCSh (Zadeh & Chalaturnyk, 2015)

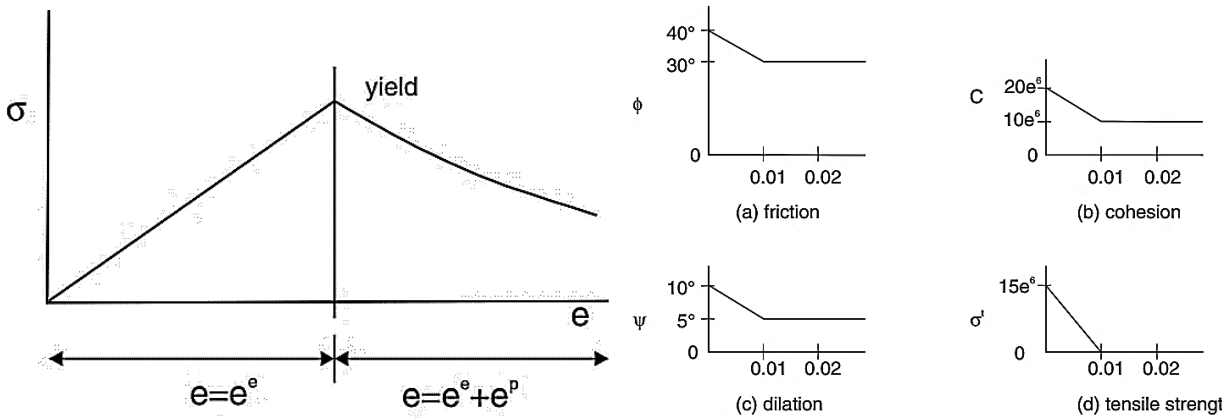

(a) (b)

Figure 7-10 (a) Strain softening relationship and (b) residual geomechanical parameters as functions of e^p (Itasca 2016)

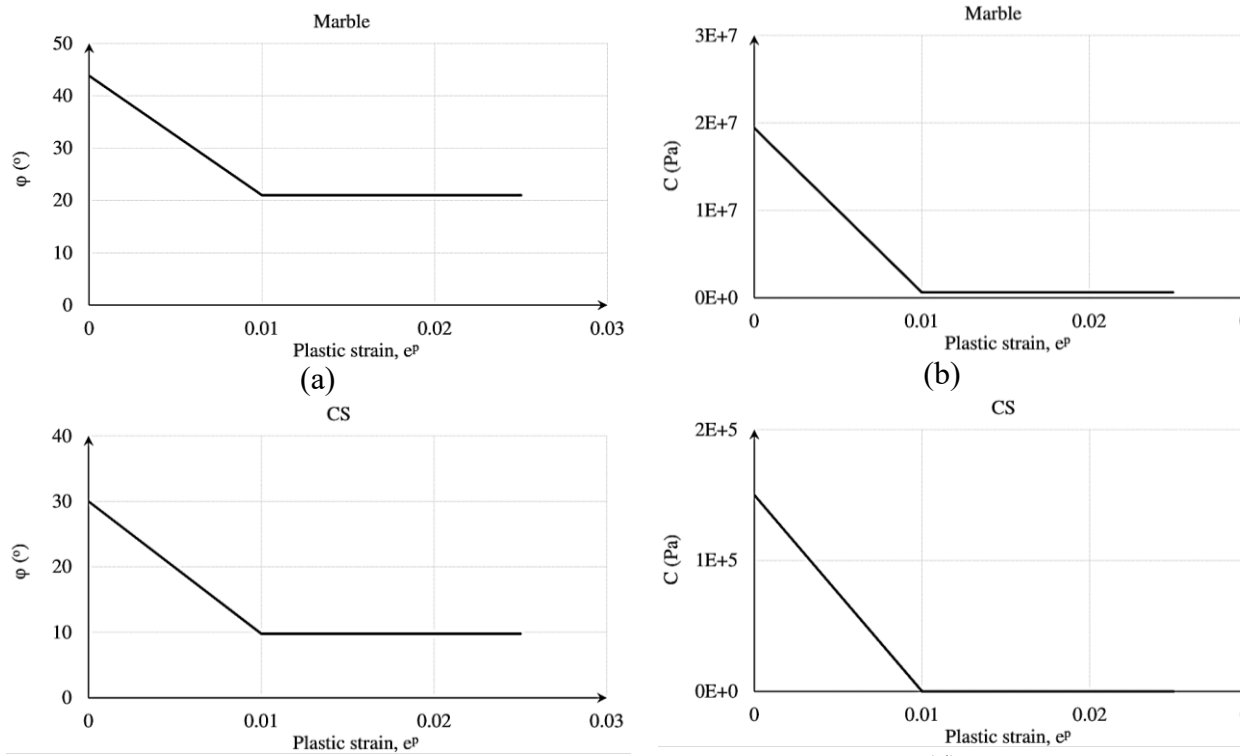

(a) (b)

(c) (d)

Figure 7-11 Friction and cohesion defined as functions of e^p for (a) and (b) marble and (c) and (d) CCSh

7.5.2 DISCONTINUITIES

The discontinuities constitutive model was assumed to be *jcons1,* where the failure in shear or tension results in the use of cohesion, tension and friction residual values (Itasca Consulting Group, Inc. 2016). Normal and shear stiffness, K_n and K_s, were modeled as illustrated in Figure

7-12. Figure 7-13 illustrates contours development of a discontinuity normal displacement magnitude at two stages during the runs and the applied velocity vectors on the 3D model.

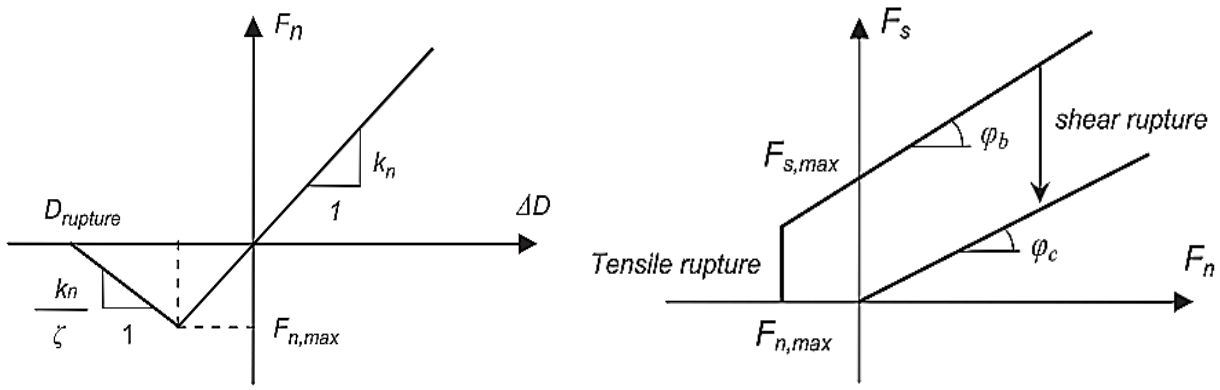

(a) (b)

Figure 7-12 (a) Normal interaction force (K_n) and (b) rupture criterion (K_s) (Scholtès & Donzé, 2013)

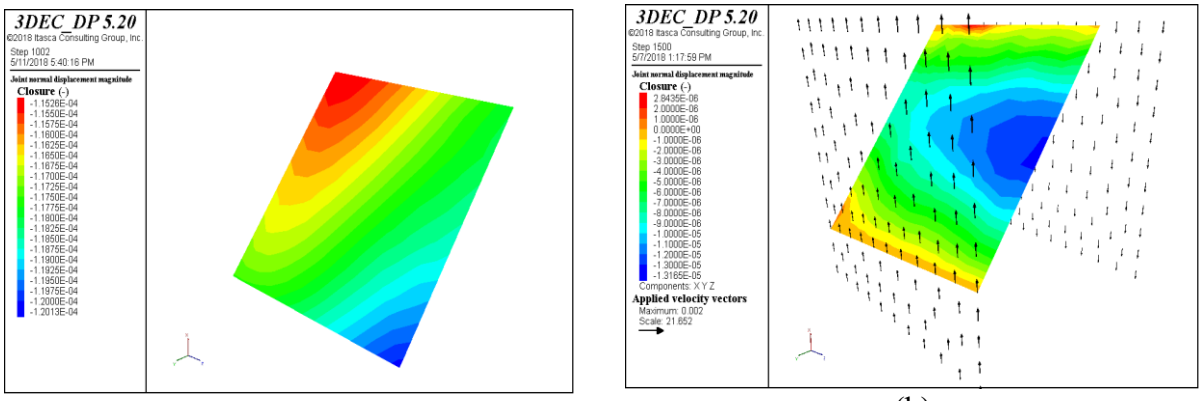

(a) (b)

Figure 7-13 Joint normal displacement magnitude; (a) earlier and (b) later with applied velocity vectors – DFN II – third relaization

7.6 EQUIVALENT CONTINUUM MODELLING

In their study, (Sitharam et al., 2001) recommended that it is necessary to replace a discontinuous rock mass with an equivalent continuum body for analysis with an appropriate associated constitutive model (Figure 7-14). The equivalent continuum model (Min & Jing, 2003) is usually used for the estimation of local and global deformability. The applicability of the equivalent continuum approach is conditioned firstly by examining the existence of an REV (Figure 7-15) and secondly, by estimating equivalent mechanical parameters and whether they could be represented in a tensor form (Min & Jing, 2003).

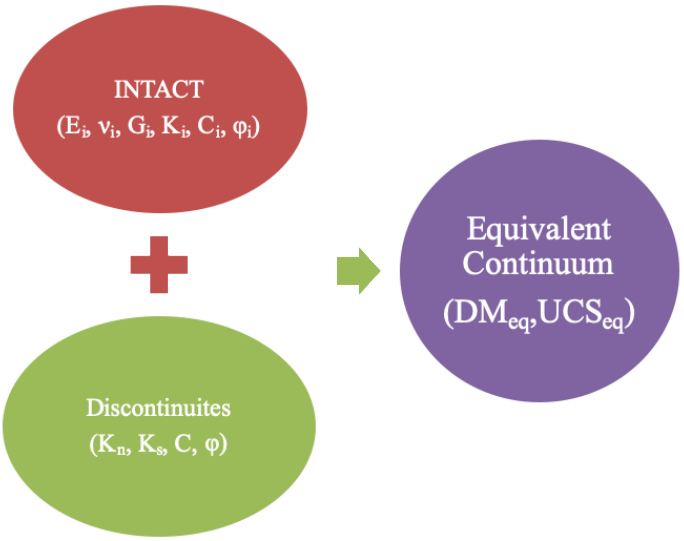

Figure 7-14 Equivalent mechanical parameters of a rock mass

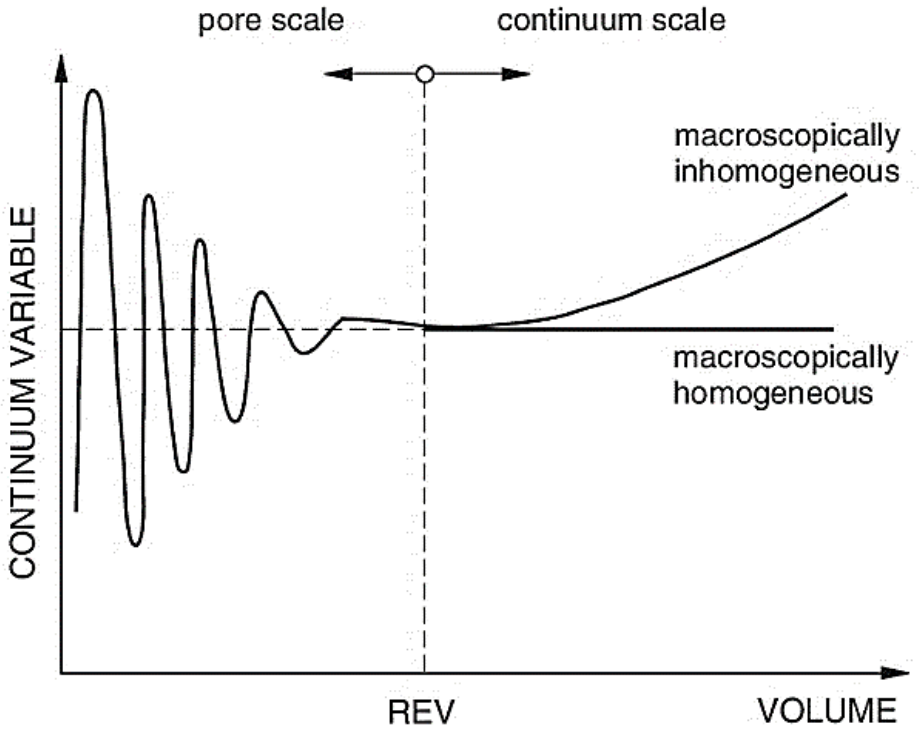

Figure 7-15 Representative elementary volume in homegeneous versus inhomogeneous media (White, Borja, & Fredrich, 2006)

7.7 IMPLEMENTING 3DEC

3DEC is a three-dimensional geomechanical modelling code provided by Itasca Consulting Group for advanced geotechnical analysis of soil, rock, ground water, structural support, and masonry. 3DEC can simulate the response of discontinuous media (such as discontinuous rock

(Figure 7-16a) or masonry bricks) subject to either static or dynamic loading. The discontinuous structure can be built into the model directly from geologic mapping data. The discontinuities are treated as boundaries between blocks where large displacements and rotations of the blocks are allowed.

The discontinuous media is represented as an assemblage of discrete blocks. Individual blocks may be set to behave as rigid or deformable (i.e., meshed into finite difference zones) material (Figure 7-16b). In 3DEC, discontinuous materials are represented by polyhedral elements within a three-dimensional grid. Each element behaves according to a prescribed constitutive model and failure criterion in response to applied forces and boundary restraints.

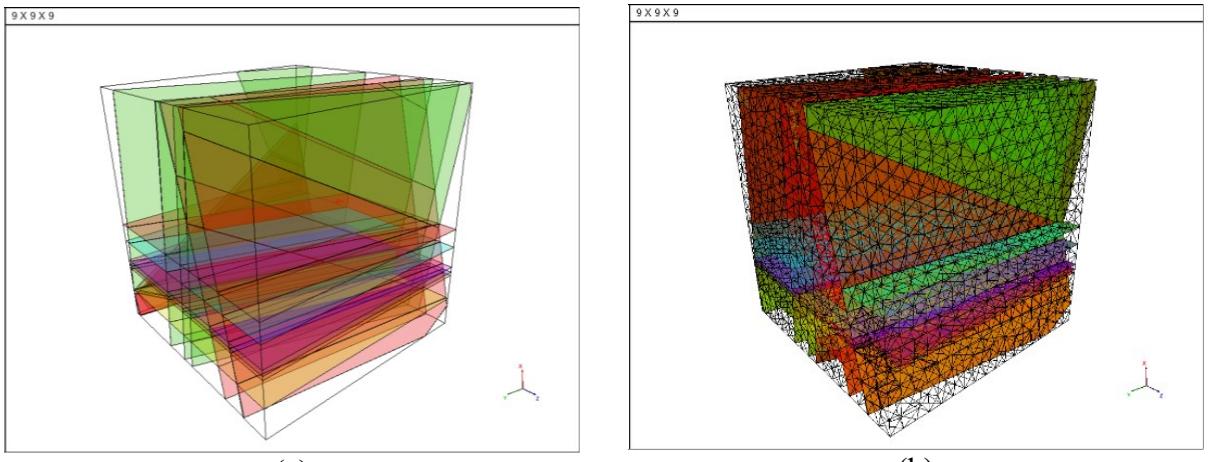

(a) (b)

Figure 7-16 9-m^3 fractured block based on realistic DFN; (a) discontinuities planes; joint sets and bedding planes and (b) meshed model

7.8 BOUNDARY CONDITIONS

The 3D numerical testing mechanics was composed of three stages; 1) the first stage was a validation step, where numerical mechanical experiments were carried out on intact blocks of the two rock types by loading them until failure. This step was meant to validate the FISH script in producing a geomechanical behaviour that is reasonably matching what is proved and confirmed in literature and reported from laboratory testing. In this step, parts of the FISH script was adjusted several times by trial and error. The output mechanical parameters values were validated against the input index parameters values as listed in Table 7-9 and Figure 7-21; 2) the second stage involved numerical mechanical experiments per the procedure presented in (WeiZhong et al., 2011) to study the scale effect and strength anisotropy (Figure 7-3) for the two rock types under

investigation; and 3) the third stage included assigning boundary conditions similar to those presented in (Kulatilake, Wang, & Stephansson, 1993) and seen in Figure 7-17 on the discontinuum blocks to examine and assess the REV size of the two rock types.

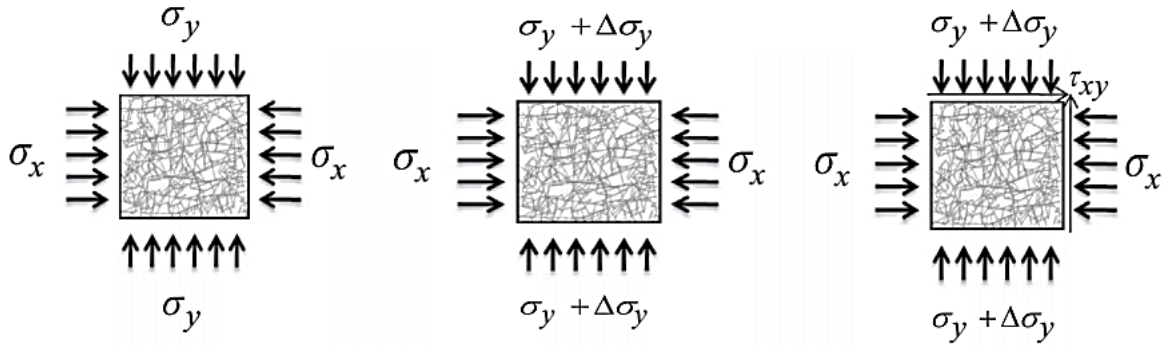

Figure 7-17 Loading and boundary conditions (Q. Wu & Kulatilake, 2012)

7.8.1 INITIAL EQUILIBRIUM

Before conducting numerical testing, initial equilibrium was first accomplished in each model. Every model was primarily set under in situ stresses and was set to run until initial equilibrium is achieved. Based on literature, in situ stresses were assumed to be: $\sigma_v = 21.31$ kPa/m, $\sigma_h = 18.00$ kPa/m, and $\sigma_H = 23.75$ kPa/m as listed in Table 7-7.

7.8.2 UNIAXIAL COMPRESSION LOADING

In order to estimate the equivalent uniaxial compressive strength (UCS), deformation modulus (DM), Poisson's ratio (ν) considering the scale effect, 3D models with various scales of the two rock mass types were tested under uniaxial compression (UC) (Figure 7-19). To evaluate the strength anisotropy in each rock type, the models were tested at different directions. Two cases of DFN orientations were investigated as stated in Table 7-8. In Case I, numerical compression tests were performed on 3D fractured rock masses along three orthogonal directions; X, Y and Z. The strength anisotropy was studied in Case II by rotating the DFN of every block size of the two rock types at FOUR orientations; 0, 45, 90, and 135^o as seen in Figure 7-3.

7.8.3 SHEAR LOADING

To assess the scale effect and strength anisotropy in estimating the equivalent shear modulus (G_{equiv}), XY, XZ, and YZ shear loadings as illustrated in Figure 7-18 (a)-(c) were applied at each two perpendicular directions on every block size (Figure 7-3).

Table 7-7 In situ stresses

Vertical Stress (kPa/m)	Minimum Horizontal Stress (kPa/m)	Maximum Horizontal Stress (kPa/m)	Reference
22.3	-	-	(Ansari et al., 2012)
21	20.57	-	(Yuan, Xu, & Palmgren, 2013)
20	-	-	(Collins & Walters, 2013)
21	19.6 - 20.63 or 15	-	(Prost & Newsome, 2016)
22.3	18.4	22	(Chin, Tomberlin, Ramos, & Chalturnyk, 2012)
21 – 22 (21)	15 – 18 (16)	-	(Saeedi & Settari, 2016)
20.8	21.2	-	(Khan et al., 2011)
23.11	13.76 – 14.49	-	(Mishra, Lywood, Ayan, & Schlumberger, 2011)
-	14.3 – 15.6	18.5 - 25.5	(Zadeh, 2016)
21.4	16 – 20	-	(Xu et al., 2013)
20.1 – 21.5	24	29	(CN, 2014)
21.2	15.29	-	(Big Guns, 2013)

Table 7-8 Investigation cases of comporession testing along different DFN orientations

Case study #	I	II
Loading along	X, Y, and Z	0^o, 45^o, 90^o, 135^o
Source	(Kulatilake et al., 1993)	(WeiZhong et al., 2011)
Layout	Figure 7-17	Figure 7-3

7.9 FISH SCRIPT VERIFICATION

FISH-Lab developed by Itasca was used to build and configure the discontinuity systems and the rock mass blocks. First stage in the numerical modelling was verifying the mechanics of the composed FISH script versus WeiZhong et al. (2011) findings by trial and error adjustments of the time step and/or loading rates. The verification included; the constitutive behaviour of the marble, UCS, E, ν, the convergence in the equivalent mechanical parameters, and the corresponding REV size. These will be mentioned and discussed in detail following corresponding sections. Second, to verify the syntax and confirm the logic meant of the composed FISH scripts, two identical intact block models of 1 m × 1 m × 1 m size from each rock type were simply tested

under UC at three orthogonal directions; X, Y, and Z as presented in Figure 7-19a-c. Input parameters based on laboratory geomechanical testing for the intact' modulus of elasticity (E_i) and the uniaxial compressive strength (UCS_i) were input in the codes per Table 7-4.

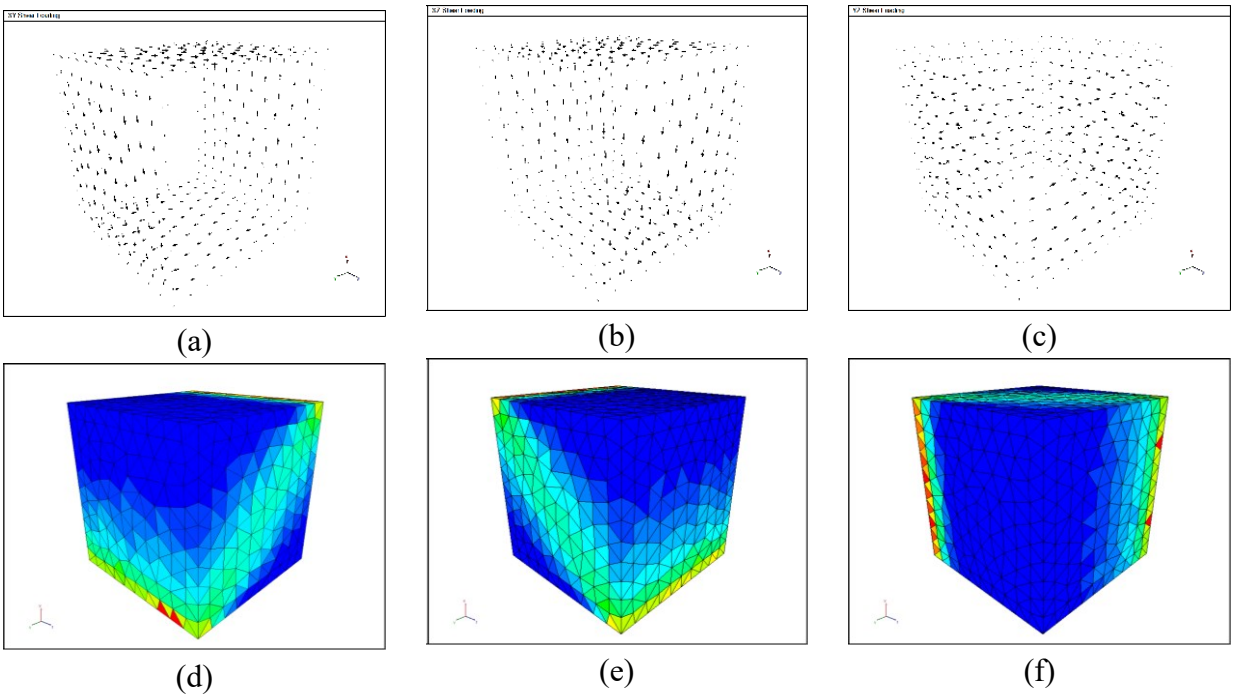

Figure 7-18 Boundary conditions; (a) XY, (b) XZ, and (c) YZ shear loadings – Resulted (d) XY, (e) XZ, and (f) YZ shear stress distribution – Case II

The UCS loadings were run along X, Y and Z in small and large strain simulation settings. The resulted stress-strain relationships were plotted for each model, and the UCS, DM, and ν (an example procedure is in Figure 7-20) were calculated and verified versus the input values as illustrated in Figure 7-21 and Table F-1 in Appendix F. Table 7-9 includes the results of the FISH scripts second verification step. Figure 7-22 contains a comparison between the stress-strain relationships of intact blocks of marble and CCSh. It clearly shows the non-linearity of the CCSh behaviour even at intact model scale.

7.10 STRESS-STRAIN RELATIONSHIP

Comparison between the input and output mechanical parameters, for blocks of 1 m^3 size (intact – no discontinuity) between the two rock type extremes, is illustrated in Table 7-9. Figure 7-21 illustrates the data fitting between laboratory mechanical parameters results (input) and the output of the DEM modeling where a good match was achieved after multiple trials. Accordingly

the 3DEC FISH scripts were approved for further and more complex modeling including discontinuities addition.

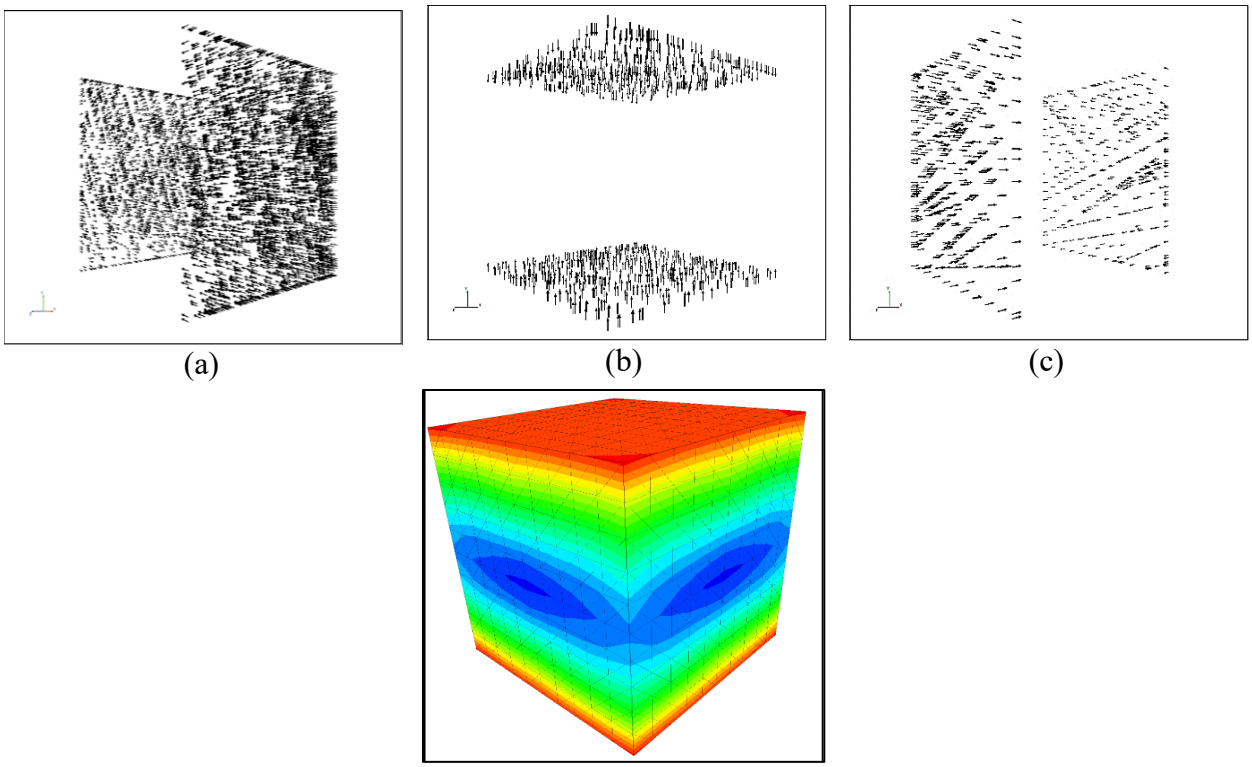

(a) (b) (c) (d)

Figure 7-19 UC loading along (a) X, (b) Y, (c) Z and (d) resulted velocity distribution – Case I

Table 7-9 Verifying input versus output values resulted from UCS loadings on 1 m^3 intact blocks of marble and CCSh

Rock type		Marble				CCSh			
Parameter		UCS (MPa)		E (GPa)		UCS (MPa)		E (GPa)	
		Large strain	Small strain	Large strain	Small strain	Large strain	Small strain	Large strain	Small strain
Input value		100		50		0.5 – 1.0		0.5	
Output	Along X	91.64	91.55	50	50	0.59	0.59	0.4	0.4
	Along Y	91.64	91.55	50	50	0.59	0.59	0.4	0.4
	Along Z	91.64	91.54	50	50	0.59	0.59	0.4	0.4

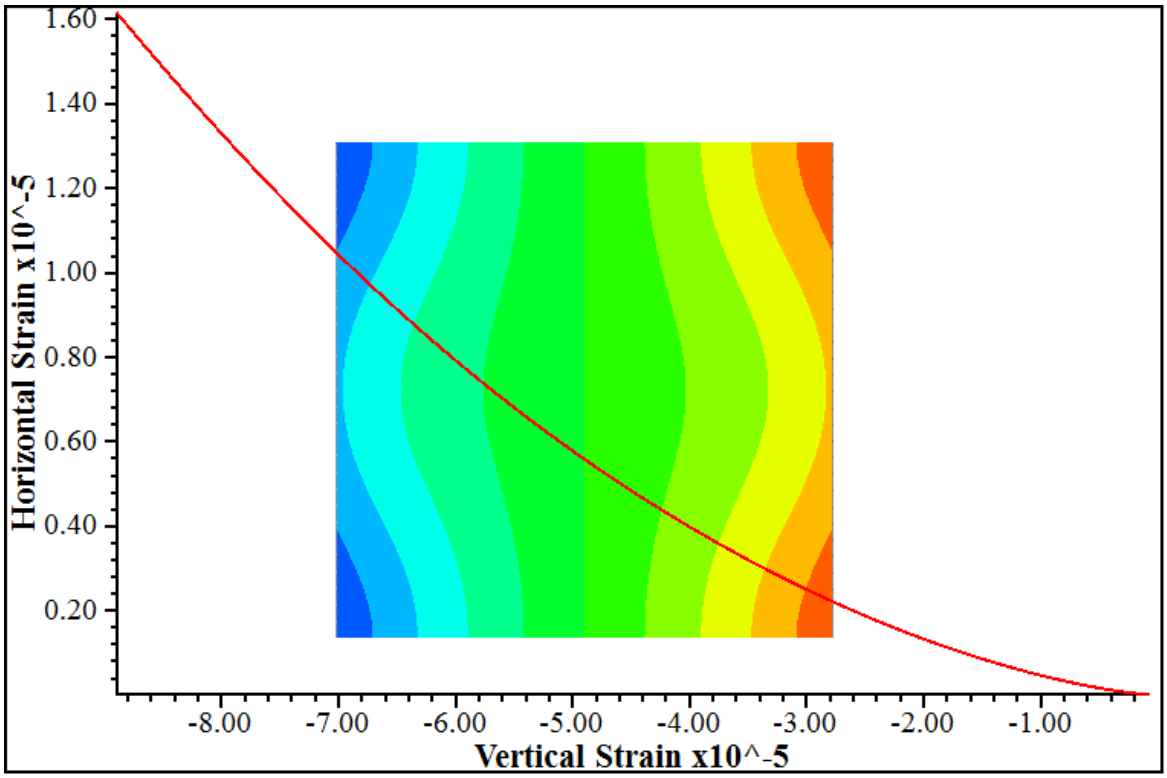

Figure 7-20 Contours of a marble 3D block tested under UC and strains plot for Poisson's ratio calculations

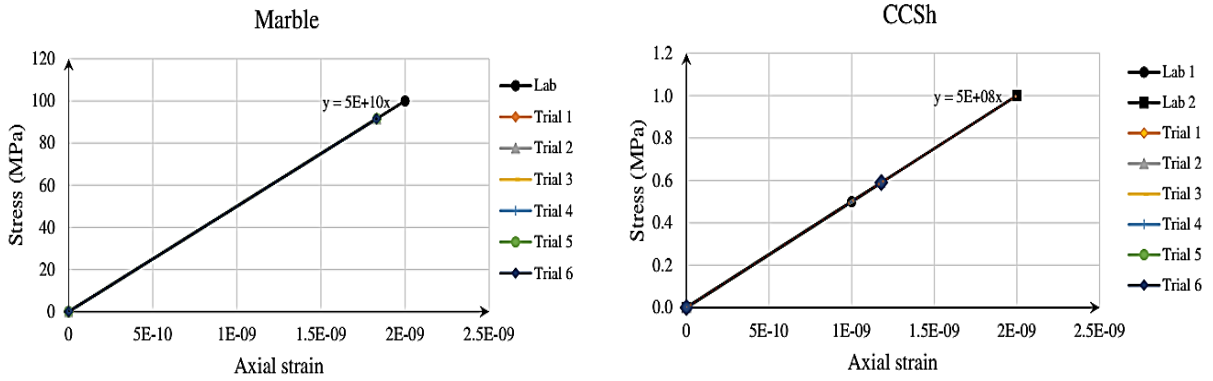

(a) (b)

Figure 7-21 Fitting laboratory mechanical results of (a) marble and (b) CCSh

In Figure 7-22 it is noticed that, the pre-peak portion of the stress-strain relationship for CCSh shows distinct nonlinearity as well as ductility post-peak compared to the marble stress-strain relationship. This supports and confirms an important fundamental distinction in the constitutive behaviour of the two rock types. Figure 7-23 includes the smallest block (intact) model of 1 × 1 × 1 m^3 size and the largest (Case II) 9.4 × 9.4 × 9.4 m^3 fractured model that will be

considered for the analyses in the following sections. Similarly Figure 7-24 illustrates nonlinearity in the CCSh stress-strain compared to marble.

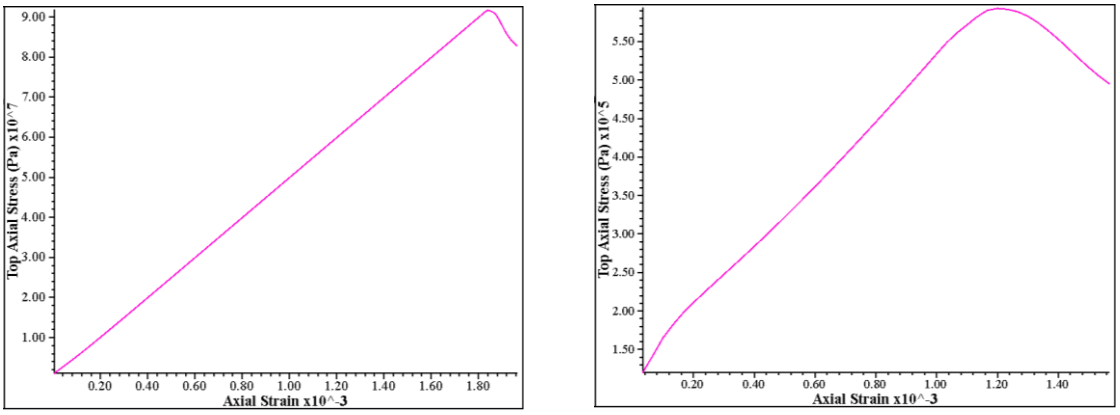

(a) (b)

Figure 7-22 Stress strain relationships of (a) marble and (b) CCSh

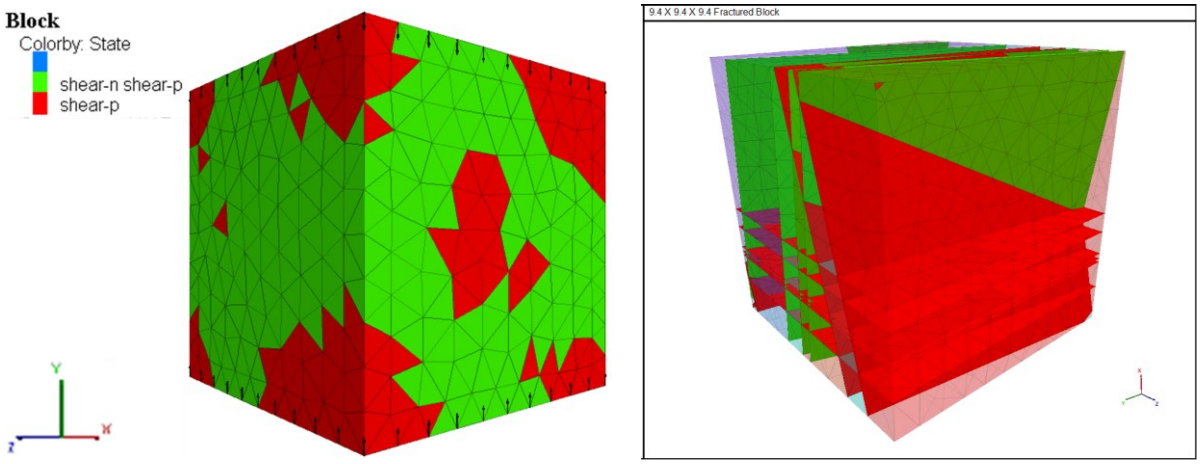

(a) (b)

Figure 7-23 (a) State of failure of 1 × 1 × 1 m^3 intact marble block under UCS along Y direction and (b) fractured block model of 9.4 m^3 size – Case II

7.11 DEFORMABILITY

In the DEM modelling, the blocks representing the intact/matrix (rock bridges) can be set to be rigid or deformable. In the latter setting, the blocks are being zoned into tetrahedral and/or hexahedral to form deformable blocks. Deformable blocks is mainly about implementing shear and tensile strength reduction techniques which can be achieved by introducing higher order strain fields or by subdividing each block into a set of simply deformable sub-blocks (Lisjak & Grasselli, 2014). The automatic zone generator in 3DEC allows the user to divide the deformable blocks into finite difference tetrahedral zones. *GENERATE* command can be used to specify as fine a

discretization as needed, and to vary the discretization throughout the model. A quick and simple fundamental comparison of the mechanical behaviour between rigid and deformable block models is given in Figure 7-25.

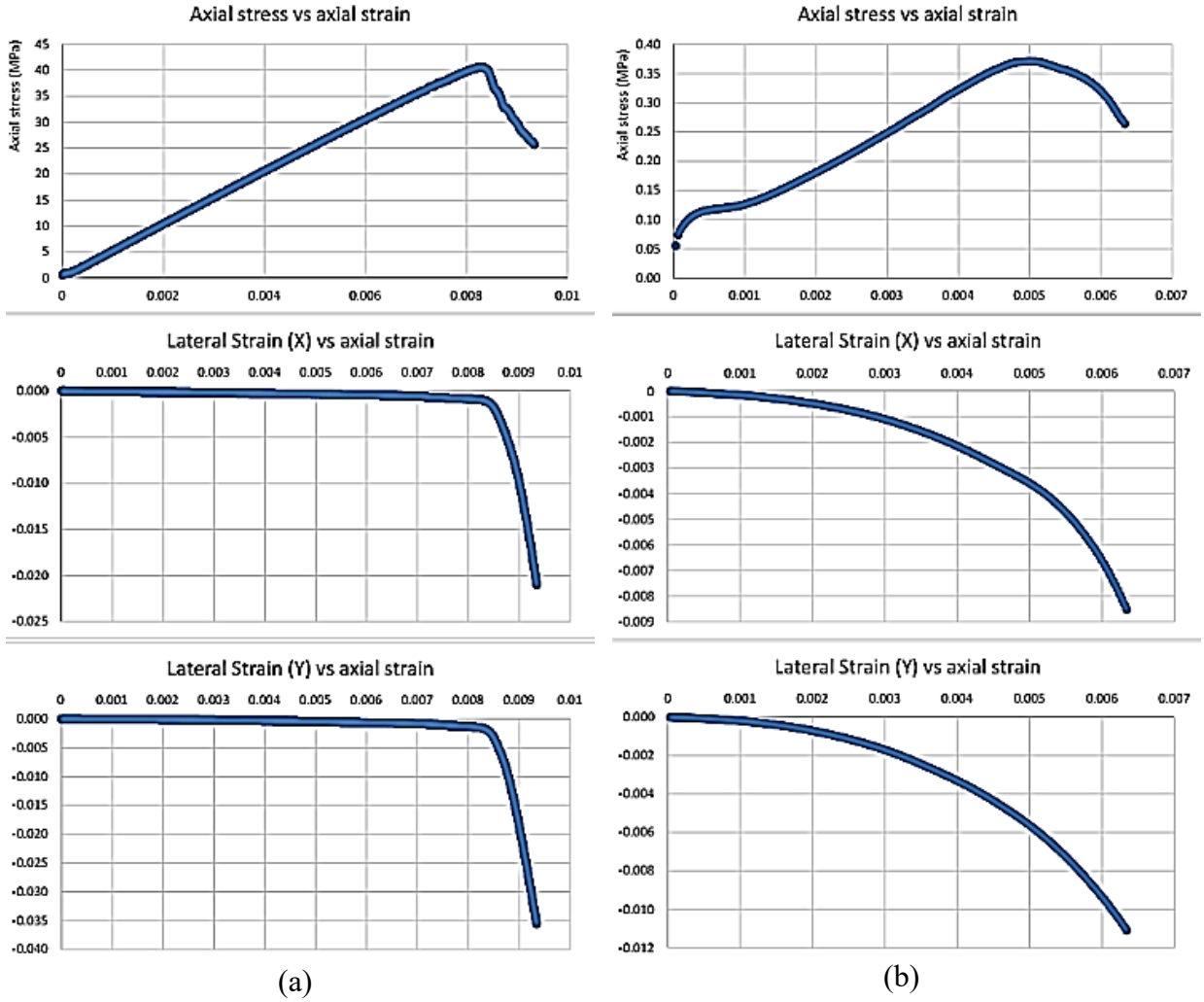

(a) (b)

Figure 7-24 Comparison between marble and CCSh – 1-m^3 blocks uniaxially loaded along Z

It can be clearly observed that deformable models are more realistic in representing a typical geotechnical material. In this chapter, deformable blocks will be used to simulate the CCSh since they can realistically represent the energy-storing behaviour characteristic for the soft rock.

7.11.1 STRAIN AT FAILURE

Under same loading conditions, the strain at which the CCSh fails was found to be much larger than that in case of marble as listed in Table 7-10. The CCSh suffers a lot of deformability as it reaches its peak strength and till failure.

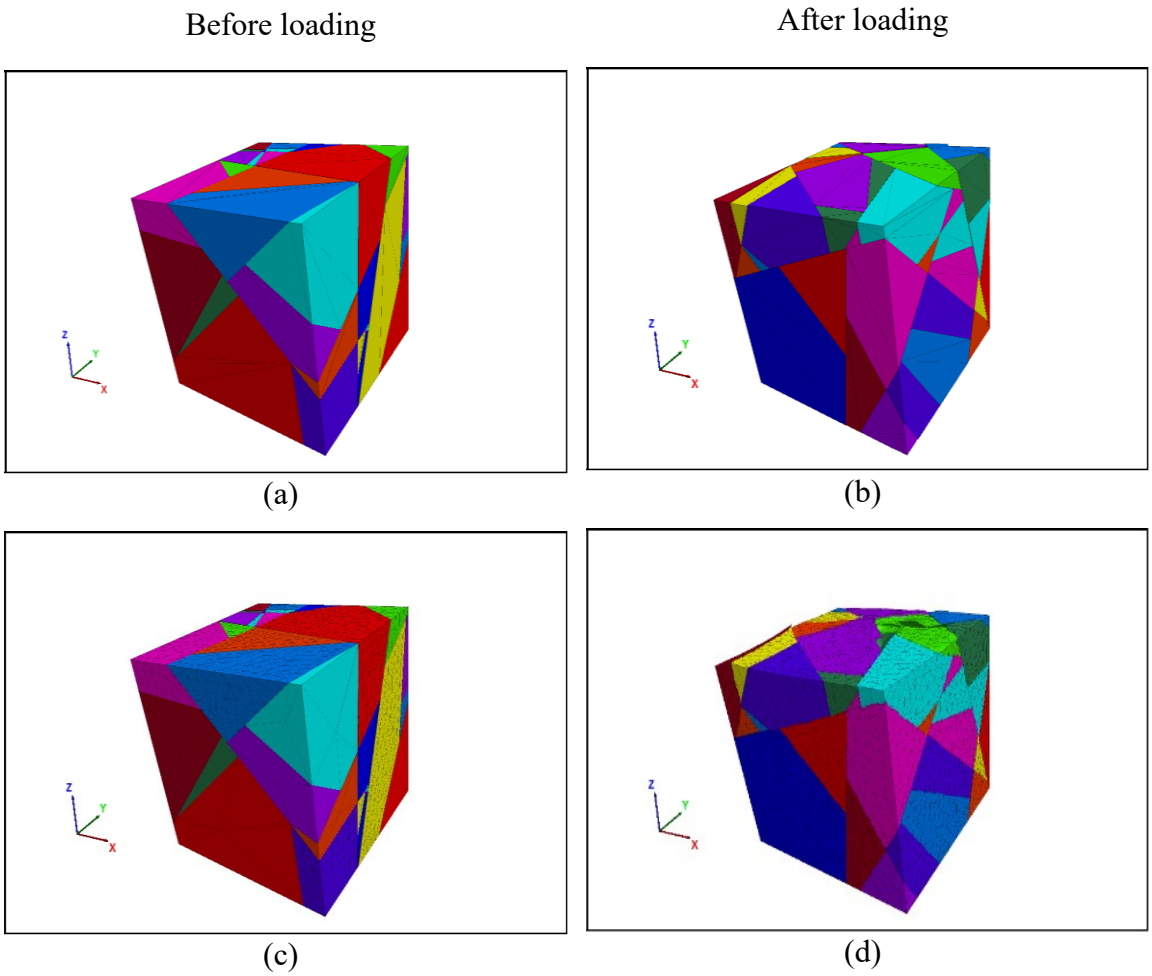

Figure 7-25 Comparison between (a) and (b) rigid- versus (c) and (d) deformable-blocks

7.12 SCALE EFFECT

Mechanical parameters obtained from laboratory tests are not adequate for representing the behaviour of a field scale rock mass due to issues associated with scale effect (Figure 7-26). To tackle this issue, the equivalent continuum approach has been proposed by researchers such as in (Ivars, Min, & Jing, 2001) and it is usually used in design when dealing with rock masses at macroscale. To assess and evaluate the scale effect on the mechanical properties of marble and CCSh rock masses, two sets of modelling series were investigated as listed in Table 7-11. In Case # I, eight discontinuum blocks with side size ranging from 1 m to 10 m were numerically tested under compression similar to the procedure introduced in WeiZhong et al. (2011). In Case # II, thirteen blocks with a side size varying from 0.1 m to 9.4 m were investigated. Figure 7-27 includes 2D view of fractured models from Case # II investigation.

Table 7-10 Comparison between marble versus CCSh of strain at peak compressive stress

Rock type	Marble	CS
Input UCS_i (MPa)	81.6	6.5
Input E_i (GPa)	50	0.5
Strain at peak stress	0.00165	0.013

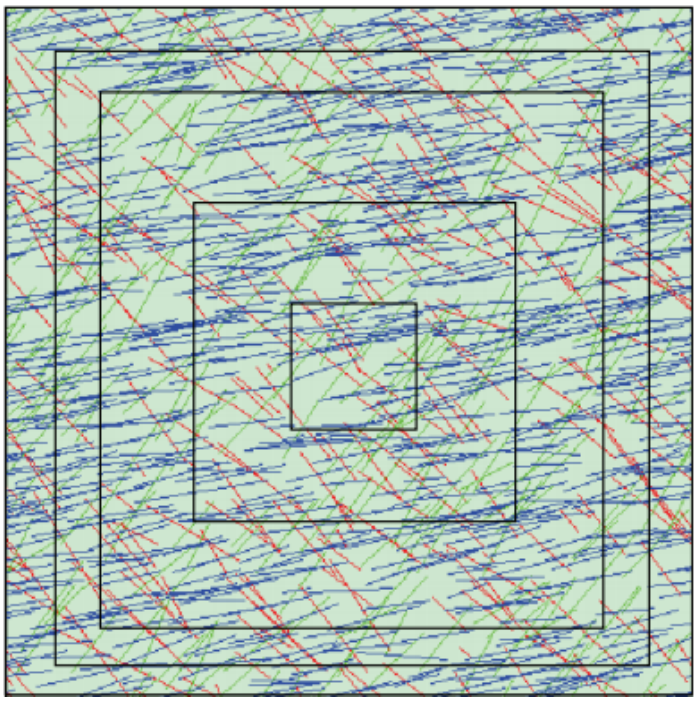

Figure 7-26 Scale effect

Table 7-11 Scale effect investigation cases

Case study #	I	II
Smallest size (m)	1	0.1
Largest size (m)	10	9.4
Step wise (m)	1 and varying	1 and varying
Total number	8	13

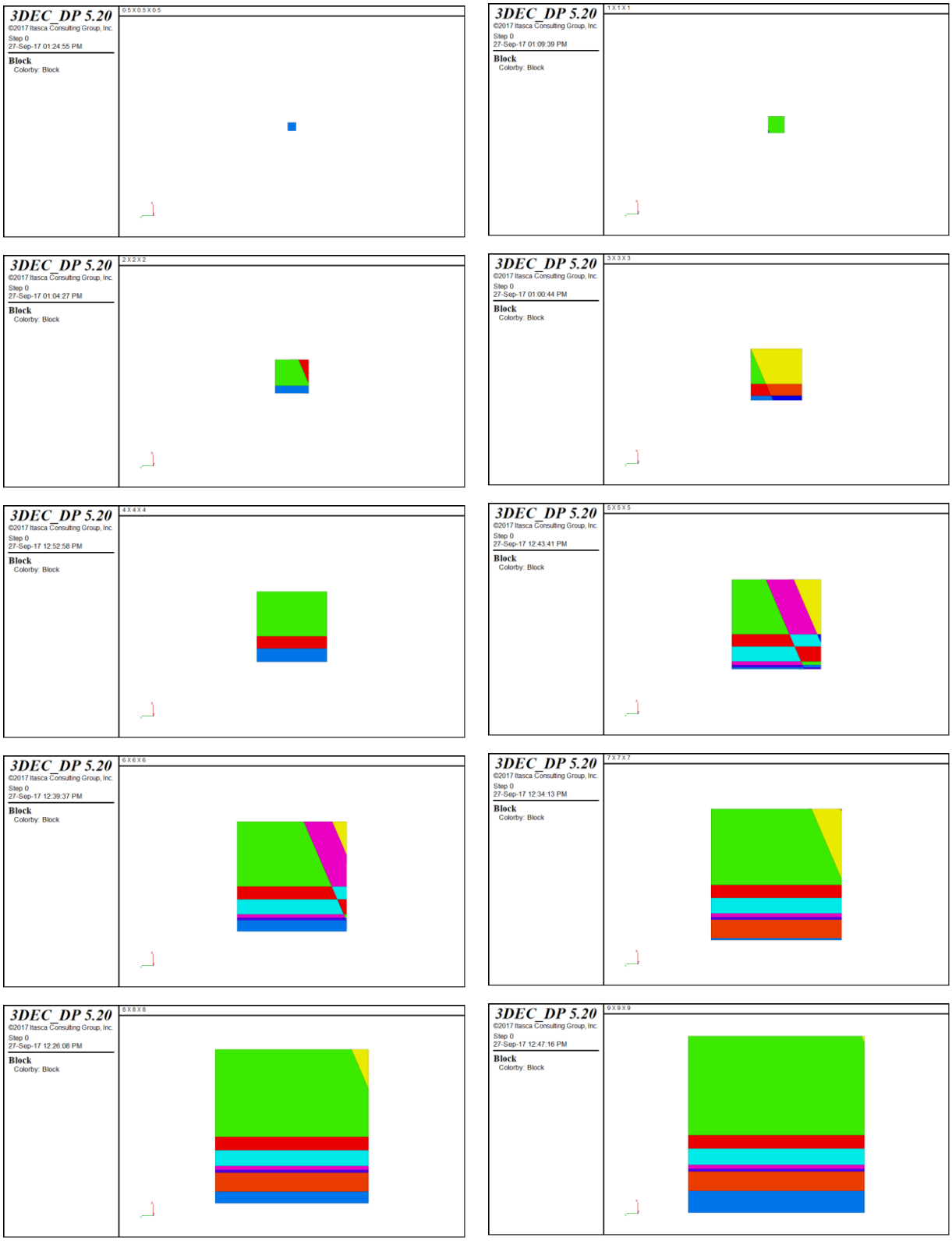

Figure 7-27 Block models of sizes ranging from $0.5 \times 0.5 \times 0.5$ m^3 to $9 \times 9 \times 9$ m^3 Case # II – 2D view

Analyzing the compression loading results (till peak) shown in Figure 7-28, it was found that generally as the model size increases the strength and stiffness decrease in both rock types. This is matching what is expected due to the scale effect; as the model scale increases more discontinuities are encountered reducing the rock mass' strength and stiffness regardless the rock type. It is however clear how the axial stress magnitudes (Y-axis) between the two rock type extremes significantly differ by almost two orders of magnitude difference. It is worth noting that, nonlinearity in the stress strain relationships at small (≈ intact) model scale is recognized in case of CCSh. Implying that the intact CCSh (soft rock) as a DIANE material poses intrinsic nonlinearity unlike hard rock (marble) as a CHILE material. Moreover, as the model size increases and more discontinuities are introduced, nonlinearity in the pre-peak portions of the stress strain relationships start to result but is significantly recognizable in CCSh model cases.

7.12.1 REPRESENTATIVE ELEMENTARY VOLUME (REV)

A REV is the minimum volume (Figure 7-15) at which the size of the tested sample contains sufficient number of inhomogeneities for an ‘‘average mechanical value" to be reasonably consistent as the volume increases. Presence of a REV can help in determining whether a rock mass may appropriately be treated with the equivalent continuum concept or not. In this section, two sets of block models configurations (Table 7-11) were examined to study the scale effect and the presence of a mechanical REV for the CCSh. First, models with the same geometry, dimension and scale were tested under same degree of fracturing and loading conditions, to compare the REV of marble versus CCSh and for verification purposes against WeiZhong et al. (2011) published findings.

In case of marble, the numerical mechanical testing results showed that the fractured rock mass strength decreases rapidly from intact rock and tend towards stability at the REV similar as what has been reported in (WeiZhong et al., 2011). Figure 7-29 includes a comparison of the scale effect on the uniaxial compressive strength between marble versus CCSh. The UCS values of the two rock types vary by at least two orders of magnitude. In case of marble the values eventually settle (convergence) unlike in case of CCSh. Another set of UCS results for the CCSh at three orthogonal directions is given in Figure 7-30. Similarly, the UCS values of the CCSh don't converge as the block size increases. Following conventional procedure to estimate equivalent UCS, an equivalent UCS cannot be estimated for the CCSh.

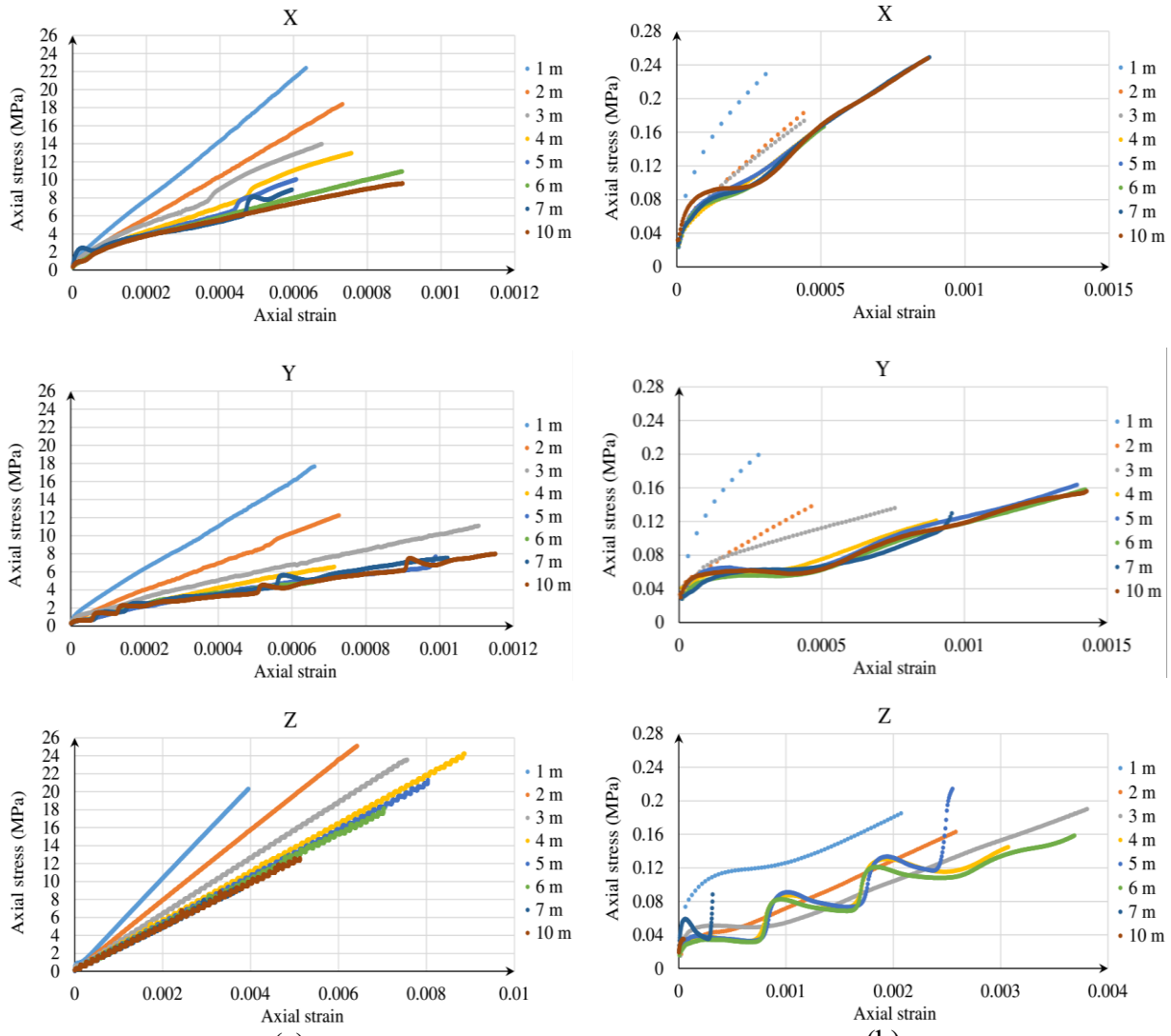

Figure 7-28 Comparison of stress-strain relationships till peak resulted from compression loading on the models at X, Y, and Z between (a) marble versus (b) CCSh

7.12.1.1 NORMALIZED UCS

Figure 7-31 includes marble and CCSh results of the scale effect on the normalized UCS (UCS_{RM}/UCS_i). The REV of marble for the UCS can be estimated as ~ 7 m which is as reported in (WeiZhong et al., 2011). Results of CCSh in an attempt to estimate the equivalent UCS using the normalized values are not successful. The UCS results don't converge in case of CCSh (Figure 7-13b).

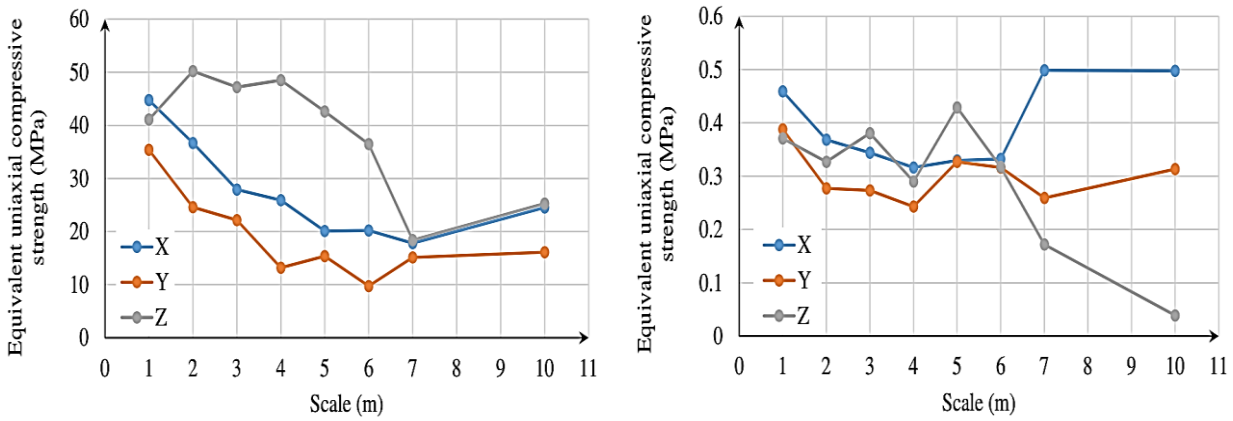

Figure 7-29 Scale effect (Case I) and anisotropy (Case I) on UCS_{eq} of (a) marble and (b) CCSh

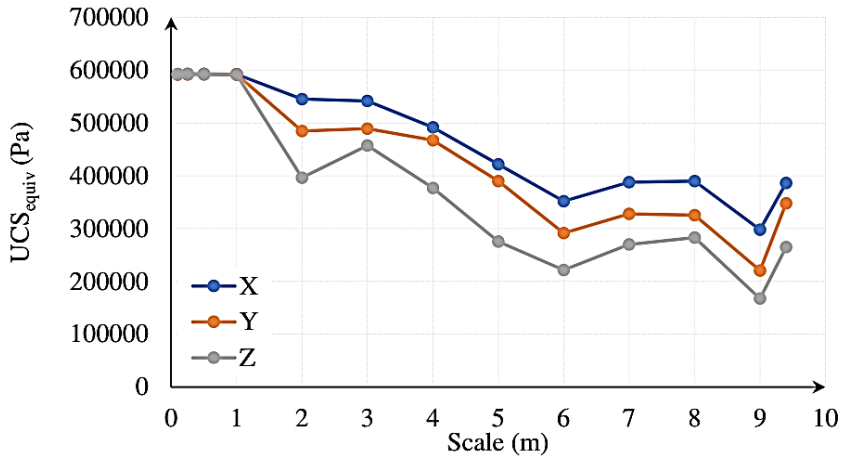

Figure 7-30 Scale effect on UCS for CCSh – Case II

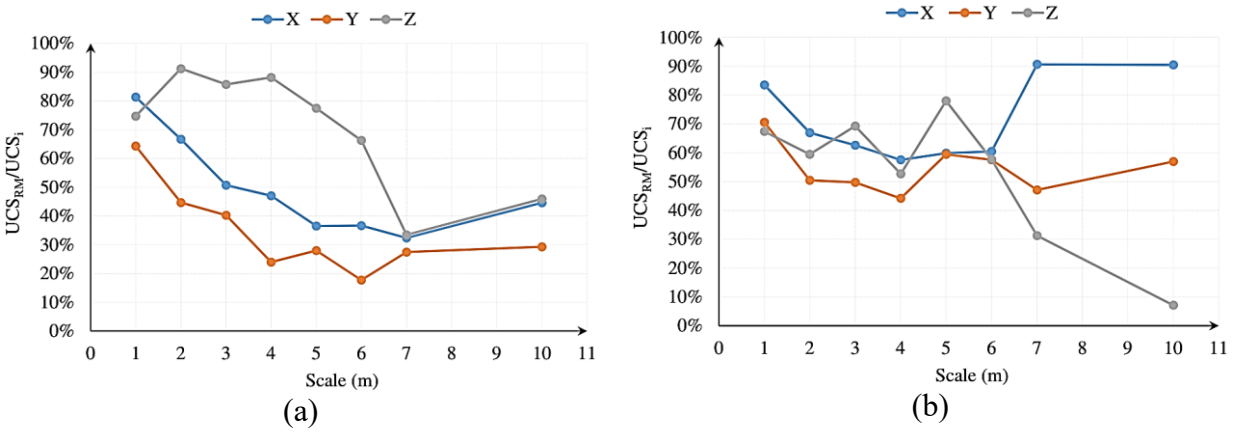

Figure 7-31 Scale effect on normalized UCS of (a) marble and (b) CCSh

7.12.1.2 COEFFICIENT OF VARIATION

Coefficient of variation (CV) is defined as the ratio of a property standard deviation to its mean value at a given size (Min, 2002). The CV quantifies the variation of a mechanical property per Equation (7-3) which was developed by Jianping et al. (2015) to study the scale dependency of strength in fractured rock masses, i.e. estimating the REV, as follows:

$$CV_{\sigma i} = \frac{|\sigma_i - \sigma_I|}{\sigma_I} \tag{7-3}$$

where $CV_{\sigma i}$ is the coefficient of variation, σ_i is the strength of a model with size i, and σ_I is the average strength of the models whose sizes are larger than or equal to size i (JianPing et al., 2015). Figure 7-32a and Figure 7-32b include plots of the CV for marble and CCSh, respectively. All the CV values start with high percentage then typically begin to converge or settle and should mathematically and eventually collapse to 0% per Equation (7-3).

The REV size can be estimated at 7 m in case of marble (which supports (WeiZhong et al., 2011) findings) with a coefficient of variation of less than 20%. However in case of CCSh, the values vary as the scale increases and don't plateau smoothly or converge eventually. Due to the fluctuation in the CCSh results regardless the increase in the scale, an REV again cannot be clearly nor confidently estimated from the CV plot in Figure 7-32b. There is a significant fundamental difference between the scale effect on the UCS in case of marble (hard rock) and CCSh (soft rock), and an equivalent UCS cannot be clearly estimated in case of CCSh because the values don't eventually converge as the size is increased.

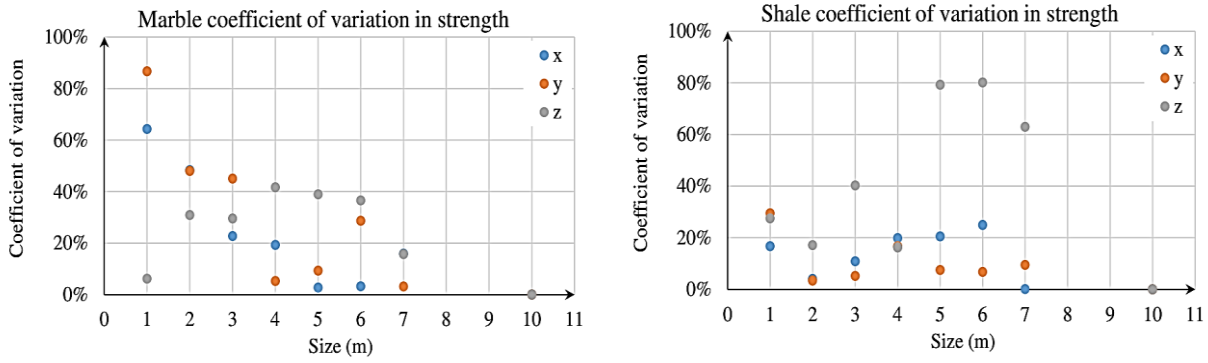

(a) (b)

Figure 7-32 Comparison of coefficient of variation in strength between (a) marble versus (b) CCSh

7.12.1.3 EQUIVALENT DEFORMATION MODULUS

The fact that discontinuum rock masses do not behave elastically has prompted the usage of the term modulus of deformation or deformation modulus (DM) rather than modulus of elasticity or Young's modulus (E) (Palmström & Singh, 2001). The DM of a rock mass relates the change in the applied stress to the change in the resulting deformation (Zhang, 2004). The DM is a key parameter that is required for numerical and analytical analysis of structures constructed in or on rock masses (Zoorabadi, 2016). Yoshinaka & Yamabe (1986) defined the deformation of a discontinuous rock mass to be equal to the summation of the deformations of the discontinuities and the intact rock (Yoshinaka & Yamabe, 1986) as follows:

$$\delta = \delta_{dis.} + \delta_i \tag{7-4}$$

where δ, $\delta_{dis.}$ and δ_i are the deformations of the rock mass, discontinuities and intact rock, respectively. Accordingly, the rock mass DM can be estimated as:

$$\frac{1}{DM} = \frac{1}{E_i} + \frac{1}{K_n S} \tag{7-5}$$

where E_i is the intact modulus of elasticity, K_n is the normal stiffness of the discontinuities, and S is the discontinuities spacing.

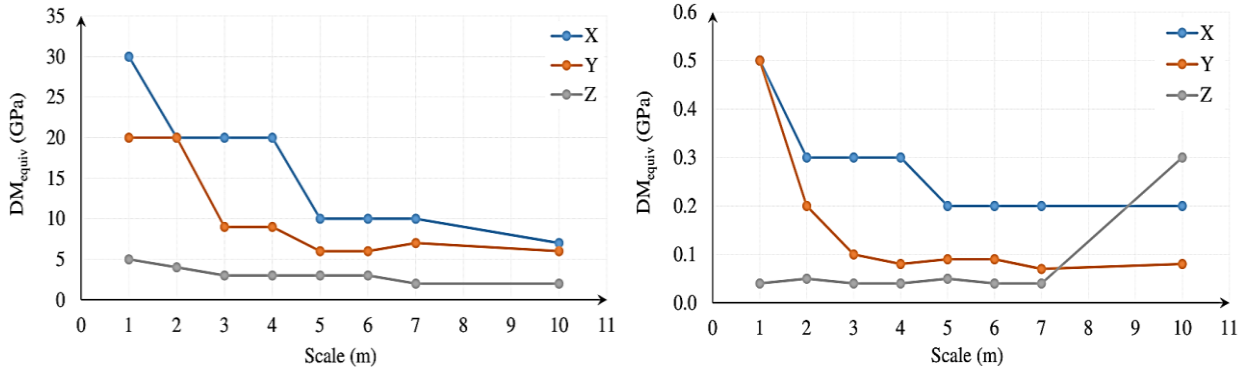

Figure 7-33 Scale effect on DM between (a) marble versus (b) CCSh – Case I

Figure 7-33 shows the scale effect on the DM values of marble and CCSh. The investigation on scale effect of the DM of the two rock masses shows that stiffness decreases with increasing model scale. Two other sets of results of the DM values of CCSh at three orthogonal directions are plotted in Figure 7-34. Owing to the stiffness anisotropy, the strongest direction during the UCS loadings was found to be along X in case of marble and CCSh except at size 10 m in CCSh. The UCS loading along Z resulted in the lowest DM (softer) values compared to the other loading directions for both rock types. For marble, the results for the three directions started

to level at size 5 m (WeiZhong et al., 2011). For CCSh however, the DM values at the three loading directions don't eventually converge, similarly as described from Figure 7-33. An equivalent DM cannot be clearly estimated in case of CCSh.

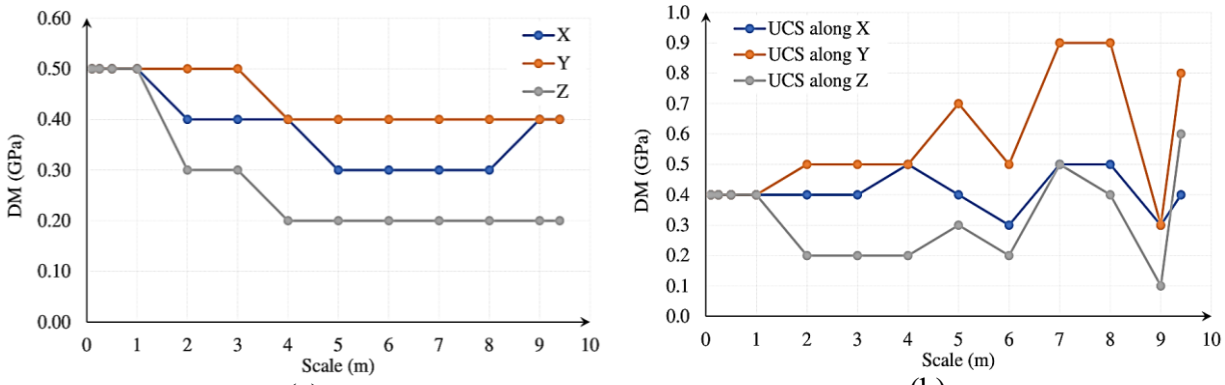

(a) (b)

Figure 7-34 Scale effect on DM in CCSh (a) and (b) results from two different loading conditions – Case II

For clay shale material, the input E_i of 0.5 GPa was achieved for the 1-m fractured CCSh block loaded along X and Y directions, fundamentally implying the close compliance of the intact CCSh compared to its discontinuities as illustrated schematically in Figure 1-6 (Chapter 1).

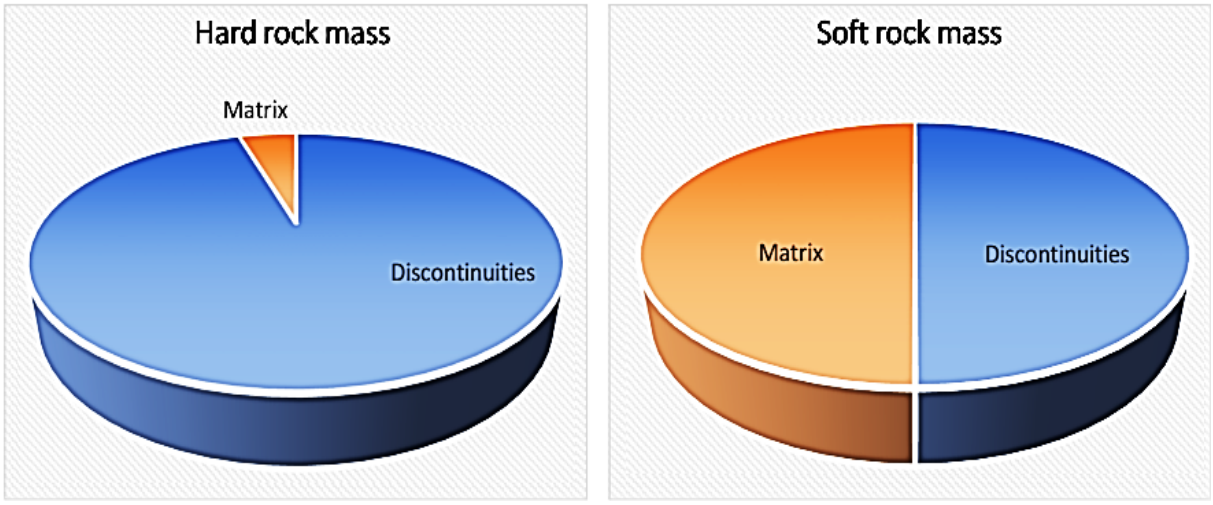

Figure 7-35 Deformability contributions of matrix and discontinuities in rock masses

The subtle presence of discontinuities did not affect the DM value in case of CCSh at that scale. However, this is not the case for marble, where the same subtle presence of discontinuities in 1-m scale model immediately reduced the stiffness from the E_i of 50 GPa to a DM of 30 GPa. This supports and confirms the research scientific hypothesis by illustrating the fundamental differences between hard and soft rock masses.

7.12.1.4 SIDE LENGTH RATIO

In their study to determine the mechanical REV, (Gutierrez & Youn, 2015) introduced a relative measure for the sampling volume, that was specified as side length ratio (SLR) parameter. It equals to the length of a side of a square sampling area (Figure 7-26) divided by the length of the region of interest, also assumed to be square, per:

$$SLR = \frac{Side\ length\ of\ sampling\ area}{Side\ lenght\ of\ total\ area} \quad (7\text{-}6)$$

At small SLR, less than a certain threshold, the mean DM values oscillate and are high, representing the intact properties, where the volume scale is small. When the SLR value relatively enlarges, the mean values of the DM remain almost constant (~ REV size) and behave as a continuum independent of the increase in the size of the sampling box. In this study, the SLR was plotted as given in Figure 7-36 for the DM results of marble and CCSh. In case of marble, a stability was reached almost at the right end of the plot (Figure 7-36a), however, the CCSh did not follow that settling trend (Figure 7-15). The REV can be estimated for marble at a value of an SLR ≈ 0.5 where the equivalent mechanical parameter starts to deviate to asymptotic constant values. On the other hand, an equivalent DM and consequently an REV for the DM cannot be estimated in case of CCSh.

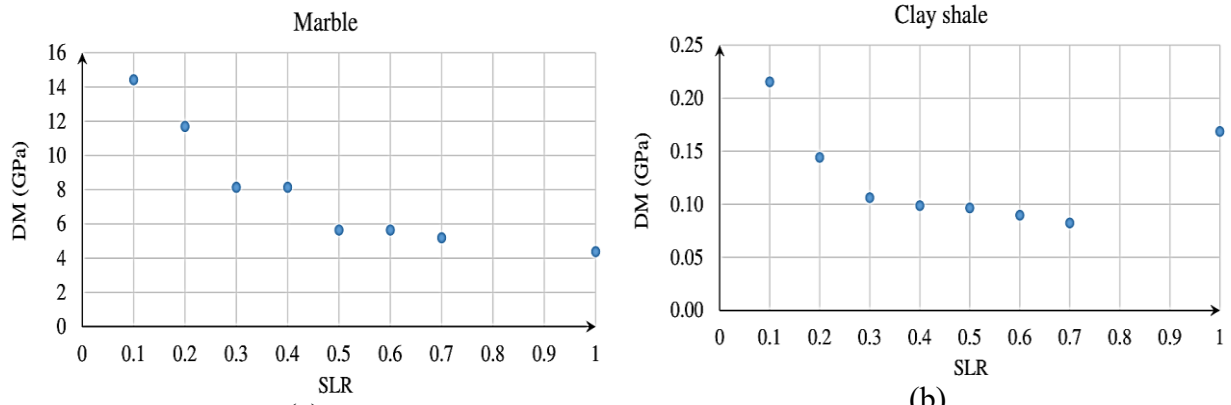

Figure 7-36 Comparison of DM as function of SLR between (a) marble versus (b) CCSh

7.12.1.5 POISSON'S RATIO

Poisson's ratio (ν_{ij}) is the ratio of normal strain in the j direction to that in the i direction when stress is applied in the i direction (Min & Jing, 2003). The basic assumptions that ν was built on, in Hook's Law, are continuum, homogeneous, isotropic, linear

and elastic (CHILE) behaviour. A strain-softening over-consolidated fully saturated material that is full of discontinuities as the CCSh will not follow CHILE behaviour known for hard rocks.

In an attempt to estimate an equivalent ν for the CCSh, the constitutive model for zones was set to be strain softening, which resulted in an "apparent" ν of the fractured rock masses to be greater than 1 as plotted in Figure 7-37 (a) and (b). Moreover, anisotropy in ν is evident as can be seen. As the rock mass scale increases, the ν results didn't converge accordingly an REV for the ν cannot be estimated for the CCSh.

7.12.1.6 SHEAR MODULUS

The equivalent shear modulus (G_{equiv}) of a rock mass is one of the required mechanical parameters when performing equivalent continuum modelling. In this chapter, two cases of shear loading mechanisms were considered as listed in Table 7-12. The G_{equiv} is calculated from the shear stress versus shear displacement relationships at each block model scale and loading direction. To eliminate the bias in results as possible, the shear displacements were measured at various locations on the faces of each 3D model as depicted in Figure 7-38. Table 7-12 Cases of shear loading

Case study #	I	II
Mechanism	Two opposite forces along opposing faces	Two perpendicular forces along perpendicular faces
Source / based on	(WeiZhong et al., 2011)	(Kulatilake & Wu, 2013)
Illustrated in	Figure 7-38	Figure 7-18
Orientation	X force along YZ face	XY
	Y force along XZ face	XZ
	Z force along XY face	YZ

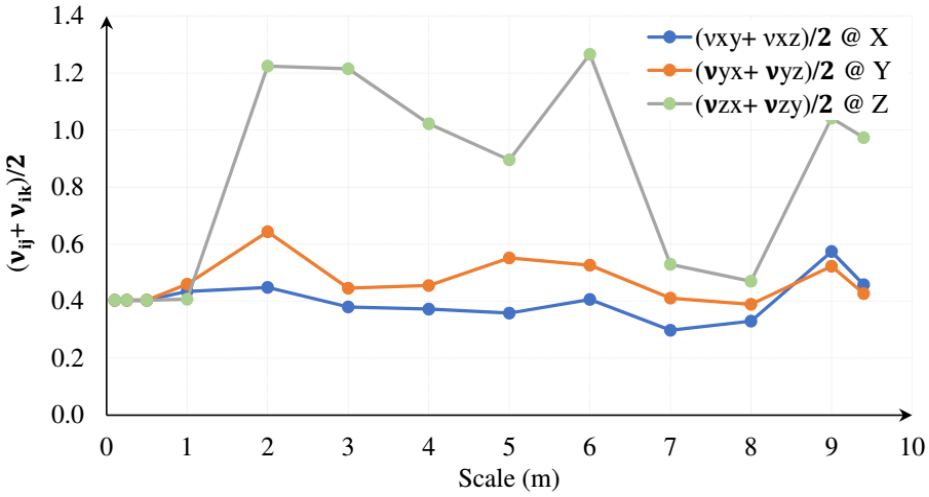

(a)

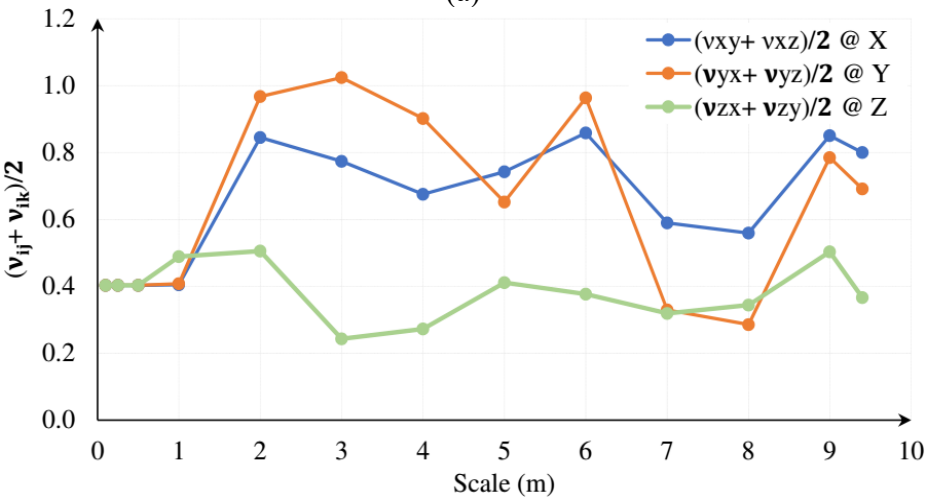

(b)

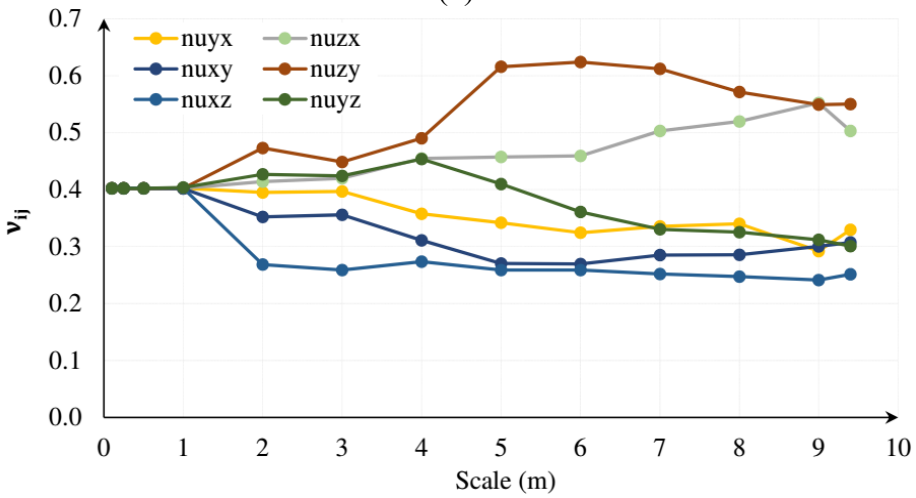

(c)

Figure 7-37 Scale effect on Poisson's ratio in CCSh (a), (b) and (c) results of three different loading conditions – Case II

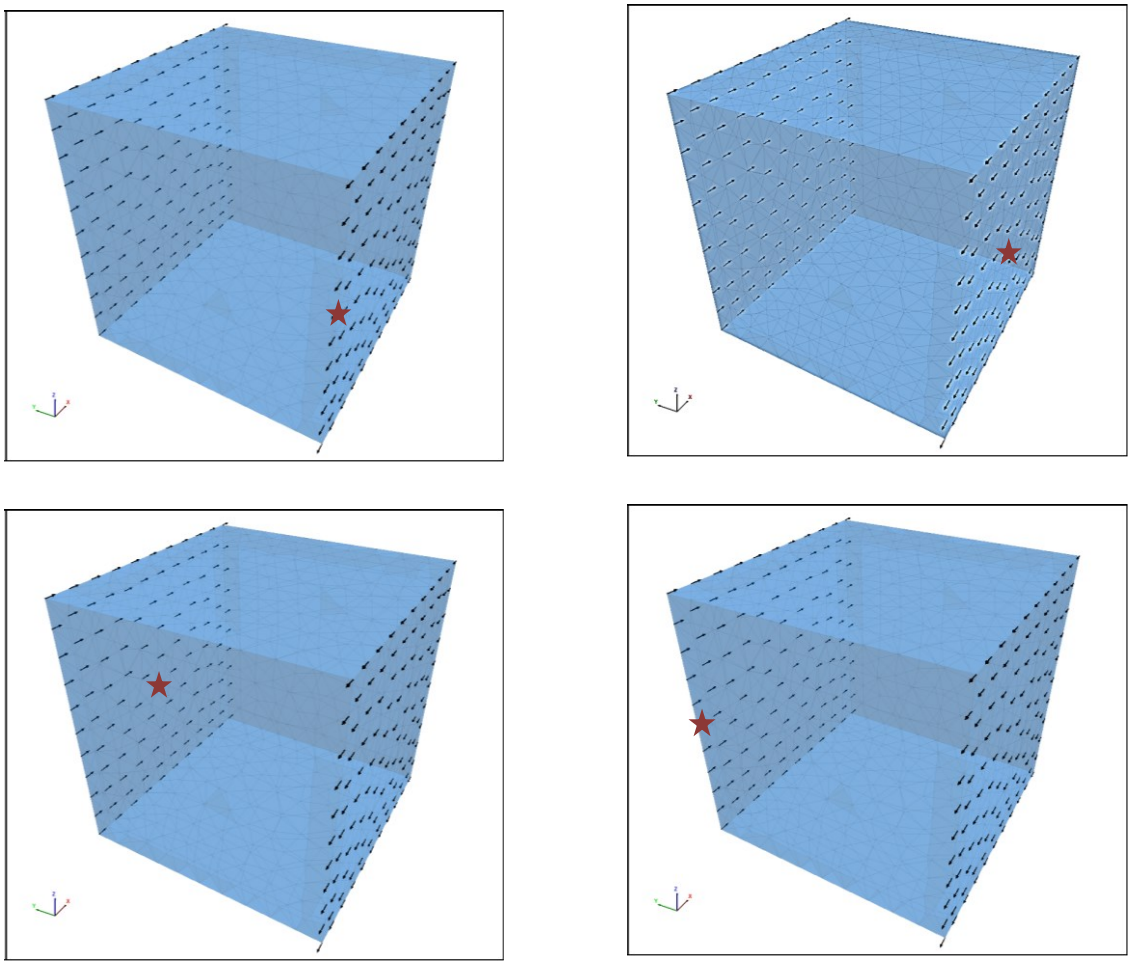

Figure 7-38 Shear loads vectors and shear disablement monitoring locations (noted by red star)

The shear displacement is defined as illustrated in Figure 7-40 (a). After applying the shear loading, the blocks were deformed and the state of failure of the 3D models is provided in Figure 7-39 where the green zones represent tensile failure areas. The G_{equiv} of CCSh were calculated for each model scale at three orthogonal shear loading directions as plotted in Figure 7-40 (b). Shear stiffness anisotropy is evident. An equivalent G nor an REV for G of CCSh could be clearly estimated (Figure 7-15).

7.12.2 STRENGTH AND STIFFNESS DEGRADATION

Generally, as a rock mass size increases, both the strength and stiffness decrease. Numerical simulation results in this study showed that the intact rock strength (UCS_i) and stiffness or deformation modulus (DM_i) generally decreased in both marble and CCSh as the model scale increases. However, the degradation was significant in case of the argillaceous CCSh (the soft rock) under same loading conditions as indicated from interpreting the values listed in Table 7-13.

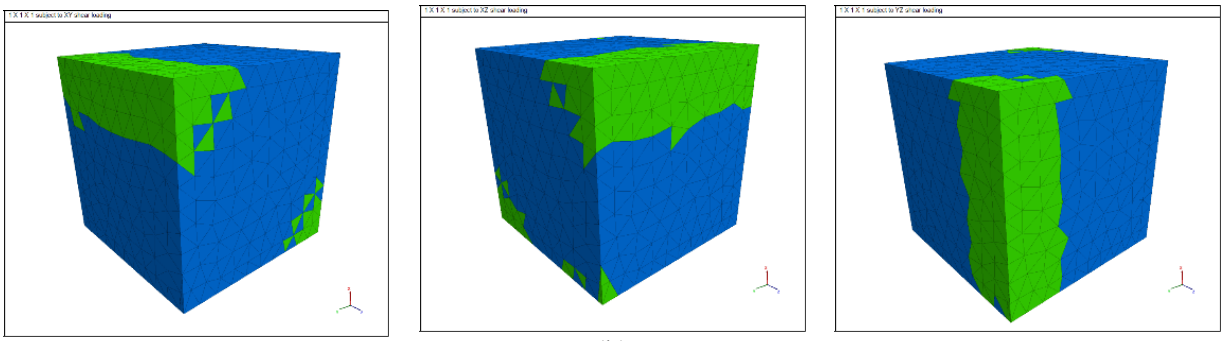

(a) (b) ©

Figure 7-39 Shear loading along; (a) XY, (b) XZ, and (c) YZ on 0.1-m^3 block (≈intact) – blocks colored by state of failure – Green color indicates zones failed under tension

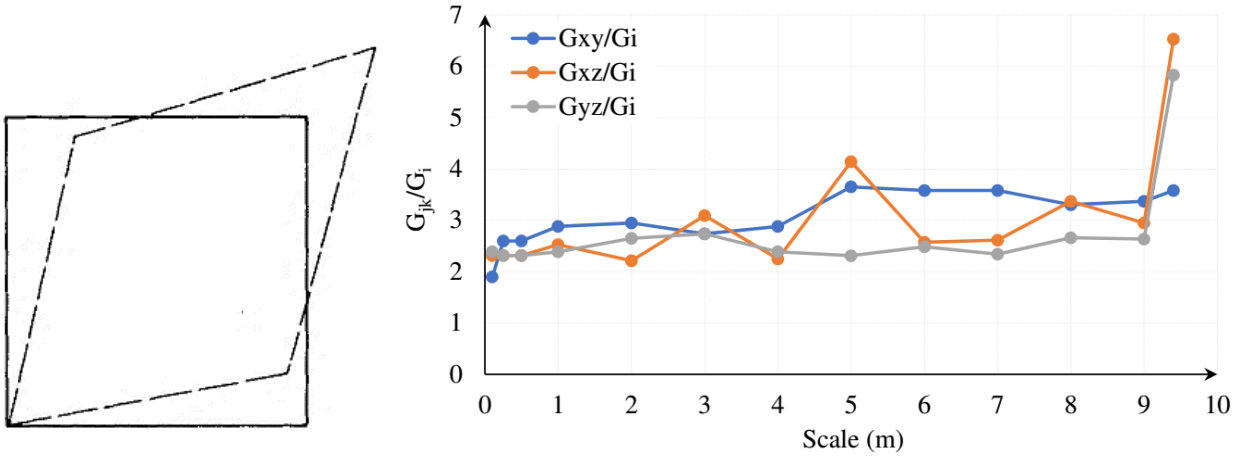

(a) (b)

Figure 7-40 (a) Shear deformation schematic (Shi & Goodman, 1989) (b) scale effect on normalized shear modulus for CCSh – Case II

Figure 7-41 includes a comparison in the UCS degradation between marble versus CCSh in case of compression loading along four DFN orientations as listed in Table 7-8 in Case II. The intact uniaxial compressive strength (UCS_i) for marble and CCSh were set to equal 100 and 0.6 MPa, respectively. The CCSh results of the DFN oriented at 45°, generally followed marble trend with an odd increase at the 3 m model scale, this is can be because of the DFN structure. Agreements between marble and CCSh in the strength degradation at the largest scale are met at all DFN orientations except 45° orientation. The ratios of the strength and stiffness decrease from the smallest model size (intact) to the largest size (10 m) are listed in Figure 7-14. For instance, the stiffness degradation ratio in hard to soft rock equals 1:144 times. The two schematics in Table 7-14 illustrate the degradation in strength and stiffness of marble versus CCSh. Again, these

findings confirm the research scientific hypothesis basis that hard and soft rocks are fundamentally different.

Table 7-13 Comparison of scale effect on UCS and DM between marble versus CCSh – Case I

Block size (m)	Marble		CS	
	UCS (kPa)	DM (MPa)	UCS (kPa)	DM (MPa)
10	90.89	20000	0.05	2
7	162.82	20000	0.13	4
6	134.32	20000	0.12	4
5	172.29	20000	0.14	5
4	169.47	20000	5.62	20
3	14364.00	10000	197.89	100
2	23811.70	20000	340.71	100
1	81236.90	70000	6412.27	700
Intact	81558.00	50000	6474.88	500

7.12.3 MECHANICAL ANISOTROPY

The variation, in the mechanical parameters due to rotating the loading direction, is studied to assess the rock mass mechanical anisotropy. The block models were loaded at multiple directions as stated in Table 7-8. In Case I, the models were uniaxially compressed along three orthogonal directions; X, Y, and Z while in Case II, the DFN was rotated and loaded at 0, 45, 90, and 135^{o} orientations.

The stochastic DFNs at 0^{o} and 90^{o} orientations are illustrated in Figure 7-42. Owing to the rock mass anisotropy, both the UCS and DM magnitudes were found to be dependent on the direction of loading. The resulted mechanical parameters values varied with changing axial loading direction in both marble and CCSh as depicted in Figure 7-43. The directional variations of strength and DM in fractured rock masses must be treated properly with respect to the directions of in situ stresses. Strength and stiffness anisotropy are more pronounced in case of CCSh models.

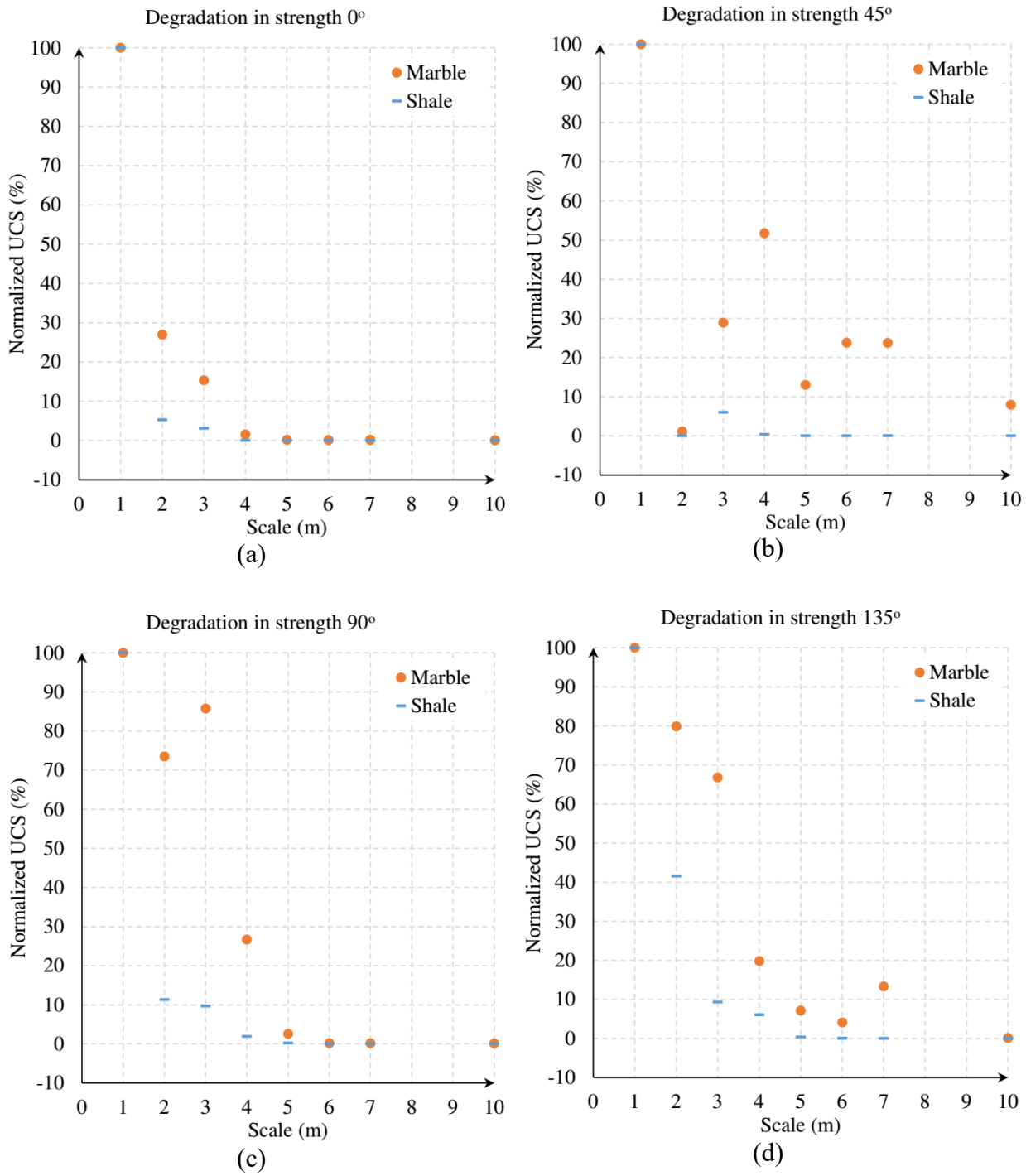

Figure 7-41 Comparison of scale effect on strength anisotropy and degradation between marble versus CCSh due to UCS along (a) 0°, (b) 45°, (c) 90°, and (d) 135° orientations

Table 7-14 Comparison of degradation in strength and stiffness between marble versus CCSh

UCS_i / $UCS_{RM=10\ m}$	DM_i / $DM_{RM=10\ m}$
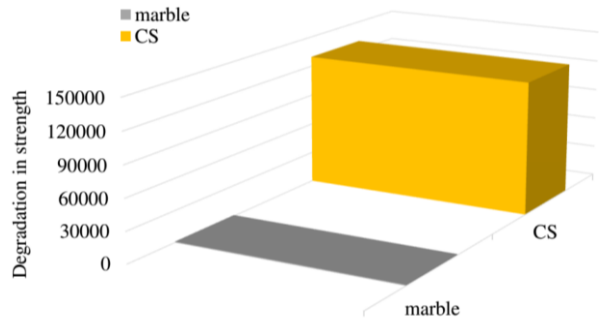	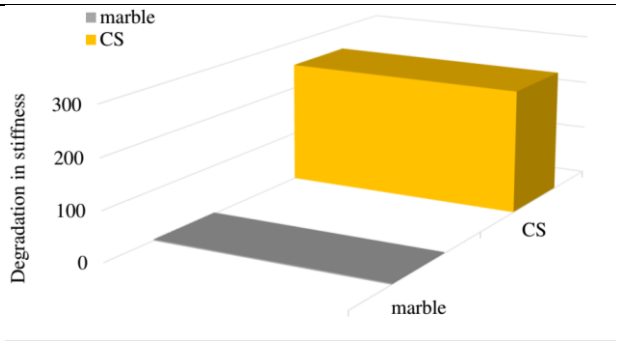

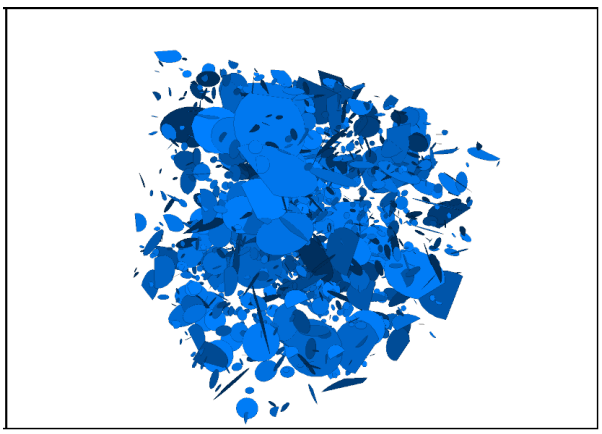

(a)

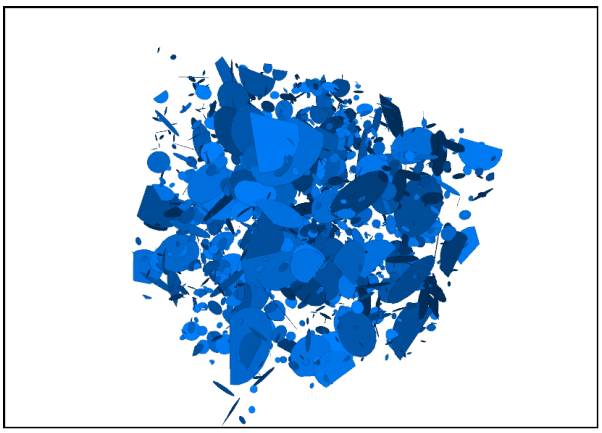

(b)

Figure 7-42 Stochastic DFN Case I dip angle rotated at (a) 0 º and (b) 90 º – boundary conditions Case II

7.13 COMPLIANCE TENSOR

To describe the pre-peak behaviour of a hard rock mass, a linear elastic constitutive model is typically assumed to represent the equivalent continuum behaviour of the rock mass in 3D. As stated earlier, the second condition in the equivalent continuum modelling applicability, is that the values of the equivalent mechanical parameters can be presented in a compliance tensor form. This compliance tensor can then be used in the constitutive equations for the continuum analysis (Min & Jing, 2003). Basically, the compliance tensor [C] is the inverse of the stiffness tensor [S] and vice versa per:

$$[S] = [C]^{-1} \tag{7-7}$$

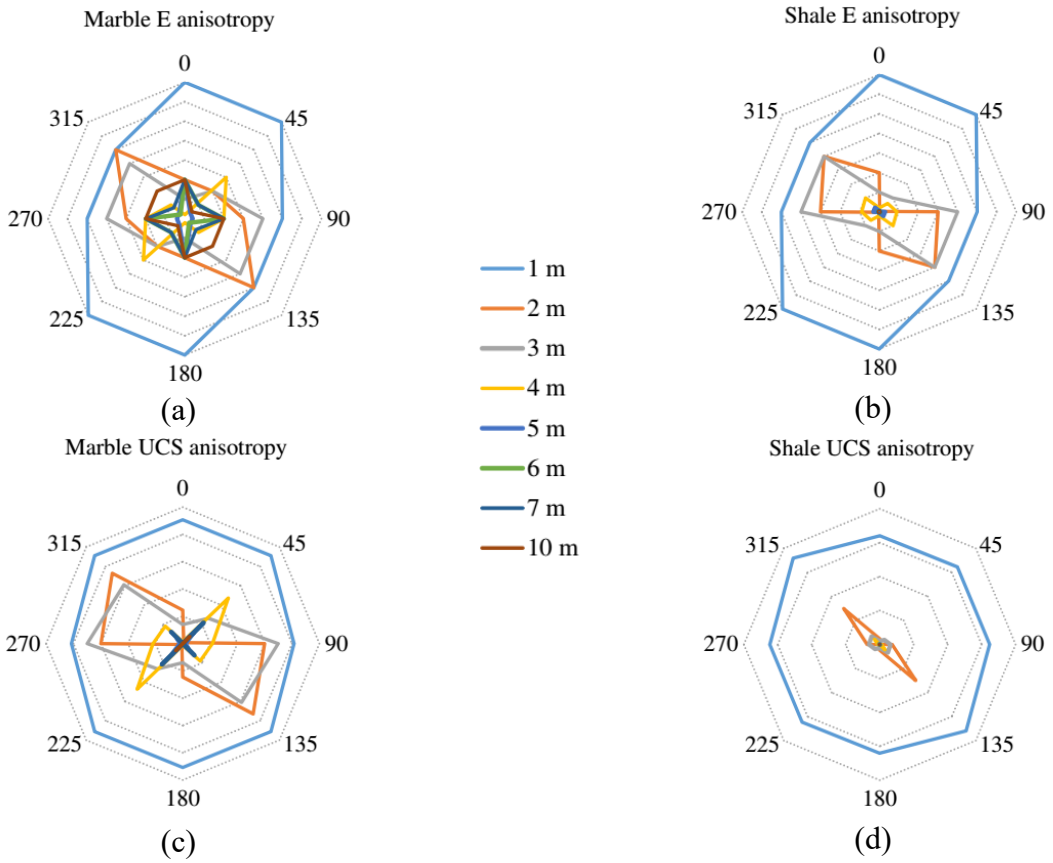

Figure 7-43 Anisotropy in (a) and (b) stiffness (DM) and (c) and (d) strength (UCS) for marble and CCSh

In its basic form, the generalized Hook's law (1678) defines the stiffness (S) as:

$$S = \frac{\sigma}{\varepsilon} \tag{7-8}$$

where σ is the stress and ε is the strain. The constitutive equation for a linear elastic solid relates stress and strain tensors as follows:

$$\varepsilon_{ij} = S_{ijkl}\sigma_{kl} \tag{7-9}$$

$$\sigma_{ij} = C_{ijkl}\,\varepsilon_{kl} \tag{7-10}$$

where S_{ijkl} and C_{ijkl} are fourth order stiffness and compliance tensors, respectively. The strain ε_{ij} (Min & Jing, 2003) is defined in terms of the displacement (U) as:

$$\varepsilon_{ij} = \frac{1}{2}\left(U_{ij} + U_{ji}\right) \tag{7-11}$$

The fourth order compliance tensor (C_{ijkl}) in the general stress-strain relationship can be expressed as (Ting, 1996):

$$\begin{bmatrix} \sigma_{11} \\ \sigma_{22} \\ \sigma_{33} \\ \sigma_{23} \\ \sigma_{31} \\ \sigma_{12} \\ \sigma_{32} \\ \sigma_{13} \\ \sigma_{21} \end{bmatrix} = \begin{bmatrix} C_{1111} & C_{1122} & C_{1133} & C_{1123} & C_{1131} & C_{1112} & C_{1132} & C_{1113} & C_{1121} \\ C_{2211} & C_{2222} & C_{2233} & C_{2223} & C_{2231} & C_{2212} & C_{2232} & C_{2213} & C_{2221} \\ C_{3311} & C_{3322} & C_{3333} & C_{3323} & C_{3331} & C_{3312} & C_{3332} & C_{3313} & C_{3321} \\ C_{2311} & C_{2322} & C_{2333} & C_{2323} & C_{2331} & C_{2312} & C_{2332} & C_{2313} & C_{2321} \\ C_{3111} & C_{3122} & C_{3133} & C_{3123} & C_{3131} & C_{3112} & C_{3132} & C_{3113} & C_{3121} \\ C_{1211} & C_{1222} & C_{1233} & C_{1223} & C_{1231} & C_{1212} & C_{1232} & C_{1213} & C_{1221} \\ C_{3211} & C_{3222} & C_{3233} & C_{3223} & C_{3231} & C_{3212} & C_{3232} & C_{3213} & C_{3221} \\ C_{1311} & C_{1322} & C_{1333} & C_{1323} & C_{1331} & C_{1312} & C_{1332} & C_{1313} & C_{1321} \\ C_{2111} & C_{2122} & C_{2133} & C_{2123} & C_{2131} & C_{2112} & C_{2132} & C_{2113} & C_{2121} \end{bmatrix} \begin{bmatrix} \epsilon_{11} \\ \epsilon_{22} \\ \epsilon_{33} \\ \epsilon_{23} \\ \epsilon_{31} \\ \epsilon_{12} \\ \epsilon_{32} \\ \epsilon_{13} \\ \epsilon_{21} \end{bmatrix} \quad (7\text{-}12)$$

In 2016, Abel Sánchez Juncal developed a virtual rock mass laboratory (VRMLab) to universally derive the equivalent continuum model mechanical parameters for rock masses. In this virtual lab, the linear elastic components of the equivalent compliance tensor can be obtained for an anisotropic rock mass posing up to an orthotropic constitutive behaviour. The VRMLab (Juncal, 2016) mainly performs numerical tests on 3D models (virtual rock mass specimens), where the discontinuities are explicitly modeled. The mechanical tests are loading and unloading of; compression, extension and shear conducted at X, Y, and Z directions to account for the strength anisotropy. These tests are performed in the VRMLab to estimate the equivalent mechanical components of the compliance tensor (Equation (7-12)). The VRMLab is claimed to be designed to accommodate all rock mass types.

The steps of running the VRMLab are:

1. Applying stresses; compression, extension, or shear,
2. Measuring displacements; u and δ,
3. Calculating strains; ε and ɣ (Equation (7-11)), and
4. Estimating the equivalent compliance tensor components; C_{ijkl} (Equation (7-12).

As an illustrative example, results from the VRMLab testing a hard rock mass are given in Table 7-15 and Table 7-16. The intact rock stiffness was assumed to be 40 GPa and its ν = 0.25. Notice the close agreement between the values of the corresponding tensor components, meaning a REV size has been reached. Also note the tensor symmetry along the diagonal manifesting the linear, elastic, and isotropic nature of the product tensor (equivalent continuum) for this rock type. These two conditions imply an REV has been reached and the equivalent continuum approach is applicable to that (hard) rock mass example.

Table 7-15 Compliance tensor for hard rock – DFN effect on mechanical anisotropy (GPa × 10^{-11}) (Juncal, 2016)

16.88	-5.78	-4.54	-9.01	6.08	7.10
-5.81	15.05	-3.77	7.26	-8.07	9.45
-4.52	-3.75	12.64	9.01	10.08	-6.97
-8.99	7.15	9.10	22.97	4.83	-0.01
5.98	-8.02	10.19	4.83	24.03	-3.63
7.10	9.43	-7.03	0.05	-3.57	23.10

Table 7-16 Compliance tensor for hard rock – continuum model with orthotropic regions (GPa × 10^{-11}) (Juncal, 2016)

16.82	-5.81	-4.54	-8.98	6.06	7.02
-5.84	15.07	-3.72	7.32	-8.03	9.39
-4.52	-3.74	12.64	9.00	10.07	-6.96
-9.02	7.17	9.17	22.98	4.85	-0.06
6.02	-8.04	10.10	4.72	23.96	-3.59
7.10	9.32	-6.98	0.03	-3.45	22.96

Additional effort to assess equivalent continuum model mechanical parameters and examine a mechanical REV existence for the CCSh was undertaken by utilizing the VRMLab (Juncal, 2016). Two fractured blocks of 7 × 7 × 7 m and 9 × 9 × 9 m sizes of the CCSh were tested in the VRMLab aiming to derive the equivalent continuum parameters and the results are provided in Table 7-17 and Table 7-18. Results from the VRMLab testing showed that the CCSh rock mass was more compliant along the X-direction, but no consistent agreement was resulted between the tensors parameters. Not only are the values not in a close match between the two rock mass sizes but also some mechanical values increased as the rock mass volume increased, which is counterintuitive. For example, the DM in the X-direction for a block size of 9 m is larger than the 7 m block size.

Table 7-17 Compliance tensor for CCSh – 3D block side = 7 m (GPa × 10^{-11})

1445.59	-75.20	-68.54	3.91	33.38	-25.29
-75.36	248.32	-66.82	35.13	0.02	-19.82
-68.39	-66.93	600.33	130.23	90.98	3.46
5.33	33.64	134.22	794.17	1.52	36.43
18.69	0.14	75.16	1.03	6355.75	7.51
-3.12	-19.12	3.95	18.20	33.32	6198.30

Table 7-18 Compliance tensor for CCSh – 3D block side = 9 m (GPa × 10^{-11})

1075.69	-73.27	-70.92	3.90	15.57	-17.80
-72.46	254.99	-67.84	30.72	-0.67	-25.19
-70.60	-68.20	534.63	115.80	48.02	1.22
3.85	29.98	116.82	767.75	-4.30	8.23
13.61	-0.13	48.36	-0.33	4463.18	29.43
-5.37	-18.57	-0.26	11.95	36.41	4355.21

Surprisingly, the tensors were found to be anisotropic as no consistent symmetry along the diagonals has resulted. An equivalent elastic tensor cannot be formed for the CCSh. Hence, the CCSh behaviour cannot be represented in an equivalent continuum behaviour. This provides an additional piece of evidence supporting the research hypothesis that soft rocks such as CCSh are unlike hard rocks and models and procedures developed for hard rocks must not be interchangeably applied to soft rocks.

7.14 DISCUSSION

This study was primarily intended for illustrating how a fractured rock mass can fundamentally alter its geomechanical behaviour and response when replacing a hard rock matrix

with a softer matrix. In 2011, a FEM procedure for equivalent continuum modelling of fractured marble (=hard rock) in 2D, was proposed. In the current chapter, a similar procedure was investigated for its applicability to a Clearwater clay shale (CCSh) rock mass.

Stochastic as well as realistic DFNs were implemented into 3D distinct element modelling (DEM) comparing equivalent deformability, stiffness, and strength between two rock type extremes; marble and CCSh. Scale effect and mechanical anisotropy in fractured models of marble and CCSh were studied by numerically loading these models, using the three-dimensional distinct element code (3DEC) provided by Itasca. At the intact block scale, the stress-strain relationship, pre-peak in case of CCSh, was non-linear where post peak was plastic and ductile compared to marble which posed a linear, elastic, and brittle behaviour. Testing a fractured soft rock mass and assigning SS constitutive model to its zones, CHILE hypothesis vanishes.

In case of the CCSh, the intact Young's modulus (E_i) of 0.5 GPa was closely achieved at $1 \times 1 \times 1$ m^3 fractured block loaded uniaxially at X and Y directions. This implies that the CCSh rock mass possess a close compliance between its matrix and discontinuities, as the subtle presence of discontinuities did not affect the DM far from its intact value. This was not the case for marble, where at the same model size ($1 \times 1 \times 1$ m^3), same subtle presence of discontinuities immediately reduced the stiffness E_i from 50 GPa for the intact marble model to a DM of 30 GPa for the $1 \times 1 \times 1$ m lightly fractured marble model.

The rock mass' DM generally revealed a decrease tendency as the model size increases in both rock types. The DM of discontinuum rock masses at different DFN orientations were notably anisotropic. The DM and UCS values of fractured rock masses change as the loading direction changes implying stiffness and strength anisotropy. It was noticed that in case of marble as the size increases (more discontinuities), the stress-strain behaviour starts to show nonlinearity and ductility. As the model size increases the strength decreases, the strength of an intact marble is more than three times the strength of a marble rock mass. Some modelling findings are summarized below:

1. The strain (at peak stress) decreases as the model size increases i.e. encountering more discontinuities, which means that the discontinuities take up of the system deformability (Figure 1-6),

2. In calculating the Poisson's ratio (ν), the lateral versus longitudinal displacement relationship was linear at small model sizes but starts to be nonlinear as the model size increases, i.e. encountering more discontinuities,
3. A fractured rock block with a strain softening (SS) constitutive model assigned to its intact zones in addition to system discontinuities, produced a $\nu > 1$,
4. As the size of the rock block increases, the non-linearity in the stress-strain relationship starts to be clearer. Small block size (≈ intact) posed linear behaviour pre-peak (homogeneous behaviour),
5. At small model sizes, ν is isotropic along conjugative directions, but as the block size increases, ν starts to show anisotropy. It increases at one direction and at the other direction it decreases, keeping a constant average value though,
6. The UCS decreases greatly and quickly from the integrate rock value in case of CCSh unlike marble,
7. The number of time steps required to reach initial equilibrium increases as the fractured block size increases. This is due to the complicated geomechanical behaviour as more discontinuities being added to the model,
8. As the size of the loaded block increases, the model run time increases, more time steps are required to reach the peak stress and failure,
9. The smaller (≈ intact) marble blocks failed following a brittle behaviour, compared to bigger fractured blocks which posed ductile behaviour, and
10. The 3D DEM results show a strong geomechanical behaviour dependency on the DFN orientation (anisotropy).

The coefficient of variation (CV) (i.e. the ratio of standard deviation to the mean value), was used to estimate the REV size of the two fractured rock types under investigation. For the same DFN, the REV and the strength degradation were not similar. A mechanical REV does not exist for the CCSh because once in softening, material loses the ‘‘representative properties" (Gitman et al., 2007). General similar conclusion was referred to in Lacy et al., 1999; Graham and Yang 2003; Gitman et al., 2006; and Swaminathan et al., 2006 for strain softening materials. Moreover analogous result has been reported in finite element simulations of 1D (Bazant, Belytschko, & Chang, 1984) and 2D (Pijaudier-Cabot & Bažant, 1988) models.

7.15 SUMMARY AND CONCLUSIONS

The deformation modulus (DM) and uniaxial compressive strength (UCS) of a rock mass are greatly influenced by the mechanical properties and geometric structure of its micro-structure. Unlike hard rocks, where the discontinuities dominate the failure mode, a soft rock matrix absorbs energy and considerably deforms carrying up from the rock mass' strain. The problem is that, there is a widespread practice in the industry and academia applying CHILE-based models to soft fractured Clearwater clay shale (CCSh) formations (DIANE) in Alberta. The CCSh is a heterogeneous composite geomaterial, which its intact poses a strain softening behaviour. This chapter included an integrated numerical study in 3D of a soft rock mass aiming to assess its mechanical REV taking into consideration the anisotropy and scale effect.

As a preliminary validation step in the numerical simulations, equivalent UCS of a fractured marble mass was found to be ≈ 15% of the integrate rock strength same as what was reported in (Weizhong et al., 2011). Numerical testing results showed that, the UCS decreases from intact rock strength more greatly and quickly in case of CCSh compared to marble. An increase in the discontinuity intensity resulted in a decrease in the model mechanical isotropy. The strength anisotropy is clear; however, it is unique for each rock type. The DM of a no discontinuities model is ≈ 1.6 times of the DM of jointed CCSh. An REV could not be conventionally estimated for the CCSh as the mechanical parameters' values did not converge forming plateau. Moreover, equivalent mechanical parameters of CCSh were not able to fit in an equivalent continuum compliance tensor form, accordingly, the equivalent continuum modelling is not applicable to CCSh.

It is the first time such numerical investigation for estimating equivalent stiffness and strength of an over consolidated argillaceous rock to be performed at that scale combining the geomechanical anisotropy and scale effect. This investigation provided a new insight into evaluating the impacts of the anisotropy in strength and deformability of fractured soft rocks, such as CCSh in Alberta. The contributions from the present study can be summarized as follows:

- Use of real geologic field data to build a realistic DFN,
- Use of DEM in 3D geomechanical modelling of fractured Albertan CCSh,
- Implementation of a advanced SS constitutive model to represent the intact CCSh, and

- Modelling, large size discontinuum 3D models under uniaxial and shear loadings along different directions, cannot be performed in the laboratory and difficult to be conducted in a mine site.

Part of the study strength is the preliminary validation of the numerical simulations, of testing intact marble models, against those resulted in (WeiZhong et al., 2011) under similar boundary and loading conditions. The validation included confirming the output values versus the input mechanical parameters values; the UCS, stiffness, Poisson's ratio (Table 7-9), the constitutive behaviour, the convergence in the equivalent mechanical parameters results, and the REV size.

The numerical testing on blocks of the two rock type extremes confirmed that marble and CCSh are fundamentally different in their deformability, strain at failure, scale effect (REV) equivalent compressive strength, equivalent stiffness, strength degradation, stiffness degradation, and trend of their stress-strain relationships. Even having same DFN, geometry, boundary conditions and scale, the two rocks deformed, behaved, and failed differently. This basically supports and confirms the basics of the research scientific hypothesis moreover fulfils the first research objective as stated in Chapter 1.

For the studied fractured soft rock, REV cannot be determined, and equivalent compliance tensor parameters cannot be estimated for the CCSh. A conscious distinguish between discontinuous-inhomogeneous-anisotropic-non-elastic (DIANE) and continuous-homogeneous-isotropic-linear-elastic (CHILE) behaviours need to be in place when assessing, designing and modelling the CCSh within engineering applications.

CHAPTER 8 NEW INSIGHT INTO QUANTIFYING MECHANICAL STIFFNESS OF NATURAL DISCONTINUITIES IN CLEARWATER CLAY SHALE

8.1 INTRODUCTION

The deformation characteristics of rock masses are mainly governed by discontinuities. The discontinuities' normal stiffness (K_n), defined as the rate of change in the effective normal stress with respect to the discontinuity closure, is one of the key parameters in estimating the deformation characteristics of rock masses (Jiang et al., 2009). Based on laboratory testing of five different rock masses, Bandis (1983) found that, there is a nonlinear (hyperbolic) relationship between the normal stress (σ_n) and the corresponding normal displacement (δ_n) per (Oda, 1986) as:

$$\sigma_n = \frac{\delta_n}{a - b\delta_n} \tag{8-1}$$

where a and b are the hyperbola constants.

Rutqvist (1995) used numerical modelling integrated with laboratory testing to estimate the mechanical K_n in hard rocks. The K_n depends not only on the Young's modulus of the material but also on the geometry of the structure (Pariseau, 2006). Therefore, the K_n of a discontinuity cannot be defined as a single constant value, because for each increment of normal stress ($d\sigma_n$), the corresponding K_n value can be estimated per (Koçal, 2008) as:

$$K_n = -\frac{d\sigma_n}{d\delta_n} \tag{8-2}$$

The K_n varies with the evolution of σ_n per:

$$\delta_n = \frac{\sigma_n V_m}{\sigma_n + K_{ni} V_m} \tag{8-3}$$

In testing a hard rock under consolidation, σ_n loading stages are conducted, monitored, and recorded continuously, since the normal displacement is guaranteed to be only taken up via the discontinuity due to the harness of the hard intact. On the other hand, for a soft rock specimen, such as the Clearwater clay shale (CCSh) under investigation in this research, the normal loading during consolidation is applied on steps. This again supports the research scientific hypothesis,

that hard rocks and soft rock are not alike accordingly procedures and models derived based on hard matrix should not be unconsciously applied to soft rock masses.

The K_n is an important mechanical parameter in engineering design as it is related to the shear strength, scale effect, σ_n level, and the rock mass deformation modulus. Table 8-1 includes number of mechanical stiffness values mainly of hard rock types collected from literature. The K_n of a rock discontinuity is a basic input parameter for physical models in numerical simulations. It is implicitly and critically linked to fluid flow through discontinuous rock masses (Lee & Harrison, 2001). Numerical analyses showed that the flow rate at each pressure magnitude is strongly dependent on the aperture and consequently K_n of the discontinuity in the vicinity of the rock mass, where the pressure changes the most (Rutqvist & Stephansson, 2003). Obviously, higher K_n results in smaller aperture deformations for a given σ_n (Wang et al., 2004). Bandis et al. (1983) recognized that K_n of a discontinuity can be influenced by the following parameters (Elmo, 2006):

(i) initial contact area,

(ii) discontinuity wall roughness,

(iii) thickness, type, and physical properties of any infill material, and

(iv) strength and deformability of the asperities along the discontinuity plane.

Mechanical stiffness is a structural feature and not an intrinsic material property (Pariseau, 2006). Better understanding and estimation of the discontinuities mechanical stiffness help in securing a safer and economical practice. Attention should be paid when lower σ_n magnitudes are expected, as the fluid flow, porosity and permeability are highly stress dependent (Rutqvist & Stephansson, 2003) and (Jiang et al., 2009). The mechanical stiffness of a discontinuity is scale and stress dependent (Baghbanan & Jing, 2008), and that dependency of the K_n is most profound at low stresses and almost diminishes at high stress levels (Leijon, 1993). Rutqvist (1995) found that, the K_n was one of the two parameters dominating the pressure-flow responses at low flow rate regime. Importance of accurately estimating the K_n is helpful in estimating the rock mass equivalent deformation modulus (DM).

In the light to fulfil the research second objective, this chapter includes an integrated procedure utilizing laboratory testing results combined with coupled 3D numerical simulations to back analyze normal and shear stiffness (K_n and K_s) of CCSh natural discontinuities. No data was ever reported for the discontinuities' mechanical properties in the CCSh in the Joslyn incident reports nor the literature (Khani et al., 2018). In this chapter, the K_n of the CCSh is estimated at

zero change in the pore pressure immediately after normal load application. This chapter proposes pioneer procedures for estimating the K_n and K_s values of natural discontinuities in soft CCSh, which is classified as a hard soil/soft rock.

8.2 SITE DESCRIPTION

In the Athabasca oil sands region, the regional Clearwater Formation is a marine shale (Wightman et al., 1995). Small and Morgenstern (1991) described the formation as an upper Cretaceous soft mudstone overlying the unconventional resources i.e. the oil sands. Lithology (stratigraphy) succession of the CCShs include geological facies of silt and fine sand as seen in Figure 8-1. The formation includes various sort of pre-existing discontinuities. The specimens studied in this chapter came from two different locations in Western Canada (Alberta), where the CCSh typically overlies the McMurray formation (sands) (Hein et al., 2000).

Figure 8-1 Upper McMurray and overlying Clearwater Formation

8.3 LABORATORY TESTING

The tested CCSh specimens were extracted from relatively shallow depths. Special and extra attention was taken to minimize sample disturbance following coring and during core handling, preserving, and specimen preparation in the laboratory. During core logging (Figure 8-2) three natural discontinuities (not drilling induced) were fortunately discovered in the cores. Detailed laboratory records of complied raw data and results of four consolidated drained (CD) direct shear tests providentially became available for mechanical stiffness estimation.

Table 8-1 Mechanical stiffness values from literature

Rock type	Location	Reference	K_n (GPa/m)	K_s (GPa/m)
Hard rock	Sellafield, Nirex, UK	(Min, Rutqvist, Tsang, & Jing, 2004)	434	434
BaiShan marble (T2)	Jinping, China	(WeiZhong et al., 2011)	17	9
Sandstone	Lane Cove Tunnel	(Badelow, Best, Bertuzzi, & Maconochie, 2005)	10	5
Shale	Lane Cove Tunnel	(Badelow et al., 2005)	0.2	0.1
Rock	Circular Tunnel	(Chen & Zhou, 2003)	200	100
Neiriz & Baghat Marble	NA	(Norouzi, Baghbanan, & Khani, 2013)	25000	150000
Lac du Bonnet granite	Southern Manitoba, CA	(Gao & Stead, 2014)	241,200	96,480
Granite	Stripa Site, Sweden	(Rutqvist, 1995)	1000-5000	NA
Conglomerate	Rufi Landslide, Zurich	(Eberhardt, Thuro, & Luginbuehl, 2005)	5	1
Marl	Rufi Landslide, Zurich	(Eberhardt et al., 2005)	1	0.5
Precambrian crystalline	Hydropower Dam, Sweden	(Bondarchuk, Ask, Dahlström, Knutsson, & Nordlund, 2012)	10	10
Sandstone	NA	(Lee, Bang, Mok, & Joh, 2000)	3.1	1
Granite	NA	(Hoang, Gasc-Barbier, Marache, Riss, & Sulem, 2010)	0.0043	0.00055
Rock	Lornex pit	(Tuckey, 2012)	4	1
Granitic rock	Kamaishi Mine, Japan	(Nguyen et al., 2001)	416	28.7
Olkiluoto migmatitic gneiss	Posiva's POSE niche tunnel	(Shen, Siren, & Rinne, 2015)	20,000	2000
Limestone	Coaraze Laboratory, France	(Cappa, Guglielmi, Rutqvist, Tsang, & Thoraval, 2006)	43-55	NA
Granitic gneiss	Salt Lake, UT, USA	(Kulatilake, Ucpirti, Wang, Radberg, & Stephansson, 1992)	67.2	2.7
Heishan Granite	Chengde city, China	(Wang, Yang, Xu, Cai, & Li, 2016)	28	28
Weak Coal	Queensland, Australia	(Gao & Stead, 2014)	5760	2304
Soft Rock (CCShC)	Alberta, CA	(Khani et al., 2018)	0.45	0.045

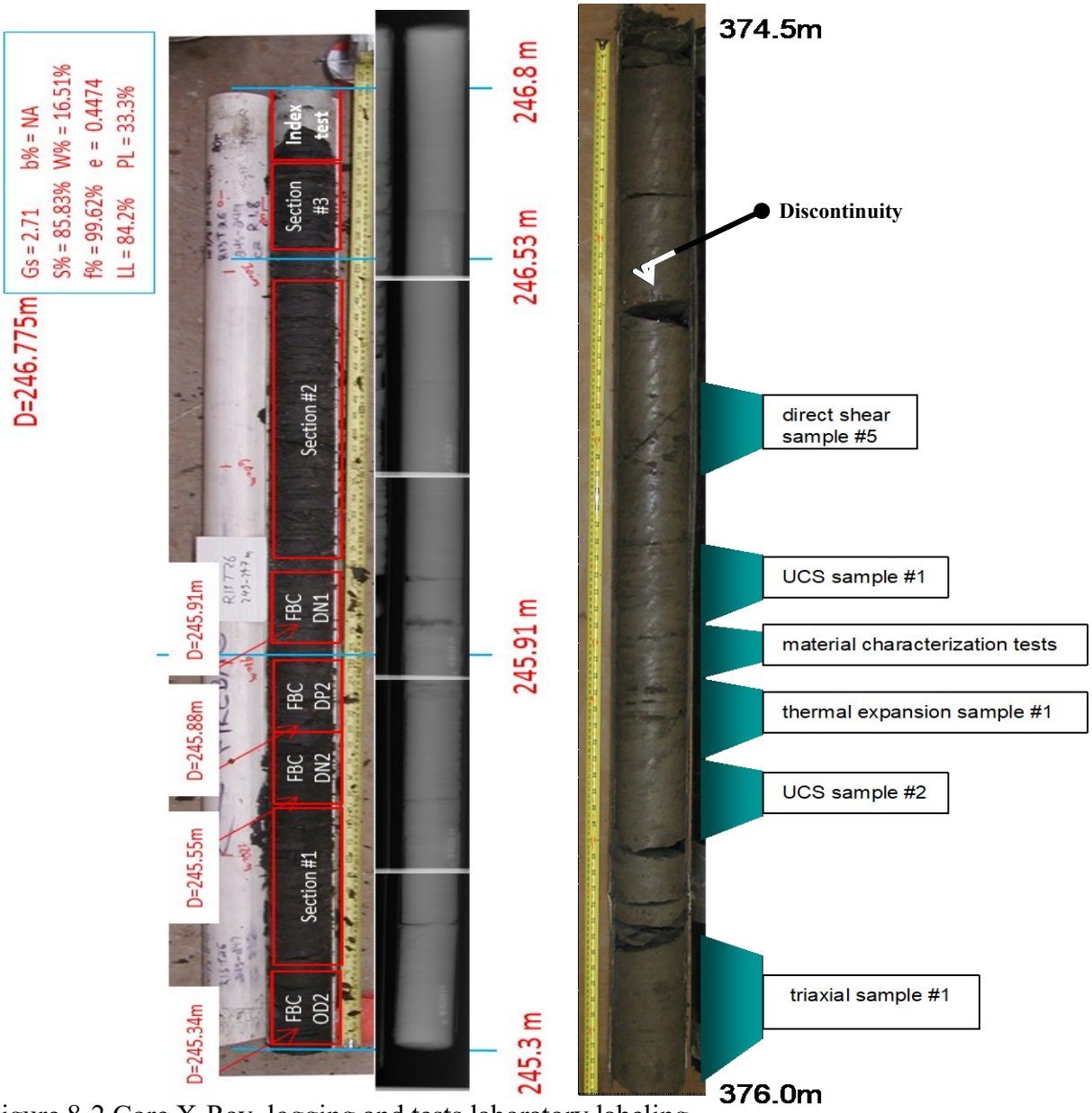

Figure 8-2 Core X-Ray, logging and tests laboratory labeling

Three CCSh specimens that fortunately containing natural discontinuities were carefully subsampled (Figure 8-3). Cylinder-shaped specimens were extracted using circular metal cutting ring of a same diameter as the direct shear box (Figure 8-4). The undisturbed CCSh specimen would fit perfectly in the mold in the direct shear apparatus similar to the one seen in Figure 8-4. Normal loading was applied on stages, unlike in hard rock testing where the consolidation is continuously imposed and recorded. Table 8-2 includes the specimens information and corresponding normal loading magnitudes. All tests were conducted under constant normal load (CNL) condition as it is more representative of shallow rock structure cases.

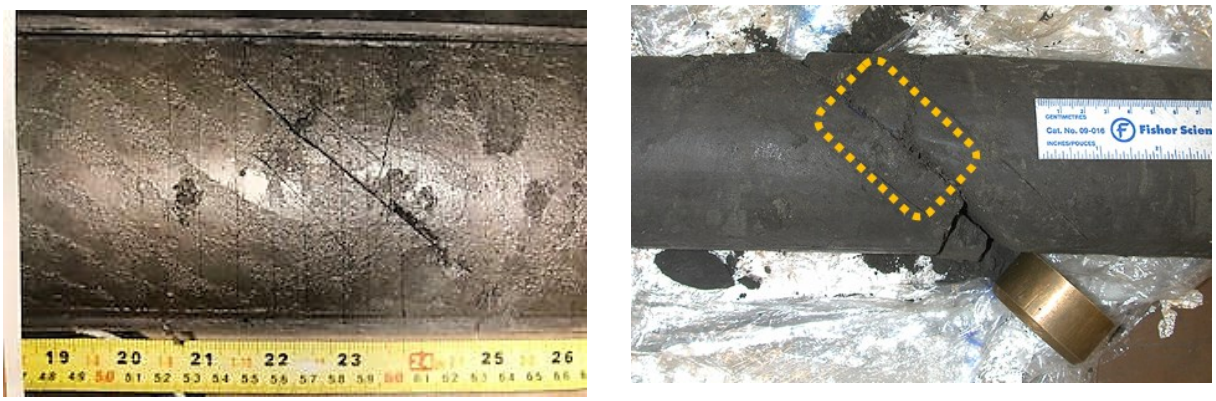

Figure 8-3 Laboratory core logging and specimen (S3) extraction with circular steal cutting ring

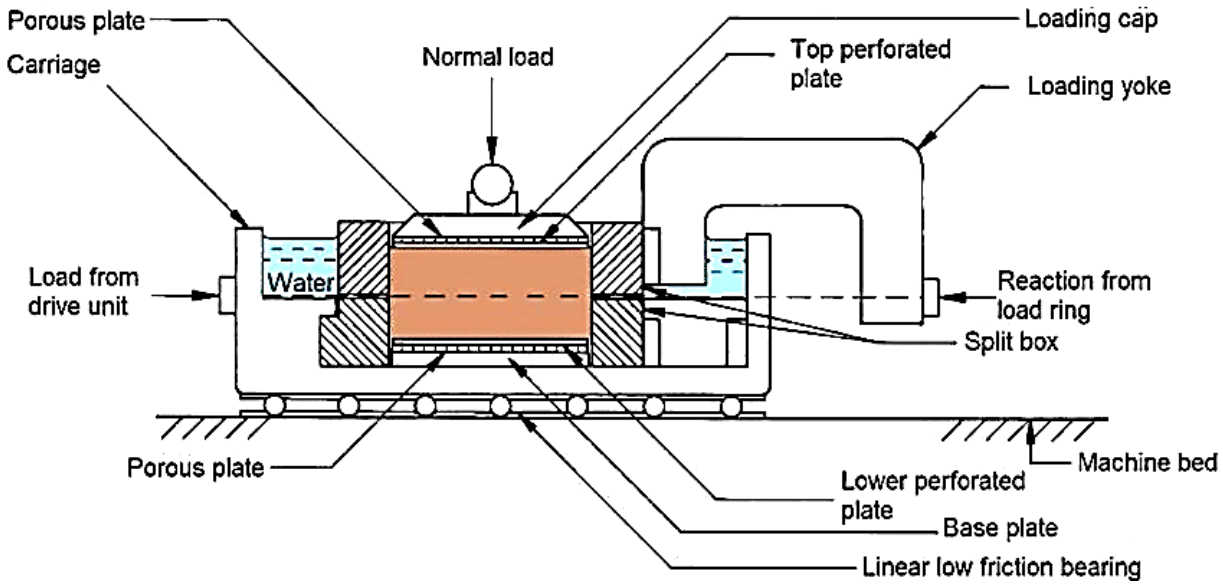

Figure 8-4 Direct shear box apparatus (Head and Epps, 2011)

Table 8-2 Specimens information

Specimen attribute	Units	S1	S2	S3
Depth	(m)	245.40	245.45	375.10
Diameter	(mm)	63.00	50.80	50.74
Height	(mm)	44.45	44.45	40.43
Normal stress	(kPa)	994	3038	3769

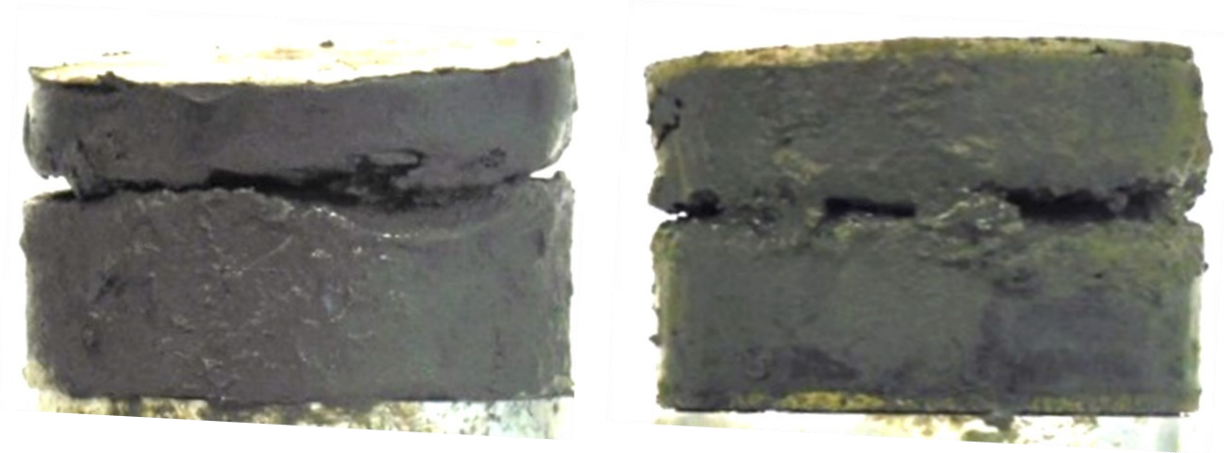

S1 S2

Figure 8-5 Two CCSh specimens after shear testing

8.4 LABORATORY SHEAR TESTING RESULTS

The shear stress versus shear displacement plots of the four direct shear tests conducted are illustrated in Figure 8-6 (a). Nonlinear relationships are depicted as shear is occurring along aperture asperities along discontinuity planes. The relationship between the shear stress and the normal (downward) displacement is plotted in Figure 8-6 (b).

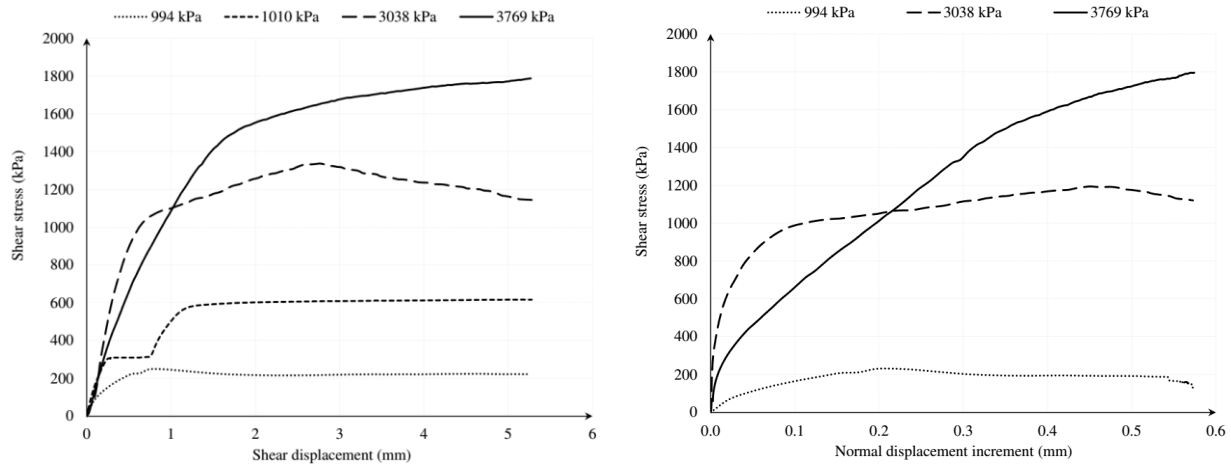

(a) (b)

Figure 8-6 (a) Shear stress versus shear displacement and (b) shear stress versus normal displacement (laboratory results)

8.4.1 SHEAR STIFFNESS (K_S)

From the shear stress versus shear displacement relationships, the shear stiffness (K_s) can be estimated as the; unloading modulus, tangent modulus of the real laboratory data, modulus of an equivalent curve fitting, or as the secant modulus. The unloading modulus option was not

available due to lack of laboratory unloading cycles. The tangent modulus of the real laboratory data was tried however due to the data, curve nonlinearity and the intrinsic material softness, negative K_s values resulted. Hyperbolic curve fitting option is less representative to the real laboratory data. Hence the K_s was estimated from the shear stress versus shear displacement relationships based on the secant modulus estimation.

Figure 8-7 includes illustrations of the procedure to estimate the secant modulus for constraining the K_s for all the four CCSh specimens tested in the shear box under σ_n levels ranging from 994 to 3769 kPa. The K_s of the natural discontinuities in CCSh based on direct shear laboratory testing was found to range from 80 to 1217.9 kPa/mm as summarized in Table 8-3.

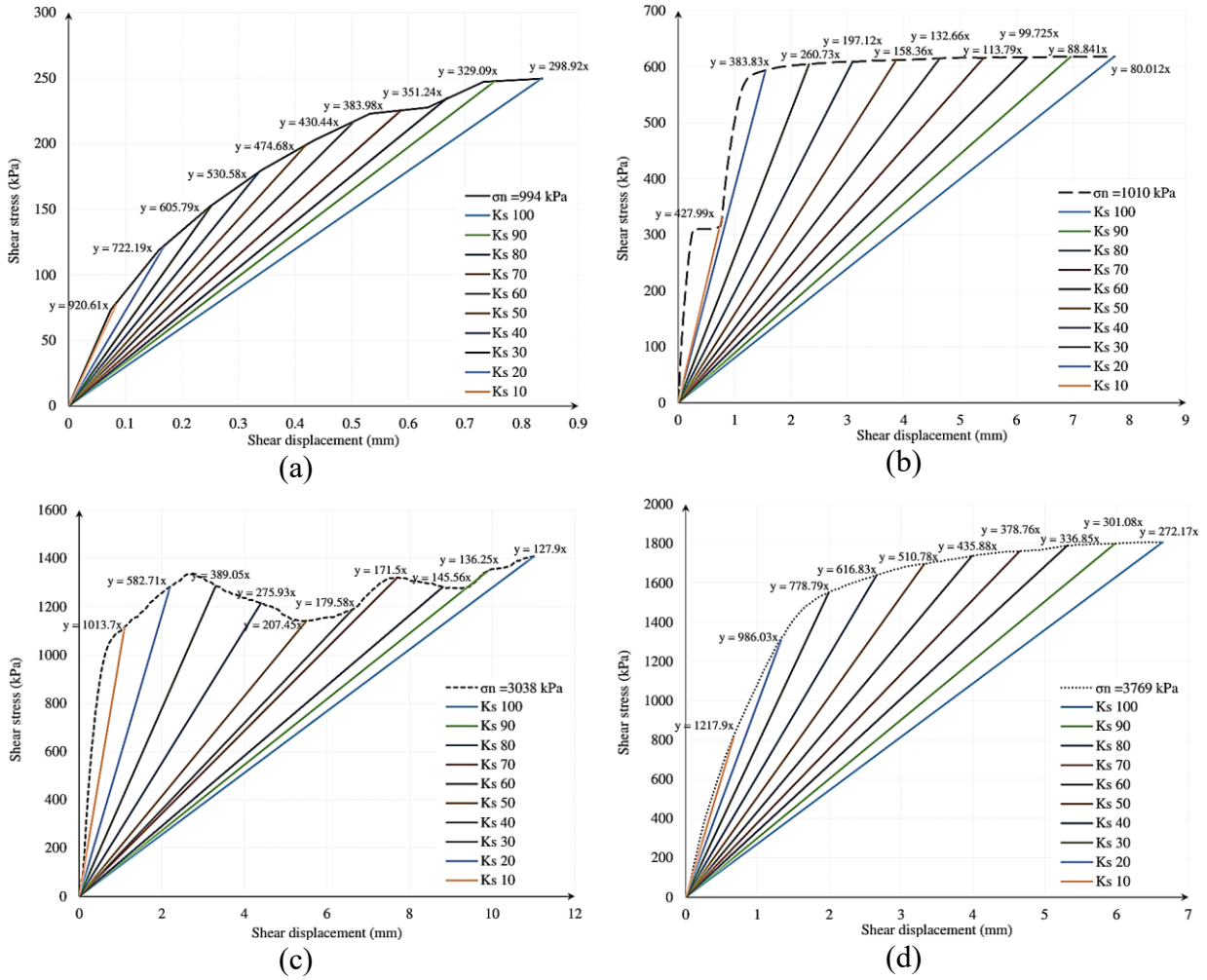

Figure 8-7 Estiamtion of secant shear stiffness (K_s) at normal stress of (a) 994 kPa, (b) 1010 kPa, (c) 3038 kPa, and (d) 3769 kPa

Table 8-3 Maximum and minimum secant K_s values

Specimen ID	Normal stress (kPa)	Max. K_s (kPa/mm)	Min. K_s (kPa/mm)
S1	994	920.61	298.92
S2	1010	427.99	80.02
S3	3038	1013.70	127.90
S4	3769	1217.90	272.17

Changes of the K_s versus shear stress and shear displacement are plotted in Figure 8-8 (a) and (b) respectively. It was found that, the K_s values depend on:

1. normal stress
2. percentage of the shear strength (maximum shear stress) Figure 8-8 (a)
3. level of horizontal (shear) strain (displacement) Figure 8-8 (b)

For this class of soft rock, there is a need to acknowledge the K_s reduction as the shear displacement increases i.e. as the shear strength is approached, implying that, this soft rock is sensitive to deformation. This is a concern as it impacts the reflected hydraulic integrity of a soft rock formation. Take for example the test under σ_n = 3769 kPa in Table 8-3, when the shear stress increases from 0.18 – 1.81 MPa, the K_s reduces from 1217 to 272 kPa/mm. However, it only needs the shear displacement to increase by 6 mm to drop this difference of K_s. Change of K_s versus σ_n is plotted in Figure 8-9a and change of K_s versus percentage of shear strength is in Figure 8-9b.

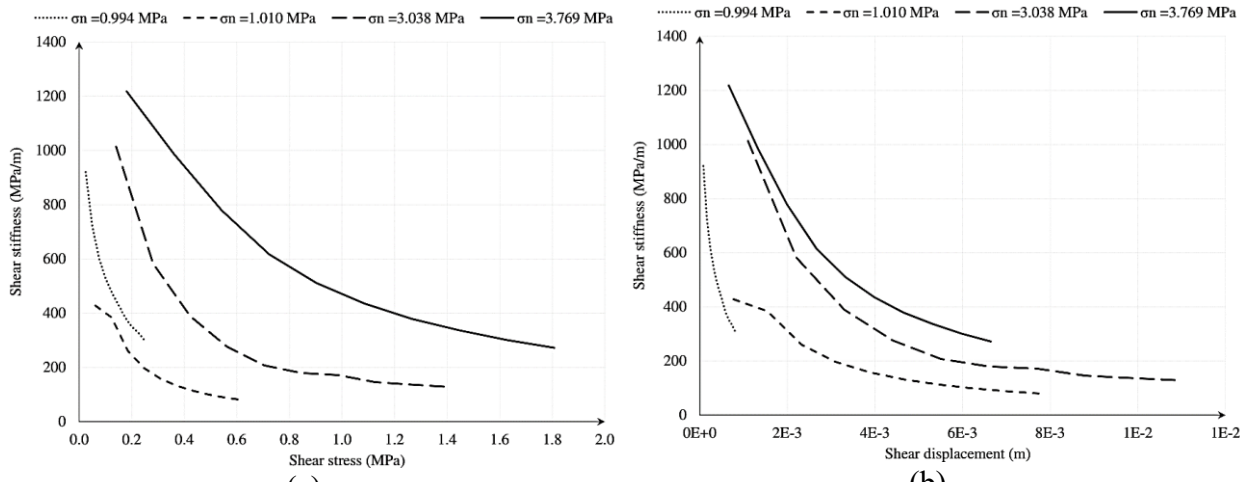

Figure 8-8 Changes of shear stiffness (K_s) versus (a) shear stress and (b) shear displacement

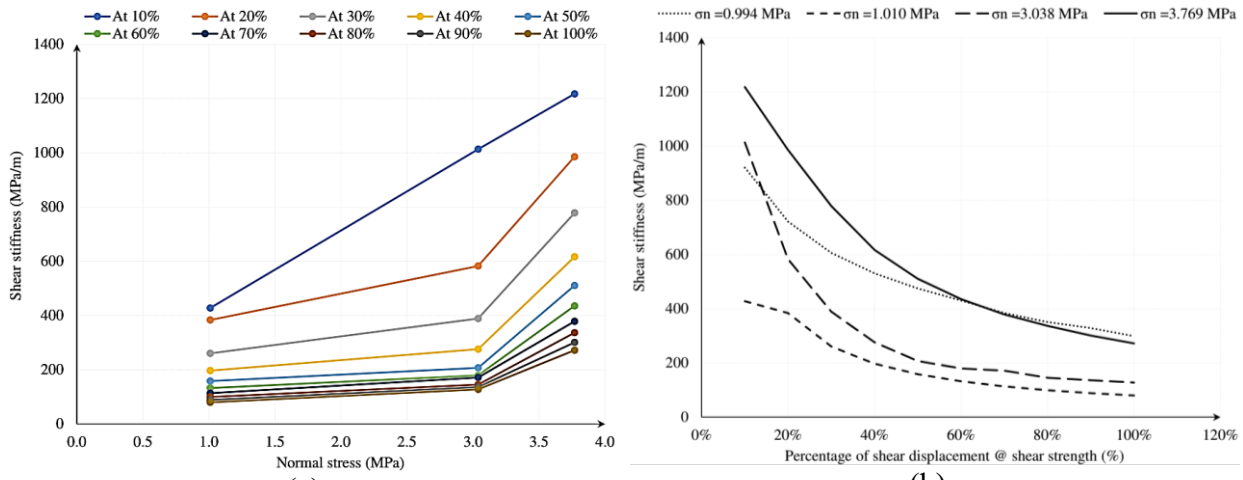

(a) (b)

Figure 8-9 Changes of K_s versus (a) normal stress and (b) percentage of shear displacement at shear strength

8.4.2 NORMAL STIFFNESS (K_N)

8.4.2.1 CONVENTIONAL METHODOLOGY

Conventionally to estimate a discontinuity' normal stiffness (K_n), laboratory results of consolidation stages during direct shear tests for discontinuous specimens as well as intact specimens are needed. For a tested cylinder loaded axially in compression that contains a discontinuity perpendicular to the load axis, the stress-displacement curve is as shown in Figure 8-10 (Pariseau, 2006). The σ_n acting across the discontinuity is simply the axial load (F) divided by the discontinuity area (A). Relative displacement between he sample ends is a total of (δ_t) that is the sum of displacement of the intact rock (δ_i) and the discontinuity closure (δ_n). Thus:

$$\delta_t = \delta_i + \delta_n = \frac{F}{A\,K_t} = \frac{F}{A\,K_i} + \frac{F}{A\,K_n} \qquad (8\text{-}4)$$

where K_t and K_i are the total and intact rock stiffnesses, respectively. Hence, the K_n may be obtained from subtracting the inverse of the slopes of normal stress normal displacement curves of intact rock minus discontinuous rock specimens (Pariseau, 2006). Thus:

$$\frac{1}{K_n} = \frac{1}{K_t} - \frac{1}{K_i} \qquad (8\text{-}5)$$

The normal stress versus normal displacement plots of the three CCSh specimens are provided in Figure 8-11. The K_n values listed in Table 8-4 were calculated from relations in Figure 8-11 following (Pariseau, 2006) conventional procedure per equations (8-4) and (8-5). Based on

the experimental results, the K_n of CCSh discontinuities would conventionally range from 242 to 3210.6 kPa/mm. The K_n increases as the effective σ_n increases.

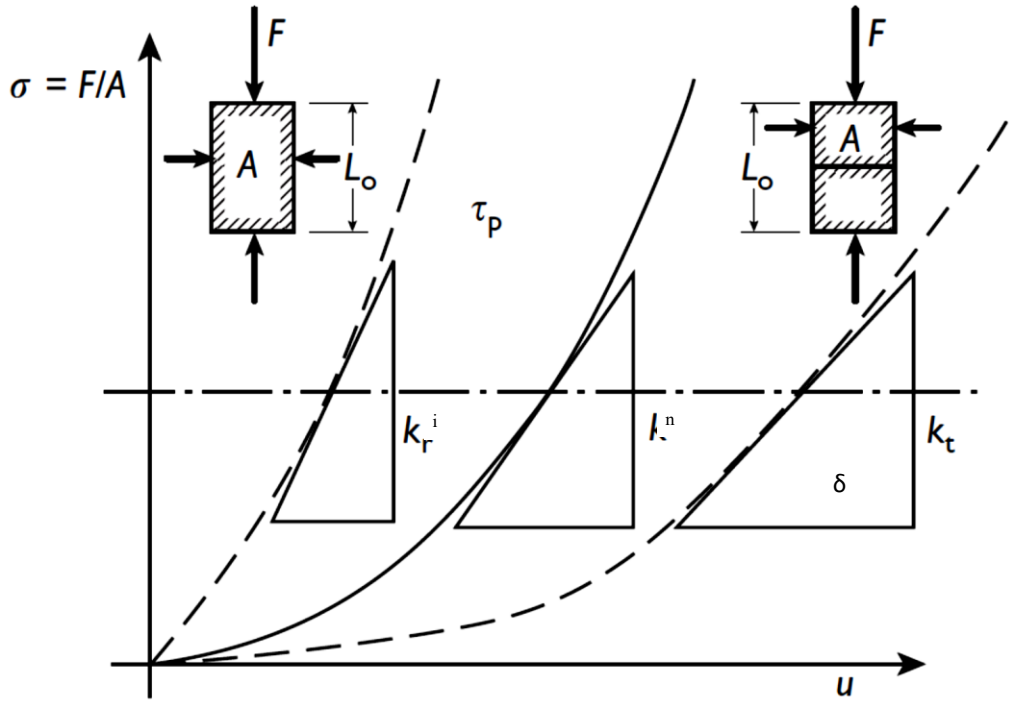

Figure 8-10 Joint normal stiffness (K_n) estimation using conventional procedure using direct shear test results on intact and jointed specimens (Pariseau, 2006)

Table 8-4 Normal stiffness (K_n) (kPa/mm) estimated from laboratory tests using conventional procedure

S1 σ_n (kPa) = 994			S2 σ_n (kPa) = 3038			S3 σ_n (kPa) = 3769		
Intact	Dis. sample	Dis.	Intact	Dis. sample	Dis.	Intact	Dis. sample	Dis.
1000	200	200	500	400	2500	1600	1000	3000

8.4.2.2 LACK OF DETAILED LABORATORY RECORDS

Due to the soft rock nature, only the discontinuity normal deformation is essentially needed to estimate the K_n, basically when there is no change in the pore pressure (i.e. ΔPp is zero) (Figure 8-12). Detailed records of the normal displacement immediately upon normal loading application on stages were not reported in the CCSh direct shear tests being analyzed in this investigation.

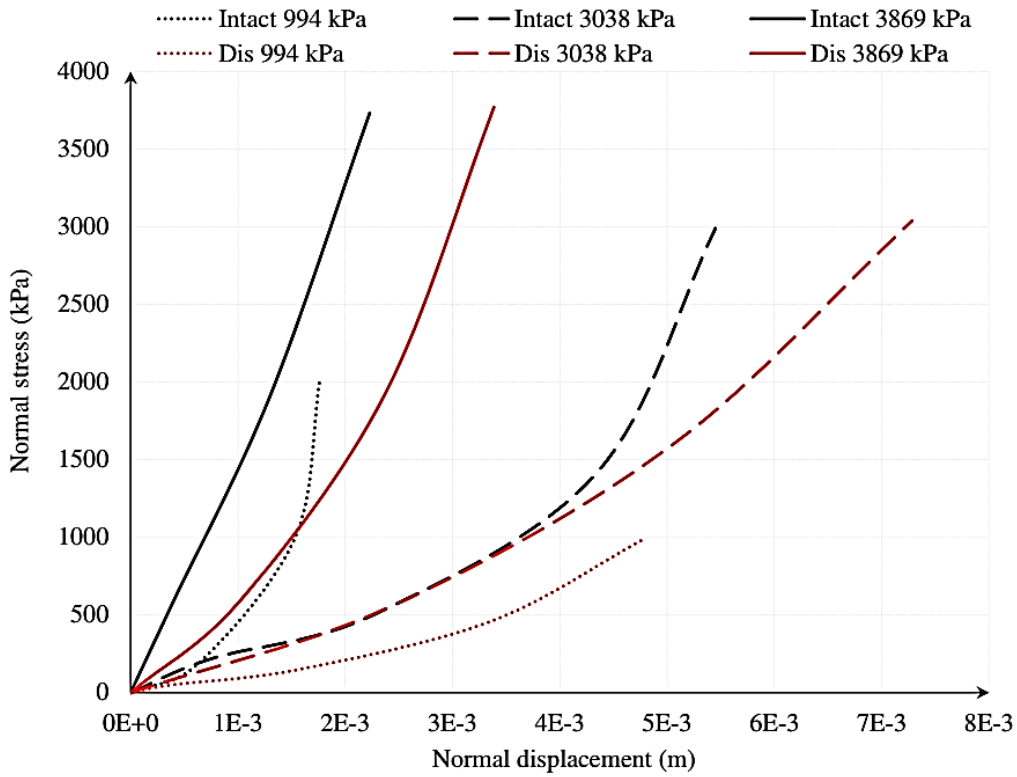

Figure 8-11 Normal stiffness (K_n) from laboratory results using conventional procedure

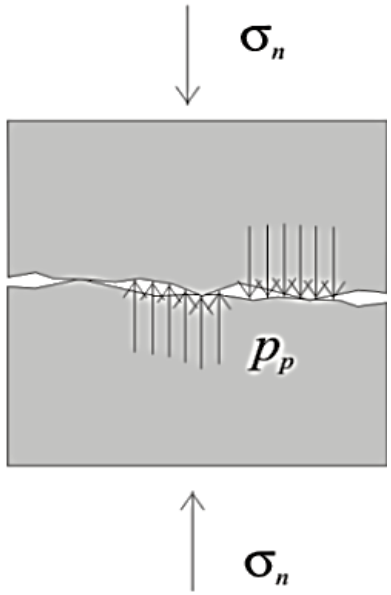

Figure 8-12 Normal discontinuity deformation and pore pressure mobilization immediately upon loading (Itasca, 2019)

In order to capture the instantaneous normal displacement (at zero change in pore pressure) of the pre-existing discontinuity, numerical simulations were resorted to understand and gain more details of how a natural discontinuity in CCSh (soft rock) specimen inside direct shear box deforms as the normal loading being applied.

8.5 NUMERICAL SIMULATIONS

Unlike laboratory testing, which is limited to represented and undisturbed specimens availability, one of the advantages of numerical simulations is that it enables repeating models testing under wide range of boundary conditions as desired. Due to lack of detailed laboratory (especially instantaneous) readings upon normal load application, numerical modelling was chosen as an assistance to closely simulate the discontinuity deformation upon consolidation loads application. Hydromechanically coupled fluid-flow formulation using Itasca 3DEC was used. The instantaneous normal displacement immediately after load application prior to any pore pressure change was assessed. This normal displacement value was used in the estimation of the K_n of CCSh natural discontinuities.

8.5.1 THEORETICAL BACKGROUND OF THE NUMERICAL SIMULATIONS

Theoretically, with each application of the normal load, the normal displacement is shared between the intact rock, discontinuity, and the fluid. The fluid is incompressible, so the remaining two components are participating in the total measured downward displacement when load is applied on the system. Incompressible fluid flow is occurring dominantly in discontinuities (planar flow channels).

Coupling between the fluid flow and mechanical deformation of the discontinuity was investigated in this chapter to assess the instantaneous mechanical response of the discontinuity at zero change in the pore pressure. The assessment was based on hydromechanically coupled fluid-flow assuming fully saturated analysis. No negative pore pressures were allowed. There are four aspects of the hydromechanical coupling in discontinuum rocks as illustrated in Figure 8-13 (Itasca 2016). The fluid pressure in the discontinuity affects its normal deformation. When the rock discontinuity is filled with fluid under a certain pressure (Figure 8-14a), the normal deformation of the discontinuity is a linear function of combination of the confining pressure (or total normal stress) on the rock, σ_n, and the fluid pressure, p_p (Figure 8-14b). The linear combination of σ_n and p_p produces same discontinuity deformation is termed an "effective stress," σ_n of the discontinuity. The discontinuity aperture, u, is a function of the local discontinuity stiffness (K_n) and fluid pressure (Pp). As illustrated in Figure 8-15, it is essential to estimate the pressure change in the

water “trapped” (i.e., under undrained conditions) within the rock discontinuity in particular due to the deformation of the rock discontinuity (Itasca 2016).

Figure 8-13 Hydromechanical coupling of deformation effect on pore pressure (Itasca, 2016)

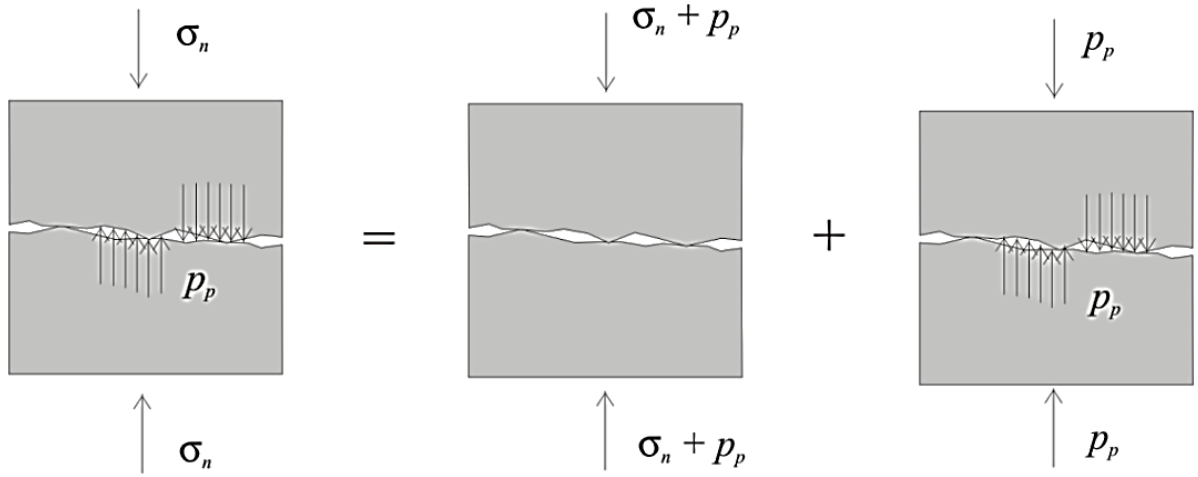

Figure 8-14 Effects of normal stress application and instantaneous pore pressure adjustments on discontinuity aperture closure (Itasca, 2019)

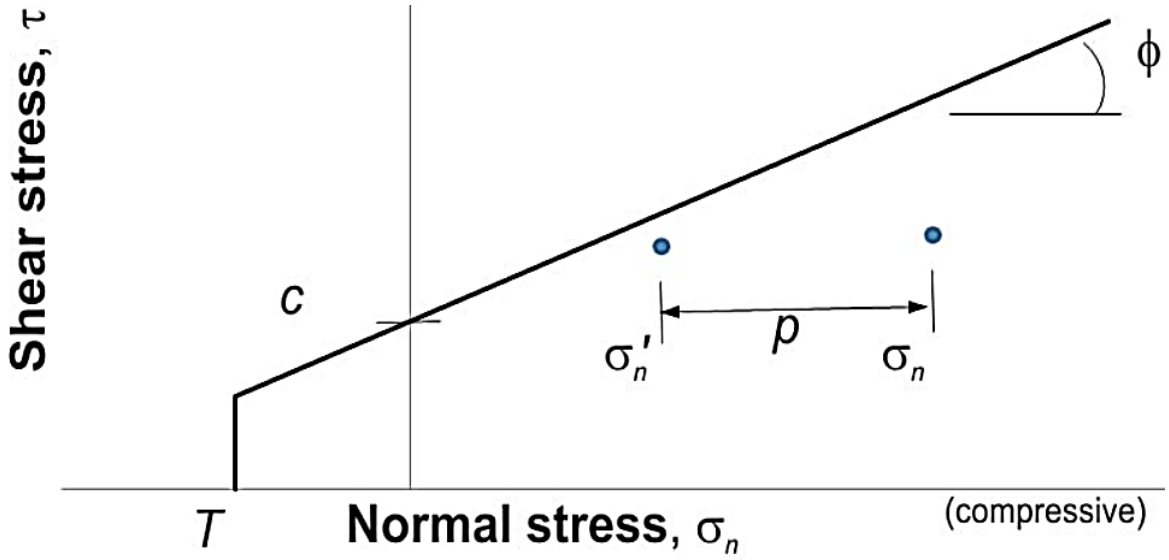

Figure 8-15 Effect of pore pressure (P) on sliding of aperture with cohesion, c, and friction angle ϕ (Itasca, 2016)

8.5.2 HYDROMECHANICALLY COUPLED FLUID-FLOW FORMULATIONS

Briefly, the general steps, of a one-way hydromechanically coupled fluid flow DEM analysis in 3D, are (Itasca Consulting Group Incorporation, 2016):

1. Apply in situ stress state and pore pressure,
2. Set up fluid boundary conditions,
3. Solve for fluid pressures, and
4. Solve for the effect of fluid pressures on the solid.

8.5.3 CONSTITUTIVE MODELS

In the current chapter, the model zones were assigned isotropic elastic constitutive models for simplicity and fast simulation times. The discontinuity was assigned a Coulomb slip constitutive model. In 3DEC, normal and shear aperture stiffness are represented as linearly elastic springs, where the shear resistance of the aperture is usually characterized by the Coulomb slip law. The aperture effective stress constitutive response implemented in 3DEC is relatively simple and is schematically illustrated in Figure 8-16. The relationship between hydraulic aperture and the effective stress is basically a bilinear curve with the effective stress coefficient α assumed to be 1.0.

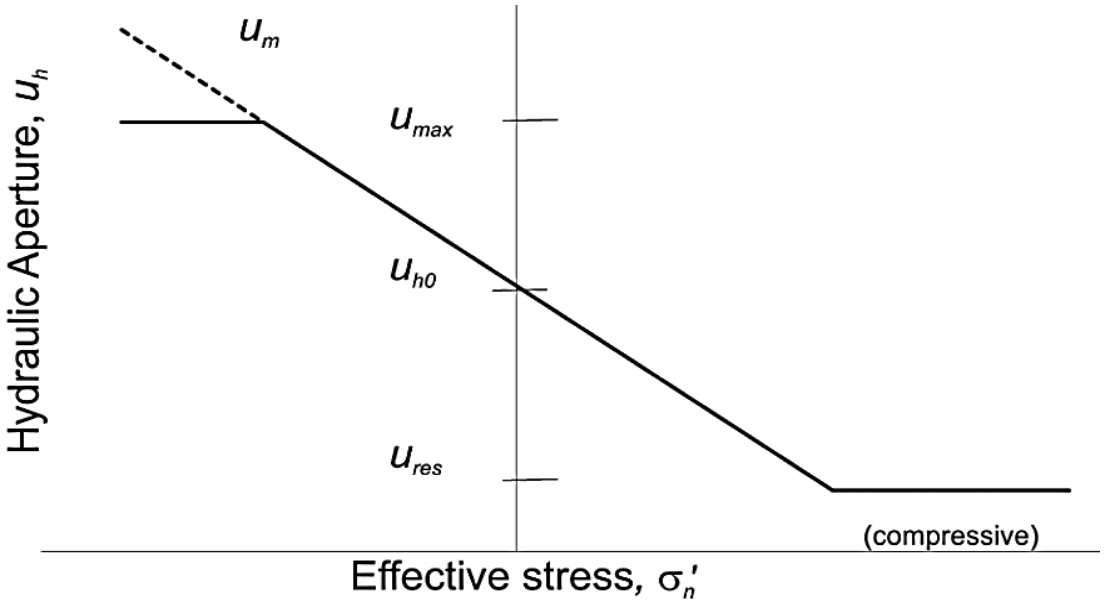

Figure 8-16 Hydraulic aperture-effective normal stress constitutive response (Itasca, 2016)

8.5.4 INPUT PARAMETERS

For fluid flow simulations within apertures, parameters representing the constitutive response of the aperture with respect to effective stress are typically defined by the user. The input parameters assumed in these simulations are listed in Table 8-8.

8.5.5 PRELIMINARY VALIDATION

Preliminary validation of the composed FISH scripts in ITASCA 3DEC interface to build, design and load horizontally discontinuum drum-shaped models mimicking the laboratory direct shear specimens (S1, S2, and S3) was carried out. To firstly accomplish a match and fit the laboratory reported results; normal stress, normal displacement, shear stress, and shear displacement magnitudes, of the 3D DEM models built were checked for validation where the time steps and loading rates were adjusted several times until a reasonable match was reached. Table 8-5, Table 8-6, and Table 8-7 include the validation details listing the percentage deviations for S1, S2, and S3 models mechanical results, respectively.

8.5.6 DISTINCT ELEMENT MODELLING (DEM)

The distinct element method (DEM) was used in the hydromechanically coupled simulations conducted in this study. The deformation was induced by a mechanical loading over relatively short timescales such that pore-pressure change can be neglected. This is generally called

an undrained deformation (zero change in pore pressure) simulation. Using the input parameters listed in Table 8-8, FISH scripts were built to replicate and compliment the laboratory consolidation tests. Three polyhedron drum-shaped models (Figure 8-17 mimicking Figure 8-5) have been built typically identical in dimensions to the three specimens tested in the laboratory.

Table 8-5 Validation of numerical simulation output versus laboratory recorded direct shear S1 results

Results	Laboratory	Numerical simulation	%
σ_n (Pa)	9.94×10^5	9.9961×10^5	99.994
Total consolidation (m)	4.267×10^{-3}	4.3086×10^{-3}	99.990
Shear stress (Pa)	2.3145×10^5	2.6259×10^5	99.866
Shear displacement (m)	8.36×10^{-4}	9.138×10^{-4}	99.907

Table 8-6 Validation of numerical simulation output versus laboratory recorded direct shear S2 results

Results	Laboratory	Numerical simulation	%
σ_n (Pa)	3.038×10^6	3.2227×10^6	99.939
Total consolidation (m)	7.281×10^{-3}	7.245×10^{-3}	99.995
Shear stress (Pa)	1.19436×10^6	1.2165×10^6	99.982
Shear displacement (m)	2.606×10^{-3}	2.5676×10^{-3}	99.985

First, a validation of the composed FISH scripts of the built 3D DEM models mechanical response results against the direct shear specimens mechanical behaviour laboratory results were conducted. In order to approve the composed 3DEC FISH scripts, a preliminary match between the laboratory recorded (raw) data and the designed DEM models results is needed. Various modelling elements such as; meshing, segmentation, stiffness, shear stress shear displacement constitutive behaviour, and number of time steps were designed and adjusted as needed to reach a reasonable fit.

8.5.6.1 BOUNDARY CONDITIONS

Three DEM models S1, S2, and S3 were built and Figure 8-17 includes two views of one of the drum-shaped models with a horizontal discontinuity under compressive loading and post shearing mimicking a CCSh specimen in direct shear (circular) apparatus. The boundary conditions on the three models were as illustrated in Figure 8-18. The values of consolidation loadings on stages as imposed in the laboratory are included in Table 8-9.

Table 8-7 Validation of numerical simulation output versus laboratory recorded direct shear S3 results

Results from	Laboratory	Numerical simulation	%
σ_n (Pa)	3.769×10^6	3.8243×10^6	99.985
Total consolidation (m)	3.382×10^{-3}	3.0814×10^{-3}	99.911
Shear stress (Pa)	1.807763×10^6	2.2436×10^6	99.759
Shear displacement (m)	6.6428×10^{-3}	3.3826×10^{-3}	99.036

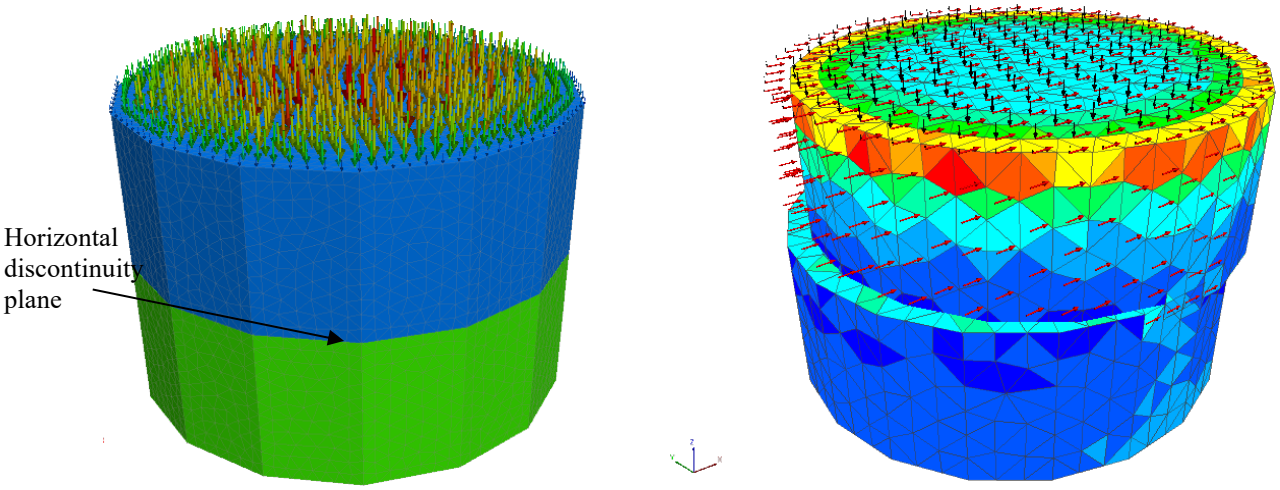

Figure 8-17 Drum-shaped DEM model including horizontal discontinuity subject to normal stress mimicking a cylinder specimen in direct shear box under normal compression

8.5.6.2 ESTABLISHING INITIAL EQUILIBRIUM

Each drum-shaped model included two deformable blocks (Figure 8-17). As an example, the number of edges in one of the models was 5123, interesting interior grid-points was 151, faces was 2193, sub-contacts was 1054, and grid points was 19381. Initial equilibrium was assured to

be established before starting any loading and at every subsequent loading stage as a condition for the next command in the FISH script to be executed. The value of the unbalanced force accumulated in the model governs whether the initial equilibrium has been achieved or not as illustrated in Table 8-10.

Table 8-8 Input parameters

Element	Property	Symbol	unit	Value	Reference
Fluid (brine)	Density	ρ	(kg/m^3)	1170	Francke and Thorade 2010
	Viscosity	μ	(Pa.s)	0.00175	Francke and Thorade 2010
	Fluid bulk modulus (True)	K_w	GPa	3	
	Apparent fluid bulk modulus	K_{aw}	GPa	3	
Discontinuity	Normal stiffness	K_n	MPa	450	Khani et al., 2018
	Shear stiffness	K_s	MPa	45	Khani et al., 2018
	Discontinuity friction angle	$\varphi_{discontinuity}$	(°)	9.8	
	Initial aperture	u_{h0}	m	1e-4	Itasca 2016
	Hydraulic aperture	u_h	m	1e-4	Itasca 2016
	Mechanical aperture	u_m	m	1e-4	Itasca 2016
	Residual aperture	u_{res}	m	1e-15	Itasca 2016
	Maximum aperture	u_{max}	m	1e-2	Itasca 2016
	Aperture spacing	S	m	2	Itasca 2016
Intact Rock	Bulk modulus	B	MPa	833	Pers. Comm.
	Shear modulus	G	MPa	178	Pers. Comm.
	Density	ρ	Kg/m^3	2129	Literature

The solve ratio was assigned a threshold that when reached, the next step in the FISH script gets processed. Number of time steps required to achieve initial equilibrium in every model was as shown in Table 8-10. Initial equilibrium is dependent on multiple factors; model size, its discretization, number of loading steps, magnitude of each loading step, final normal load, and the constitutive models assigned for the zones and discontinuities.

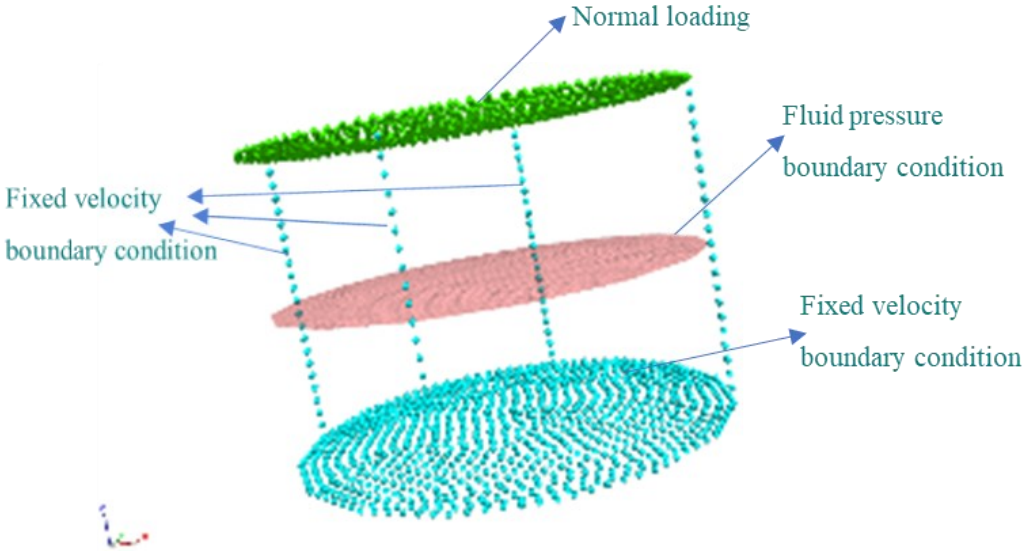

Figure 8-18 Model S1 boundary conditions

Table 8-9 Consolidation loading stages assumed in numerical simualtions per laboratory records

Specimen ID	Consolidation loading stages			Final (total)
	1st	2nd	3rd	σ_n (kPa)
S1	226	247	521	994
S2	560	902	1576	3038
S3	605	1320	1844	3769

8.5.6.3 HISTORY-MONITORING LOCATIONS

The pore pressure and displacement history-monitoring locations on each model were set as illustrated in Figure 8-19. These locations were monitored for the history of the pore pressure Figure 8-19a and normal Z-displacement Figure 8-19b.

8.6 NUMERICAL SIMULATION RESULTS

Estimation of K_n of natural discontinuities in soft argillaceous CCSh are presented and discussed in this section. Plots of the fluid pore pressure versus time-step at the five knot locations on the discontinuity level for the three models are shown in Figure 8-20. The evolution of pore pressure in the middle of the aperture is depicted in Figure 8-20 as well.

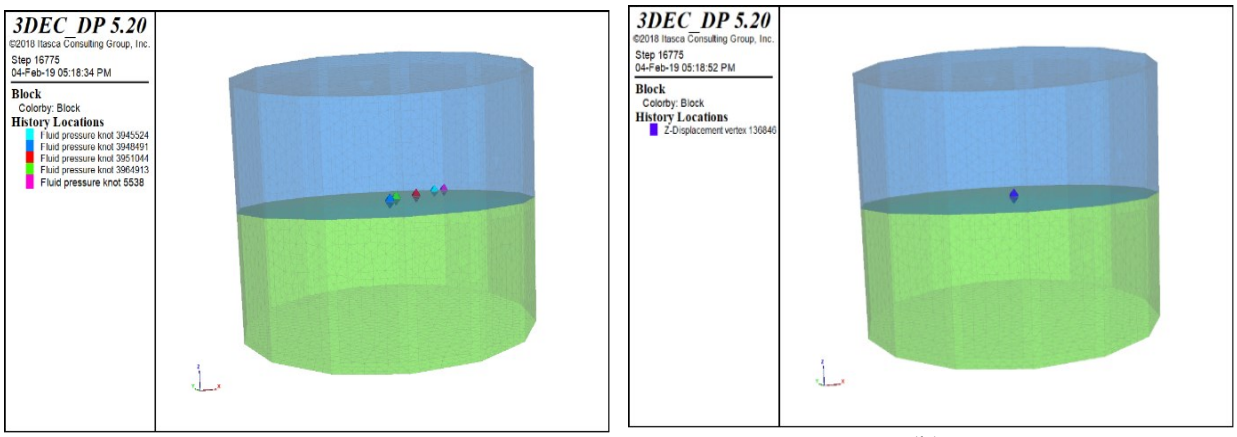

(a) (b)

Figure 8-19 History-monitoring at discontinuity level; (a) five knot locations for pore pressure and (b) one for normal Z-displacement

The pressure at the discontinuity level is generally close to the targeted (applied) normal (consolidation) stress (σ_n) on each model, indicating that the applied mechanical stress is completely taken up by the fluid. This is when the effective σ_n at the discontinuity is close to zero. Accordingly, the measured normal displacement at the discontinuity level is solely due to aperture closure and the matrix does not contribute in yet. The history of the normal displacement (Z-Displacement) at the discontinuity in each model is plotted in Figure 8-21b.

Vertical (normal) displacement contours in the whole model, at discontinuity, and at the top of the model are seen in Figure 8-22. Results of the numerical consolidation stages analyzed to estimate the K_n values. Plot of the σ_n versus the corresponding discontinuity (solely) vertical displacement as resulted from 3DEC numerical simulations is given in Figure 8-23. The tangent stiffness (K_n) for each discontinuity can be calculated at each normal stress (σ_n) step in Figure 8-23 as listed in Table 8-11. Based on 3D numerical simulations, the K_n of natural discontinuities in soft argillaceous formations ranges from 20,000 to 50,000 kPa/mm for the range of 994 to 3769 kPa normal stress. The K_n increases as the σ_n increases.

8.6.1 STIFFNESS COMPLIANCE CONSIDERATION

The normal displacements at two history locations (Figure 8-24a) were monitored at the model top and center (at the discontinuity level) and plotted in Figure 8-24b for comparison. Recalling the compliance factor, this comparison provides an effective method to assess the difference in the deformations recorded in a soft rock model.

Table 8-10 Maximum unbalanced force versus number of time steps

S1	11373	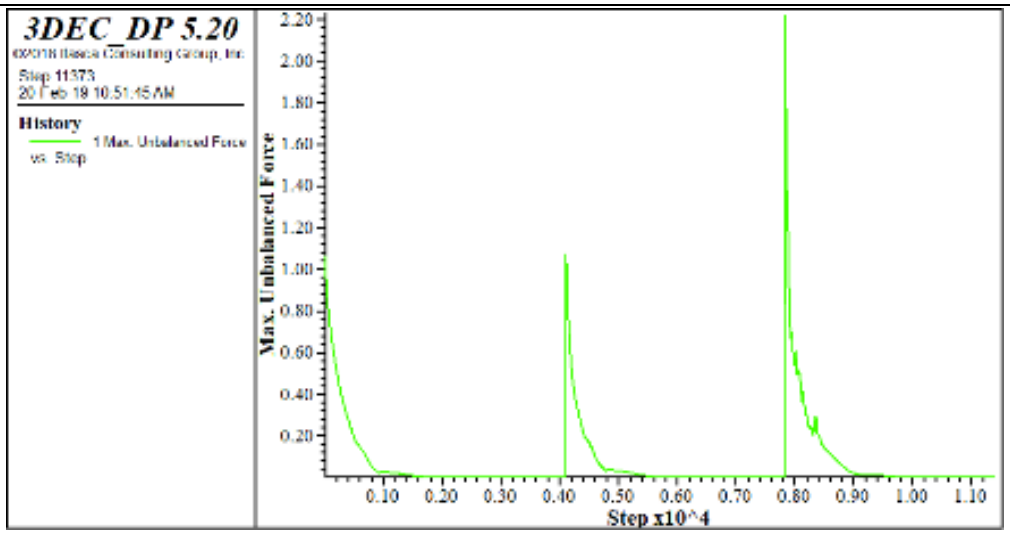
S2	10425	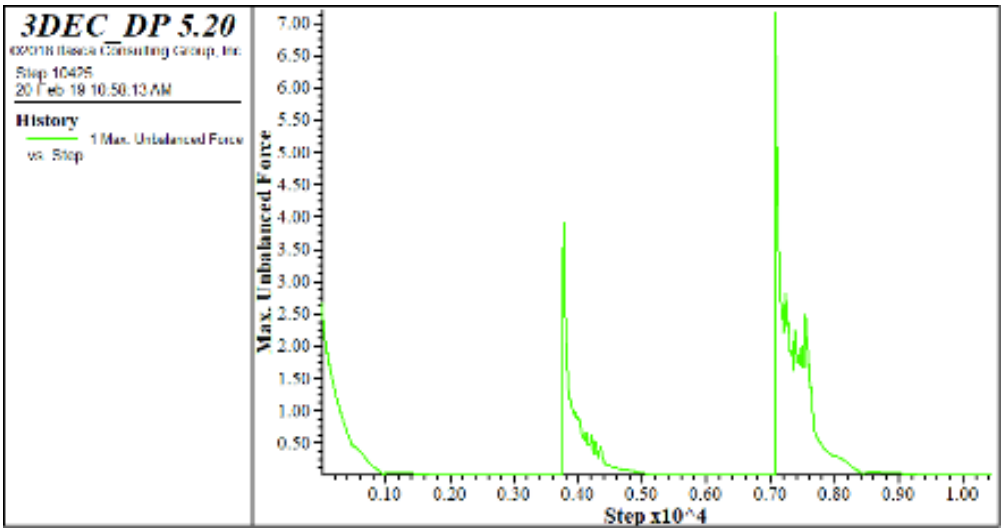
S3	10910	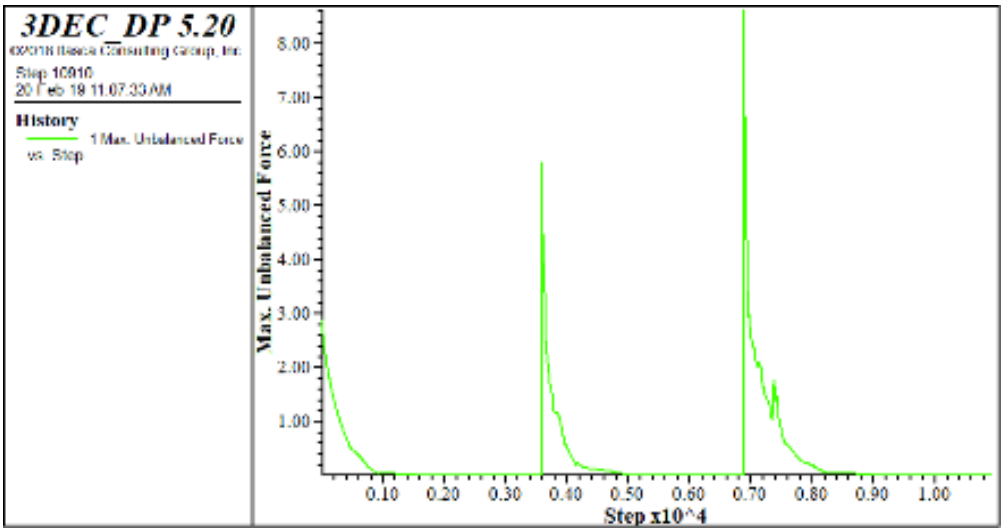

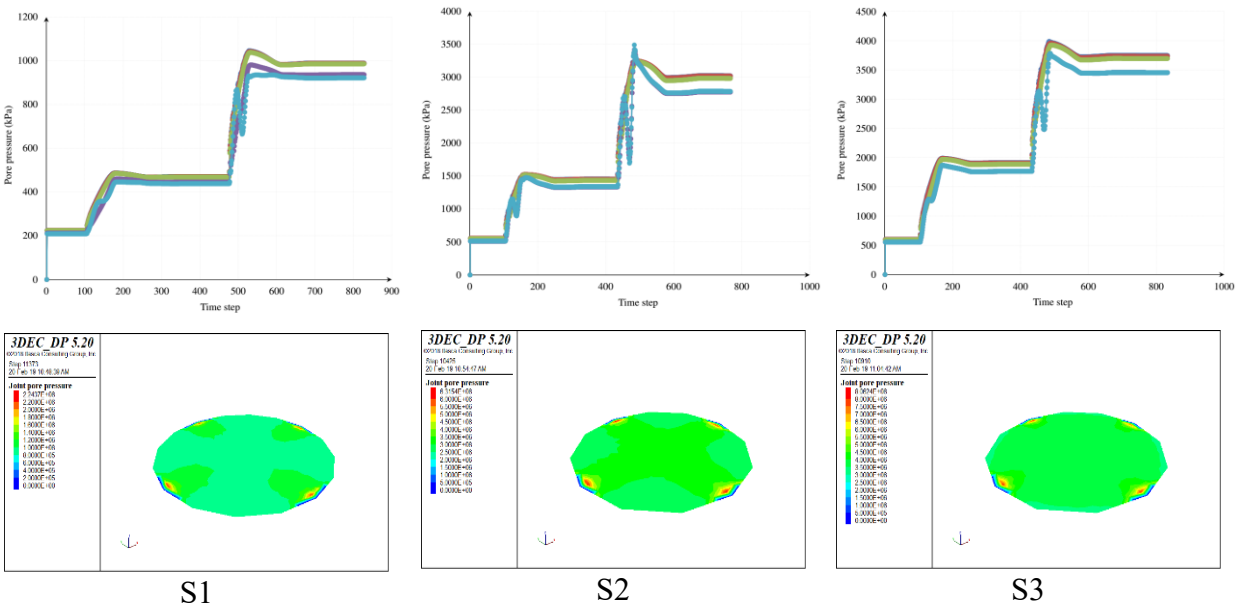

Figure 8-20 Pore pressure at five knot locations on discontinuity level and aperture pore pressure in three models

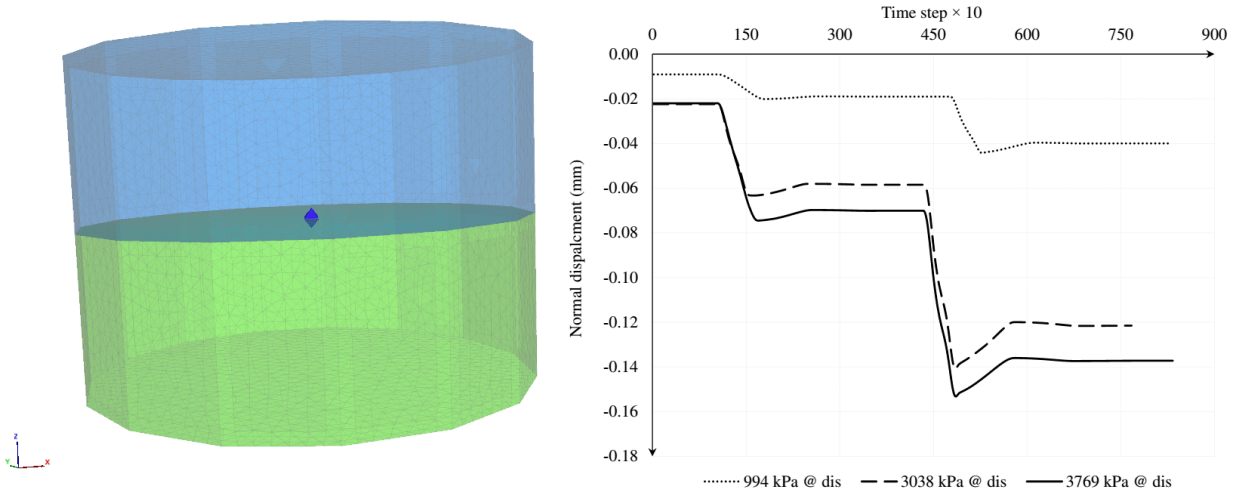

Figure 8-21 Normal displacement (aperture closure) at discontinuity (a) history monitoring location and (b) displacement versus time step for three models

Table 8-12 includes values of the discontinuity (solely) aperture closure as resulted from the numerical simulations at 0 change in the pore pressure (before any effective stress evolution and mobilization). The table also includes the resulted instantaneous normal displacement magnitudes measured at the model top due to each load addition, as a validation with what was typically reported in the laboratory readings. It is shown in this table that there is a difference between the values measured at the discontinuity level and values measured at the top of the model.

However, the later are typically the conventionally measured magnitudes in the laboratory direct shear tests.

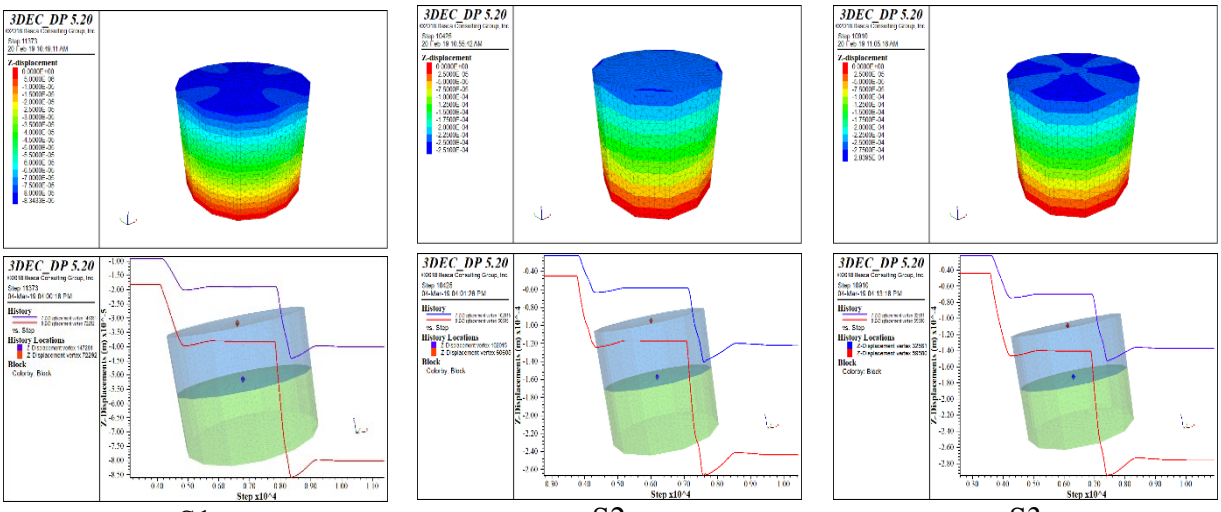

Figure 8-22 Normal displacement contours and plots of the measured normal dispalcments at two locations; at the discontinuity center and at center top of the three models

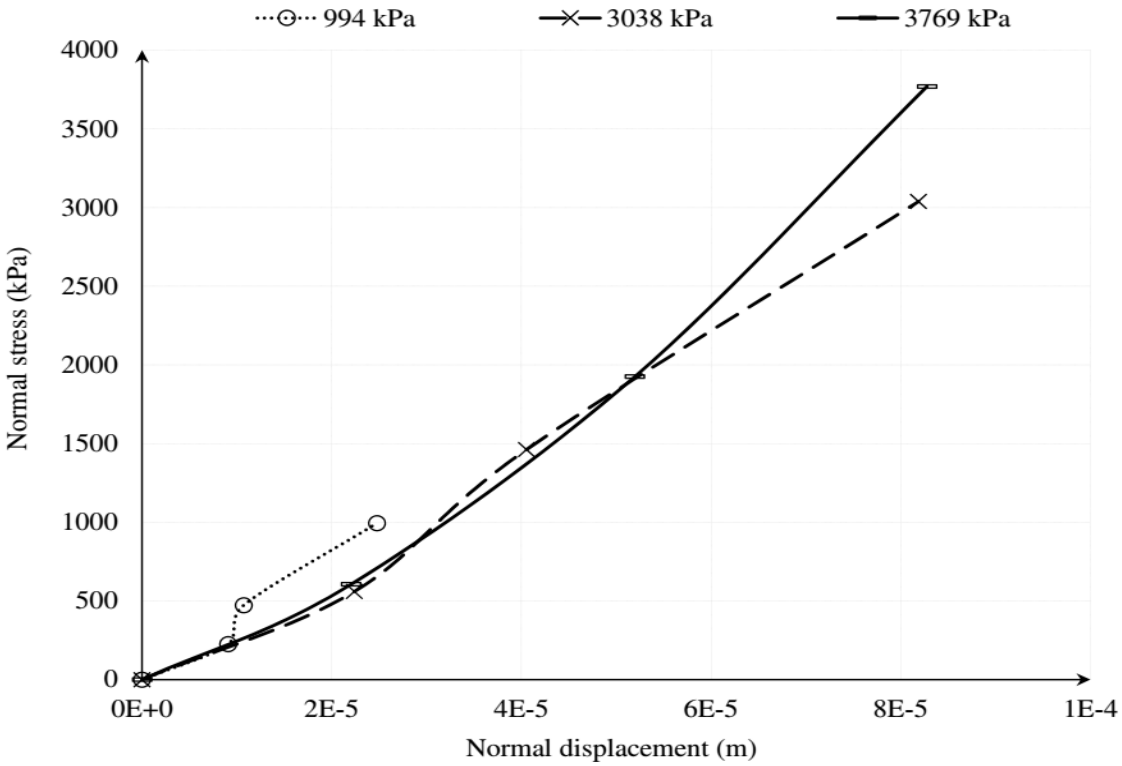

Figure 8-23 Normal stress-displacement resulted from hydro-mechanically coupled numerical simulation

Values measured at the model top are proved (Figure 8-25) to be not representative of what is happening at the discontinuity due to the stiffness issue of the soft CCSh in the direct shear mould. This confirms the basis of the research scientific hypothesis that there is a fundamental difference in compliance between hard and soft rock masses (Figure 8-25) as the latter deform and carry out of the model overall displacement unlike in the hard rock case. Hence especial precautions and custom procedures should be practiced when testing soft rocks in conventional direct shear apparatus (if any) with a special emphasize on the material stiffness consideration.

Table 8-11 Normal stiffness (K_n) based on hydro-mechanically coupled numerical simulations

Loading stage	S1		S2		S3	
	σ_n (kPa)	K_n (kPa/mm)	σ_n (kPa)	K_n (kPa/mm)	σ_n (kPa)	K_n (kPa/mm)
1st	226	20,000	560	30,000	605	30,000
2nd	473	40,000	1462	40,000	1925	40,000
3rd	994	40,000	3038	40,000	3769	50,000

Table 8-12 Aperture vertical downward displacement (solely) as resulted from 3DEC simulations

Loading step	S1			S2			S3		
	σ_n (kPa)	Total model δ_n (mm)	Aperture δ_n (mm)	σ_n (kPa)	Total model δ_n (mm)	Aperture δ_n (mm)	σ_n (kPa)	Total model δ_n (mm)	Aperture δ_n (mm)
1st	226	0.018	0.009	560	0.045	0.022	605	0.044	0.022
2nd	473	0.021	0.011	1462	0.078	0.040	1925	0.102	0.049
3rd	994	0.048	0.025	3038	0.149	0.080	3769	0.154	0.081

8.7 PROCEDURES COMPARISON

If Pariseau's (2006) conventional procedure for hard rock is applied, the K_n values of discontinuities in CCSh would be as listed in Table 8-13. Comparing, these values versus the values in Table 8-11 as in Table 8-14, emphasizes and confirms the thesis scientific hypothesis basis acknowledging the distinct differences between hard and soft rocks (Figure 8-25) and accordingly fulfills both the research first and second objectives.

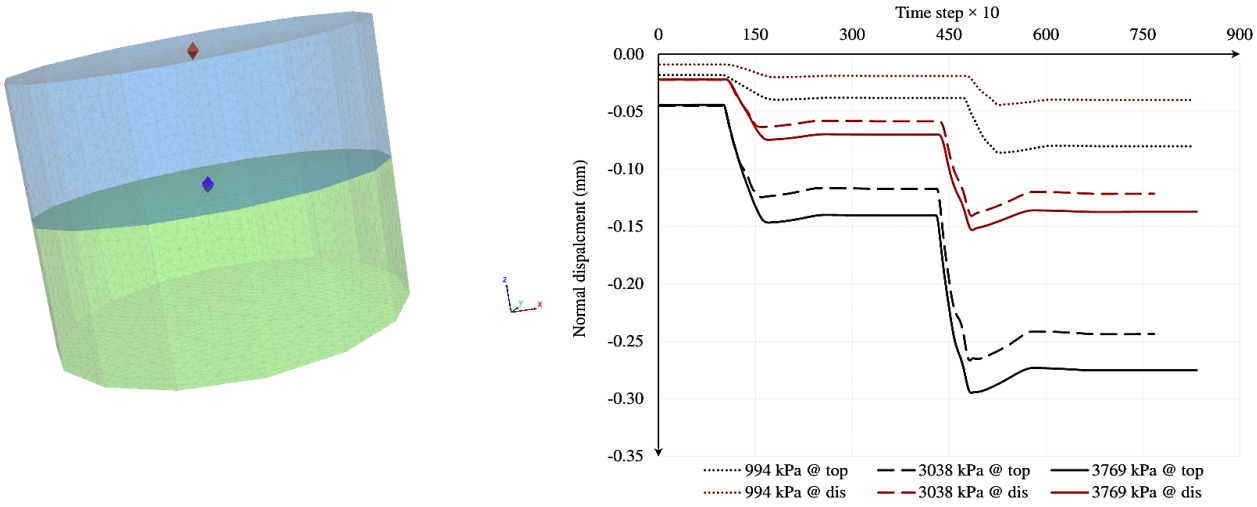

(a) (b)

Figure 8-24 Normal displacement (a) two monitoring locations on the model and (b) versus time step plot

Table 8-13 Normal stiffness (K_n) (conventional procedure) (Pariseau, 2006)

K_n	S1	S2	S3
(kPa/mm)	242	2514	3210.6

Table 8-14 Estimated normal stiffness (K_n) values comparison

Normal stress (kPa)	K_n (experimental) (kPa/mm)	K_n (numerical) (kPa/mm)
994	200	40,000
3038	2500	40,000
3769	3000	50,000

8.8 SUMMARY AND CONCLUSIONS

The main objective of this chapter stemmed from the need for a new insight into quantifying the mechanical stiffness of natural discontinuities in a soft argillaceous rock mass in Alberta. An integrated approach implementing experimental testing results and coupled numerical modelling was used. Results of four direct shear tests conducted in the laboratory under CNL condition fortunately became available and were used to estimate normal and shear stiffness (K_n and K_s) of discontinuities in a CCSh formation.

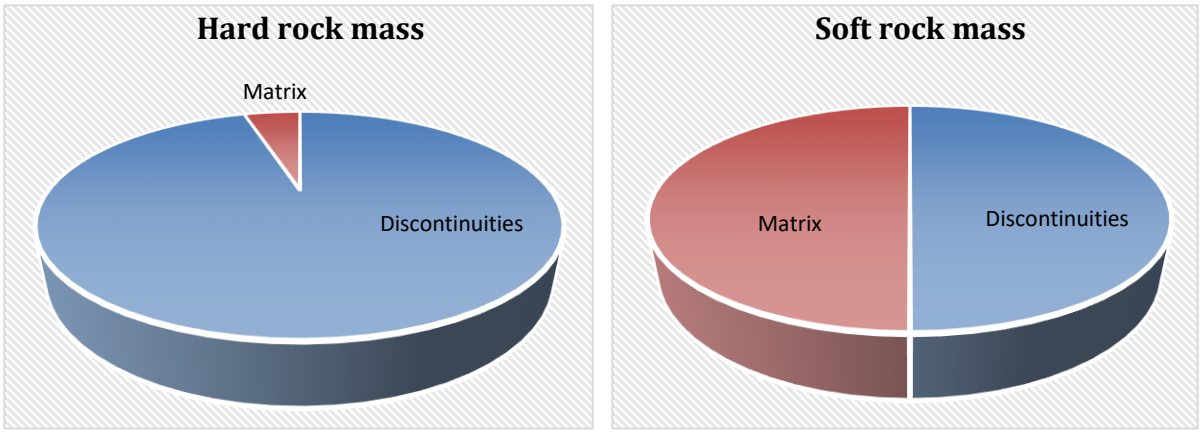

Figure 8-25 Schematic illustrating contribution of matrix versus discontinuities in rock mass deformability

During the quantification of the tangent K_s, negative values resulted, due to the non-linearity of the shear stress shear displacement relationships. Moreover, during the K_n estimation, the laboratory records were found to be lacking readings of the instantaneous normal displacement experienced immediately upon the application of the normal loads. Hence, there was a need for alternative methodologies to identify the mechanical stiffness values.

Secant modulus was used to estimate the K_s values. Hydromechanically coupled fluid-flow numerical simulations were used to isolate/separate and identify the instantaneous displacement of the discontinuity solely at zero (no) change in the pore pressure for K_n estimation.

The DEM analyses started by fitting the geomechanical response of the 3D models built versus the direct shear specimens data reported in the laboratory. When a reasonably matching geomechanical response is achieved, the DEM models were approved for analyses and considered a good mimic of the real specimens in the laboratory.

The numerical results showed that, the K_n increases as the normal stress increases and the K_n value of the natural discontinuities in the soft argillaceous rock ranges from 20,000 to 50,000 kPa/mm where, the K_s ranges from 80 to 1218 kPa/mm. It was found that, the numerical simulations produced non-matching K_n values compared to the values calculated using traditional (conventional) hard rock procedures. This confirms the dissertation scientific hypothesis, that there is a fundamental difference between hard and soft rocks and procedures and/or models derived based on hard rock matrix are not representatively capable to capture the soft rock' geomechanical behaviour. Study novelty resides in its pioneer attempt to constrain the values of K_n and K_s of pre-existing discontinuities in upper Cretaceous mudstones in Alberta concluding the second research objective aimed to characterizing soft rock mass (CCSh).

Generally, the importance of assessing discontinuities K_n stems from its critical and direct effect on the rock mass deformability, permeability, and storativity/transmissivity (hydraulic aperture). Constraining the K_n is helpful in estimating a rock mass equivalent deformation modulus. Variations in the discontinuities mechanical stiffness influence the shear strength of a rock mass. However, the normal and shear stiffnesses (K_n and K_s) of natural discontinuities in rock masses are significantly influenced by the σ_n magnitude. Hence, close attention should be paid when lower σ_n magnitudes are expected because shallow formations under low confinement are more vulnerable to dramatic permeability changes.

Soft rocks are unlike hard rocks, hence each soft rock case needs to be evaluated separately. Typical recommendations of $K_n = 10 \times K_s$ should not be applied to the class of (hard soil soft rock) material studied here, unless this has been proved correct via integrating laboratory testing results and 3D coupled numerical simulations. To conclude, traditional procedures developed to estimate the mechanical stiffness of discontinuities in hard rocks should not be always used nor unconsciously reapplied to soft rock masses. Integrating the results of experimental tests and 3D numerical simulations should be the way to quantify the mechanical stiffness of natural discontinuities in soft rock masses. Laboratory testing should always be conducted on undisturbed specimens. The introduced procedure is recommended to be used and applied in assessing mechanical stiffness of pre-existing discontinuities in soft rock masses. A strength point of this study resides in the preliminary validation of the DEM models versus the laboratory behaviour prior adopting and approving the developed FISH scripts for advanced hydro-mechanically coupled investigations. It is important though to note that the results of the proposed procedure are likely applicable only to the geological formation tested in this study under the investigated loading ranges.

CHAPTER 9 CONCLUSION AND RECOMMENDATIONS

9.1 SUMMARY AND CONCLUSIONS

In western Canada, the Clearwater Formation is laterally continuous and consists largely of clay shale with a minor component of interbedded siltstone or sandstone. Regional geological processes have created a laminated structure within the Clearwater clay shale (CCSh) distinguished with epigenetic features such as fissures and fractures. From a geotechnical engineering point of view, CCSh is a soft, fully saturated, and over consolidated shale deposit. All these features together resulted in a heterogenous material with anisotropic strength and deformation properties. Generally, when encountered these clay shales known to be challenging and complex to deal with in engineering projects.

Due to its large lateral extent, the CCSh serves as the caprock in Alberta for almost all steam assisted gravity drainage (SAGD) projects. Caprock integrity assessments are typically undertaken to ensure the CCSh caprock (CCShC) performs adequately as a containment seal of reservoir fluids during the high pressure and temperature SAGD decades-long operation. The heterogeneity, in particular the presence of discontinuities such as fissure, joints and fractures, within the CCShC requires special attention to ensure representative constitutive models are adopted during integrity assessments. Unfortunately, models for these class of heterogeneous systems are developed from studies focused on rock formations where the compliance of the fractures dominates the behavior of the rock mass.

In this research, it has been postulated that models developed based on hard rock matrix are uncapable to representatively capture the soft CCSh geomechanical behaviour and these models must not be interchangeably applied. Consequently, the objectives of this research included illustrating the fundamental distinction between hard and soft rocks, proposing a characterization protocol for a soft rock mass (i.e. CCSh) and highlighting the importance and need to recognize the discontinuities existence in the CCShC. The research objectives were successfully fulfilled supporting the scientific hypothesis unequivocally. The resulted findings and conclusions are summarized below based on the dissertation chapters' sequence.

- After performing a comprehensive literature review of the discrete fracture network (DFN) history, evolution, and modelling techniques covered in Chapter 2, a geological

clarification, of the distinguished structural features regionally exist in the CCSh formation, was presented in Chapter 3. Chapter 4 included fundamental comparisons at multiple levels between hard and soft rocks. Discontinuities compliance (C_d) to matrix compliance (C_m) ratios have been generated based on literature for tens of rock types. These ratios were employed to propose thresholds delineating boundaries to identify soft, medium-hard, and hard rocks. The following relationships were generated as guides to boundaries defining categories of discontinuum rock types based on their compliance ratios:

$$\frac{C_d}{C_m} \leq 0.001 - 0.01 \text{ for hard rocks}$$

$$\frac{C_d}{C_m} = 0.01 - 0.1 \text{ for medium} - \text{hard rocks}$$

$$\frac{C_d}{C_m} \geq 0.1 - 1 \text{ for soft rocks}$$

- Numerical analyses in 2D, including discontinuum finite element modelling (FEM) were utilized to emphasize and support the fundamental distinctness between hard and soft rocks deformability. Similarly, a three-dimensional (3D) distinct element modeling (DEM) study was conducted asserting the contrast of the behaviour and deformability between two rock type extremes.
- Multiple data processing platforms were examined and utilized to process a light detection and ranging (LiDaR) field survey, of a CCSh mine bench in Alberta, in form of LASer (LAS) file format, as explained in Appendix A. Triangulated irregular networks (TINs) were generated based on the dense point cloud dataset and the geostatistics of the extracted structural features were extracted. These geostatistics were utilized to build a 3D DFN that was employed later in geomechanical modelling studies looking into the influence of discontinuities within caprocks.
- As a required element in design of steam injection maximum operating pressure (MOP) into oil sands reservoirs and to control the coupling consequences due to pressure and temperature rise, the behaviour of fractured CCShC during the operation of SAGD process was examined. 3D coupled geomechanical simulations of the CCShC overlying a SAGD reservoir were completed. These simulations included sensitivity analyses of the effect of confinement, i.e. overburden (OB), degree of discontinuity

configuration and the MOP magnitude on the surface heave, shear stress, tensile stress values within the CCShC as well as the microscale (discontinuities) mechanical behaviour.

- As anticipated, the OB, degree of discontinuity configuration and the MOP magnitude were proven to affect the integrity, deformability, and stability of the caprock. It is hence crucial to robustly understand the alteration in the geomechanical behaviour of a CCShC overlying a SAGD reservoir. As the number of discontinuities increased in the CCShC models, the maximum upward displacement of the caprock model decreased as a result of local deformations, both normal and shear displacements, along the discontinuities. Slippage along the discontinuities was governed by the geometry of the DFN. The presence of a single favorably oriented discontinuity was shown to significantly alter the deformation pattern within the CCShC.
- For discontinuous systems (e.g. CCSh), it is traditionally and conveniently important to determine the size of the rock mass' representative elementary volume (REV) when estimating its equivalent mechanical parameters. To assess the REV of CCSh, 3D numerical analyses were conducted considering both strength anisotropy as well as scale effect. Based on these analyses, it was not possible to establish an REV for the CCSh.
- An alternative methodology, involving the use of a virtual rock mass laboratory (VRMLab) approach, was adopted to assess the equivalent continuum model applicability for the CCSh. Simulations using the VRMLab were unable to produce consistent nor diagonally symmetric elastic equivalent compliance tensors of fractured blocks of CCSh over two macroscales (7 m × 7 m × 7 m and 9 m × 9 m × 9 m). These series of studies provide evidence that the concept of REV may not apply to this class of material (discontinuous overconsolidated soft rocks) and that the equivalent continuum modeling approach applicability should be always assessed prior adoption.
- Given the importance of discontinuities deformation on overall caprock deformability, stiffness and strength, determining the CCSh discontinuities' normal and shear stiffnesses (K_n and K_s) is a key element in assessing caprock integrity. For any rock type, however, quantifying the K_n and K_s is a challenging task nonetheless it becomes even more complex for hard soil /soft rock material such as the CCSh. A novel

procedure was introduced to estimate the mechanical K_n and K_s of the natural discontinuities within CCSh integrating the use of experimental results as well as coupled hydro-mechanical numerical analyses. The K_n value of the natural discontinuities in soft argillaceous CCSh was found to range from 20 MPa/mm to 50 MPa/mm as the σ_n changes from 994 kPa to 3769 kPa, respectively. While the K_s ranged from 0.08 MPa/mm to 1.2 MPa/mm.

The research results generally showed that the effect of problem scale, discontinuity pattern and properties can be readily and powerfully investigated using the DEM. The study is of a direct importance to the SAGD projects practitioners especially shallow reservoirs. It is important to stress on that soft rock masses are unlike hard rock masses in compliance, deformability, geomechanical behaviour, scale effect, discontinuities stiffness magnitude, ratios, estimation procedures, strength and stiffness degradation and anisotropy. Models developed based on hard rock matrix' assumption should not be assumed to be valid for describing the behaviour of soft CCSh.

9.2 CONTRIBUTIONS

The importance of studying the rock mass's structural characteristics is essential in assessing changes of porosity and permeability. The material under investigation is over-consolidated, naturally fractured, anisotropic, heterogeneous, and fully saturated soft rock mass. In Alberta, this material happens to work as the basic hydraulic seal and safeguard caprock on top of SAGD oil sands reservoirs. Over decades of thermal stimulation operations, the high pressure and temperature induce stresses from the ongoing processes due to the volumetric changes within the pay zone and as the steam chamber grows, underneath the CCShC. This thesis constituted number of contributions particularly stressing on how differently the CCShC should be examined, assessed, and designed.

The contributions of this dissertation include:

1. Presented field survey data confirming the presence of natural discontinuities in the CCSh;
2. Highlighted with evidence the importance to recognize the fundamental distinctness between the behaviour of hard and soft rocks;

3. Provided research outcomes supporting the conclusion that models developed for describing the behavior of fractured hard rock masses are not applicable for fractured soft rock masses;
4. Characterized a discontinuum CCShC using a unique in situ LiDaR survey (point cloud);
5. Demonstrated the importance of the integrated impact of confinement (overburden), degree of caprock discontinuities configuration and maximum operating pressures (MOP) on the geomechanical performance of a CCShC;
6. Illustrated that the conventional concept of the REV assessment and establishment of equivalent continuum properties for a soft rock mass (CCSh) is extremely challenging; and
7. Quantified the mechanical stiffness of natural discontinuities in CCSh based on 3D hydro-mechanical coupled numerical simulations of experimental tests.
8. Proposed a boundary-identification scheme based on rock mass compliance ratio.

9.3 RECOMMENDATIONS FOR ACADEMIC RESEARCHERS AND INDUSTRY PRACTITIONERS

For the academic practice, it is recommended to:

- Avoid modelling the CCSh as continuous homogeneous isotropic linear elastic (CHILE);
- Always, observe scale effects;
- Use 3D modelling when studying the over-consolidated soft discontinuum CCSh;
- Develop and adopt a realistic DFN;
- Employ distinct element modelling which is especially recommended for jointed and blocky material; and
- Utilize strain softening constitutive model for the intact CCSh.

For industrial applications, it is recommended to:

- Refrain from using (conventional) CHILE models derived for hard rocks in the CCShC integrity assessment and design;
- Always observe the discontinuities in the CCShC integrity assessment;

- Conduct hydro-geo-mechanical coupled analyses, integrate all associated factors, between the oil sands reservoir and the overlying caprock;
- Acquire in situ structural geology information of the rock mass under consideration;
- Perform macroscale simulations to encompass the scale effect;
- Directional variations of strength, stiffness, and deformability of a CCSh must be treated properly with respect to the directions of in situ stresses; and
- Procedures based on field geological (case-based) characterization of the soft rock mass at the macroscale in addition to laboratory experiments on preserved undisturbed specimens designed specifically for soft rocks should be integrated and implemented in CCSh projects.

9.4 FUTURE RESEARCH

Additional areas for further investigation include:

- Acquisition and processing of additional LiDaR datasets of mining benches within the CCSh. It is suggested that datasets be acquired for different areas within the oil sands region and for one particular location, captured over consecutive times as the mining bench is advanced.
- A limited experimental dataset was analyzed for this research and these experiments were not primarily executed to assess K_n and K_s. It is recommended that an extensive laboratory testing program on discontinuous clay shale specimens to be carried out.
- With the refined constitutive behavior that would be generated from the additional laboratory studies, it is recommended that sequentially coupled reservoir geomechanical macro-scale simulations to be conducted that inherently include both the behavior of the caprock and the reservoir within the SAGD process.
- While the conventional approaches selected in this research were unable to establish an REV or equivalent continuum properties for fractured soft rocks, research on other approaches such as dynamic or energy-based techniques could be explored.
- While visual evidence is clear for the presence of generic formation discontinuities in the mine benches occur in CCSh region, it is not totally confirmed whether all

features captured in a LiDaR survey are exclusively inherent defects or there are defects that have developed due to excavation unloading. It is recommended that additional field studies supported by numerical modelling be undertaken to define a methodology for discerning and replicating the evolution of discontinuities within the CCSh.

- Evaluating the sensitivity of values of joint properties on caprock heave.

BIBLIOGRAPHY

Ansari, S., Haigh, R., Khosravi, N., Khan, S., Han, H., & Vishteh, M. (2012). Caprock integrity case study for non-thermal polymer flooding project using 4D reservoir coupled geomechanical simulation, *2*, 1–15.

Badelow, F., Best, R., Bertuzzi, R., & Maconochie, D. (2005). Modelling of defect and rock bolt behaviour in geotechncial numerical analysis for Lane Cove Tunnel. In *AGS AUCTA Mini-Symposium: Geotechnical Aspects of Tunnelling for Infrastructure Projects* (pp. 1–9).

Bagheri, M., Shafiezadeh, N., & Hajihassani, H. R. (2006). Discontinuum and Continuum Modeling of Masjed E Soleyman Power House Cavern. *EUROCH 2006 - Multiphysics Coupling and Long Term Behaviour in Rock Mechanics*, 689–693.

Bazant, Z. P., Belytschko, T. B., & Chang, T. (1984). Continuum theory for strain-softening. *Journal of Engineering Mechanics*, *110*(12), 1666–1692.

Bidgoli, M. N., Zhao, Z., & Jing, L. (2013). Numerical evaluation of strength and deformability of fractured rocks. *Journal of Rock Mechanics and Geotechnical Engineering*, *5*(6), 419–430. https://doi.org/10.1016/j.jrmge.2013.09.002

Bisdom, K., Bertotti, G., & Nick, H. M. (2015). Outcrop-based Geomechanical Fracture Aperture and Flow Modeling : The Importance of Shear on Flow *, *41606*.

Bondarchuk, A., Ask, M., Dahlström, L., Knutsson, S., & Nordlund, E. (2012). *Rock mass behavior under hydropower embankment dams with focus on fracture erosion and rock mass stability (Doctoral dissertation)*. Lulea University of Technology, Luleå.

Boon, C. W., Houlsby, G. T., & Utili, S. (2015). A new rock slicing method based on linear programming. *Computers and Geotechnics*, *65*, 12–29. https://doi.org/10.1016/j.compgeo.2014.11.007

Buckley, S. J., Kurz, T. H., Howell, J. A., & Schneider, D. (2013). Computers & Geosciences Terrestrial LiDaR and hyperspectral data fusion products for geological outcrop analysis. *Computers and Geosciences*, *54*, 249–258. https://doi.org/10.1016/j.cageo.2013.01.018

Cappa, F., Guglielmi, Y., Rutqvist, J., Tsang, C. F., & Thoraval, A. (2006). Hydromechanical modelling of pulse tests that measure fluid pressure and fracture normal displacement at the Coaraze Laboratory site, France. *International Journal of Rock Mechanics and Mining Sciences*, *43*(7), 1062–1082.

Chen, S. H., He, J., & Shahrour, I. (2012). Estimation of elastic compliance matrix for fractured rock masses by composite element method. *International Journal of Rock Mechanics & Mining Sciences*, *49*, 156–164. https://doi.org/10.1016/j.ijrmms.2011.11.009

Chen, Y., & Zhou, C. (2011). Stress/strain-dependent properties of hydraulic conductivity for fractured rocks. *Developments in Hydraulic Conductivity Research*, *1*(28 February).

Chesnaux, R., Allen, D. M., & Jenni, S. (2009). Regional fracture network permeability using outcrop scale measurements. *Engineering Geology*, *108*(3–4), 259–271. https://doi.org/10.1016/j.enggeo.2009.06.024

Chin, L., Y., Tomberlin, T. A., Ramos, G. G., & Chalturnyk, R. J. (2012). Evaluation of caprock stability by coupled modeling of geomechanics and reservoir simulation under steam injection for producing oil sands reservoirs. *American Rock Mechanics Association*, 1–16.

CNRL (Canadian Natural Resources Limited). 2015. Primrose Flow to Surface Final Report. Calgary, AB: CNRL, 4179 p.

Collins, P. M., Incorporated, P. G., Walters, D. A., Reservoir, T., & Limited, S. (2013). Effective caprock determination for SAGD projects, (March), 15–17.

Corkum, A. G., & Martin, C. D. (2007). The mechanical behaviour of weak mudstone (Opalinus Clay) at low stresses. *International Journal of Rock Mechanics & Mining Sciences*, *44*, 196–209. https://doi.org/10.1016/j.ijrmms.2006.06.004

Cruden, D. M., Thomson, S., & Tsui, P. C. (1989). The geotechnical characteristics of an ice-thrust mudstone, Wabamun Lake area, Alberta. *Canadian Geotechnical Journal*, *26*(2), 227–234.

Davy, P., Le Goc, R., & Darcel, C. (2013). A model of fracture nucleation, growth and arrest, and consequences for fracture density and scaling. *Journal of Geophysical Research: Solid Earth*, *118*(4), 1393–1407. https://doi.org/10.1002/jgrb.50120

Dreuzy, J. De, Méheust, Y., & Pichot, G. (2012). Influence of fracture scale heterogeneity on the flow properties of three-dimensional discrete fracture networks (DFN), *117*(May), 1–21. https://doi.org/10.1029/2012JB009461

Duan, Y., Li, X., Maerz, N., & Otoo, J. (2011). Automatic 3D facet orientations estimation from LIDAR imaging. In *in the Proceddings of 2011 NSF Engineering Research and Innovation Conference* (pp. 3–7).

Eberhardt, E., Thuro, K., & Luginbuehl, M. (2005). Slope instability mechanisms in dipping interbedded conglomerates and weathered marls — the 1999 Rufi landslide, Switzerland, *77*,

35–56. https://doi.org/10.1016/j.enggeo.2004.08.004

ERCB. (2010). *Total E&P Canada Ltd. - Surface Steam Release of May 18, 2006 Joslyn Creek SAGD Thermal Operation*.

Francioni, M., Salvini, R., Stead, D., & Litrico, S. (2014). A case study integrating remote sensing and distinct element analysis to quarry slope stability assessment in the Monte Altissimo area, Italy. *Engineering Geology*, *183*, 290–302. https://doi.org/10.1016/j.enggeo.2014.09.003

Frash, L. P., Carey, J. W., Lei, Z., Rougier, E., Ickes, T., & Viswanathan, H. S. (2016). High-stress triaxial direct-shear fracturing of Utica shale and in situ X-ray microtomography with permeability measurement. *Journal of Geophysical Research: Solid Earth*, (121), 5493–5508. https://doi.org/10.1002/2016JB012850

Gao, F. Q., & Stead, D. (2014). The application of a modified Voronoi logic to brittle fracture modelling at the laboratory and field scale. *International Journal of Rock Mechanics & Mining Sciences*, *68*, 1–14. https://doi.org/10.1016/j.ijrmms.2014.02.003

Gitman, I. M., Askes, H., & Sluys, L. J. (2007). Representative volume: Existence and size determination. *Engineering Fracture Mechanics*, *74*(16), 2518–2534. https://doi.org/10.1016/j.engfracmech.2006.12.021

Grasselli, G., & Egger, P. (2003). Constitutive law for the shear strength of rock joints based on three-dimensional surface parameters, *40*, 25–40.

Guindon, L. M. (2015). Caprock analysis - A practical approach. *Journal of Canadian Petroleum Technology - Tech Briefs*, (September), 280–282.

Gutierrez, M., & Youn, D. (2015). Effects of fracture distribution and length scale on the equivalent continuum elastic compliance of fractured rock masses. *Journal of Rock Mechanics and Geotechnical Engineering*, *7*(2015), 626–637. https://doi.org/10.1016/j.jrmge.2015.07.006

Heidbach, O., Rajabi, M., Cui, X., Fuchs, K., Müller, B., Reinecker, J., … Zoback, M. (2018). Tectonophysics The World Stress Map database release 2016 : crustal stress pattern across scales. *Tectonophysics*, *744*(July), 484–498. https://doi.org/10.1016/j.tecto.2018.07.007

Hencher, S. (2013). *Practical Engineering Geology*. (C. Press, Ed.) (Third). Boca Raton, FL: Taylor & Francis Group.

Hoang, T. T. N., Gasc-Barbier, M., Marache, A., Riss, J., & Sulem, J. (2010). Morphological analysis of natural marble discontinuities. In *Rock Joints and discontinuities* (pp. 199–262).

2010 Taylor and Francis Group, London.

Hsu, S., & Nelson, P. (1993). Characterization of Cretaceous clay shales in North America, (February 2017).

Ince, R. (2013). Investigation of fracture parameters of self-compacting concrete produced with marble powder by peak-load method, (August 2014).

Islam, M. A., & Skalle, P. (2013). An Experimental Investigation of Shale Mechanical Properties Through Drained and Undrained Test Mechanisms. *Rock Mechanics and Rock Engineering*, *46*, 1391–1413. https://doi.org/10.1007/s00603-013-0377-8

Itasca Consulting Group Incorporation. (2016). 3DEC - Three-Dimensional Distinct Element Code, Ver. 5.2. Minneapolis: ITASCA.

Ito, Y., & Ipek, G. (2005). SPE / PS-CIM / CHOA 97729 Steam - Fingering Phenomenon During SAGD Process, 1–9.

Ivars, D. M., Min, K., & Jing, L. (2001). Homogenization of mechanical properties of fractured rocks using DEM modeling. In *Frontiers of Rock Mechanics and Sustainable Development in the 21st Century 3000*.

Jianping, Y., WeiZhong, C., Diansen, Y., & Jingqiang, Y. (2015). Numerical determination of strength and deformability of fractured rock mass by FEM modeling. *Computers and Geotechnics*, *64*, 20–31. https://doi.org/10.1016/j.compgeo.2014.10.011

Jones, M. E., & Addis, M. A. (1986). The application of stress path and critical state analysis to sediment deformation. *Journal of Structural Geology*, *8*(5), 575–580.

Juncal, A. S. (2016). *Virtual rock mass (VRM) mechanical laboratory for inclusion of DFN in large scale reservoir-geomechanical coupled simulations*. Edmonton.

Kemeny, J., & Turner, K. (2008). Ground-based LiDaR: rock slope mapping and assessment, (September), 114.

Kemthong, R. (2006). *Determination of rock joint shear strength based on rock physical properties (Doctoral dissertation)*. Suranaree University of Technology.

Khan, S., Han, H., Ansari, S., Vishteh, M., Khosravi, N., Services, C., & Canada, S. (2011). Caprock integrity analysis in thermal operations : an integrated geomechanics approach. *World Heavy Oil Congress*, 1–10.

Khani, A., Baghbanan, A., & Hashemolhosseini, H. (2013). International Journal of Rock Mechanics & Mining Sciences Numerical investigation of the effect of fracture intensity on

deformability and REV of fractured rock masses. *International Journal of Rock Mechanics and Mining Sciences*, *63*, 104–112. https://doi.org/10.1016/j.ijrmms.2013.08.006

Khani, A., Rangriz-Shokri, A., & Chalaturnyk, R. J. (2018). The influence of discontinuities on geomechanical analysis of the Joslyn SAGD steam release incident. In *Society of Petroleum Engineers* (pp. 1–15). Calgary.

Koncagül, E. C., & Santi, P. M. (1999). Predicting the unconfined compressive strength of the Breathitt shale using slake durability, shore hardness and rock structural properties. *International Journal of Rock Mechanics & Mining Sciences*, *36*, 139–153.

Kulatilake, P. H. S. W., Ucpirti, H., Wang, S., Radberg, G., & Stephansson, O. (1992). Use of the Distinct Element Method to perform stress analysis in rock with non-persistent joints and to study the effect of joint geometry Parameters on the strength and deformability of rock masses. *Rock Mechanics and Rock Engineering*, *25*(4), 253–274.

Kulatilake, P. H. S. W., Wang, S., & Stephansson, O. (1993). Effect of finite size joints on the deformability of jointed rock in three dimensions. *International Journal of Rock Mechanics and Mining Sciences & Geomechanics*, *30*(5), 479–501.

Kulatilake, P. H. S. W., & Wu, Q. (2013). REV and equivalent continuum / discontinuum 3-D stability analyses of a tunnel. In *Proceedings of the 3rd International FLAC-DEM Symposium* (pp. 1–15). China.

Lee, J. S., Bang, C. S., Mok, Y. J., & Joh, S. H. (2000). Numerical and experimental analysis of penetration grouting in jointed rock masses, *37*, 1027–1037.

Lei, Q., Latham, J. P., Xiang, J., Tsang, C. F., Lang, P., & Guo, L. (2014). Effects of geomechanical changes on the validity of a discrete fracture network representation of a realistic two-dimensional fractured rock. *International Journal of Rock Mechanics and Mining Sciences*, *70*, 507–523. https://doi.org/10.1016/j.ijrmms.2014.06.001

Li, A. J., Lyamin, A. V, & Merifield, R. S. (2009). Seismic rock slope stability charts based on limit analysis methods. *Computers and Geotechnics*, *36*(1–2), 135–148. https://doi.org/10.1016/j.compgeo.2008.01.004

Lisjak, A., & Grasselli, G. (2014). A review of discrete modeling techniques for fracturing processes in discontinuous rock masses. *Journal of Rock Mechanics and Geotechnical Engineering*, *6*(4), 301–314. https://doi.org/10.1016/j.jrmge.2013.12.007

Lisjak, A., Grasselli, G., & Vietor, T. (2014). Continuum – discontinuum analysis of failure

mechanisms around unsupported circular excavations in anisotropic clay shales. *International Journal of Rock Mechanics and Mining Sciences*, *65*, 96–115. https://doi.org/10.1016/j.ijrmms.2013.10.006

Liu, Z., & Shao, J. (2017). Strength Behavior, Creep Failure and Permeability Change of a Tight Marble Under Triaxial Compression. *Rock Mechanics and Rock Engineering*, *50*(3), 529–541. https://doi.org/10.1007/s00603-016-1134-6

Lorenz, J. C., Warpinski, N. R., Teufel, L. W., Branagan, P. T., Sattler, A. R., & Northrop, D. A. (1988). Results of the multiwell experiment in situ stresses, natural fractures, and other geological controls on reservoirs. *Eos, Transactions American Geophysical Union*, *69*(35), 817–826. https://doi.org/10.1029/88EO01079

Lu, Y. L., Elsworth, D., & Wang, L. G. (2013). Microcrack-based coupled damage and flow modeling of fracturing evolution in permeable brittle rocks. *Computers and Geotechnics*, *49*, 226–244. https://doi.org/10.1016/j.compgeo.2012.11.009

Małkowski, P. (2015). Behaviour of joints in sandstones during the shear test. *Acta Geodynamica et Geomaterialia*, *12*(4), 399–410. https://doi.org/10.13168/AGG.2015.0034

Martin, C. D. (2007). Geology, Technology and Site Characterisation. In S. & M. Eberhardt (Ed.), *Rock Mechanics: Meeting Society's Challenges and Demands* (pp. 3–10). Taylor & Francis Group, London.

Matheson, D. S., & Thomson, S. (1973). Geological implications of valley rebound. *Canadian Journal of Earth Sciences*, *10*(6), 961–978. https://doi.org/https://doi.org/10.1139/e73-085

Mayne, P. W. (2001). Stress-strain-strength-flow parameters from enhanced in-situ tests. In *International Conference on In-Situ Measurement of Soil Properties & Case Histories* (pp. 27–48). Bali, Indonisia.

Min, K.-B. B., & Jing, L. (2003). Numerical determination of the equivalent elastic compliance tensor for fractured rock masses using the distinct element method. *International Journal of Rock Mechanics and Mining Sciences*, *40*(6), 795–816. https://doi.org/10.1016/S1365-1609(03)00038-8

Min, K. (2002). *Determination of equivalent hydraulic and mechanical properties of fractured rock masses using the Distinct Element Method*. *Department of Land and Water Resources Engineering*. KTH.

Min, K., Rutqvist, J., Tsang, C., & Jing, L. (2004). Stress-dependent permeability of fractured rock

masses : a numerical study. *Rock Mechanics and Mining Sciences*, *41*, 1191–1210. https://doi.org/10.1016/j.ijrmms.2004.05.005

Mishra, V. K., Lywood, P., Ayan, C., & Schlumberger, S. P. E. (2011). Application of wireline stress testing for SAGD caprock integrity, (November), 15–17.

Mollard, J. D. (1977). Regional Landslide Types in Canada. *Reviews in Engineering Geology*, *3*, 29–56. https://doi.org/10.1130/reg3-p29

Morgenstern, N.R. (1979). Geotechnical behaviour of clay shales - An overview. In *Proceedings of the International Symposium on Soil Mechcnics - Vol 1 - Session 2* (pp. 29–42). Mexico: Oaxaca. https://doi.org/019074090

Morgenstern, N.R., & Cruden, D. M. (1977). Description and classification of geotechnical complexities.pdf. In *Proceedings of the international symposium on the Geotechnics of Structurally Complex Foramtions. Volume II* (pp. 195–204). Rome, Italy.

Morgenstern, N R, Fair, A. E., & Mcroberts, E. C. (1988). Geotechnical engineering beyond soil mechanics-a case study1.

Morgenstern, Norbert R. (2000). Performance in geotechnical practice. *The Hong Kong Institution of Engineers*, *3733*(2000), 2–15. https://doi.org/10.1080/1023697X.2000.10667819

Nguyen, T. S., Borgesson, L., Chijimatsu, M., Rutqvist, J., Fujita, T., & Hernelind, J. (2001). Hydro-mechanical response of a fractured granitic rock mass to excavation of a test pit } the Kamaishi Mine experiment in Japan, *38*, 79–94.

Niandou, H., Shao, J. F., Henry, J. P., & Fourmaintraux, D. (1997). Laboratory investigation of the mechanical behaviour of Tournemire shale. *International Journal of Rock Mechanics & Mining Sciences*, *34*(1), 3–16.

Norouzi, S., Baghbanan, A., & Khani, A. (2013). Investigation of grain size effects on micro/macro-mechanical properties of intact rock using Voronoi element — Discrete Element Method approach. *Particulate Science and Technology: An International Journal*, *31*(5), 507–514. https://doi.org/10.1080/02726351.2013.782929

Öhman, J. (2005). *Upscaling of flow, transport, and stress-effects in fractured rock (Doctoral dissertation)*. Uppsala University.

Ortega, J. A. (2010). *Microporomechanical modeling of shale (Doctoral dissertation)*. Massachusetts Institute of Technology.

Otoo, J. N. A. (2012). *Surface expressions of discontinuities, and the estimation of their 3-D*

orientations using combined LiDAR and optical imaging (Doctoral dissertation). Missouri University of Science and Technology.

Palmström, A., & Singh, R. (2001). The deformation modulus of rock masses - comparisons between in situ tests and indirect estimates. *Tunnelling and Underground Space Technology*, *16*(3), 115–131.

Pariseau, W. G. (2006). *Design Analysis in Rock Mechanics*. Taylor & Francis.

Park, E., Martin, C. D., & Christiansson, R. (2004). Simulation of the mechanical behavior of discontinuous rock masses using a Bonded-Particle Model. *American Rock Mechanics Association*, *4*(480), 1–8.

Pijaudier-Cabot, G., & BaSant, Z. P. (1987). Nonlocal damage theory. *Journal of Engineering Mechanics*, *113*(10), 1512–1533.

Powell, J. S. (2010). *Geotechnical characterization of the Bearpaw shale (Doctoral dissertation)*. Queen's University.

Pratt, H. R., Swolfs, H. S., Lingle, R., & Nielsen, R. R. (1977). In Situ and Laboratory Measurements of Velocity and Permeability. *The Earth's Crust: Its Nature and Physical Properties, Geophys.*, *1*(20), 215–231. https://doi.org/10.1029/gm020p0215

Prost, G. L., & Newsome, J. (2016). Caprock integrity determination at the Christina Lake Thermal Recovery Project, Alberta, *64*(2), 309–323.

Rahmati, E. (2016). *Numerical assessment of caprock integrity in SAGD operations considering mechanical anisotropic behavior of shale layers (Doctoral dissertation)*. University of Alberta.

Rahmati, E., Nouri, A., & Fattahpour, V. J. T. (2015). Numerical assessment of the maximum operating pressure for anisotropic caprock in SAGD projects. *SPE Heavy Oil Conference - Canada 2015*.

Ruban, A. F., Patrick, R. A., & Skirrow, R. (2004). Approach fill design of North Saskatchewan River bridge. In *57th Canadian Geotechncial Conference. October 24-26, 2004* (pp. 1–8). Quebec.

Rutqvist, J. (1995). Determination of hydraulic normal stiffness of fractures hard rock from well testing. *International Journal of Rock Mechanics and Mining Sciences & Geomechanics*, *32*(5), 513–523.

Rutqvist, J. (2015). Fractured rock stress-permeability relationships from in situ data and effects

of temperature and chemical-mechanical couplings. *Geofluids*, *15*, 48–66. https://doi.org/10.1111/gfl.12089

Rutqvist, Jonny, & Stephansson, O. (2003). The role of hydromechanical coupling in fractured rock engineering. *Hydrogeology Journal*, *11*(1), 7–40. https://doi.org/10.1007/s10040-002-0241-5

Saeedi, M., & Settari, A. T. (2016). SAGD operation in interbedded sands with application of horizontal multistage fracturing: geomechanics and fracturing aspects. *Society of Petroleum Engineers*, 1–29. https://doi.org/https://doi.org/10.2118/180721-MS

Saraji, S., & Piri, M. (2015). The representative sample size in shale oil rocks and nano-scale characterization of transport properties. *International Journal of Coal Geology*, *146*, 42–54. https://doi.org/10.1016/j.coal.2015.04.005

Schmitt, D. R., Smither, C. L., Ahrens, T. J., & Jensen, B. L. (1986). Holographic Measurement of Elastic Moduli. In *The 27th U.S. Symposium on Rock Mechanics (USRMS), 23-25 June, Tuscaloosa, Alabama* (pp. 185–191). Tuscaloosa: American Rock Mechanics Association.

Scholtès, L., & Donzé, F. V. (2013). A DEM model for soft and hard rocks: role of grain interlocking on strength. *Journal of the Mechanics and Physics of Solids*, *61*, 352–369. https://doi.org/10.1016/j.jmps.2012.10.005

Shen, B., Siren, T., & Rinne, M. (2015). Modelling fracture propagation in anisotropic rock mass. *Rock Mechanics and Rock Engineering*, *48*, 1067–1081. https://doi.org/10.1007/s00603-014-0621-x

Shi, G., & Goodman, R. E. (1989). Generalization of two-dimensional discontinuous deformation analysis for forward modelling. *International Journal for Numerical and Analytical Methods in Geomechanics*, *13*(November 1987), 359–380.

Sitharam, T. G., Sridevi, J., & Shimizu, N. (2001). Practical equivalent continuum characterization of jointed rock masses. *International Journal of Rock Mechanics & Mining Sciences*, *38*, 437–448.

Ting, T. C. T. (1996). *Anisotropic elasticity theory and applications* (45th ed.). Oxford University Press on Demand.

TOTAL E&P Canada Ltd. (2007). *Summary of investigations into the Joslyn May 18 th 2006 Steam Release*. Calgary.

Tsui, C., Cruden, D. M., & Thomson, S. (1989). Ice-thrust terrains and glaciotectonic settings in

central Alberta. *Canadian Journal of Earth Sciences*, *26*, 1308–1318.

Tuckey, Z. (2012). An integrated field mapping-numerical modelling approach to characterising discontinuity persistence and intact rock bridges in large open pit slopes, 1–475.

Umili, G., Ferrero, A., & Einstein, H. H. (2013). A new method for automatic discontinuity traces sampling on rock mass 3D model. *Computers and Geosciences*, *51*, 182–192. https://doi.org/10.1016/j.cageo.2012.07.026

Uwiera-Gartner, M., Carlson, M. R., & Palmgren, C. T. (2011). Evaluation of the Clearwater Formation caprock for a proposed, low pressure, steam-assisted gravity-drainage pilot project in Northeast Alberta. *International Society of Petroleum Engineers*, (May 2006), 1–14.

Wang, P., Yang, T., Xu, T., Cai, M., & Li, C. (2016). Numerical analysis on scale effect of elasticity, strength and failure patterns of jointed rock masses. *Geosciences Journal*, *20*(4), 539–549. https://doi.org/10.1007/s12303-015-0070-x

Warpinski, N. R., & Teufel, L. W. (1992). Determination of the effective-stress law for permeability and deformation in low-permeability rocks. *Proceedings - SPE Annual Technical Conference and Exhibition*, *7*(2), 453–464. https://doi.org/10.2118/20572-pa

WeiZhong, C., Jianping, Y., XianJun, T. A. N., & HongDan, Y. U. (2011). Study on mechanical parameters of fractured rock masses. *Science China Technological Sciences*, *54*(December), 140–146. https://doi.org/10.1007/s11431-011-4632-5

White, J. A., Borja, R. I., & Fredrich, J. T. (2006). Calculating the effective permeability of sandstone with multiscale lattice Boltzmann/finite element simulations. *Acta Geotechnica*, *1*(2006), 195–209. https://doi.org/10.1007/s11440-006-0018-4

Wong, R. C. K., Schmitt, D. R., Collis, D., & Gautam, R. (2008). Inherent transversely isotropic elastic parameters of over-consolidated shale comparison with static and acoustic in situ log measurments. *Journal of Geophysics and Engineering*, *5*, 103–117. https://doi.org/10.1088/1742-2132/5/1/011

Wu, J., Zambrano-Narvaez, G., & Chalaturnyk, R. J. (2015). Newly developed centrifuge testing program of SAGD caprock integrity. In *the 49th US Rock Mechanics/Geomechanics Symposium. American Rock Mechanics Association (ARMA) 2015* (Vol. 557, p. 9). San Francisco: American Rock Mechanics Association. https://doi.org/ARMA-2015-557

Wu, Q., & Kulatilake, P. H. S. W. (2012). REV and its properties on fracture system and mechanical properties, and an orthotropic constitutive model for a jointed rock mass in a dam

site in China. *Computers and Geotechnics*, *43*, 124–142. https://doi.org/10.1016/j.compgeo.2012.02.010

Xu, B., Yang, B., & Yuan, Y. (2013). *Appendix 1-IV - Caprock integrity and InSAR report*. Calgary.

Yang, J. P., Chen, W. Z., Wu, G. J., & Yang, D. S. (2018). Analytical estimation of the equivalent elastic compliance tensor for fractured rock masses, *18*(1), 1–11. https://doi.org/10.1061/(ASCE)GM.1943-5622.0001035.

Yoshinaka, R., & Yamabe, T. (1986). 3. Joint stiffness and the deformation behaviour of discontinuous rock, *23*(I), 19–28.

Yuan, Y., Xu, B., & Palmgren, C. (2013). Design of caprock integrity in thermal stimulation of shallow oil-sands reservoirs. *Journal of Canadian Petroleum Technology*, *52*(4), 266–278. https://doi.org/10.2118/149371-PA

Yue, Z. Q. (2013). Micro-gas hypothesis for behaviors of rocks under loading. In *Constitutive Modeling of Geomaterials* (pp. 381–386). Berlin, Heidelberg: Springer Series in Geomechanics and Geoengineering. https://doi.org/10.1007/978-3-642-32814-5_53

Zadeh, N. S. (2016). *Multiple packer techniques for in situ stress measurement in hard soils-soft rocks (Doctoral dissertation)*. Univeristy of Alberta.

Zadeh, N. S., & Chalaturnyk, R. (2015). Geotechnical characterization of Clearwater clay shale and comparison of the properties with other Cretaceous clay shales in North America. *Society of Petroleum Engineers*, (July 2014), 1–18.

Zambrano-Narvaez, G., & Chalaturnyk, R. (2014). *Suncor Energy Inc. Firebag SAGD Project - Geomechanical Laboratory Test Program*. Edmonton.

Zhang, J., Standifird, W. B., Zhang, Y., Roegiers, J. C., & Zhang, Y. (2007). Stress-dependent fluid flow and permeability in fractured media: From lab experiments to engineering applications. *Rock Mechanics and Rock Engineering*, *40*(1), 3–21. https://doi.org/10.1007/s00603-006-0103-x

Zhang, L. (2004). Deformability and strength of rock. In *Drilled Shafts in Rock. Analysis and Design* (pp. 71–150). Taylor & Francis.

Zhang, Lianyang. (2013). Aspects of rock permeability. *Frontiers of Structural and Civil Engineering*, *7*(2), 102–116. https://doi.org/10.1007/s11709-013-0201-2

Zhang, Lianyang, & Einstein, H. H. (2000). Estimating the intensity of rock discontinuities, *37*.

Zhang, W., Chen, J., Yuan, X., Xu, P., & Zhang, C. (2013). Analysis of RVE size based on three-dimensional fracture numerical network modelling and stochastic mathematics. *Quarterly Journal of Engineering Geology and Hydrogeology*, *46*, 31–40. https://doi.org/10.1144/qjegh2011-045

Zhao, G. (2010). *Development of micro-macro continuum-discontinuum coupled numerical method*. Lausanne, EPFL. https://doi.org/10.5075/epfl-thesis-4807

Zoorabadi, M. (2016). Deformability modulus of jointed rocks, limitation of empirical methods and introducing a new analytical approach. In Faculty of Engineering and Information Sciences (Ed.), *Proceedings of the 16th Coal Operators' Conference* (pp. 132–137). University of Wollongong.

APPENDIX A. INVESTIGATION OF PLATFORMS FOR RAW LIDAR DATA MANIPULATION

A.1 PREFACE

Light detection and ranging (LiDaR) technology enables surveying and capturing, at traffic speed, a rock face, over continual distances of up to hundreds of kilometers per day. There is many publicly available software and modules that can analyze, process, and manipulate LiDaR raw data to produce a 3D surface from the laser-scanned points. Several software packages are explored in this appendix with respect to best practices for processing a LiDaR point cloud.

In this appendix it was found out that LiDaR point cloud combined with high resolution digital images enabled a representative geological characterization of an exposed mine bench in Alberta via provided a knowledge about the formation discontinuities statistics. That, structural characterization included discontinuity size, location, spacing, dip angle, and dip direction identification. Eventually, a triangulated irregular network (TIN) was generated for the sedimentary formation mine bench using the in situ captured LiDaR survey. It is proven in this appendix study that majority if not most important types of discontinuities information needed for a rock mass characterization, that used to be acquired from hand mapping, can be identified from LiDaR point clouds associated with high resolution digital images. Luckily, these information can now be automatically extracted using currently available software.

Results of this appendix include comparing and highlighting the capabilities of five platforms in manipulating point cloud datasets, mainly extracting discontinuities geologic statistics. The input to the five modules in the comparison was a single point cloud .LAS (raw) file. The generated digital surface model (DSM) quality depended on the point cloud density, noise, possible holes on the surface, vegetation, rock fragment/rubble, light, shadow, etc. Application of the proposed procedure in this appendix, can help realistically characterize discontinuous rock masses remotely without a need for human access to the site, eliminating the traditional safety concerns in similar in situ geological assessments maintaining high precision results. The current appendix findings illustrate the potential of using LiDaR and high-resolution digital images in rock structural characterization.

A.2 INTRODUCTION

Two centuries ago, William Smith produced the first ever geological map of England and Wales which was published in 1815; an achievement that spotlighted the importance of mapping geological contacts and structures as perhaps the most fundamental skill set in earth science (Knell 2009). Structural characterization of slopes is widely documented (Francioni, Salvini, Stead, & Litrico, 2014). It is used and in some cases needed in engineering applications such as in managing rockfalls risk through remotely monitoring susceptible slopes using a terrestrial laser scanner (Kromer et al., 2016). Geological mapping has been used in slope stability assessment including transitional rock slope failures.

In the past few decades, light detection and ranging (LiDaR), also often referred to as "3D laser scanning", started to emerge as a three-dimensional (3D) geological mapping technology. It employs laser and a rotating mirror (Figure A-1) or housing to rapidly scan and image volumes and surficial extended areas such as rock slopes, outcrops, buildings, bridges as well as any other natural or man-made objects. Ground-based or terrestrial LiDaR refers to tripod-based measurements, as opposed to airborne LiDaR measurements captured from airplanes or helicopters (Kemeny & Turner, 2008). Discontinuity location, orientations, spacing, and block size (volume) of a rock mass, maybe delivered with an acceptable detail and accuracy from LiDaR data.

As a technique for acquiring digital field data, LiDaR advantages over conventional hand mapping include (Kemeny & Turner, 2008):

- Repeatability
- Higher spatial productivity
- Ease and convenience in the acquisition
- High-resolution digital models of physical objects
- Faster processing and geological feature extraction
- Elimination of human-inaccessibility issues (e.g. steep slopes, high, hidden/confined areas)
- Accuracy and reliability of the mapping results by eliminating the human error and bias
- Minimal personnel safety-hazards that an engineer or geologist may be exposed to during in situ visits

Figure A-1 Terrestrial laser scanners (Kemeny & Turner, 2008)

LiDaR data can be used to digitally measure the geological structure of a rock mass. Moreover, the point cloud data can be interchanged between users (providers and consumers) using a public file format (i.e. .LAS) that was developed primarily for exchanging LiDaR raw data. The .LAS format was originally developed by the American Society for Photogrammetry and Remote Sensing (ASPRS). It stores the LiDaR data that is collected by optical remote sensors in a binary file format maintaining information specific to the LiDaR nature while not being overly complex. The LiDaR mapping community currently can customize the .LAS file format to meet their application-specific needs.

A LiDaR survey was conducted of an exposed mine bench in Alberta as seen in Figure A-2, and stored in a large (≈ 0.4 GB) binary file format of the raw point cloud data. The results from this geologic survey formed the basis for the geological feature extraction of the exposed mine bench. Initial challenges included identifying suitable modules for manipulating the .LAS file format and extensive dataset. Afterwards selecting the most effective method for generating a 3D meshed surface of the point cloud for geomechanical engineering applications.

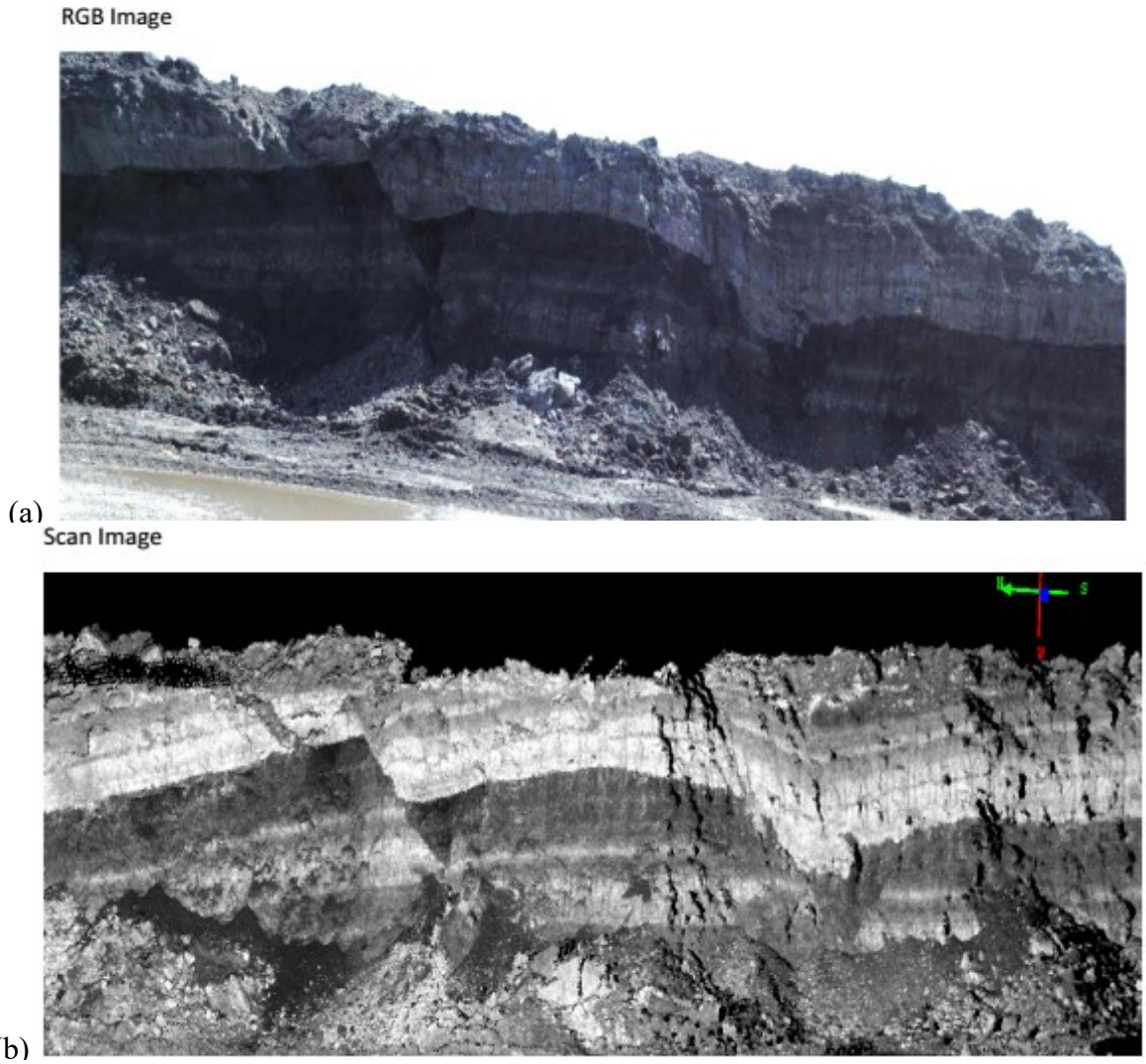

Figure A-2 (a) Red-Green and Blue (RGB) and (b) scan images of mine bench in Alberta

Point clouds are typically interpreted to generate and build 3D gridded rasters called triangulated irregular networks (TINs) in a process simply illustrated in Figure A-3. Several point cloud programs can fit a (discontinuity) plane through a selected set of points and calculate its orientation and size. Exporting this kind of information is straightforward in point cloud processing programs, if the point cloud program can calculate the information in the first place. The targeted outcomes of the point cloud processing in this appendix include visualizing, manipulating, structural features identification and reconstruction of 3D textured surface for the scanned mine bench. Accordingly, the methodology of this study was to explore then construct a database of software, codes, engines and modules that support manipulating .LAS files. Second, carry out a practical comparison between number of these procedures via evaluating each's capability in

constructing a TIN of the point cloud dataset. Lastly, nominating the ideal and most reliable tool for generating the geostatistics from the point cloud.

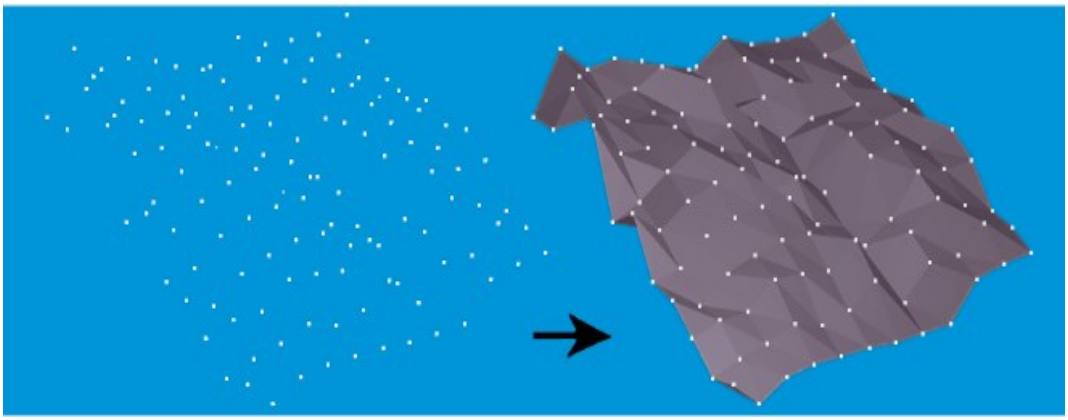

Figure A-3 From points to 3D raster/triangulated irregular network (TIN)

A.3 METHODOLOGY

In July 2014, a LiDaR scan (exchanged later in .LAS file format) seen in Figure A-2 (b) was acquired in an oil sands mine in northeastern Alberta. Publicly available software, codes, modules, and engines for point cloud, manipulation were examined for assessing each's ability to view, import, visualize, call, process, and/or analyze the raw .LAS file. Table A-1 includes a list of the platforms investigated and examined having different levels of capabilities. Later in the appendix, results of a comparison between five selected procedures to check their capabilities is presented.

A.4 SITE DESCRIPTION

The surveyed mine bench is located near Fort McMurray in Northeastern Alberta, Canada. It falls within the Clearwater Formation which is a stratigraphic unit of early Cretaceous (Albian) age in Western Canada sedimentary basin. As seen in the scan image of the 3D point cloud in Figure A-2 (b), the North direction is to the left.

A.5 DATA ACQUISITION

A point cloud is a set of vertices in a 3D coordinate system (space). Point clouds can be assigned red, green and blue (RGB) values by projecting each point into an appropriate image (Buckley, Kurz, Howell, & Schneider, 2013). The point cloud under investigation was acquired using LiDaR surveying technique and primarily produced in a .LAS file format.

Table A-1 List of .LAS file manipulation platforms

Software name	version	by	License Type/ Free Trial	Price ($)	Comments
AMLS		Ohio State University	free		TAMAL
ArcGIS for Desktop	10.3.1	esri Canada	60-day free		ArCCShCene, ArcCatalogue, ArcMap, does not open, gives error
AutoCAD Civil	3D	Autodesk®			IST U of A
AutoCAD®2016	Suite	Autodesk®			U of A
CloudCompare[v2] Stereo	V2.7	Danielgm	open source		Personal comm.
CloudWorx		Leica Geosystems	free		
Coltop3D	Terranum		30-day		
Cyclone		Leica Geosystems	free		
DSE		Adrián Riquelme	open source		based on MATLAB
FME Desktop	2016	Safe Software	free 30-day		
FracPaQ toolbox		MATLAB	open source		publicly available on GitHub™ and the MathWorks™ FileExchange
FugroViewer	2.0	©2014 Fugro Geospatial, Inc.	free		could open the files successfully, but no processing or analysis. It is just viewer
Gaia-GeoRoc	2012	SNCF	free		
Geomatica		Focus PCI			Personal comm.
Global Mapper	v17	Blue Marble geographics	2-week free	$1,000	can open it. $499 US, upgrade for $199 + LiDaR module for $499 US
KUBRIX		Itasca	30-day free		
LAStools	Lasview	rapid lasso			
LP360 Viewer	Evaluation	QCoherent	30-day free		Node locked License. After discussions with the company, will not work
MapInfo Pro	v15.2.0	Pitney Bowes			
MATLAB®			free		I have it from IST U of A
Online LIDAR point cloud viewer					can open it. http://LiDaRview.com/
Point Cloud Mapper	PCM	Vosselman			
PointCloudViz		Mirage	free, server		Upload and shared via dropbox
PointCloudViz Free	2.1.0	Mirage Technologies	free		can open it. Desktop LiDaR viewer
Points2Polys	ParaForm	Software Informer	free		
PolyWorks		Innovmetric Software Inc.			Personal comm.
Quick Terrain	Reader[8] X64	Applied Imagery	free		can open it
Quick Terrain Modeler	8.0.5.2	Applied Imagery	30-day free		
Rhino Terrain	5	Itasca	90-day free	794	no LAS files, very limited support for point cloud, from Claude Vuattoux based in France
SAGA	GIS		FOSS		free open source software, does not open .LAS files
Split-FX®		Split Engineering	30-day free	$495 USD	single academic license. Opens only ASCII
VeloView	Version 3.1.1	ParaVIEW			Velodyne LiDaR

The .LAS file format typically supports including large amounts of data associated to the points. These associated data are called components, which contain values that describe different attributes for each point. While the point cloud attributes may have other terminologies, there are common components, as listed in Table A-2, that exist within several modules.

Table A-2 Points' attributes in LiDaR data

x	The x component of the geometry.
y	The y component of the geometry.
z	The z component of the geometry.
intensity	The magnitude of the intensity of the pulse return.
color_red	The red image channel value at the point.
color_green	The green image channel value at the point.
color_blue	The blue image channel value at the point.
classification	The class of the point. Categorizes a point into fields, such as ground, building, water, and others. Values correspond to the ASPRS LAS specification.
return	The pulse return number for a given output pulse.
number_of_returns	The total number of detected returns from a single pulse.
gps_time	The number of seconds since the beginning of the week.
gps_week	The week number, counting from January 6th, 1980.
angle	The angle of the pulse that the point was scanned at.
flight_line	The flight line number the point was detected in.
flight_line_edge	Whether this point lies on the edge of the scan, along the flight line.
scan_direction	The direction in which a scanning mirror was directed when the point was detected.
point_source_id	A value that indicates the source of the file, such as a file number.
posix_time	Used to express the time, as the number of seconds elapsed since UTC January 1st, 1970.
user_data	Data to be used at the user's discretion.

The LiDaR dataset captured in June 2014 as well as an RGB image of the exposed mine bench were illustrated in Figure A-2. The studied point cloud can be imported and displayed in CloudCompare user interface as depicted in Figure A-4. If zoomed in, the point cloud is basically a dense cluster of points in 3D (Figure A-3).

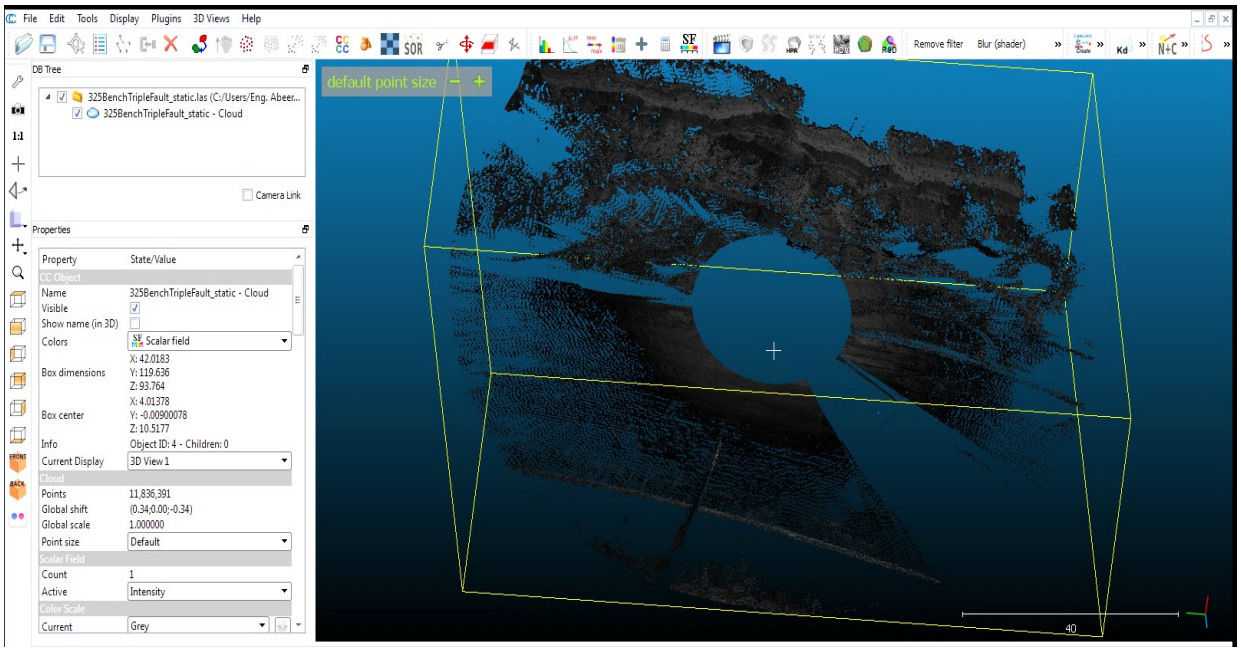

Figure A-4 Raw 2.5D point cloud loaded in CloudCompare GUI

A.6 POINT CLOUD MANIPULATION

Manipulating a point cloud refers to visualizing, displaying, managing, processing, analyzing, features generating, detecting, delineating, extracting, etc. Point clouds can be cropped, so the density of the points might be decimated, and accordingly the file size is appreciably optimized. As mentioned above and listed in Table A-1, several platforms were examined and their capabilities to manipulate the .LAS file were evaluated as will be discussed in detail below. The analyses of the point cloud were carried out on a standard laptop using with Intel Core™ i7 CPU (2.4 GHz) with a video card.

A.7 DISPLAYING LIDAR DATASET

The original x, y, and z extents of the scanned rock face were found to be 25.06 m × 119.63 m × 101.89 m respectively as detected using multiple software (Table A-6). The total number of points in the raw LiDaR point cloud was found to be 11,836,391 points. Each point was typically associated with x, y, and z attributes and a laser return intensity (I) number. Next sections include discussion about multiple viewers; which just support; loading, viewing, opening, importing, and displaying the original point cloud without processing.

A.7.1. MapInfo Pro v15.2.0

Figure A-5 illustrates the raw point cloud as a LAS map in MapInfo Pro interface. Few capabilities exist from this software however it was not examined further.

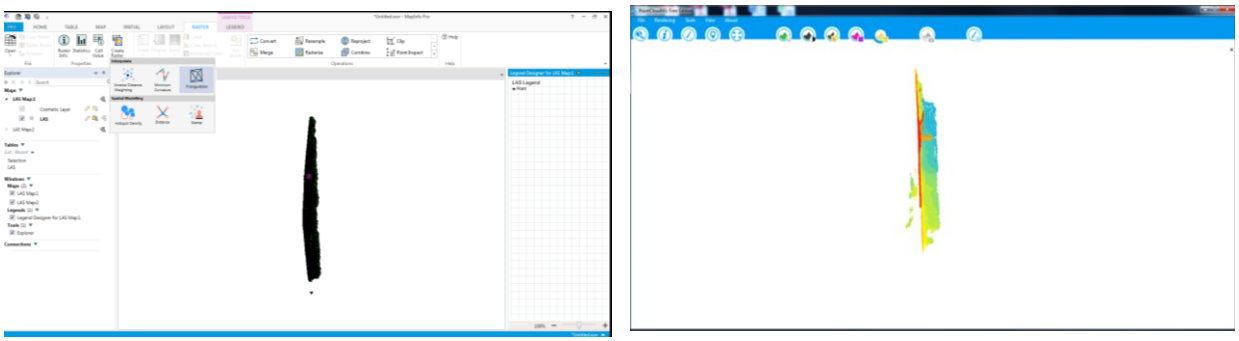

(a) (b)

Figure A-5 Raw point cloud in MapInfo colored (a) by intensity and (b) in RGB

A.7.2. PointCloudViz-2.1.0

PointCloudViz is available via a free server. It can display .LAS files as seen in Figure A-6. It renders the point cloud classification based on RGB, intensity, gradient, or elevation.

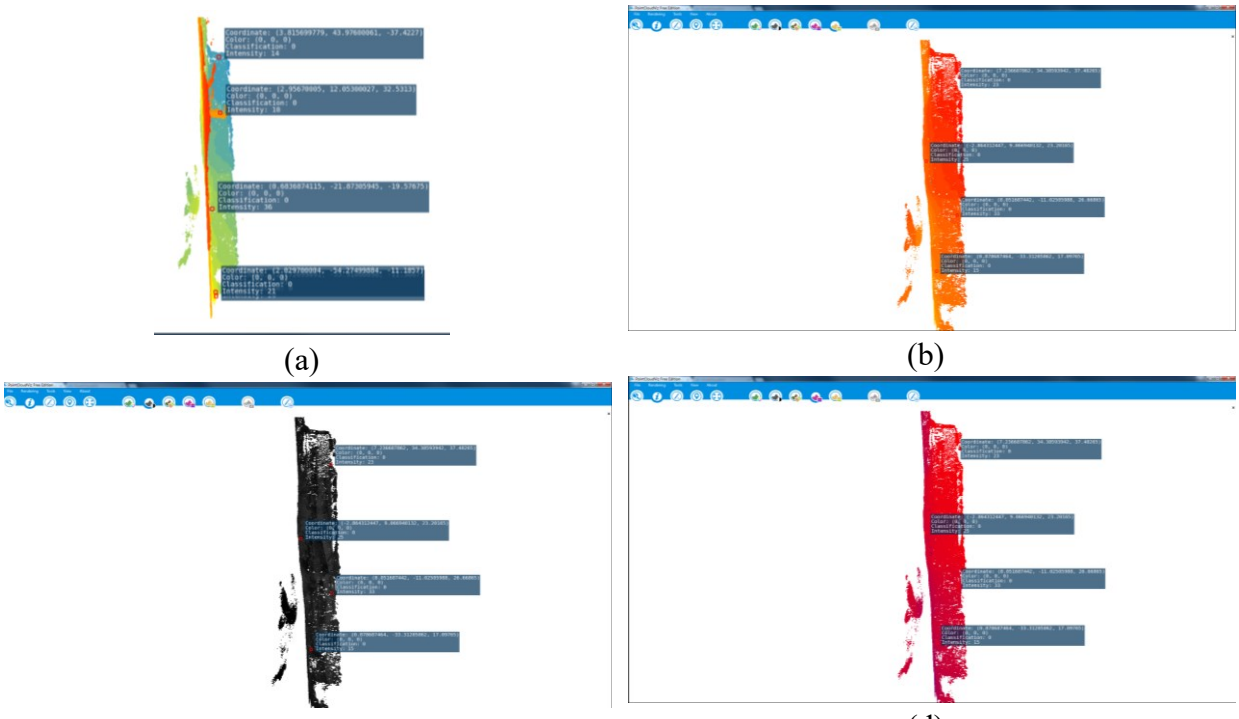

(a) (b)

(c) (d)

Figure A-6 PointCloudViz (a) displaying raw data set, rendering point cloud in (b) intensity, (c) gradient and (d) elevation classifications

A.7.3. Split-Fx®

Split-Fx® is a point cloud software for rock mass characterization. Point's data that can be imported into Split-Fx are X, Y, Z, I, r, g, and b. Split-Fx can display four fields of the attributes associated with each point in the cloud at a time as seen in Figure A-7 (a).

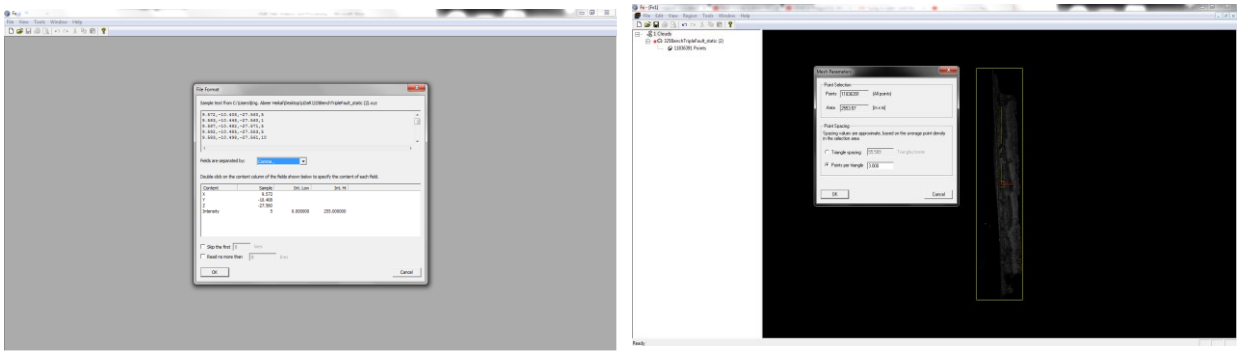

(a) (b)

Figure A-7 Split-Fx® interface (a) displaying four attribute fields of a selected point and (b) parameters of the whole point cloud mesh

A.7.4. Quick Terrain (QT) Reader

Quick Terrain Reader x64, v8.0.3.1 was successfully used to import, load and view the point cloud dataset as given in Figure A-8. The software specifications are listed in Table A-3.

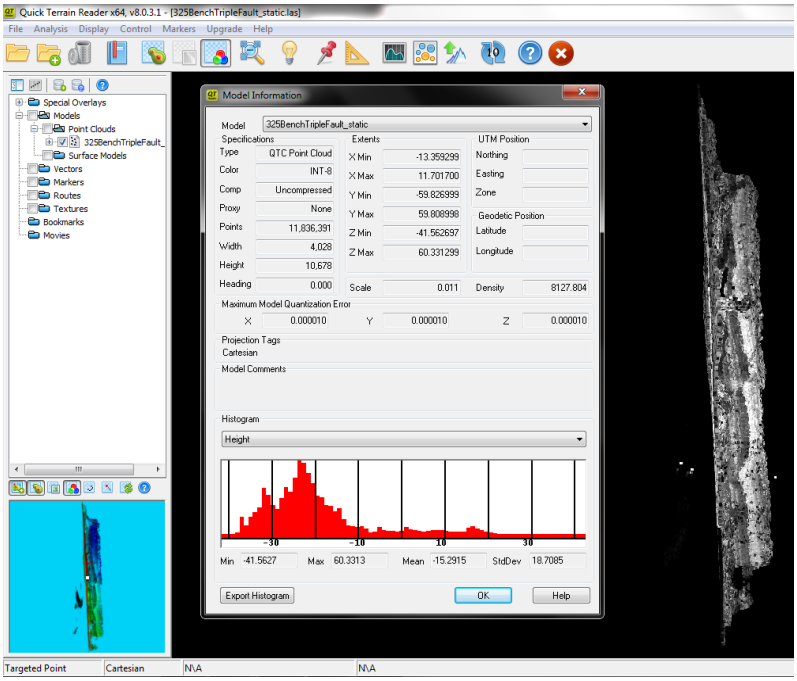

Figure A-8 Quick Terrain Reader displaying point cloud information and height histogram

Table A-3 Specifications of Quick Terrain reader

Version Info	Third Party Libraries
	PDAL, v0.8.6
Build Number: Build 80854	LASzip, v2.1.0: 2012-01-04
Build Date: April 30, 2014	GDAL, v1.11dev: 2013-04-13
Registration Type: Node Lock	CGAL, v3.6.1: 2010-06-01
Registered To: Eng. Abeer Heikal	
Expiration Date: Unknown	LizardTech MrSID
	Decode SDK v8.5: 2012-02-29
	Erdas ECW JPEG 2000
	SDK v4.3: 2012-09-26

A.7.5. AUTOCAD CIVIL 3D 2016

AutoCAD Civil 3D 2016 was able to recognize the point cloud and generate multiple of its attributes information as seen in Figure A-9.

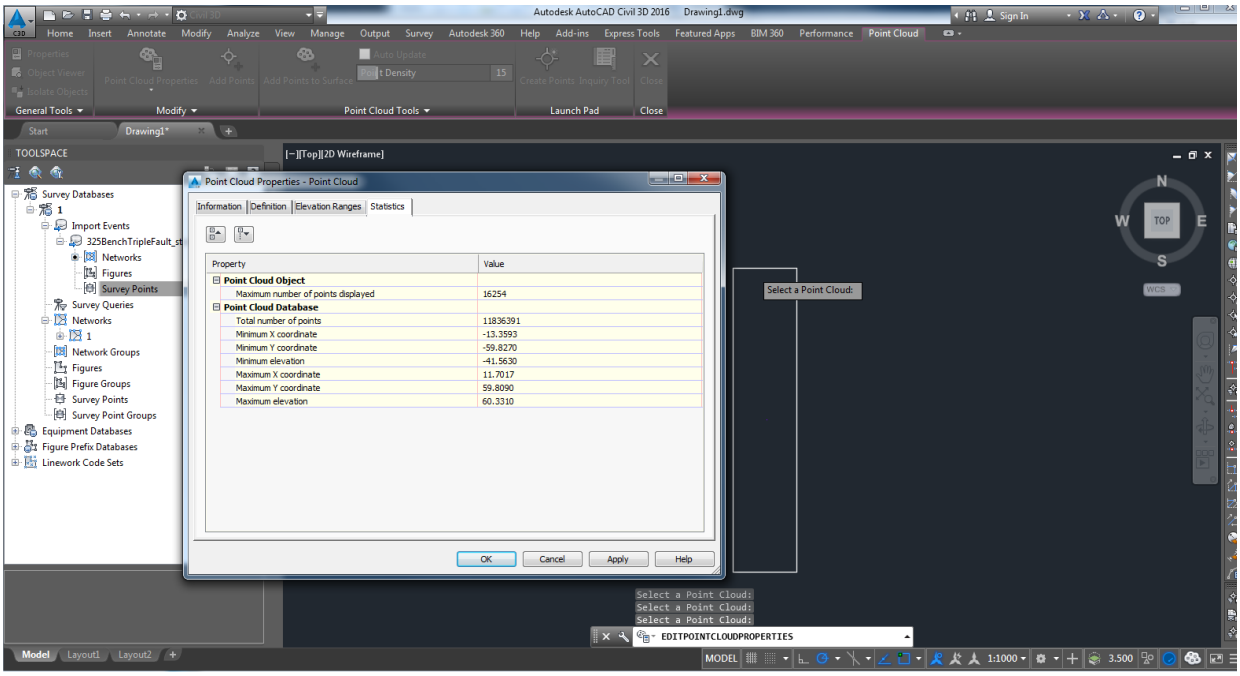

Figure A-9 AutoCAD Civil 3D 2016 displaying point cloud properties and their values

A.8 LIDAR DATASET PROCESSING

In engineering applications, extracting joint set structural statistics is the point cloud interpretation main target. The structural statistics consist of joint density, dip angle, dip direction, trace length, and spacing. Dip Angle is the deviation of the discontinuity plane from the horizontal

plane. Dip Direction is the direction of the horizontal trace of the line of the dip, measured clockwise from the north.

In structural characterization, the mesh type in a model is critical. Measurements on meshed surfaces provide means of obtaining discontinuities characteristics from the laser scanned point cloud. Automated extraction of the discontinuity characteristics is attractive in its ability to 'objectively detect discontinuities. Features extraction automatically identifies 'patches in the data, i.e. groups of mesh triangles with similar normal vectors. Basically, setting couple of thresholds, then the processing operation is automatically performed.

An interpolated surface with a simple representation makes use of points, edges, and triangles to represent a surface in a form of TIN as illustrated in Figure A-10. A TIN surface is created by forming a series of triangles between each three neighboring data points. Table A-1 list a number of platforms made professionally to support manipulating .LAS files, generating a TIN and extracting joint set geostatistics. Some of these platforms, such as FME, Global Mapper, CloudCompare and DSE, will be discussed in detail in the following sections.

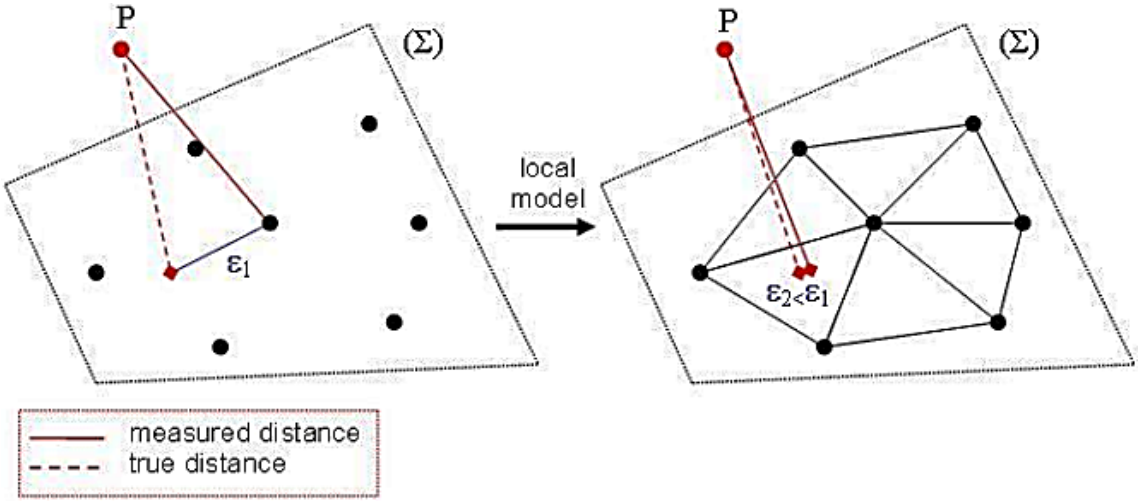

Figure A-10 From points to TIN (CloudCompare manual)

A.8.1. FME WORKBENCH 2016.0

Feature Manipulation Engine (FME), produced by Safe Software Inc. in Surrey, British Columbia, provides an integrated collection of tools for powerful data transformation and translation. The FME graphical workbench enables the user to powerfully move data between 345+ formats. An example of transforming the raw point cloud (.LAS file format) to MapInfo format is illustrated in Figure A-11 (a).

A.8.1.1. FME DATA INSPECTOR

FME Data Inspector is a standalone viewer within the FME platform. Figure A-11 (b-d) encompasses the FME data inspector interface displaying; raw point cloud feature information, .LAS file property inspection, and after finishing features processing and translation, respectively.

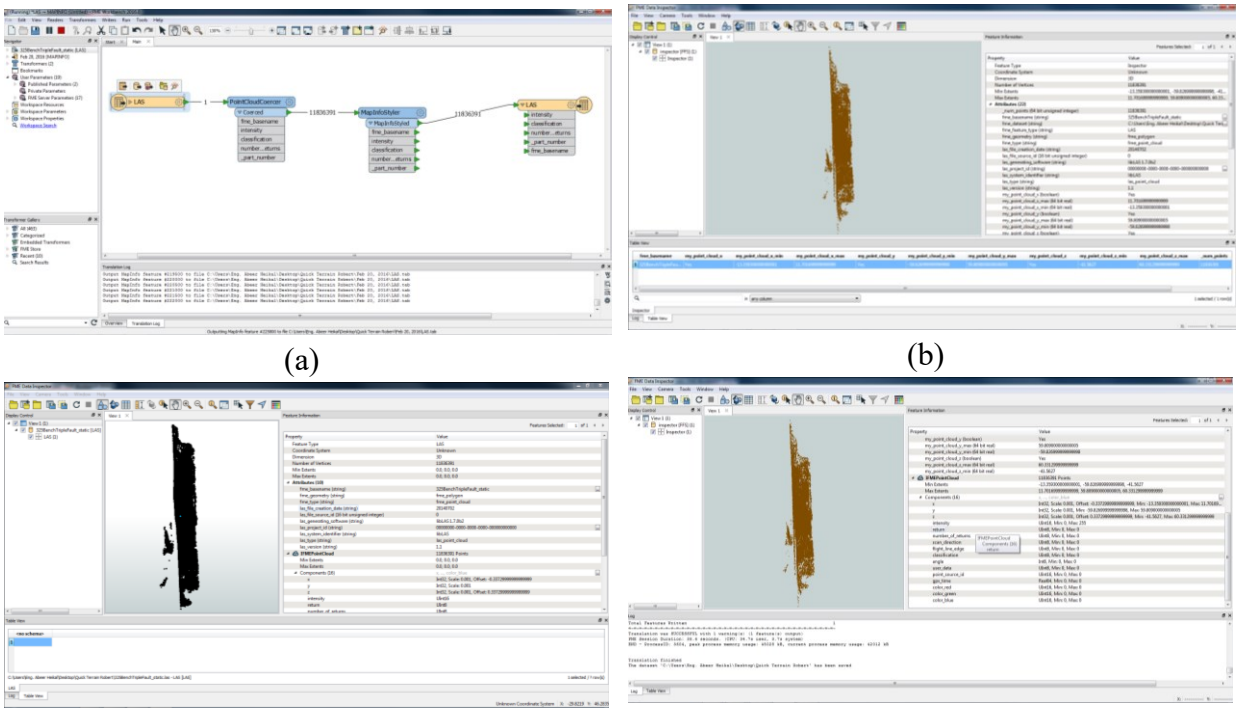

(a) (b) (c) (d)

Figure A-11 (a) MapInfoStyler transformer, (b) FME data inspector displaying original point cloud, (c) feature information of .LAS file and (d) after point cloud translation finished

A.8.1.2. FME TRANSFORMERS

FME library consists of 450+ transformers such as LAS Logger, CoordinateSwapper, Rotator, Creator, Extruder, PointCloudPropertyExtractor, Clipper and TIN Generator. The Logger transformer logs each identified feature to a translation log, and all attributes and geometry of the feature will be output. Limits can be placed on both the number of features that will be logged, and the number of coordinates that will be logged per feature.

A.8.1.3. POINT CLOUD PROCESSING

The main purpose for investigating the FME was to process the .LAS file and eventually generate a TIN of the point cloud. Constraining and updating LiDaR data extents were carried out as a **first step** in the point cloud processing as seen in Figure A-12a using

PointCloudPropertyExtractor transformer. **Second step** was reorientation of the raw dataset (using coordinate swapper X ←→ Y) as seen in Figure A-12 (b).

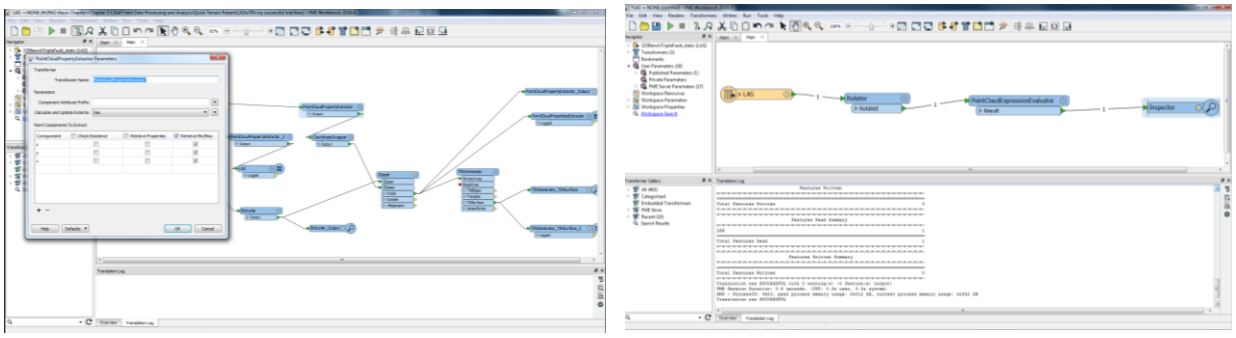

(a) (b)

Figure A-12 (a) Point cloud minimum and maximum extents and (b) FME workbench displaying the use of rotator transformer to reorient point cloud

The CoordinateSwapper (Figure A-13b) or the Rotator transformer basically swaps coordinate axes of the input features, as follows:

X with Y: Each feature x-coordinates will be swapped with its y-coordinates.

X with Z: Each feature x-coordinates will be swapped with its z-coordinates.

Y with Z: Each feature y-coordinates will be swapped with its z-coordinates.

Third step involved using the Creator transformer to create features using thresholds set by the user as seen in Figure A-14 (a). The Creator's interface allows the user to select the type of geometry and enter the coordinates and/or parameters that will create the targeted object.

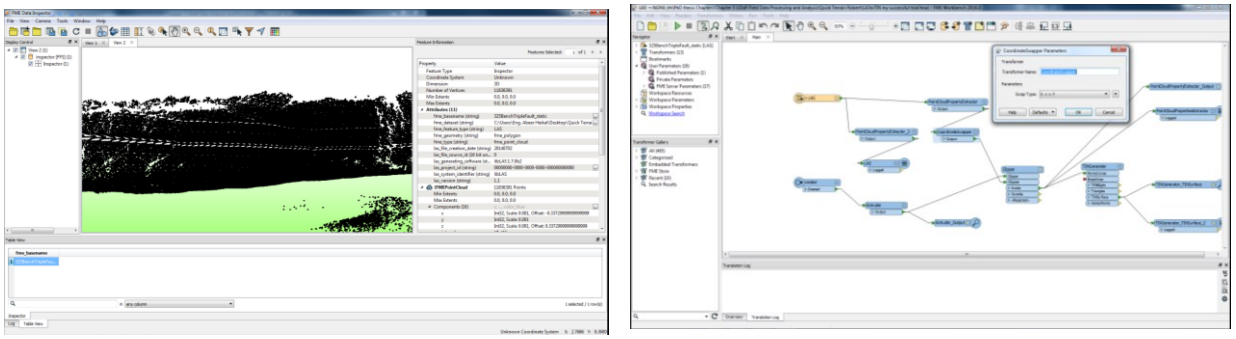

(a) (b)

Figure A-13 FME Data Inspector (a) reoriented point cloud and FME workbench (b) CoordinateSwapper transformer

Fourth step was using 3D Extruder transformer as given in Figure A-14 (b). It extracts the properties of the point cloud 3D features and exposes them as attributes as seen in Figure A-15 (a). Additional attributes may be exposed for each 3D component as the user desires.

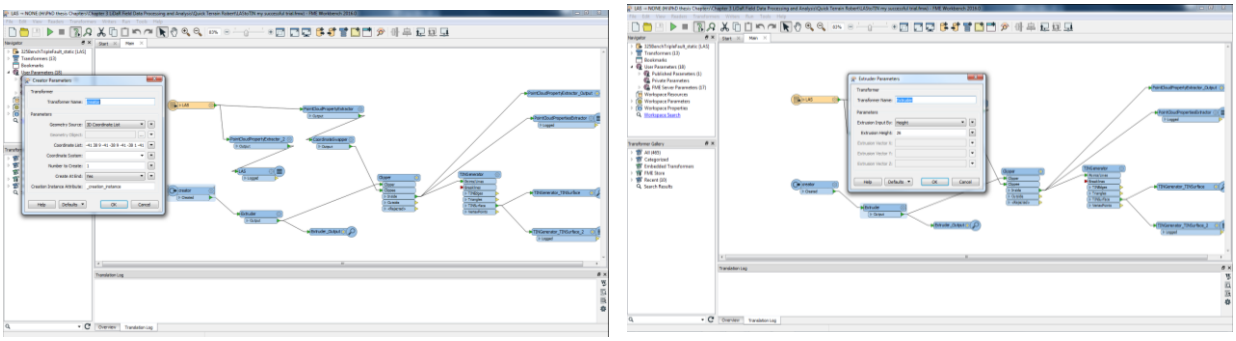

(a) (b)

Figure A-14 FME workbench (a) Creator transformer and (b) Extruder transformer

Fifth transformer used in the point cloud processing was the Clipper as given in Figure A-15 (b). It basically performs a geometric clipping operation, where this geometry clipping is made by area. Clipper transformer identifies several clip boundaries (Clippers) and several features to be clipped (Clippees). The Clippees output is split into two groups; the parts of the Clippees that are within the clip boundaries, and the parts of the Clippees that are not within the clip boundaries. The Clippees that intersect the clip boundaries will be cut into multiple sections (along the clip boundaries), and then each section will be added to an appropriate group. The Clippees that do not intersect are added directly to the appropriate group and are output without modification as seen in Figure A-15 (b).

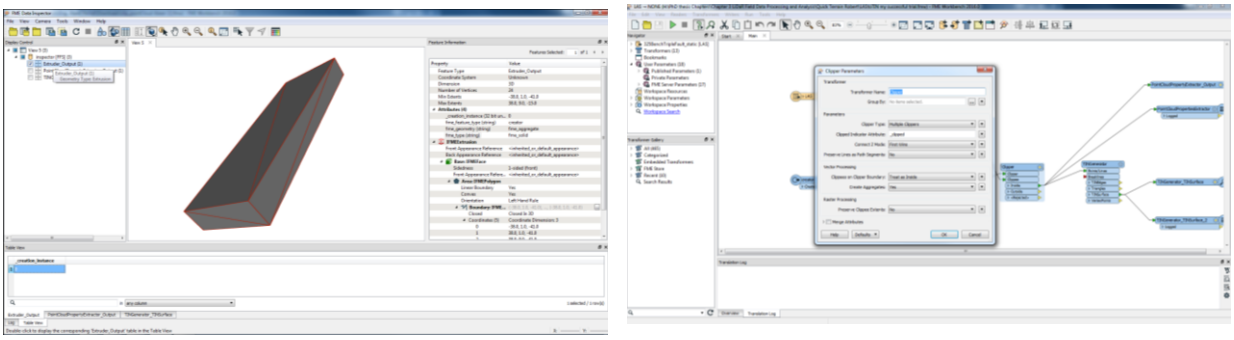

(a) (b)

Figure A-15 FME Data Inspector (a) showing 3D Extruder_Output and (b) Clipper transformer

The **final step** was the TIN generation using the TINGenerator transformer (Figure A-16). The transformer creates a TIN using the points of the point cloud. The point cloud data stream is connected to the TINGenerator points input port. The surface tolerance determines which input points are added as vertices to the model. The larger the value, the more input points will be filtered out (Figure A-17).

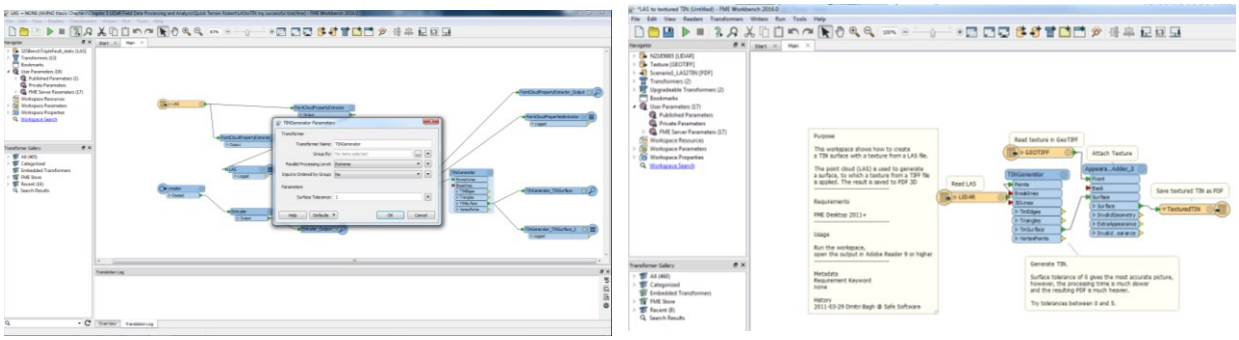

(a) (b)

Figure A-16 (a) TINGenerator transformer (before running) and (b) LAS to textured TIN

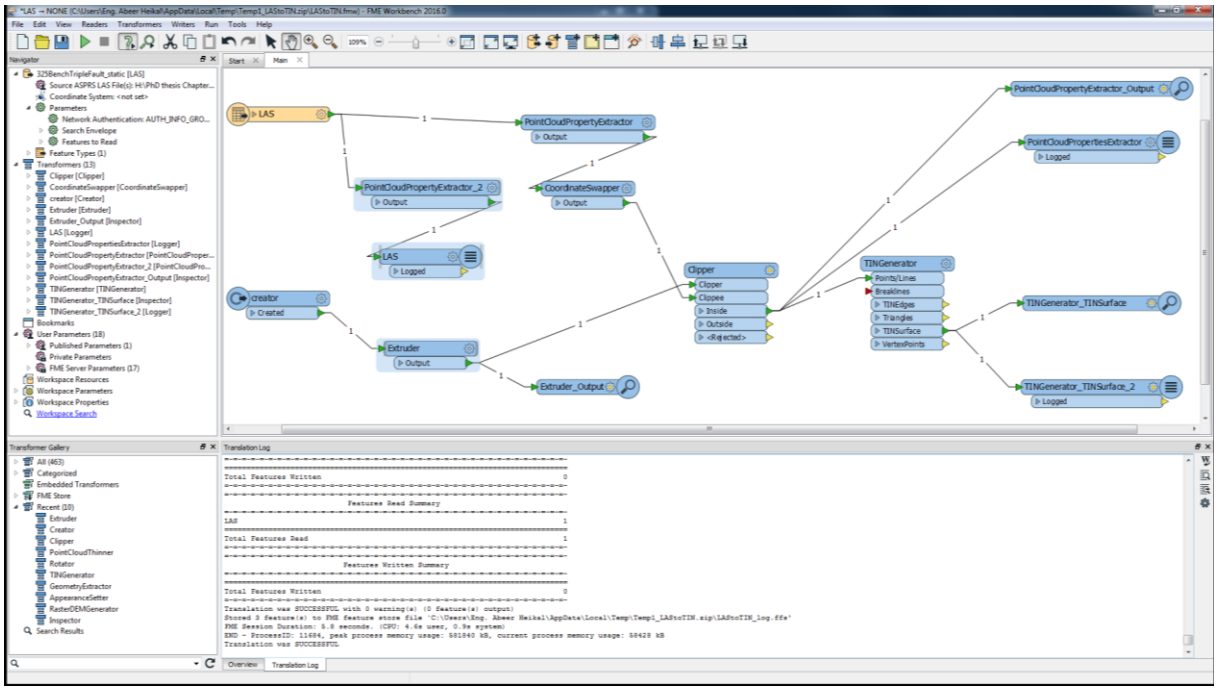

Figure A-17 After successfully translating LAS file to raster digital elevation model (DgEM) using TINGenerator transformer

The TINGenrator transformer basically constructs a Delaunay triangulation based on input points and break lines. The surface model may be output in several representations; a TIN, TIN vertices, TIN edges, or triangles (Figure A-18). Using a TIN_Generator transformer, the best recommended practice is to not split the point cloud by class rather generate the TIN with an ortho texture using .LAS to textured TIN transformer (LAS_TO_TIN). The TIN was generated as displayed in Figure A-18 (d) in the FME Data Inspector.

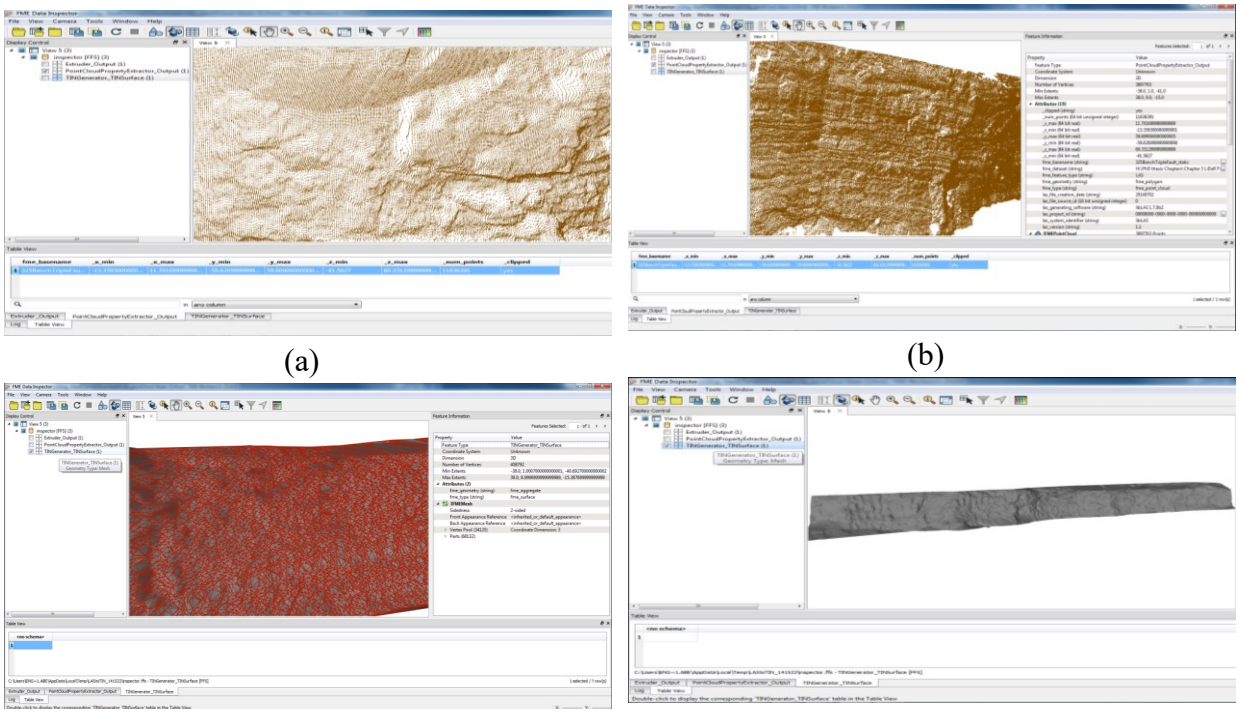

(a) (b)

(c) (d)

Figure A-18 (a) PointCloudPropertyExtractor, (b) TINGenerator, (c) mesh and (d) TIN surface

A.8.2. GLOBAL MAPPER

Global Mapper v17.0 is a GIS application offered by Blue Marble (GEOGRAPHICS). In this appendix Global Mapper was used to process the point cloud under investigation. The original LiDaR dataset is depicted in Figure A-19 (a) after rotating it 90^{o} in Global Mapper interface. The 11 million plus point cloud can be displayed and filtered based on point index, scan angle, color (RGB), classification, elevation or intensity of the returned strength of the laser pulse that generated the point as given in Figure A-19. The applications search feature allows the user to visualize the point cloud data in a tabular context (all points are listed in a table view), where the users can query, arrange points according to elevation (from higher to lower or vice versa), intensity, etc. Global Mapper displays the elevation in meter values (with cm precision) (Figure A-19c). It has an overlay control center seen in Figure A-19 (d) where it displays features statistics of the LiDaR dataset. The point cloud bounds detected in Global Mapper were: West=-41.476, North=61.55, South=-73.586, and East=258.087. The metadata generated from Global Mapper module for the point cloud are:

Minimum intensity = 0 and the maximum intensity is 255

Number of points = 11,836,391

Point cloud memory=43.6 mb (i.e. amount of memory)

LiDaR point density=0.0000027519 samples / km^2

LiDaR scale=(0.001, 0.001, 0.001)

Upper left x=-13.3593000000

Covered area=37153902 sq. km

File load time=2.84 s

Min elevation=-41.563 meters

Max elevation=60.331 meters

Flight_date=02/07/2014

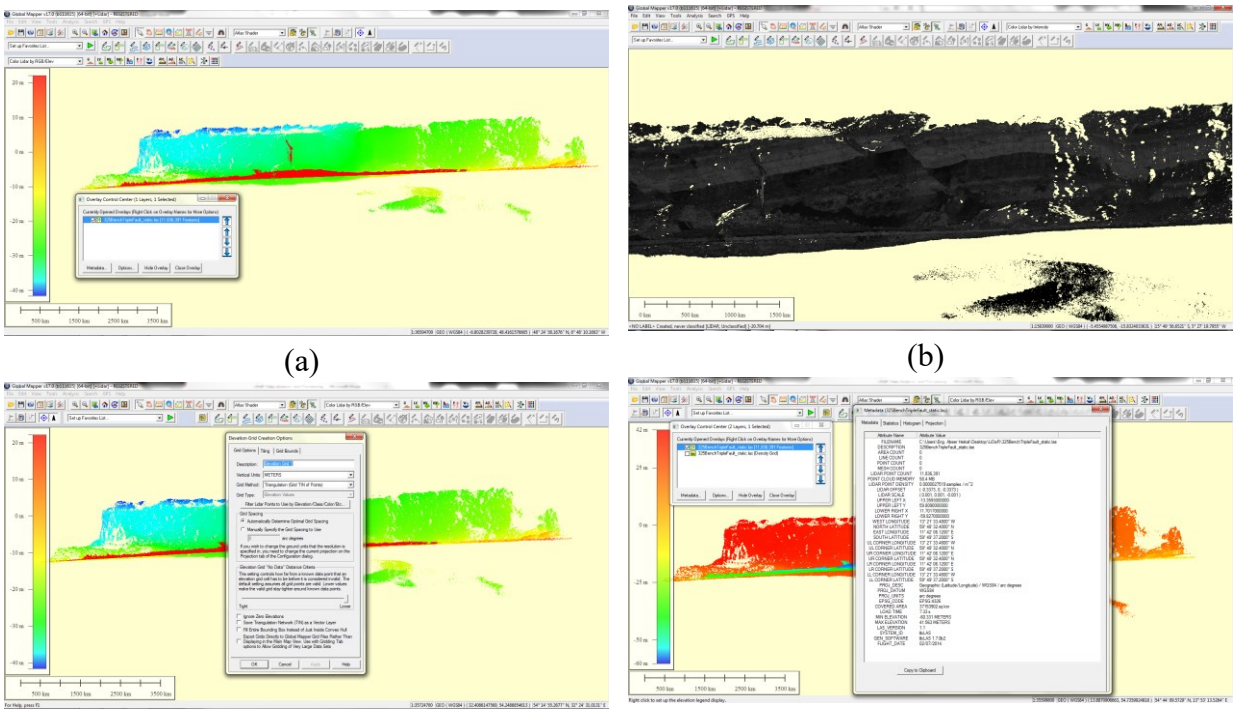

(a) (b)

(c) (d)

Figure A-19 Registered point cloud after (a) reorientation and overlay control center, (b) intensity-colored, (c) elevation-grid, (d) metadata in Global Mapper LiDaR Module

A.8.2.1. LIDAR MODULE

Blue Marble (GEOGRAPHICS) equipped Global Mapper with a LiDaR Module. The module is powered by a pixels-to-points tool. It supports manipulating high-density 3D point cloud, orthoimage, and 3D mesh from overlapping images. The LiDaR Module can powerfully edit, delete, modify, and process a point cloud as seen in Figure A-20. LiDaR Module has an option

dialog box that contains tools for establishing transparency, adjusting color balance, contrast, etc., and cropping an image to a defined area. The LiDaR tab provides settings for filtering a point cloud based on classification or laser-return intensity. Moreover, the LiDaR Module toolbar is equipped with an extract vector features button.

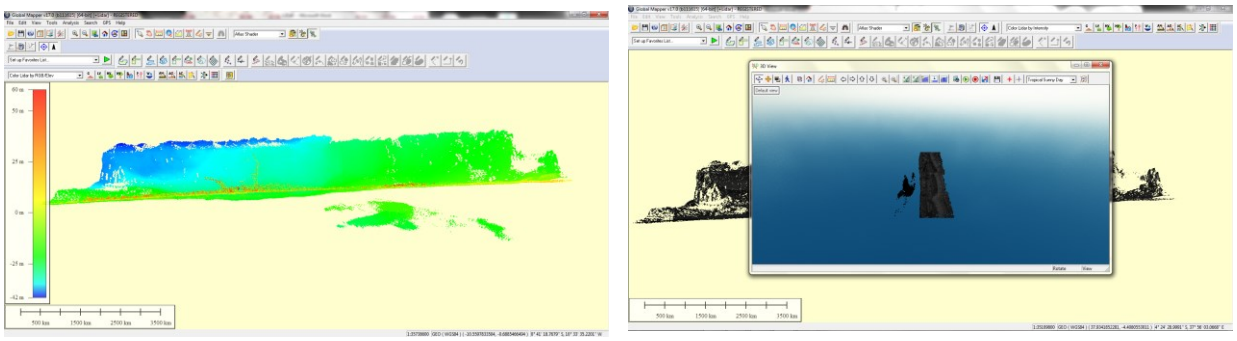

(a) (b)

Figure A-20 LiDaR point cloud colored by (a) RGB/elevation (default) and (b) 3D view of whole point cloud in LiDaR Module

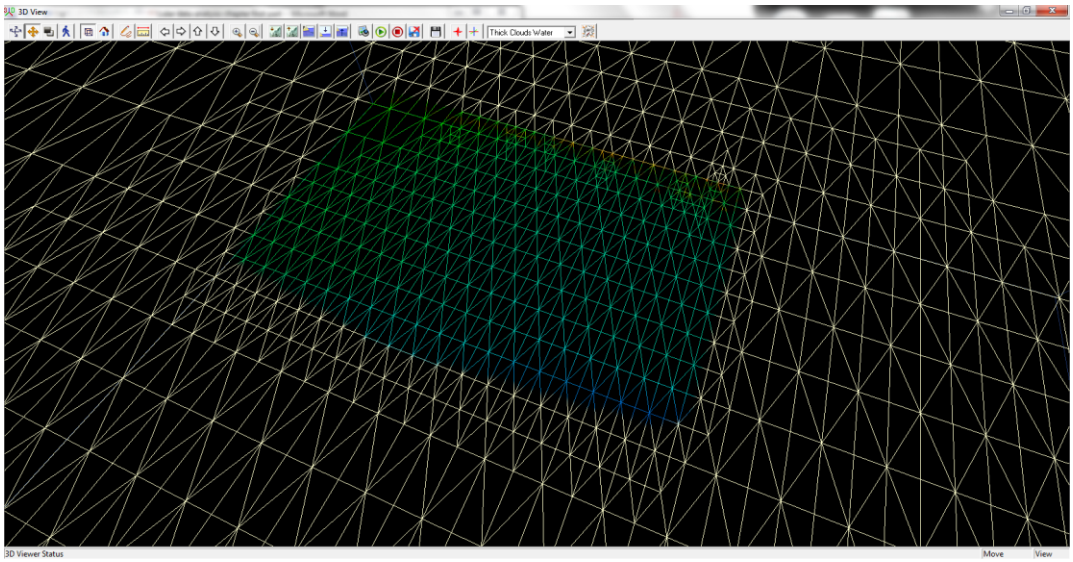

Figure A-21 3D view of TIN grid (zoomed in)

A.8.2.2. TIN GENERATION

After importing (registering) the LiDaR point cloud, into the Global Mapper LiDaR Module, it can be filtered, sampled, and can be triangularly gridded as seen in Figure A-22. Once imported, the points inherit the colors of the currently selected shader and reflect the elevation value if no other color values have been assigned to each point as seen in Figure A-20 (a). Creating a terrain surface (raster) from the loaded LiDaR data involves using Global Mapper standard

gridding tool (Figure A-23) and the resulted elevation layer. A raster is defined as a rectangular pattern of parallel scanning lines.

Steps to generate a TIN using the LiDaR Module in Global Mapper are illustrated in Figure A- (1-4). For the step of creating an elevation grid from the 3D vector data the user can choose between TIN or binning. For the created TIN, the options could be TIN loose (elevation grid 4) or TIN tight (elevation grid 5).

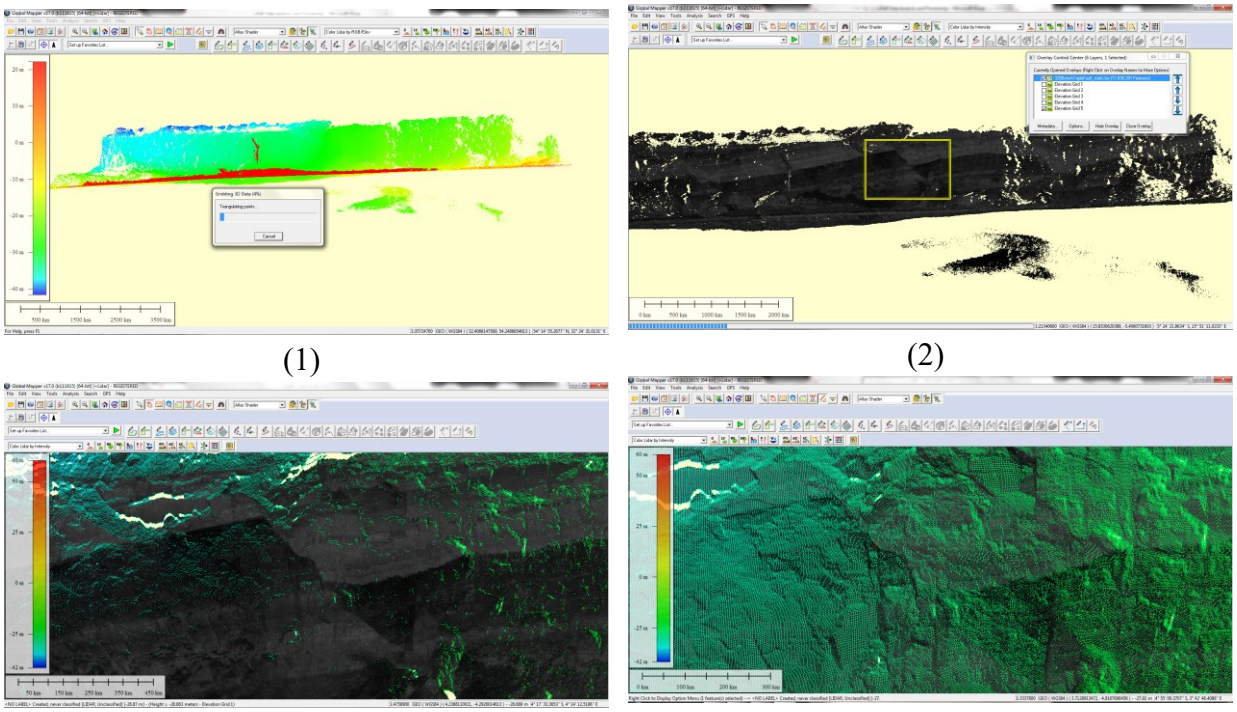

(1) (2)

(3) (4)

Figure A-22 TIN generation steps using the LiDaR Module in Global Mapper

A.8.3. CloudCompare

CloudCompareV2.6.2 Stereo developed in C++ is a 3D point cloud and triangular mesh processing software. It was originally designed to perform comparison between two 3D point clouds (such as ones obtained with a laser scanner) or between a point cloud and a triangular mesh. Afterwards, the software has been extended to a more generic point cloud processing, including implementation of many advanced algorithms (for registration, resampling, color/normal/scalar fields handling, statistics computation, sensor management, interactive or automatic segmentation, display enhancement, etc.).

A.8.3.1. CLOUDCOMPARE PRINCIPLE

CloudCompare version 2.6.2 Stereo (OpenGL) relies on a specific octree structure that enables great performance when dealing with huge point clouds usually acquired by terrestrial laser scanners (typically more than 10-million points, and up to 120 million with 2 Gb of memory) on a standard laptop (Figure A-24).

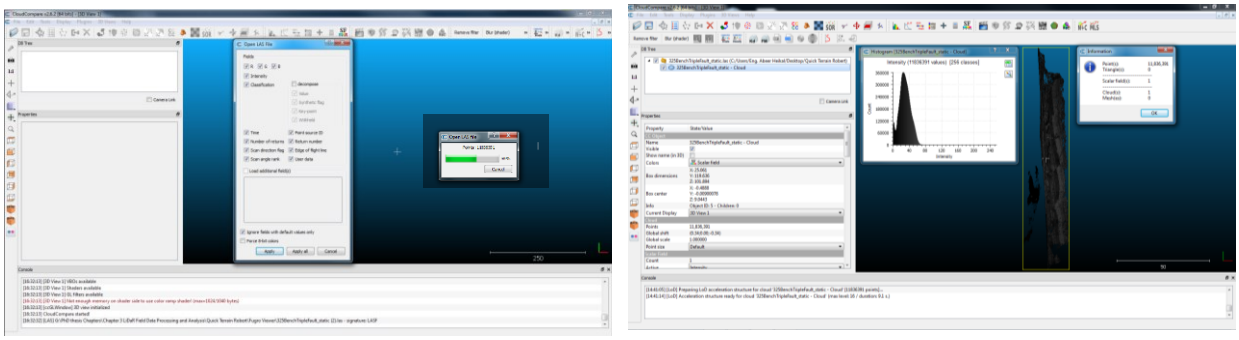

(a) (b)

Figure A-243 (a) Importing raw 11,836,391 raw LAS file into CloudCompare 3D view and (b) properties, intensity histogram and information of loaded point cloud

A.8.3.2. FACETS PLUGIN

Cloud Compare includes a facets plugin which is designed to extract discontinuity planes as 2D polygons (a facet is a rectangle fracture) from point clouds. The plugin supports automatic extraction of planar facets (discontinuity planes), exporting the facets to SHP files, classifying the facets based on their orientation and their (orthogonal) distance, displaying the orientations on a stereogram/stereoplot, and filtering the facets (or the points if they have normals) based on their orientation. Facets plugin has a feature that allows the user to select multiple 'facets (a group of facets) and save the information about them in a CSV file format (as embodied in Table B- in Appendix B). In this file, facet index #, center coordinates, dip angle, dip direction, normal, spatial extents, etc. can be found.

A.8.3.3. CLOUDCOMPARE ANALYSIS

CloudCompare v2.6.2 Stereo (64bits) can display .LAS files in 3D (Figure A-24b) and process the LiDaR data per a step-wise workflow illustrated in Figure A-25.

A.8.3.4. SURFACE REORIENTATION

The whole point cloud was rotated (Figure A-26a-d) keeping the original number of points of 11,836,391 as scanned in field.

A.8.3.5. NORMALS ESTIMATION

A normal to surface may be computed in CloudCompare. A discontinuity plane is defined by a center point, normal vector and two plane extents (dx and dy) as in Table B- in Appendix B. In CloudCompare normals computation (Figure A-28b) can be accomplished by a Quadric, Plane or Triangulation generation procedure. Normals of discontinuities were estimated using PCL wrapper plugin (Figure A-28a) where the planes were identified as seen in Figure A-28c and d.

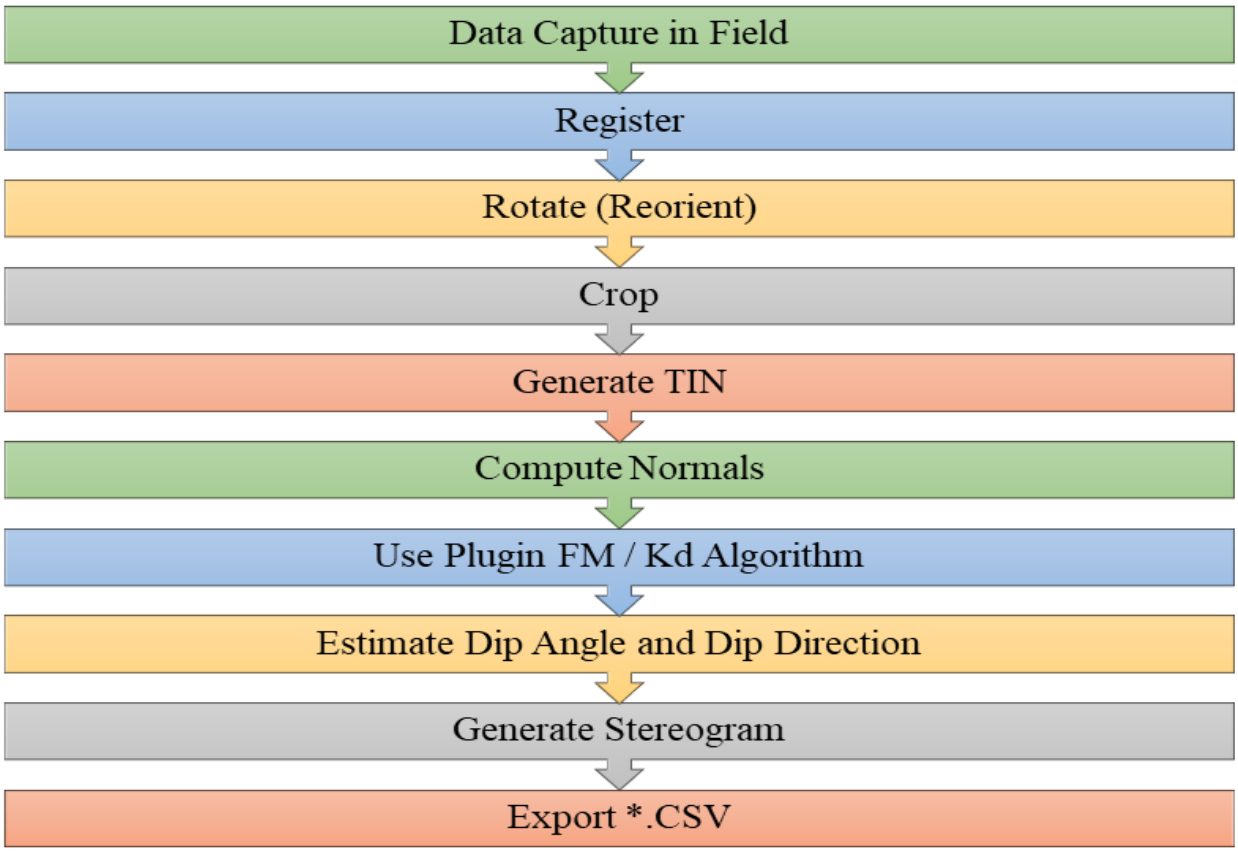

Figure A-254 Steps of processing LiDaR point cloud in CloudCompare

A.8.3.6. DISCONTINUITIES IDENTIFICATION

After smoothing and cropping the original point cloud (Figure A-27b), two algorithms; Fast Marching and Kd-Tree, that perform segmentation in CloudCompare were examined. The algorithms typically divide the point cloud into sub-cells, then compute elementary planar objects

and aggregate them progressively according to planarity threshold into polygons (Deweza et al., 2016) to extract discontinuity planes (Figure A-28).

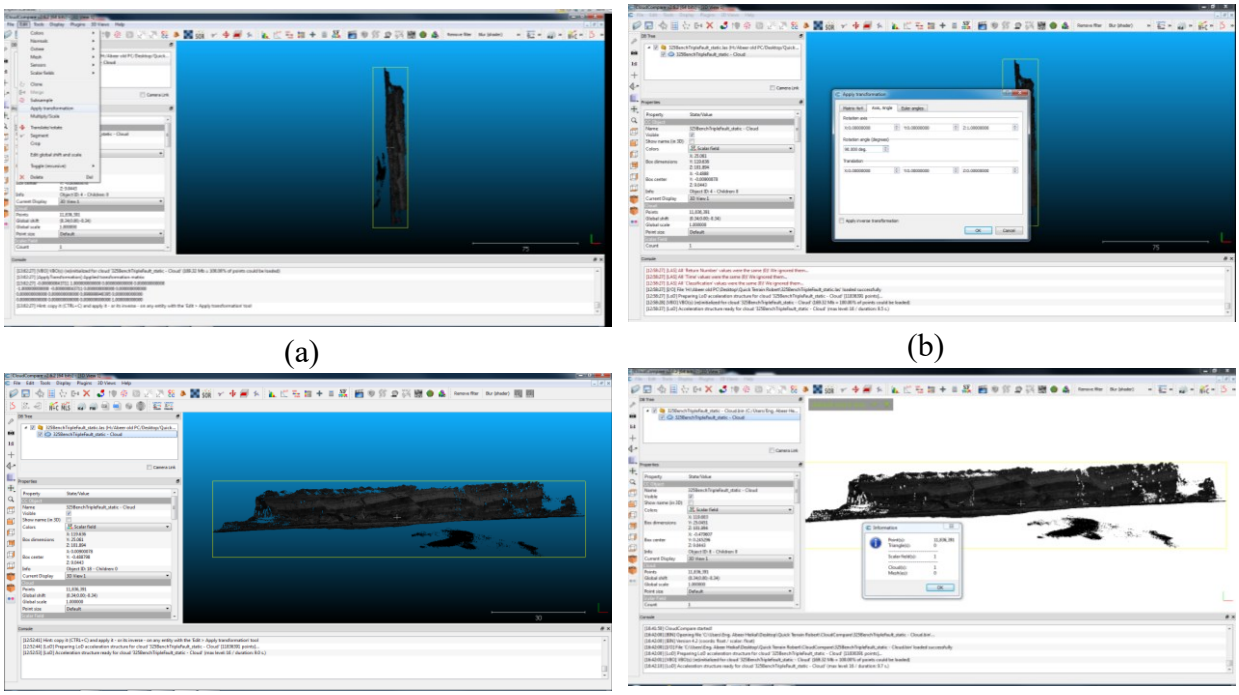

(a) (b)

(c) (d)

Figure A-265 Raw data (11,836,391 points) (a) visualization, (b) transformation, (c) rotation, and (d) information in CloudCompare

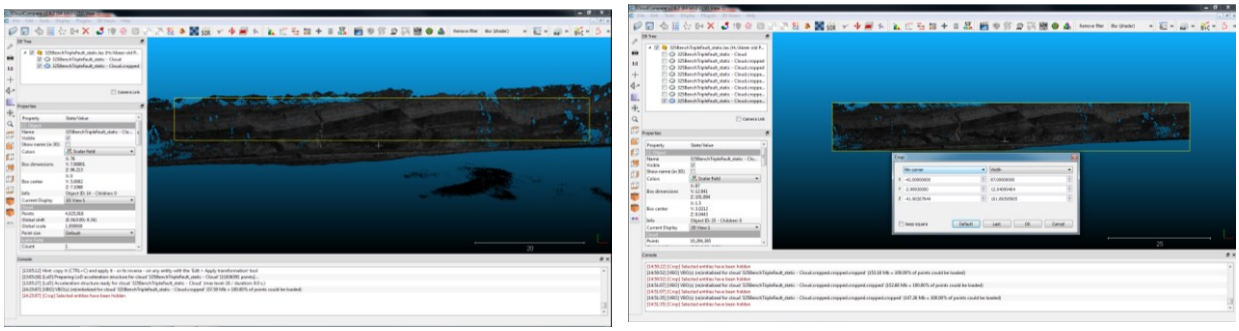

(a) (b)

Figure A-276 Smoothing (a) raw point cloud (11,836,391 – 10,294,385 – 4,025,916) (b) cropped point cloud

Extracting planar facets with a Kd-Tree algorithm recursively divide the point cloud into small patches. These planar patches are then regrouped in bigger 'facets'. Extracting planar facets with Fast Marching (FM) algorithm divide the cloud in smaller patches and then regroup them, where the subdivision is systematic and not recursive (Figure A-29). All patches have same size, but some may be flat while others not (based on the original point cloud resolution). A comparison between the point cloud processing results using the two algorithms is given in Table A-4.

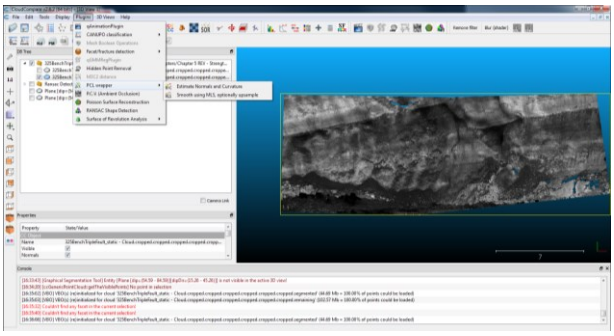

(a)

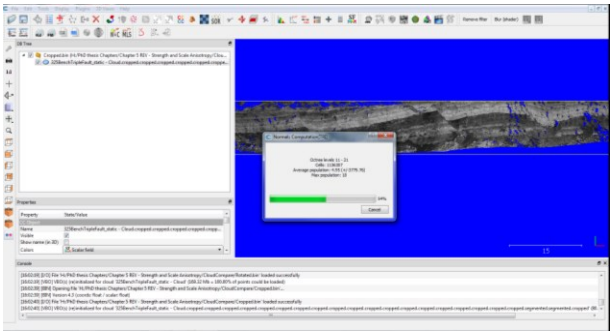

(b)

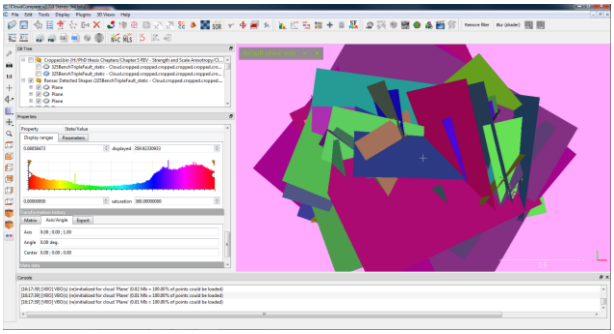

(c)

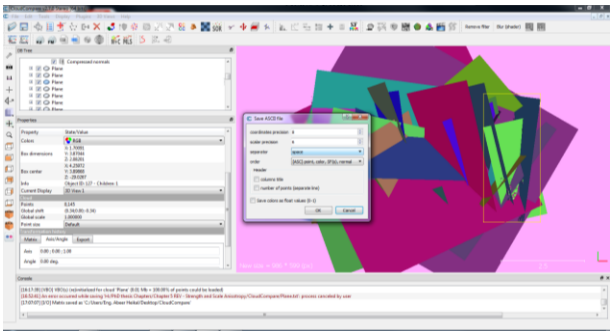

(d)

Figure A-287 Normals (a) estimation, (b) computation, (c) discontinuity planes information with properties histogram and (d) exporting

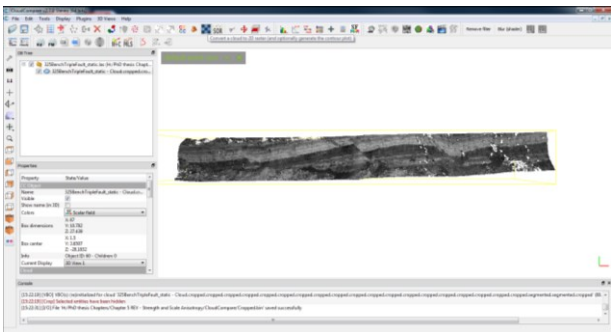

(a)

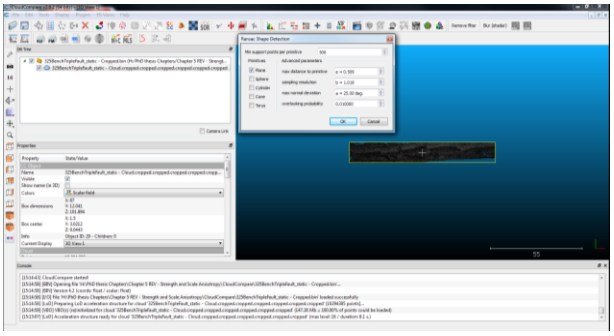

(b)

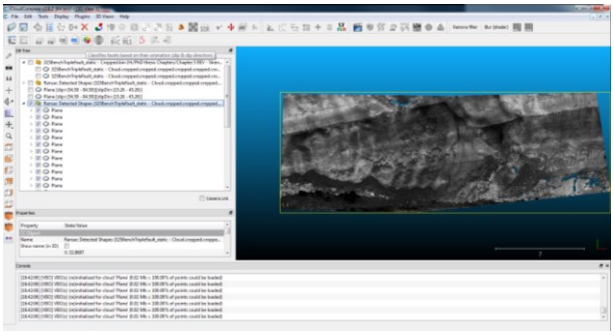

(c)

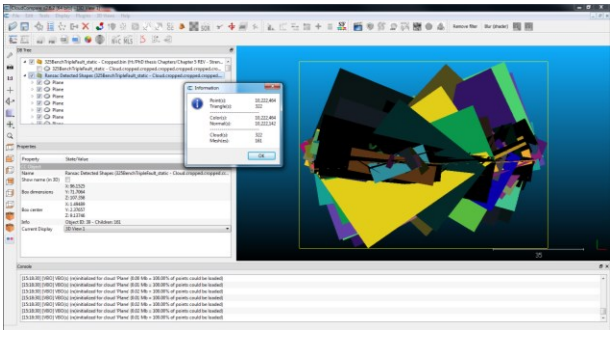

(d)

Figure A-28 (a) Cropped point cloud, (b) Ransac shape detection, (c) Ransac detected shapes and (d) information of detected shapes

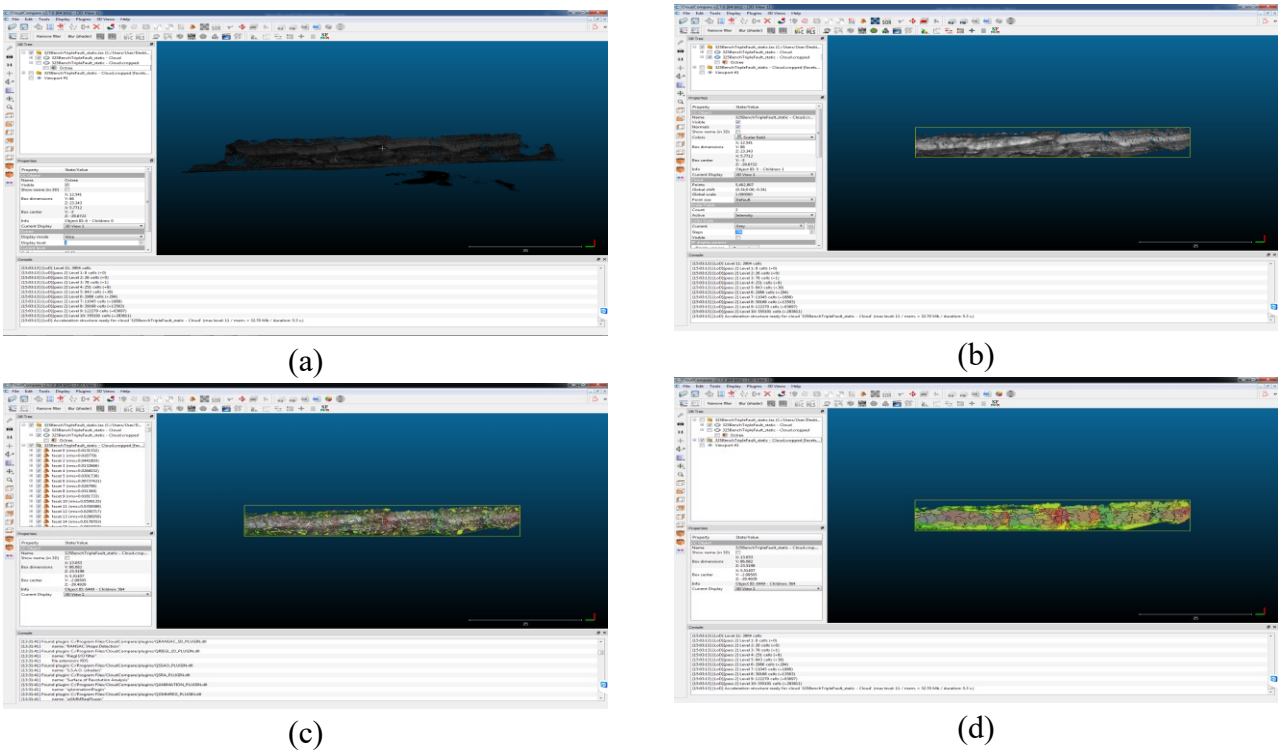

(a) (b)

(c) (d)

Figure A-29 Original point cloud (a) rotated, (b) cropped (5,402,807), (c) normals computed and (d) facets identified

A.8.3.7. DIP ANGLE AND DIP DIRECTION

The next step in TIN generation after establishing the normals, is converting these normals to dip angles and dip directions. Every normal vector can be converted into dip (inclination of the plane from the horizontal with respect to XY plane, in degrees) and strike (compass direction of a coplanar horizontal line – expressed in decimal degrees counted clockwise with 0° = Y axis) as seen in Figure A- and Figure A-.

A.8.3.8. TIN GENERATION

A TIN is a set of triangles (Figure A-3) that are represented by triplets of integer indexes. Those indexes are relative to an associated cloud (the mesh vertices). Therefore, the mesh inherits all the features associated to the point cloud. Accordingly, a mesh can be associated with:

- per-triangle materials,
- per-triangle texture coordinates textures, and
- per-triangle normal vectors (Nx, Ny, and Nz).

Table A-4 Comparison between Kd-Tree and Fast Marching (FM) algorithms in CloudCompare

Kd-Tree algorithm 1164 facets	FM algorithm 328 facets

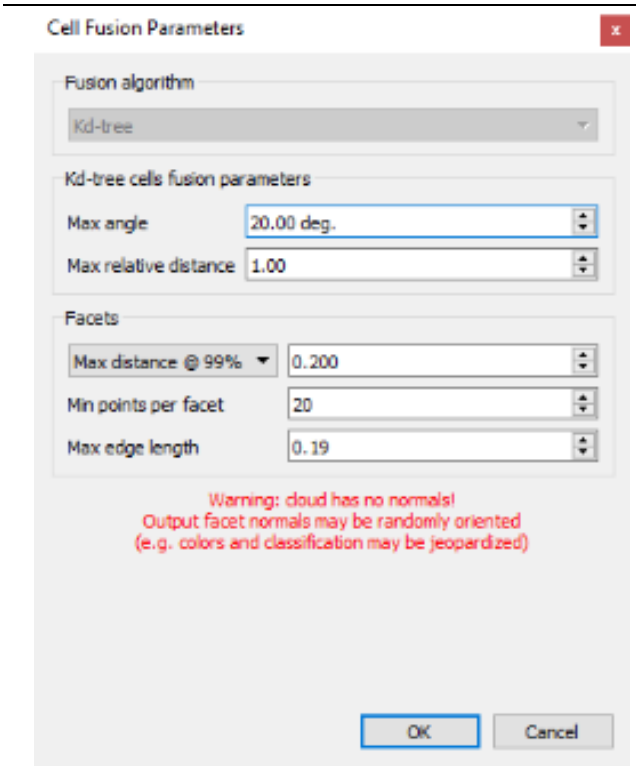

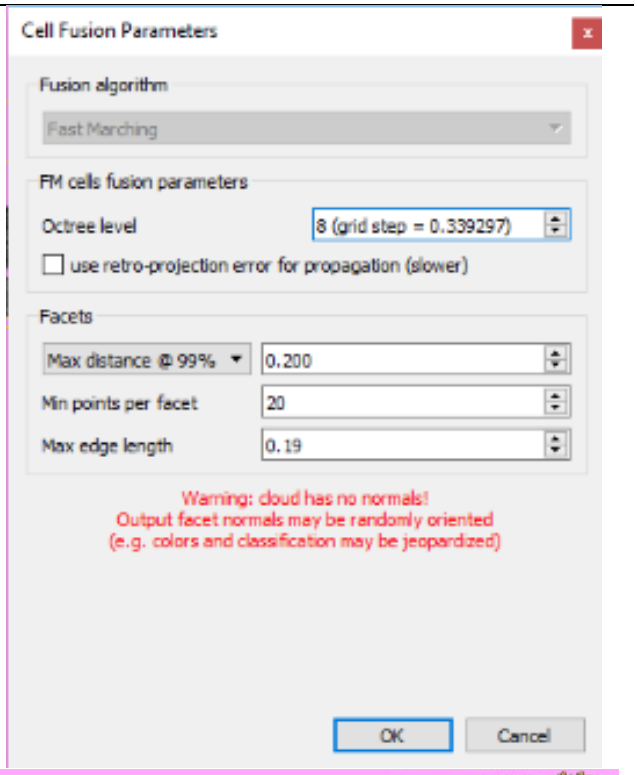

Kd_defualt

Index	CenterX	CenterY	CenterZ	NormalX	NormalY	NormalZ	RMS	Horiz_ext	Vert_ext	Surf_ext	Surface	Dip dir.	Dip
0	8.14702	70.9988	4.86898	0.844087	0.517192	0.141528	0.05221	0.656531	0.58766	0.385817	0.031875	58	81
1	7.8606	82.2126	3.59678	0.555586	-0.12142	0.822546	0.047672	0.610007	0.665418	0.40591	0.048508	102	34
2	10.1077	40.4238	10.0665	0.822191	-0.54945	0.148694	0.030284	0.524039	3.68137	1.92918	0.081364	123	81
3	9.90177	56.3464	3.62023	0.739766	0.276185	0.61357	0.045704	0.921769	0.594334	0.547839	0.089221	69	52
4	8.51687	57.4572	7.4144	0.828811	0.559292	0.016247	0.043068	0.558308	0.676074	0.377458	0.049555	55	89
5	8.64518	85.1508	1.11009	-0.69768	0.702616	0.139905	0.020155	0.171167	0.137958	0.023614	0.022075	315	81
6	7.79394	13.3986	19.4704	0.95729	0.228051	-0.17773	0.024124	0.185254	0.188167	0.034859	0.009289	256	79
7	7.62901	13.4191	19.5195	0.709739	0.445841	0.545432	0.030841	0.176034	0.261286	0.045995	0.027328	57	56
8	7.9648	84.2125	2.32053	0.309655	0.553475	0.773162	0.020464	0.435866	0.645498	0.281351	0.108247	29	39
9	9.99573	59.221	2.35293	0.602704	0.677696	0.421278	0.028419	0.412547	0.870185	0.358993	0.053354	41	65
10	7.74	83.8437	2.99327	0.789593	0.337233	0.512657	0.068904	0.573359	0.88505	0.507451	0.102741	66	59
11	11.9199	13.2439	16.7021	0.956451	-0.2155	-0.19689	0.029253	0.39126	0.382773	0.149763	0.020797	282	78
12	7.46103	84.983	3.5208	0.765928	0.12529	0.630601	0.066575	0.738456	0.709997	0.524302	0.011348	80	50
13	10.3742	40.8233	8.27817	0.25358	0.944367	-0.20945	0.039665	0.169423	0.499427	0.084615	0.001528	195	77
14	7.87015	84.5026	2.28653	0.794497	0.532987	0.291031	0.021888	0.204236	0.424218	0.086641	0.014665	56	73
15	11.6982	1.43045	19.0947	-0.22144	0.774891	-0.59204	0.024021	0.181728	0.148944	0.027067	0.020713	164	53
16	8.17122	71.4673	4.93562	-0.59362	0.795913	0.118908	0.045429	0.418741	0.518395	0.217073	0.013324	323	83
17	8.04789	71.2125	5.02098	-0.4716	0.766106	-0.43667	0.014423	0.324849	0.44671	0.145113	0.044821	148	64
18	5.67089	76.3094	4.4643	0.857744	0.514041	-0.00608	0.020669	0.429069	0.392028	0.168207	0.002877	239	89
19	8.14441	72.4178	4.57959	0.449467	0.074271	0.890204	0.024013	0.711676	0.348526	0.248037	0.084732	80	27
20	8.90857	78.3412	3.37727	0.708028	0.169394	0.685567	0.004578	0.300228	0.135063	0.04055	0.026691	76	46

FM_defualt

Index	CenterX	CenterY	CenterZ	NormalX	NormalY	NormalZ	RMS	Horiz_ext	Vert_ext	Surf_ext	Surface	Dip dir.	Dip
0	3.41265	85.4283	4.53427	0.740879	-0.02652	0.671115	0.093812	1.26903	1.19516	1.5167	0.801459	92	47
1	3.37222	82.8703	3.87683	-0.01149	-0.07536	0.99709	0.017904	0.668112	1.01695	0.679437	0.360075	188	4
2	3.61413	79.4791	4.04112	0.633593	0.021663	0.773363	0.018832	0.327488	0.405358	0.13275	0.105159	88	39
3	3.90792	82.312	3.77587	0.149403	0.143609	0.978292	0.015053	0.223465	0.235424	0.052609	0.026086	46	11
4	3.91999	75.6997	4.64182	-0.09392	0.343685	0.934377	0.027092	0.399159	0.411353	0.164195	0.117068	344	20
5	3.92099	82.1892	3.93937	-0.0119	-0.03642	0.999266	0.077286	2.71721	4.13951	11.2479	4.72585	198	2
6	4.35967	70.9059	5.53503	-0.08278	0.372798	0.924213	0.001786	0.136215	0.169259	0.023056	0.018081	347	22
7	4.58436	74.7336	4.68596	-0.12325	0.147897	0.981292	0.015503	0.45338	0.442522	0.200631	0.111055	320	11
8	3.77792	63.6451	7.32113	0.310053	-0.25066	0.917079	0.053292	0.529629	0.733403	0.388432	0.219695	128	23
9	3.97612	62.5391	7.073	0.326832	-0.04796	0.943864	0.031657	0.313656	0.275211	0.086322	0.070749	98	19
10	5.28793	80.4619	3.73132	0.283027	-0.45695	0.843264	0.006521	0.443058	0.345476	0.153066	0.097886	148	32
11	4.5775	79.242	3.9395	-0.01922	0.367825	0.929696	0.062812	1.93524	0.978226	1.89311	1.22079	357	21
12	4.59622	68.6271	6.25462	-0.08905	0.101985	0.990792	0.027903	0.463466	0.443641	0.205613	0.112173	318	7
13	4.2492	68.0185	6.31321	0.034322	0.061847	0.997495	0.028098	1.18872	1.03407	1.22923	0.572615	29	4
14	5.6405	80.7255	3.77429	0.180596	-0.44222	0.878537	0.003771	0.364484	0.174531	0.063614	0.039968	157	28
15	5.94868	84.2098	4.1049	-0.00974	-0.18158	0.983329	0.013183	0.342696	0.351101	0.120321	0.111026	183	10
16	6.28814	84.683	4.07061	0.308932	-0.09424	0.946403	0.035845	0.726556	0.532174	0.386654	0.230114	106	18
17	5.27371	71.3269	5.5819	-0.22781	0.351002	0.908241	0.011666	0.449851	0.451899	0.203287	0.119791	327	24
18	5.24722	70.3356	5.80049	-0.10921	0.084831	0.990392	0.02446	0.397748	0.428896	0.170592	0.094833	307	7
19	4.4571	77.6823	4.32361	0.075983	0.058443	0.995395	0.069325	3.50375	3.24246	11.3608	5.33938	52	5
20	5.44791	75.5202	4.64597	0.11506	0.039744	0.992563	0.055951	1.03202	1.52344	1.57222	0.716354	70	6

The TIN algorithm, in CloudCompare, was run to generate a surface over the data points. The triangular mesh is generally considered to be a cloud, either by considering only its vertices or by sampling points on the mesh surface. In order to compute the triangulation, the point cloud is first projected in 2D on the (XY) plane. Then the corresponding 2D points are triangulated and the mesh structure (patches) is applied to the 3D points (Figure A-b).

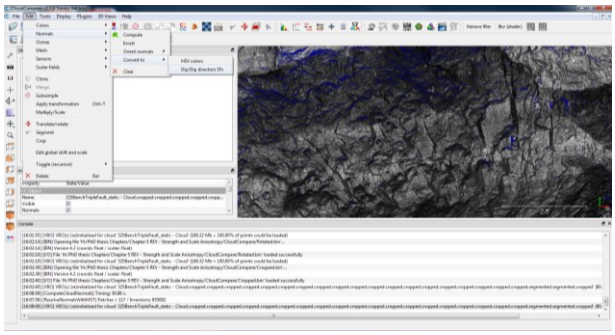

(a)

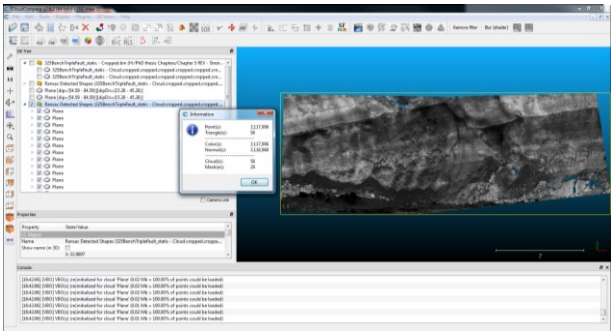

(b)

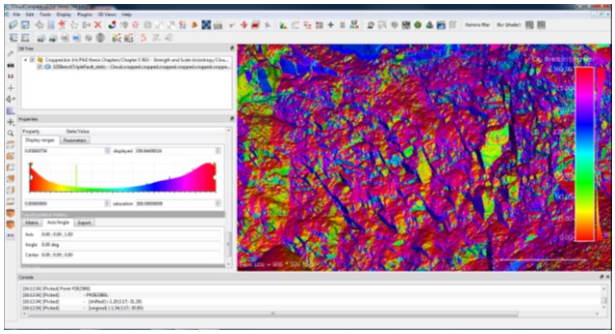

(c)

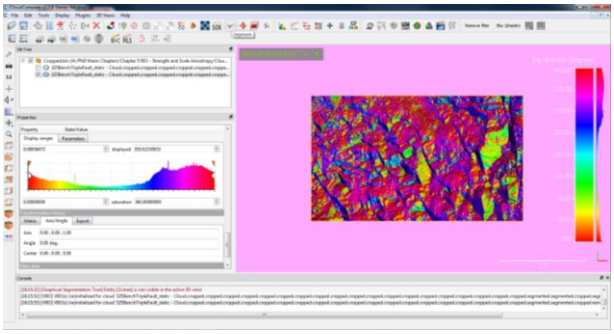

(d)

Figure A-30 (a) Segmented rectangle, (b) converting normals to dip/dip directions, (c) property histogram and shape information and (d) dip direction (°)-histogram

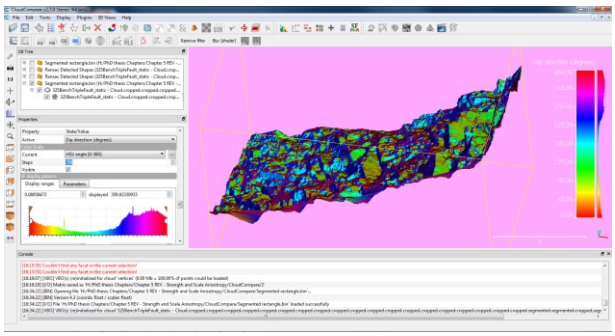

(a)

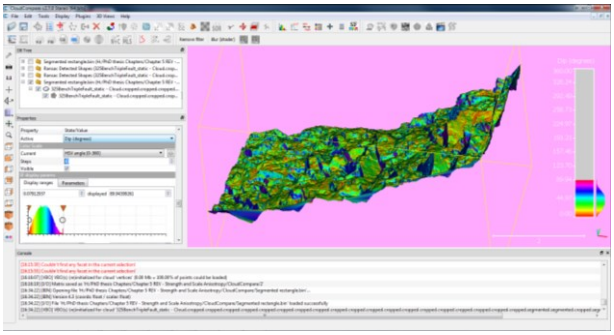

(b)

Figure A-31 (a) Dip direction (°) and (b) dip angle (°) histograms for segmented rectangle

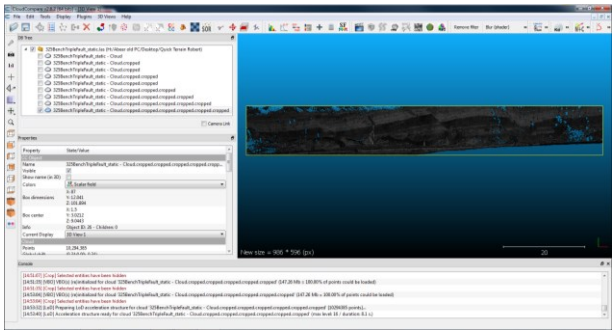

(a)

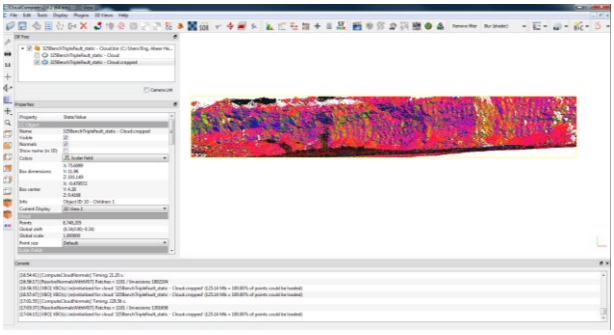

(b)

Figure A-32 (a) Cropped point cloud (10,294,385) and (b) identified patches (8,748,205)

A.8.3.9. STRUCTURAL STATISTICS

Stages of facets (patches) identification for a segmented rectangle of the LiDaR point cloud using CloudCompare are depicted in Figure A-. Detailed geostatistics information of the generated facets can be exported in a Microsoft Excel spread sheet .CSV format as in Table B-1 in Appendix B.

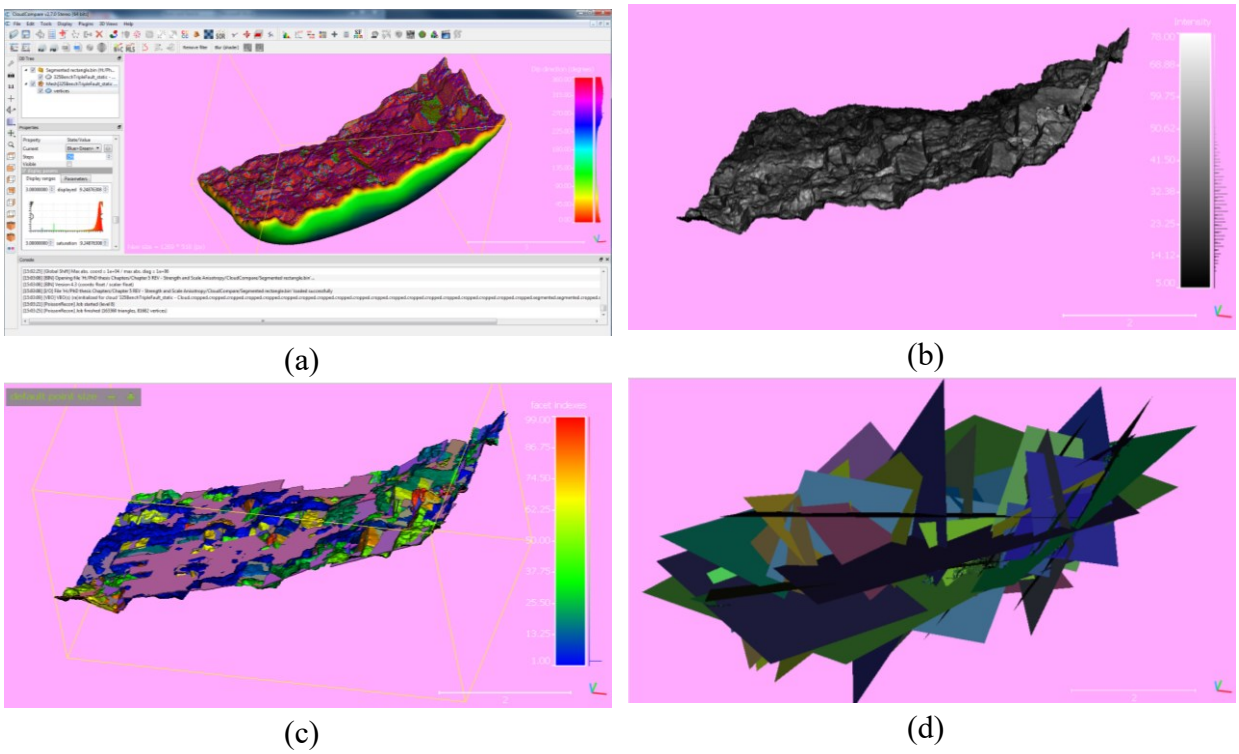

(a) (b)

(c) (d)

Figure A-33 (a) Mesh vertices, (b) dip-direction, (c) intensity, and (d) facets – discontinuity planes

A.8.4. DISCONTINUITY SET EXTRACTOR SOFTWARE

Discontinuity Set Extractor (DSE) software was developed and programmed by Adrián Riquelme from the University of Alicante for a testing part in his graduate studies. The DSE was aimed to extract discontinuity sets from a rock mass. The software input is a 3D point cloud, which can be acquired by means of a 3D laser scanner (LiDaR or TLS), digital photogrammetry techniques (such as SfM) or even synthetic data. The DSE applies a methodology to semi-automatically identify points members of an unorganized 3D point cloud that are arranged in 3D space by planes.

The DSE is an open source software programmed in MATLAB. It can run on Windows, MAC or Linux. In this appendix, DSE was used to manipulate the point cloud data set as seen in

Figure A- (a). First, smoothing of the raw point cloud was conducted where the number of points was reduced from 11,836,391 to 2,025,209 points. Second, ten joint sets were extracted from the point cloud and third a stereograph was generated as depicted in Figure A- (b). Finally, the statistical information, of the ten joint sets extracted, were as listed in Table A-5.

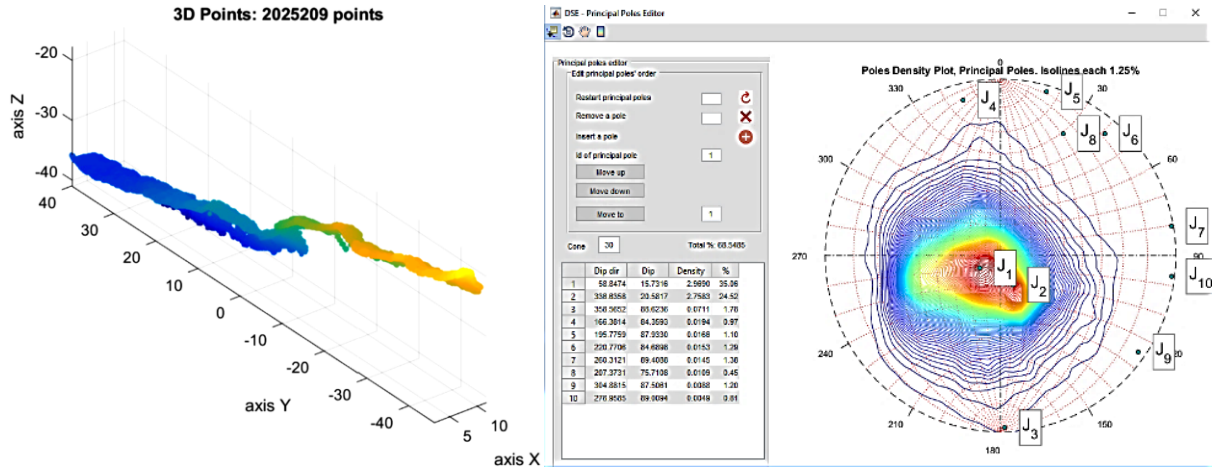

(a) (b)

Figure A-34 DSE (a) point cloud and (b) stereonet generated using DSE (10 joint sets)

Table A-5 Statistics of ten joint sets extracted using DSE

J. S.	Dip Direction	Dip Angle	Density	Fisher Constant K %
1	58.85	15.73	2.97	35.06
2	336.64	20.58	2.76	24.52
3	358.57	88.62	0.07	1.78
4	166.38	84.36	0.02	0.97
5	195.78	87.93	0.02	1.10
6	220.77	84.69	0.02	1.29
7	260.31	89.41	0.01	1.38
8	207.37	75.71	0.01	0.45
9	304.88	87.51	0.01	1.20
10	276.96	89.01	0.00	0.81

A.9 TRIANGULATED IRREGULAR NETWORK (TIN)

LiDaR data provide raw material needed for creating a realistic surface that can be used in engineering applications. The target in processing LiDaR data is generating a TIN surface from the points. In this appendix TIN generation was performed using FME, Global Mapper, and CloudCompare to verify the geologic data extracted and the generated TIN geometrical characteristics and for comparison purposes. The three generated TINs are depicted in Table A-6.

A.10 PROCEDURES COMPARISON

Five modules capable of manipulating LiDaR point cloud .LAS files were compared and investigated in processing the dataset as illustrated in Table A-7. The comparison was aimed to verify the point cloud extents, information, statistics, geologic data extracted, the generated TIN geometrical characteristics, flight date, size, and intensity. The modules are different in their capabilities, power of point cloud analyzing and degree of structural information-extraction.

A.11 SUMMARY

LiDaR technique compared to manual or hand mapping is much quicker, safer, cheaper, convenient and efficient in geological scanning of large areas. Terrestrial LiDaR survey methods can provide high-resolution data needed for volumetric and structural analyses. Those methods potentially facilitate making the analyses straightforward and routine. A LiDaR point cloud is a series of closely spaced points, each is associated with 3D coordinates, laser-intensity index and sometimes a classification that denotes the type of feature the point represents.

The motivational objectives of this appendix were; exploring publicly available LiDaR manipulation modules, generating a 3D TIN from a point cloud, and nominating satisfactorily processing platform/s. A large raw LiDaR dataset (≈ 0.4 GB) in .LAS format derived from a dense in situ point cloud (11,836,391) was used and processed in this investigation. A workflow was presented of how a LiDaR raw data can be registered, manipulated, and processed using open-source software. A 3D implicit structural model was built to visualize and identify the discontinuities planes and eventually extract their geological attributes statistics in a user friendly format (e.g. .csv). This appendix included a detailed step-by-step workflow of processing a raw point cloud until generating a 3D triangulated irregular network (TIN) needed for geomechanical modelling purposes.

Table A-6 Comparison of TINs generated using FME, Global Mapper and CloudCompare

FME	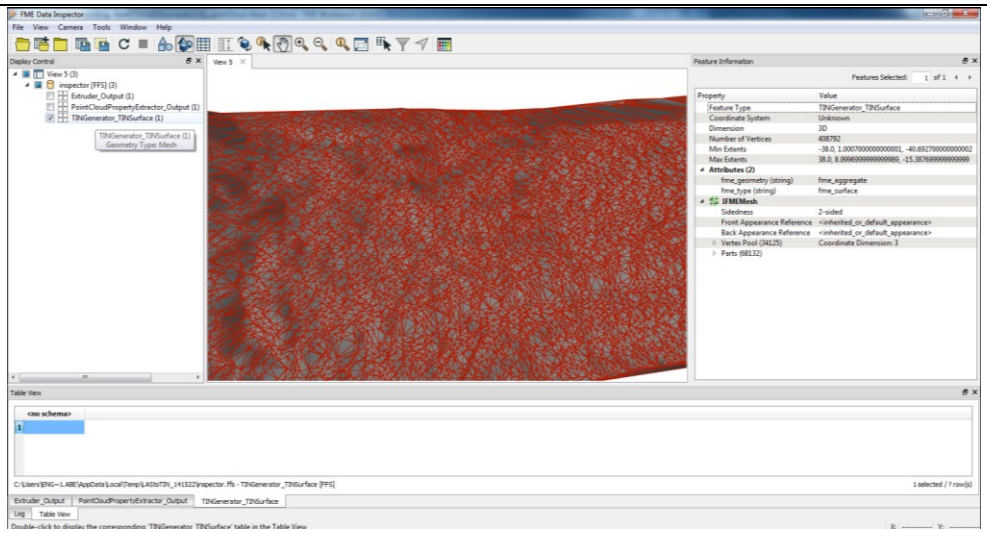
Global Mapper	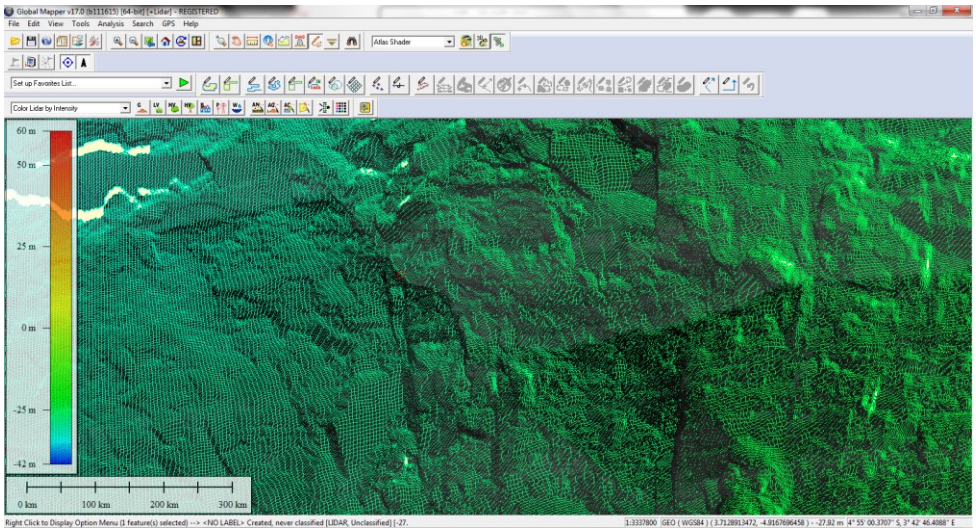
CloudCompare	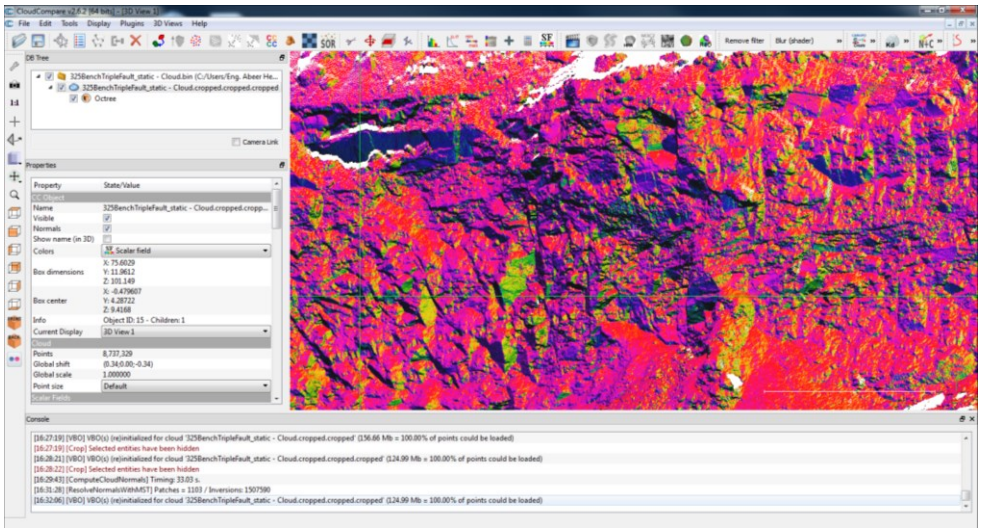

Table A-7 Comparison between five .LAS files manipulation modules

Module Attribute	CloudCompare	Global Mapper	FME	Split-FX	Quick Terrain Reader
Number of points	11,836,391	11,836,391	11,836,391	11,836,391	11,836,391
x-extents (m)	25.06	-13.35 : 11.70	-13.35 : 11.70		
y-extents (m)	119.63	-59.82 : 59.80	-59.82 : 59.80		
z-extents (m)	101.89	-41.56 : 60.33	-41.56 : 60.33		
Center X	-0.4888				
Center Y	-0.00900078				
Center Z	9.0443				
x-scale	1	0.001	0.001		
y-scale	1	0.001	0.001		
z-scale	1	0.001	0.001		
TIN (Y or N)	Y	Y	Y		
Dip & Dip Direction	Y				
Normals	Y				
Facets	Y				
Planes	Y				
Flight Date		02/07/2014	20140702		Jul 02 2014
Covered Area (km^2)		37153902		2553.57 m^2	
Latitude & Longitude		Lat=-6.0152869 Lon=108.30571			
Memory size (KB)		43600			402,437
Intensity	256 classes	0 : 255	UInt16		

This study contained a list of tens of explored open source software publicly available for LiDaR data (.LAS format) viewing and processing. In addition, the appendix included a comparison between multiple modules that support .LAS files manipulation at different levels. The generated point cloud attributes information was verified between five programs where, repeatable results were given higher reliability. Finally, an evaluation of the recommended software nominee was discussed. The generated TIN was examined in a comparison between three nominated modules.

A.12 CONCLUSIONS

The work presented here illustrates that starting from a mine bench scan with a laser camera in field, a LiDaR point cloud (millions of points) can be stored and registered. Scan data comprise the basic input in a long process of building a 3D TIN and extracting dip angle and dip direction values of the mine bench's discontinuities. Manipulating a point cloud includes registering, aligning, processing, loading, importing, visualizing, and reorienting of the LiDaR dataset. In this study, a point cloud was processed to generate a TIN via examining number of software. The generated TIN quality and the extracted geological features from each software were compared against each other.

The study strength in this appendix is embedded in the broad exploration of platforms publicly available to manipulate .LAS files. Moreover, comparing five of these platforms to process a single dataset scanned in situ. The comparison has been carried out in order to clarify the main bros and cons of each module. Differences in the generated TINs were outlined in order to assess in detail each software accuracy in extracting geological features. When geostatistics data is provided, it is not complicated to extract the geological attributes automatically. Eventual generation of a 3D TIN in CAD and the discontinuities geological attributes data in *.csv file format is of a practical significance within the geomechanical engineering applications.

The target of creating a 3D TIN out of scan points was accomplished in this appendix. The recommended method could help guiding first-time users of .LAS file format to process raw point cloud, generate structural statistics of discontinuities, and construct a stereonet. The appendix findings spotlight the potential of using LiDaR and high-resolution digital images in rock mass geological characterization maintaining convenient accuracy. The proposed procedure advantages include encountering minimal safety concerns and least possible in situ accessibility issues though maintaining a high productivity rate. It is emphasized though, when analyzing a LiDaR point cloud, it is necessary to adopt the suitable code according to the user's final targeted deliverable/s since each case is unique.

APPENDIX B. GEOSTATISTICS GENERATED USING CLOUDCOMPARE

The joint sets attributes generated for the studied point cloud using CloudCompare, are:

- Index
- Center (X,Y,Z)
- Normal (X,Y,Z)
- retro-projection error (RMS)
- Horiz_ext: horizontal extension
- Vert_ext: vertical extension
- Surf_ext: surface of the bounding rectangle (*in the facet plane*)
- Surface
- Dip direction
- Dip
- Family index (if any - see the Classification method below)
- Sub-family index (if any - see the Classification method below)

Structural spatial information, of each individual polygon of the 50 facets generated using CloudCompare, are listed in Table B-1.

Table B-1 CloudCompare 50 facets geostatistics - .csv file format

Index	CenterX	CenterY	CenterZ	NormalX	NormalY	NormalZ	RMS	Horiz_ext	Vert_ext	Surf_ext	Surface	Dip dir.	Dip	Family ind.
0	3.21978	3.73692	-29.6478	-0.06545	0.623816	0.778826	0.019262	0.148891	0.18038	0.026857	0.021015	354	38	0
1	0.624103	4.89208	-31.0454	0.513963	0.314538	0.798065	0.010487	0.19892	0.20708	0.041192	0.022809	58	37	0
2	3.27206	3.68531	-29.5434	-0.29093	-0.02124	0.956508	0.030094	0.174653	0.243181	0.042472	0.018906	265	16	0
3	-0.0179	4.5831	-31.3081	-0.1933	0.358972	0.913112	0.015804	0.348263	0.244165	0.085034	0.044196	331	24	0
4	0.558891	4.73793	-31.0831	-0.65454	-0.37148	0.658475	0.022777	0.235	0.345895	0.081286	0.046147	240	48	0
5	2.94624	2.7919	-29.3585	-0.90575	0.070364	0.417931	0.013756	0.357759	0.260814	0.093308	0.056708	274	65	0
6	3.25835	3.54665	-29.5114	0.088752	0.482134	0.871591	0.018589	0.257343	0.206327	0.053097	0.039832	10	29	0
7	-0.53446	3.91698	-31.1946	-0.03728	0.289466	0.956462	0.014285	0.314279	0.312252	0.098134	0.078506	352	16	0
8	0.01538	3.0593	-30.7993	-0.62435	0.450214	0.638358	0.024133	0.389898	0.499456	0.194737	0.111257	305	50	0
9	0.025391	3.91245	-30.9997	-0.6942	-0.29038	0.658606	0.018989	0.340965	0.455216	0.155213	0.09489	247	48	0
10	2.96473	3.53267	-29.6407	-0.7506	0.32215	0.576905	0.024797	0.700174	0.466727	0.32679	0.142613	293	54	0
11	0.566683	3.63883	-30.7599	-0.10294	0.0721	0.992072	0.027757	0.368672	0.373234	0.137601	0.07225	305	7	0
12	2.14969	3.47146	-30.1181	-0.17069	0.098214	0.980418	0.015443	0.529596	0.34837	0.184496	0.071092	299	11	0
13	0.039285	4.28888	-31.0913	-0.4888	0.466043	0.737478	0.024228	0.58492	0.59107	0.345729	0.175719	313	42	0
14	2.05611	3.93708	-30.2734	-0.35292	-0.02074	0.935425	0.025107	0.298396	0.568513	0.169642	0.147673	266	20	0
15	2.80188	2.86413	-29.4712	0.080604	0.101079	0.991608	0.03437	0.382697	0.637176	0.243845	0.099287	38	7	0
16	0.018422	3.63058	-30.9744	-0.55657	0.495326	0.666998	0.019823	0.398963	0.501144	0.199938	0.107647	311	48	0
17	1.64456	4.35668	-30.4387	-0.14367	0.241703	0.959656	0.021993	0.509744	0.639949	0.32621	0.1529	329	16	0
18	1.10932	3.9223	-30.5717	-0.35283	-0.19321	0.91552	0.043397	0.361258	0.36281	0.131068	0.07434	241	23	0
19	0.569726	4.50768	-31.0256	-0.74086	0.295674	0.603075	0.020415	0.364624	0.508818	0.185527	0.11379	291	52	0
20	3.20448	4.23767	-29.6186	-0.76793	0.404628	0.496548	0.02736	0.386907	0.425866	0.16477	0.114401	297	60	0
21	3.41439	3.94318	-29.3102	0.099591	-0.08759	0.991166	0.021668	0.344371	0.368736	0.126982	0.064568	131	7	0
22	-0.24632	4.50352	-31.3591	-0.13053	-0.07872	0.988314	0.025611	0.372493	0.378919	0.141145	0.076688	238	8	0
23	-0.52764	4.65831	-31.4632	-0.50404	0.425027	0.751863	0.039247	0.643207	0.673581	0.433252	0.210385	310	41	0
24	1.64511	3.22045	-30.2332	0.322571	0.321326	0.890336	0.028833	0.996096	1.02507	1.02106	0.326513	45	27	0
25	1.11067	3.63332	-30.5405	-0.79835	-0.15837	0.581	0.021376	0.315673	0.454767	0.143558	0.105356	258	54	0
26	1.25139	3.21468	-30.3959	-0.85261	-0.32011	0.413012	0.075247	0.706806	0.626467	0.442791	0.108206	249	65	0
27	-0.2542	4.80785	-31.4451	-0.14158	0.696916	0.703039	0.017295	0.332605	0.476081	0.158347	0.115636	348	45	0
28	3.00859	4.59926	-29.9742	-0.57408	0.423847	0.700563	0.028182	0.597428	1.122	0.670313	0.211082	306	45	0
29	2.71385	4.08562	-30.0224	-0.34843	0.159347	0.923692	0.019934	0.600668	0.494784	0.297201	0.15535	294	22	0
30	1.85261	4.58509	-30.5532	0.010646	0.469962	0.882622	0.035168	0.557157	1.03826	0.578473	0.38592	1	28	0
31	3.03944	4.0342	-29.7527	-0.72358	-0.13035	0.677817	0.035667	0.636089	0.737923	0.46937	0.279687	259	47	0
32	3.42134	4.19988	-29.3331	-0.01579	0.245123	0.969363	0.023561	0.345614	0.306765	0.106022	0.073644	356	14	0
33	-0.39487	4.20338	-31.2429	-0.25448	0.604638	0.754755	0.028999	0.640431	0.560464	0.358939	0.203388	337	40	0
34	-0.24917	3.91366	-31.122	-0.27762	-0.17041	0.945457	0.023009	0.367034	0.391168	0.143572	0.078026	238	19	0
35	2.48611	4.55904	-30.2543	-0.00097	0.479432	0.877578	0.01246	0.200567	0.572859	0.114896	0.088557	359	28	0
36	2.33707	2.73325	-29.6144	-0.62475	0.53398	0.569691	0.02064	0.445104	0.556682	0.247781	0.106551	310	55	0
37	3.44671	4.81547	-29.8004	-0.81848	0.30361	0.487767	0.017285	0.458015	0.427482	0.195793	0.133867	290	60	0
38	2.32137	3.06342	-29.8032	-0.7065	0.140818	0.693564	0.017643	0.431689	0.800081	0.345386	0.188895	281	46	0
39	1.90264	3.4377	-30.279	-0.79119	0.05839	0.608777	0.021221	0.445246	0.401355	0.178702	0.142444	274	52	0
40	0.436047	2.7833	-30.4561	-0.08388	0.337961	0.937415	0.018962	0.582358	0.419948	0.24456	0.158198	346	20	0
41	3.45212	3.56835	-29.3325	-0.33801	0.028758	0.940703	0.029323	0.48429	0.191618	0.092799	0.067641	274	19	0
42	2.66593	3.24989	-29.6808	-0.51119	0.392314	0.764705	0.056945	1.87607	2.55016	4.78428	1.72703	307	40	0
43	1.05543	4.60439	-30.8083	-0.29471	0.46881	0.832684	0.025042	1.00479	1.15445	1.15998	0.583752	327	33	0
44	2.66916	4.58673	-30.157	-0.48878	0.479921	0.728537	0.059949	1.61742	2.08388	3.37051	1.08325	314	43	0
45	0.301048	4.36102	-31.0347	0.034019	0.604655	0.795761	0.017986	0.313499	0.820327	0.257171	0.207438	3	37	0
46	0.294761	3.63072	-30.8033	-0.0448	0.410643	0.910695	0.027085	0.308931	0.328136	0.101371	0.077965	353	24	0
47	1.43182	3.94026	-30.4235	0.011373	0.277154	0.960758	0.058454	0.55461	1.71325	0.950184	0.452505	2	16	0
48	0.205616	4.83547	-31.2903	-0.47478	0.067589	0.877508	0.053328	0.368833	0.853317	0.314731	0.201341	278	28	0
49	0.335677	3.31978	-30.7265	-0.37409	0.264942	0.888742	0.050274	2.35009	2.68471	6.30931	2.33678	305	27	0

APPENDIX C. MATLAB SCRIPT

The MATLAB script, that was built as mentioned in Chapter 5 to visualize, display, and manipulate each discontinuity individually in 3D space, is given below.

```
Point at (x1,y1,z1) and normal vector v = [a,b,c], (v should be a row vector)
a(x-x1)+b(y-y1)+c(z-z1) = 0 ;
w = null(v); % Find two orthonormal vectors which are orthogonal to v
[P,Q] = meshgrid(-50:50); % Provide a gridwork (choose the size)
X = x1+w(1,1)*P+w(1,2)*Q; % Compute the corresponding Cartesian coordinates
Y = y1+w(2,1)*P+w(2,2)*Q; %  using the two vectors in w
Z = z1+w(3,1)*P+w(3,2)*Q;
surf(X,Y,Z)
G = sin((a*pi)/180)*tan((d*pi)/180).*(X - L_x*0.5) + cos((a*pi)/180)*tan((d*pi)/180).*(Y -
L_y*0.5) + E
L_x = 11.70;
L_y = 59.80;
s=1;
x = -13.35:s:L_x;
y = -59.82:s:L_y;
[X,Y] = ndgrid(x,y);
G = zeros(size(X));
E=-29.5434
a =265;
d =16;
G = sin((a*pi)/180)*tan((d*pi)/180).*(X - L_x*0.5) + cos((a*pi)/180)*tan((d*pi)/180).*(Y -
L_y*0.5) + E;
% option 2, fold train
surf(X,Y,G,'EdgeColor','none','FaceColor','b','FaceAlpha',0.33); hold on
```

A script example for discontinuity # 15:

```
%# Index # 15
filename='facets from cloud compare July1.xlsx';
xlRangep='B18:D18';
xlRangen='E18:G18';
point = [xlsread(filename,xlRangep)];
normal = [xlsread(filename,xlRangen)];
%# a plane is a*x+b*y+c*z+d=0
%# [a,b,c] is the normal. Thus, have to be calculated
%# d and are set
  d = -point*normal'; %'# dot product for less typing
%# create x,y
xlimmax=xlsread(filename,'','I18')
ylimmax=xlsread(filename,'','J18')
```

```
xLim = [0 xlimmax];
yLim = [0 ylimmax];
[X,Y] = meshgrid(xLim,yLim);
%# calculate corresponding z
G = zeros(size(X));
%# a = dip direction of plane:
   a =xlsread(filename,'','M18');
%# d = dip of plane:
   d =xlsread(filename,'','N18');
   G = sin((a*pi)/180)*tan((d*pi)/180).*(X)+ cos((a*pi)/180)*tan((d*pi)/180).*(Y);
surf(X,Y,G)
xlabel('X-Axis')
ylabel('Y-Axis')
zlabel('Z-Axis')
```

APPENDIX D. 3DEC FISH SCRIPT

Based on the manipulation of the in situ LiDaR data, the studied domain extents of the argillaceous rock mass scanned were 9.5 m × 86 m × 23 m as indicated in Appendix A and Chapter 5 discussion. A fractured model for the caprock was built using the FISH scripting language in the Itasca DEM suite (3DEC) Version 5.2 as follows (Unconfined_Intact_1800kPa model):

```
new
set small on
; The Caprock domain from CloudCompare
domain extent 2.2387 11.7017 0 86 0 23.23
;Ten Joint sets as detected from DSE
;1
;dfn template create name 'dfn_template1' id 1 dipdirlimit 58.84 58.86 diplimit 15.72 15.74 size
uniform
;dfn generate template name 'dfn_template1' density 0.3506
;2
;dfn template create name 'dfn_template2' id 2 dipdirlimit 336.63 336.65 diplimit 20.57 20.59
size uniform
;dfn generate template name 'dfn_template2' density 0.2452
;3
;dfn template create name 'dfn_template3' id 3 dipdirlimit 358.56 358.58 diplimit 88.61 88.63
size uniform
;dfn generate template name 'dfn_template3' density 0.0178
;4
;dfn template create name 'dfn_template4' id 4 dipdirlimit 166.37 166.39 diplimit 84.35 84.37
size uniform
;dfn generate template name 'dfn_template4' density 0.0097
;5
;dfn template create name 'dfn_template5' id 5 dipdirlimit 195.77 195.79 diplimit 87.92 87.94
size uniform
;dfn generate template name 'dfn_template5' density 0.0110
;6
;dfn template create name 'dfn_template6' id 6 dipdirlimit 220.76 220.78 diplimit 84.68 84.70
size uniform
;dfn generate template name 'dfn_template6' density 0.0129
;7
;dfn template create name 'dfn_template7' id 7 dipdirlimit 260.30 260.32 diplimit 89.40 89.42
size uniform
;dfn generate template name 'dfn_template7' density 0.0138
;8
;dfn template create name 'dfn_template8' id 8 dipdirlimit 207.36 207.38 diplimit 75.70 75.72
size uniform
;dfn generate template name 'dfn_template8' density 0.0045
```

```
;9
;dfn template create name 'dfn_template9' id 9 dipdirlimit 304.87 304.89 diplimit 87.50 87.52
size uniform
;dfn generate template name 'dfn_template9' density 0.0120
;10
;dfn template create name 'dfn_template10' id 10 dipdirlimit 276.95 276.97 diplimit 89.00 89.02
size uniform
;dfn generate template name 'dfn_template10' density 0.0081
plot create plot 'DFN'
plot dfn value
plot set dip 125 dd -160
plot add axes
; Sets general tolerance for the model, 0.12% of the average model dimension;
set atol 0.0474772
poly brick 2.2387 11.7017 0 86 0 23.23
; geology (+ bedding planes) Block cutting
;jset dip 90 dd 138 origin 2.2387,43,23.23; One fault
;jset dip 270 dd 90 origin 6.42 0 0 join ; top bedding plane
;jset dip 270 dd 90 origin 5.73 0 0 join ;
;jset dip 270 dd 90 origin 4.91 0 0 join ;
;jset dip 270 dd 90 origin 4.71 0 0 join ; top of the dark seam
;jset dip 270 dd 90 origin 4.57 0 0 join ; bottom of the dark seam
;jset dip 270 dd 90 origin 3.58 0 0 join ; Bottom bedding plane
;jset dfn 1
;jset dfn 2
;jset dfn 3
;jset dfn 4
;jset dfn 5
;jset dfn 6
;jset dfn 7
;jset dfn 8
;jset dfn 9
;jset dfn 10
plot create plot 'Fractured Block'
plot block colorby block
plot set dip 125 dd -160
plot add axes
List block
List contact
;Mesh for deformable blocks is generated
gen edge 2
; Turns nodal mixed discretization (NMD) on for plasticity calculations
set nodal on
; 1 on the fracture
;prop jmat 1 jfric 20 jcoh 1e5 jkn 4.5e8 jks 4.5e7
;; 2 outside the fracture = like intact
```

;prop jmat 2 jfric 30 jcoh 150e3 jkn 833e6 jks 179e6
;change dfn 1 jmat 1 2 jcons 1 2
;change dfn 2 jmat 1 2 jcons 1 2
;change dfn 3 jmat 1 2 jcons 1 2
;change dfn 4 jmat 1 2 jcons 1 2
;change dfn 5 jmat 1 2 jcons 1 2
;change dfn 6 jmat 1 2 jcons 1 2
;change dfn 7 jmat 1 2 jcons 1 2
;change dfn 8 jmat 1 2 jcons 1 2
;change dfn 9 jmat 1 2 jcons 1 2
;change dfn 10 jmat 1 2 jcons 1 2
dfn intersection id 5 name all
list dfn
plot dfn intersection
plot set dip 125 dd -160
plot add axes
zone model strainsoften density 2.129e3 bulk 833e6 shear 179e6 friction 30 &
cohesion 150e3 tension 0 dilation 20 &
ftable 1 ctable 2 dtable 3 ttable 4
table 1 0,30 .01,9.8
table 2 0,150e3 .01,0
table 3 0,20 .01,0
table 4 0,0 .01,0.0
;gravity -9.81,0,0
; Stress boundary conditions should always be applied before velocity boundary conditions
; Mechanical Boundary Conditions, vertical overburden stress= roh X gravity X H= 2129 X 9.81 X 150 = 3e6
;Bound stress -3e6,0,0,0,0,0 range x 11.7017
;Bound stress 0,-3.4e6,0,0,0,0 range y 86
;Bound stress 0,0,-4.36e6,0,0,0 range z 23.23
;Bound stress -3e6,0,0,0,0,0 range x 2.2387
;Bound stress 0,-3.4e6,0,0,0,0 range y 0
;Bound stress 0,0,-4.36e6,0,0,0 range z 0
; Initial Boundary conditions in x, y and z directions
; If no range is specified, stresses are initialized for the entire model
;INSITU stress -3e6,-3.4e6,-4.36e6,0,0,0
; pinned points on the model 2.2387 11.7017 0 86 0 23.23
; Base
;boundary xvel=0 range x 2.2387 y 0 z 0
;boundary yvel=0 range x 2.2387 y 0 z 0
;boundary zvel=0 range x 2.2387 y 0 z 0
;boundary xvel=0 range x 2.2387 y 86 z 0
;boundary yvel=0 range x 2.2387 y 86 z 0
;boundary zvel=0 range x 2.2387 y 86 z 0
;boundary xvel=0 range x 2.2387 y 0 z 23.23
;boundary yvel=0 range x 2.2387 y 0 z 23.23

;boundary zvel=0 range x 2.2387 y 0 z 23.23
;boundary xvel=0 range x 2.2387 y 86 z 23.23
;boundary yvel=0 range x 2.2387 y 86 z 23.23
;boundary zvel=0 range x 2.2387 y 86 z 23.23
hist unbal ; ratio of maximum unbalanced force to total applied forces in model
hist ratio ; solve ratio
plot hist 2
plot vel
plot block colorby state ; friction and shear failure
plot set dip 125 dd -160
plot add axes
plot block fill off zonetensor stress colorby maximum; max prin stress
plot set dip 125 dd -160
plot add axes
plot hist 1
;solve
;save 10_@_equi_OB.sav
;save 10_@_equi_OB.3dprj
;save 10_@_equi_OB.3dsav
;reset disp jdisp time
;boundary stress -0.55e4,0,0,0,0,0 range x 2.2387 y 28 57
boundary xload 2.5e5 range x 2.2387 y 28 57 xhistory linear
;Mechanical Boundary Conditions, increased by applying upward SAGD stress of 1800 kPa
boundary yvel=0 range y 0
boundary yvel=0 range y 86
boundary zvel=0 range z 0
boundary zvel=0 range z 23.23
; pinned points on the model 2.2387 11.7017 0 86 0 23.23
; Base
boundary xvel=0 range x 2.2387 y 0 z 0
boundary yvel=0 range x 2.2387 y 0 z 0
boundary zvel=0 range x 2.2387 y 0 z 0
boundary xvel=0 range x 2.2387 y 86 z 0
boundary yvel=0 range x 2.2387 y 86 z 0
boundary zvel=0 range x 2.2387 y 86 z 0
boundary xvel=0 range x 2.2387 y 0 z 23.23
boundary yvel=0 range x 2.2387 y 0 z 23.23
boundary zvel=0 range x 2.2387 y 0 z 23.23
boundary xvel=0 range x 2.2387 y 86 z 23.23
boundary yvel=0 range x 2.2387 y 86 z 23.23
boundary zvel=0 range x 2.2387 y 86 z 23.23
; hist 3,4 ... 21,22 ... 39,40
hist xdisplacement (2.2387,43,12)
hist xdisplacement (11.7017,0,12)
hist xdisplacement (11.7017,5,12)
hist xdisplacement (11.7017,10,12)

hist xdisplacement (11.7017,15,12)
hist xdisplacement (11.7017,20,12)
hist xdisplacement (11.7017,25,12)
hist xdisplacement (11.7017,30,12)
hist xdisplacement (11.7017,35,12)
hist xdisplacement (11.7017,40,12)
hist xdisplacement (11.7017,45,12)
hist xdisplacement (11.7017,50,12)
hist xdisplacement (11.7017,55,12)
hist xdisplacement (11.7017,60,12)
hist xdisplacement (11.7017,65,12)
hist xdisplacement (11.7017,70,12)
hist xdisplacement (11.7017,75,12)
hist xdisplacement (11.7017,80,12)
hist xdisplacement (11.7017,85,12)
hist xdisplacement (2.2387,0,0)
hist xdisplacement (2.2387,5,0)
hist xdisplacement (2.2387,10,0)
hist xdisplacement (2.2387,15,0)
hist xdisplacement (2.2387,20,0)
hist xdisplacement (2.2387,25,0)
hist xdisplacement (2.2387,30,0)
hist xdisplacement (2.2387,35,0)
hist xdisplacement (2.2387,40,0)
hist xdisplacement (2.2387,45,0)
hist xdisplacement (2.2387,50,0)
hist xdisplacement (2.2387,55,0)
hist xdisplacement (2.2387,60,0)
hist xdisplacement (2.2387,65,0)
hist xdisplacement (2.2387,70,0)
hist xdisplacement (2.2387,75,0)
hist xdisplacement (2.2387,80,0)
hist xdisplacement (2.2387,85,0)
hist sxx (2.2387,43,12)
plot create plot 'Vertical upward displacement @ caprock base'
plot hist 3 yaxis label 'Vertical Displcement @ caprock base (m)'
plot create plot 'Vertical upward displacement @ caprock top surface'
plot hist 4,5,6,7,8,9,10,11,12,13,14,15,16,17,18,19,20,21 yaxis label 'Profile of Vertical Displcement @ caprock top surface (m)'
plot create plot 'Vertical upward displacement @ caprock base'
plot hist 22,23,24,25,26,27,28,29,30,31,32,33,34,35,36,37,38,39 yaxis label 'Profile of Vertical Displcement @ caprock base (m)'
plot create plot 'Vertical upward stress @ caprock base'
plot hist 40 yrev yaxis label 'Vertical Stress @ caprock base (Pa)'
plot add contour xdisp min 0.0
plot set dip 180 dd 360 roll 180

plot add axes
plot add boundary applied load pointtobase
plot jointcontour sdisplacement
plot set dip 125 dd -160
plot add axes
plot jointcontour ndisplacement
plot set dip 125 dd -160
plot add axes
save all_@_1800_OB.sav
save all_@_1800_OB.3dsav
list contact summary
list contact state
step 5000
save all_@_1800_OB.3dprj
ret

APPENDIX E. STRAIN SOFTENING CONSTITUTIVE MODEL

The 3DEC simulations carried out in Chapter 7 include the use of a strain softening (SS) constitutive model in the comparative modelling of two rock types. Parts of the FISH scripts are listed in Table E-1 for comparison.

Table E-1 Constitutive models assignment in FISH scripts

Rock type	**Marble**	**Clearwater clay shale (CCSh)**
Zone	density 2.58e3 bulk 3.3e10 shear 2e10 friction 43.8 & cohesion 19.4e6 tension 2.84e6 dilation 25 & ftable 1 ctable 2 dtable 3 ttable 4 table 1 0,43.8 .01,20 table 2 0,19.44e6 .01,19.44e2 table 3 0,25 .01,2 table 4 0,2.84e6 .01,0.0	density 2.129e3 bulk 833e6 shear 179e6 friction 30 & cohesion 150e3 tension 0 dilation 20 & ftable 1 ctable 2 dtable 3 ttable 4 table 1 0,30 .01,9.8 table 2 0,150e3 .01,0 table 3 0,20 .01,0 table 4 0,0 .01,0.0
Discontinuities	; 1 on the fracture prop jmat 1 jfric 30.44 jcoh 0.07e6 jkn 17e9 jks 9e9 ; 2 outside the discontinuity = like intact prop jmat 2 jfric 43.8 jcoh 19.44e6 jkn 3.3e10 jks 2e10 change jmat 1 jcons 1 prop jmat 1 jkn 17e9 jks 9e9 jcohesion 0.07e6 jfriction 30.44	; 1 on the fracture prop jmat 1 jfric 20 jcoh 1e3 jkn 4.5e8 jks 5e7 ; 2 outside the discontinuity = like intact prop jmat 2 jfric 30 jcoh 150e3 jkn 833e6 jks 179e6 change jmat 1 jcons 1 prop jmat 1 jkn 17e5 jks 9e5 jcohesion 0.07e3 jfriction 20

APPENDIX F. FISH SCRIPTS VERIFICATION

Table F-1 includes the verification of the mechanical results of a 1 m × 1 m × 1 m intact to lightly fractured blocks of CCSh tested under UCS along X, Y, and Z as discussed in Chapter 7. Two constitutive models (SS and MC) were examined in the comparison and verification of the input index parameter values versus the output results. The input data were:

a. Nu = 0.4

b. Deformation modulus = 500 MPa

c. UCS (of the intact)

Table F-1 Verifying mechanical behaviour of fractured 1 × 1 × 1 m^3 blocks of CCSh

	UCS loading along		X		Y		Z	
	Constitutive Model	Set Small	E (GPa)	UCS (MPa)	E (GPa)	UCS (MPa)	E (GPa)	UCS (MPa)
Intact	M.C.	On	0.40	0.60	0.40	0.60	0.40	0.60
		Off	0.40	0.60	0.40	0.60	0.40	0.60
	S.S.	On	0.40	0.59	0.40	0.59	0.40	0.59
		Off	0.40	0.59	0.40	0.59	0.40	0.59
Fractured	M.C.	On	0.50	0.51	0.40	0.46	0.06	0.53
		Off	0.40	0.52	0.40	0.46	0.06	0.58
	S.S.	On	0.50	0.46	0.50	0.39	0.04	0.31
		Off	0.50	0.46	0.50	0.39	0.04	0.32